Study of ${}^{3}_{\Lambda}$H and ${}^{4}_{\Lambda}$H in the reaction of ^{6}Li+^{12}C at 2 A GeV

DISSERTATION
zur Erlangung des Grades
"Doktor der Naturwissenschaften"
am Fachbereich 08
Physik, Mathematik und Informatik
Institut für Kernphysik
der Johannes Gutenberg Universität
in Mainz

Olga Bertini
geb. in Chita, USSR
Mainz, den 1 März 2013

Study of ${}^{3}_{\Lambda}$H and ${}^{4}_{\Lambda}$H in the reaction of ^{6}Li+^{12}C at 2 A GeV

DISSERTATION
submitted to attain the academic degree
"Doctor of Natural Sciences"
at the Department of
Physics, Mathematics and Computer Science
Institute of Nuclear Physics
of the Johannes Gutenberg University
in Mainz

Olga Bertini
born in Chita, USSR
Mainz, 1 March 2013

Abstract

The feasibility of studying hypernuclei by means of peripheral heavy ion induced reactions was demonstrated by observing clear signals of Λ, ${}^{3}_{\Lambda}\mathrm{H}$, ${}^{4}_{\Lambda}\mathrm{H}$ in their respective invariant mass distributions from their mesonic decay. The experiment was performed with ${}^{6}\mathrm{Li}$ beams at 2 A GeV impinging on a carbon target.

This thesis presents an independent analysis which aims to corroborate previous results obtained by the HypHI collaboration. For this purpose, a track reconstruction procedure, based on the Kalman filtering approach, and two different secondary vertex reconstruction algorithms have been implemented.

The invariant masses of the Λ-hyperon, the ${}^{3}_{\Lambda}\mathrm{H}$ and the ${}^{4}_{\Lambda}\mathrm{H}$ hypernuclei were found to be 1109.6 ± 0.38, 2981.0 ± 0.30 and 3898.1 ± 0.68 MeV/c^2 with statistical significance of 9.8σ, 12.8σ and 7.3σ, respectively. The results obtained in this work are in agreement with the previous analysis.

The hypernuclei yield ratio was found to be $N({}^{3}_{\Lambda}\mathrm{H})/N({}^{4}_{\Lambda}\mathrm{H}) \sim 3$, which suggests that the production mechanism of hypernuclear in heavy ion induced reactions in the projectile rapidity region involves not only the coalescence mechanism but also secondary pion-/kaon- induced reactions and Fermi break-up.

Zusammenfassung

Die Produktion von Hyperkernen wurde in peripheren Schwerionenreaktionen untersucht, bei denen eine Kohlenstofffolie mit ${}^{6}\mathrm{Li}$ Projektilen mit einer Strahlenergie von 2 A GeV bestrahlt wurde. Es konnten klare Signale für Λ, ${}^{3}_{\Lambda}\mathrm{H}$, ${}^{4}_{\Lambda}\mathrm{H}$ in deren jeweiligen invarianten Massenverteilungen aus Mesonenzerfall beobachtet werden.

In dieser Arbeit wird eine unabhängige Datenauswertung vorgelegt, die eine Verifizierung früherer Ergebnisse der HypHI Kollaboration zum Ziel hatte. Zu diesem Zweck wurde eine neue Track-Rekonstruktion, basierend auf einem Kalman-Filter-Ansatz, und zwei unterschiedliche Algorithmen zur Rekonstruktion sekundärer Vertices entwickelt.

Die invarianten Massen des Λ-Hyperon und der ${}^{3}_{\Lambda}\mathrm{H}$- und ${}^{4}_{\Lambda}\mathrm{H}$-Hyperkerne wurden mit 1109.6 ± 0.4, 2981.0 ± 0.3 und 3898.1 ± 0.7 MeV/c^2 und statistischen Signifikanzen von 9.8σ, 12.8σ beziehungsweise 7.3σ bestimmt. Die in dieser Arbeit erhaltenen Ergebnisse stimmen mit der früheren Auswertung überein.

Das Ausbeutenverhältnis der beiden Hyperkerne wurde als $N({}^{3}_{\Lambda}\mathrm{H})/N({}^{4}_{\Lambda}\mathrm{H}) \sim 3$ bestimmt. Das deutet darauf hin, dass der Produktionsmechanismus für Hyperkerne in Schwerionen-induzierten Reaktionen im Projektil-Rapiditätsbereich nicht allein durch einen Koaleszenzmechanismus beschrieben werden kann, sondern dass auch sekundäre Pion-/Kaon-induzierte Reaktionen und Fermi-Aufbruch involviert sind.

Contents

Chapter 1

Introduction

Contents

1.1 Hypernuclear physics

The main goal of hypernuclear physics is to improve our understanding of baryon-baryon interactions under flavored $SU(3)$ symmetry. Standard nuclear reaction experiments can only provide information about the nucleon-nucleon interaction. The hypernucleus is a bound system of a hyperon (Y) and a nucleus and gives the opportunity to use it as a micro-laboratory for studying hyperon-nucleon (YN) interactions. The hyperon-hyperon (YY) interaction can be studied via double Λ hypernuclei.

Through an understanding of YN and YY interactions we expect to be able to investigate new aspects and new forms of hadronic matter. In particular, detailed information on YN and YY interactions are indispensable for our understanding of high-density nuclear matter inside neutron stars. Depending on the strength of the YN interaction, the core of the neutron star may be composed of hyperons, strange quark matter or kaon condensate [1]. The additional strangeness degree of freedom softens the equation-of-state (EOS) leading to a smaller maximum mass of neutron stars compared to a purely nucleonic EOS [2].

The main object of hypernuclear research is studying the Λ-nucleus interaction. The Λ particle bound into a nucleus is an excellent probe of nuclear properties. The mass of Λ is $M_\Lambda = 1115$ MeV/c^2, exceeding the mass of a nucleon by approximately 20%. The Λ-nucleus interaction is weaker than the NN one [3]. We can therefore expect that a Λ particle behaves similar to a neutron, however as a neutron with a strangeness quantum number $S = -1$. The Λ particle is the lightest strange baryon. It is neutral and has spin-parity $J^\pi = \frac{1}{2}^+$ and isospin $I = 0$. The free Λ decays via weak interaction $\Lambda \rightarrow N + \pi$ with a lifetime of 2.631×10^{-10} sec [4]. In nuclear matter an additional decay mode is possible $\Lambda + N \rightarrow 2N$ which is also a weak decay. This decay mode defines the lifetime of the Λ in hypernuclei with $Z > 2$.

The lifetime of heavy hypernuclei is estimated to be about 10^{-10} sec. It allows the study of strong and electromagnetic properties of hypernuclei.

The study of hypernuclei provides invaluable information on the many-body hadronic system by adding *strangeness* to the standard nuclear matter. In particular, a Λ-hyperon can be put deeply inside a nucleus as an impurity to provide a sensitive probe of nuclear matter. Since a Λ hyperon inside the nucleus is free from Pauli blocking, it can penetrate into the nuclear interior and form deeply bound hypernuclear states. This is a unique way to study hyperon-nucleon and hyperon-hyperon interactions. Indeed, due to the short lifetime of hyperons no hyperon-hyperon scattering experiments can be performed.

One of the main characteristics of hypernuclei is the binding energy of a hyperon. The Λ binding energy can be calculated from the total binding energies of hypernuclei and nuclei as follow:

$$B_\Lambda({}^{A+1}_{\Lambda}Z) = B_{tot}(({}^{A+1}_{\Lambda}Z) - B_{tot}({}^{A}Z) \tag{1.1}$$

Moreover, the binding energy of the Λ in light hypernuclei can be derived from the kinematical analysis of the decay products of hypernuclei.

There are several models which can be applied to describe the structure of hypernuclei. One of them is to consider the N-body problem within an effective interaction model with G-matrix calculations. A Λ hypernuclear wave function can be obtained by considering a core nucleus potential and a Λ hyperon within it. The hypernuclear Hamiltonian is then expressed as follows:

$$H = H_{CoreNucleus} + t_\Lambda + \sum v_{\Lambda N}^{effective} \tag{1.2}$$

where $H_{CoreNucleus}$ is the Hamiltonian for the core nucleus, t_Λ is the kinetic energy of the Λ-hyperon and $v_{\Lambda N}^{effective}$ describes the effective ΛN interaction. At first, the effective interaction can be considered from the two-body interaction in free space. One-boson-exchange models such as Nijmegen [5, 6, 7, 8] and Juelich interactions [9, 10] are widely used to describe the elementary two-body interactions.

1.1.1 Hypernuclear physics development

The first observation of a hypernucleus was made in 1952 by Danysz and Pniewski. The hypernucleus was discovered in a cosmic ray interaction in an emulsion plate and was seen to decay with a path length of 90 μm [11]. Since the first observation several stages of investigation have been performed. Figure 1.1 shows all hypernuclei [12] discovered until 2004.

Since the 50's and until the 70's, most experiments used low energy K^- beams on nuclear emulsions. Lambda hypernuclei from ${}^{3}_{\Lambda}$H to ${}^{15}_{\Lambda}$N have been identified by observing the mesonic weak decay, and their binding energy was measured. Also the ground state spins have been determined for light hypernuclei from observed branching ratios and/or the angular distribution of the decay products. The lifetimes of H and He hypernuclei were also measured [13]. However this technique is limited

to the ground states of hypernuclei. The next era in hypernuclear physics came with the possibility to perform counter experiments at CERN in the late 60's with $(K^-_{stopped}, \pi^-)$ and was continued with the in-flight (K^-,π^-) reactions at CERN and BNL. Those experiments suffered from low kaon beam intensity but they have studied the structure of p-shell hypernuclei and found that the spin-orbit splitting is quite small [14]. The third stage in the mid-1980's began with a new (π^+,K^+) reaction and associated production at BNL. The same production mechanism was developed at KEK in Japan from early 90's. This technique has been applied to investigate a large number of Λ-hypernuclei with very high quality measurements [15, 16]. Comparing to strangeness exchange with kaon beams, the associated production involves larger momentum transfers and is, therefore, suitable for studying higher spin states with larger excitation energy.

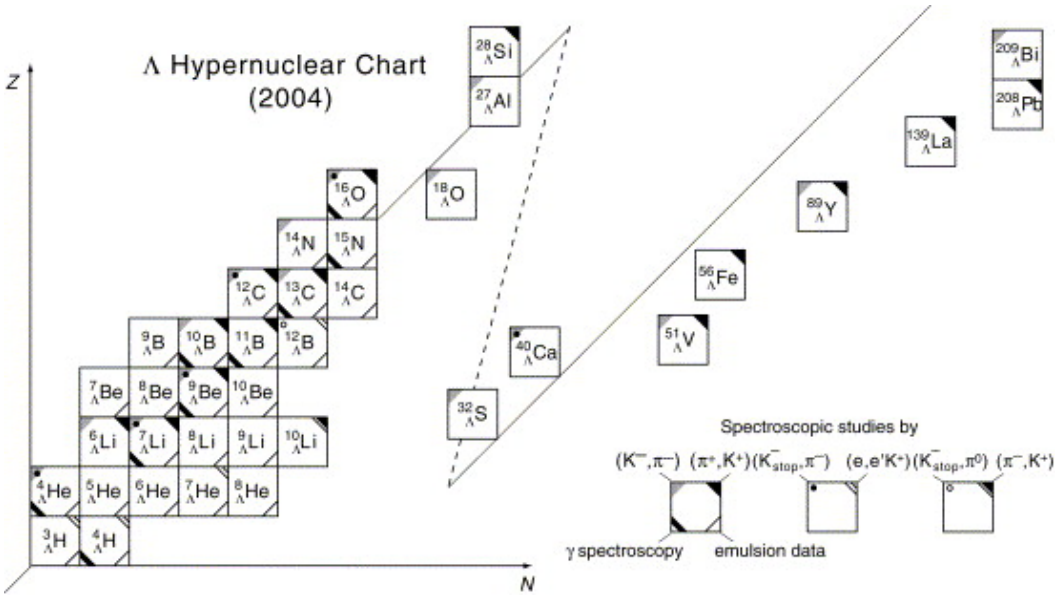

Figure 1.1: Λ hypernuclear chart [12]

The Hyperball collaboration performed γ-ray spectroscopy experiments for p-shell Λ hypernuclei by using (K^-,π^-) and (π^+,K^+) reactions. The new technique has improved the energy resolution from an order of MeV to keV, and it has shown that the Λ-hyperon has glue effect and indicated that nuclear structure may be different because of the presence of a hyperon inside the nucleus [17].

1.1.2 Formation of hypernuclei in high energy heavy ion collisions

The production mechanism of hypernuclei in reactions between heavy nuclei was first discussed by Kerman and Wiess in 1973 [18]. They pointed out that the best

way to produce hypernuclei with several hyperons is produced with a heavy ion collision. Late in 1988 the coalescence model was applied for the description of hypernucleus formation [19]. According to this model the production cross section depends mainly on three parameters: the cross sections of strangeness and fragment production and the coalescence radius or probability.

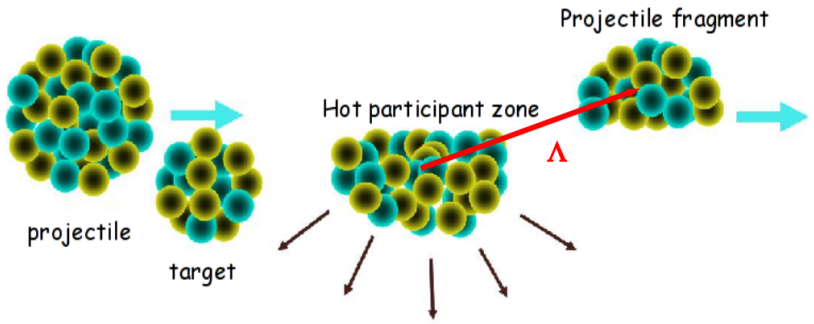

Figure 1.2: Schematic view of the scenario for the production of Λ-hypernuclei in heavy ion collisions. The Λ produced in the hot participant zone is absorbed by a projectile fragment.

The reaction mechanism between two heavy ions at relativistic energy is well explained by the participant-spectator model. As it is schematically shown in the Figure 1.2, a hyperon (Λ) in peripheral heavy ion collision is produced in the participant region at mid-rapidity and may coalesce in the projectile fragments due to the overlap of the rapidity distributions (Figure 1.3). Since the energy threshold for Λ production in elementary process $NN \rightarrow \Lambda KN$ is 1.6 GeV, high incident energies have to be chosen. Hypernuclei produced in the projectile spectator region thus will have a large velocity and a longer effective lifetime due to a large Lorentz factor. It gives a unique opportunity to study hypernuclei in flight.

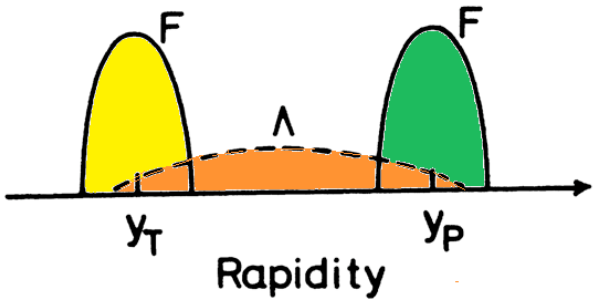

Figure 1.3: Rapidity distributions of produced Λ hyperons and fragments (F) from the target and the projectile [19]

The Ultrarelativistic Quantum Molecular Dynamics (UrQMD) event generator describes a heavy ion reaction [20]. It has been developed to reproduce the experimental data of a wide range of collision energies. The UrQMD event generator was used for the Monte Carlo simulation, for the design of the experimental apparatus of the HypHI Phase 0 experiment, and for the performance check of reconstruction methods. The collisions of ^{6}Li at 2 A GeV/c on a ^{12}C target were simulated with UrQMD. Hypernuclear events are produced in a second stage by the coalescence of produced Λ and fragments by a phase-space cut in momentum and space.

The first successful experiment with heavy ion collisions has peen performed in 1989 in Joint Institute for Nuclear Research at Dubna with ^{4}He and ^{6}Li beams on a polyethylene target. The production cross section of ${}^{3}_{\Lambda}$H and ${}^{4}_{\Lambda}$H was found to be about 0.2μb and the lifetime has been measured $\tau({}^{3}_{\Lambda}\mathrm{H}) = 240^{+170}_{-100}$ ps and $\tau({}^{4}_{\Lambda}\mathrm{H}) = 220^{+50}_{-40}$ ps [21].

In BNL AGS E864 experiment light hypernuclei were produced with Au ions with the momentum of 11.5 GeV/c per nucleon impinging on a fixed Pt target. The 10%-most-central collision events are sampled with an open geometry spectrometer. In the analysis Λ-hyperon, ${}^{3}_{\Lambda}$H and ${}^{4}_{\Lambda}$H were observed in the invariant mass spectrum after the background substraction. The study has been performed for the hypernuclei at mid rapidity region. The ${}^{3}_{\Lambda}$H yield and an upper limit on the ${}^{4}_{\Lambda}$H yield has been reported [22].

In 2010 the STAR collaboration at the Relativistic Heavy-Ion Collider at BNL has reported the observation of ${}^{3}_{\Lambda}$H and ${}^{3}_{\Lambda}\bar{\mathrm{H}}$ in Au+Au collisions at 200 GeV in the center-of-mass system. It is the first observation of an anti-hypernucleus [23]. The deduced lifetime of ${}^{3}_{\Lambda}$H is $182^{+89}_{-45} \pm 27$ ps, which agrees with previously measured values. The result on the comparison of the ratios ${}^{3}_{\Lambda}\mathrm{H}/{}^{4}_{\Lambda}\bar{\mathrm{H}}$ and ${}^{3}\mathrm{He}/{}^{4}\bar{\mathrm{He}}$ supports the coalescence model as the main process for the formation of hypernuclei in the mid rapidity region of central heavy ions collisions.

1.1.3 HypHI project

The aim of the HypHI project is to study hypernuclei produced by heavy ion collisions at the projectile rapidity region [24]. In this sense the HypHI experiment is unique. The conventional methods convert a target nucleus into a hypernucleus. In peripheral relativistic heavy ion collisions the production of hypernuclei is done by the coalescence of the projectile with a hyperon, produced in the participant zone. It gives an opportunity to study hypernuclei at extreme isospin, since the production mechanism involves the projectile fragments, which are known to have a wide isospin distribution. It is the only way to produce extremely proton- and neutron-rich hypernuclei. As previously mentioned, hypernuclei can be also produced in the central nucleus-nucleus collision (AGS, STAR), but in this case, because of the high temperature in the fireball, it is possible to produce only very light hypernuclei ($A \lesssim 4$) [25, 26].

The Phase 0 of the HypHI experiment was performed in October 2009 at GSI with ^{6}Li beams at 2 A GeV on a ^{12}C target in order to demonstrate the feasibility of

the hypernuclear production in non-central heavy ion collisions. The main goal was to observe and to study the lightest hypernuclei ($^{3}_{\Lambda}$H, $^{4}_{\Lambda}$H, $^{5}_{\Lambda}$He) by reconstructing the invariant mass of these bound states. They can be measured via their mesonic weak decay channels:

- $^{3}_{\Lambda}\mathrm{H} \rightarrow {}^{3}\mathrm{He} + \pi^{-}$
- $^{4}_{\Lambda}\mathrm{H} \rightarrow {}^{4}\mathrm{He} + \pi^{-}$
- $^{5}_{\Lambda}\mathrm{He} \rightarrow {}^{4}\mathrm{He} + \pi^{-} + p$

The reason to concentrate on the light hypernuclei is the dominance of the mesonic weak decay channels compared to non-mesonic weak decays and the fact that the heavier beam would increase the difficulty of the data analysis because of a higher particle multiplicity per event.

This thesis presents the results of the two-body final state reconstruction for $^{3}_{\Lambda}$H and $^{4}_{\Lambda}$H analyzing the data taken in October 2009 with a ^{6}Li beam at 2 A GeV on a ^{12}C target. Additionally, the invariant mass reconstruction of the well known Λ-hyperon is achieved in order to validate the dedicated reconstruction algorithms. The final results are shown in Figure 1.4 and summarized in the Table 1.1.3

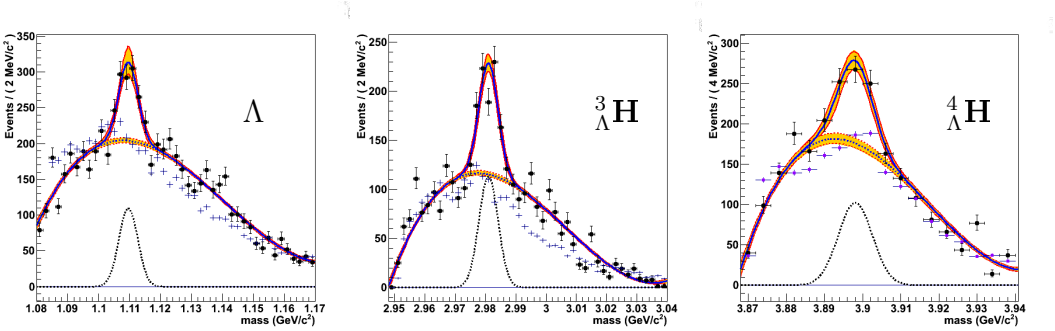

Figure 1.4: Invariant mass distribution (black dots) fitted with the *signal+ background* distribution for Λ (left), $^{3}_{\Lambda}$H (middle) and $^{4}_{\Lambda}$H (right). The blue lines represent the most probable solution returned by the fit, the red lines and yellow area show the 1σ uncertainty band. The light purple markers correspond to the scaled mixed event invariant mass distributions

Table 1.1: Summary of the results obtained in the current work

Particle	M [MeV/c^2]	σ [MeV/c^2]	Significance [σ]	Lifetime [ps]
Λ	1109.6 ± 0.4	3.04 ± 0.41	9.8	$269.37\ ^{+93.13}_{-62.57}$
$^{3}_{\Lambda}$H	2981.0 ± 0.3	3.16 ± 0.25	12.8	$239.07\ ^{+61.19}_{-43.72}$
$^{4}_{\Lambda}$H	3898.1 ± 0.7	4.47 ± 0.66	7.3	$209.39\ ^{+135.34}_{-64.72}$

The present thesis is composed of six chapters. In Chapter 2 the experimental setup used in the experiment is described. Chapter 3 is dedicated to the development of the Kalman filter based track reconstruction algorithm. The method and the performance of vertex fitting algorithms are demonstrated in Chapter 4. The Chapter 5 presents the detector calibration and final invariant mass reconstruction results obtained for Λ, ${}^{3}_{\Lambda}\mathrm{H}$ and ${}^{4}_{\Lambda}\mathrm{H}$ particles. The final summary and outlook are given in Chapter 6.

Chapter 2

HypHI@GSI

Contents

The experiment, was performed at GSI Helmholzzentrum für Schwerionenforschung GmbH in Darmstadt [27]. A schematic view of GSI laboratory is shown in Figure 2.1. The accelerator facility of GSI includes UNIversal Linear Accelerator (UNILAC), where low-charged ions can be accelerated to an energy of 11.4 MeV per nucleon, a heavy-ion synchrotron (SchwerIonenSynchrotron, SIS), where the ions with a charge-to-mass ratio 1/2 can be accelerated up to 2 A GeV/c, an Experimental Storage Ring (ESR) and a fragment separator (FRS).

For the HypHI experiment the primary beam of ^{6}Li from the ion source was preaccelerated in the UNIversal Linear Accelerator and injected into the heavy-ion synchrotron. After the acceleration it was extracted and transported into the experimental area of Cave C, where Phase 0 experiment took place.

2.1 The experimental setup of HypHI Phase 0

The HypHI experiment was designed to study the mesonic weak decay (MWD) of light hypernuclei produced by the coalescence of a projectile fragment with a Λ-hyperon at the projectile rapidity, as it was described in Chapter 1. The hypernculei are produced by the collision of a primary ^{6}Li beam at 2.0 A GeV with intensity of 3 $\times$ 10^{6} particles per second impinging into 4 cm thick ^{12}C target. The secondary decay vertex and invariant mass of the bound states of interest needs to be reconstructed, that requires precise momentum reconstruction and a Particle Identification (PID). Tracking detectors are placed up- and downstream for the momentum calculation in such a way that the decay vertex occurs before the first tracking detector. Time-Of-Flight and energy deposit measured with plastic hodoscopes are used for the particle identification. Due to the Lorentz boost because

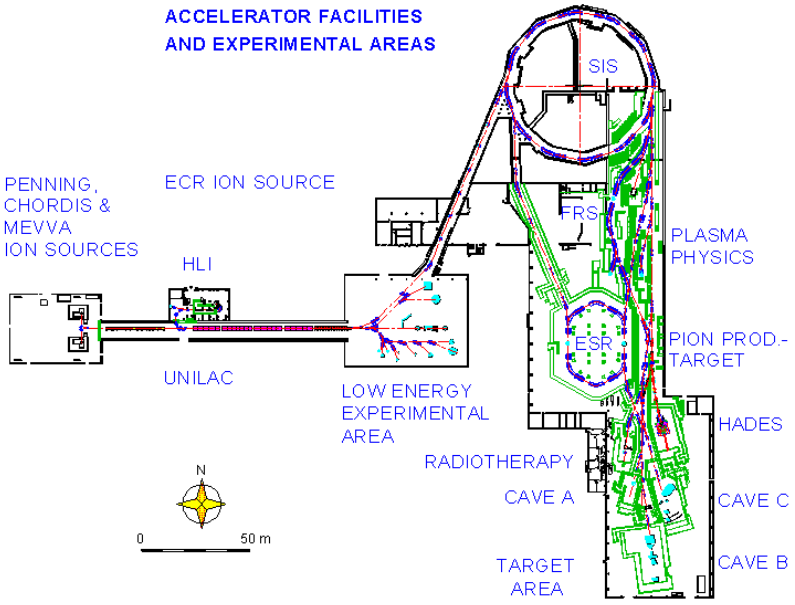

Figure 2.1: Layout of the accelerator facility at GSI and of the experimental areas

of a large projectile momentum all produced particles concentrate in a small solid angle providing an effective detection solid angle close to 4π.

One of the major challenge in the concept of the experiment was the design of the trigger system for the data taking and the reduction of the background contribution. Three stages of the trigger for the data acquisition system have been used: a Secondary Vertex trigger, a π^- trigger and a $Z = 2$ particle trigger.

The full experimental setup shown in Figure 2.2 has been placed in Cave C in summer 2009. It consists of A Large Acceptance Dipole magnet (ALADiN) [28] for the momentum reconstruction. The maximum bending power is around 2.3 Tm at 2500 A. Fragments from the heavy ion collisions are separated according to their magnetic rigidity through the ALADiN magnet. For the Phase 0 experiment, the magnetic field has been set to 0.75 T in order to have a reasonable separation between the fragments and to optimize the acceptance for π^-. The tracking detectors: three scintillating fiber detectors (TR0, TR1 and TR2) and one drift chamber (BDC) are located in front of the magnet, another drift chamber (SDC) is placed behind the magnet. For the beam measurements and for time reference the start counter is placed in front of the target. In addition, three Time-Of-Flight (TOF) detectors (TOF+, ALADiN TOF and Time-of-Flight Wall, TFW) were used as last tracking layers and as stop counters for TOF measurements.

In the following, the details of each detector used in the HypHI Phase 0 experiment will be described.

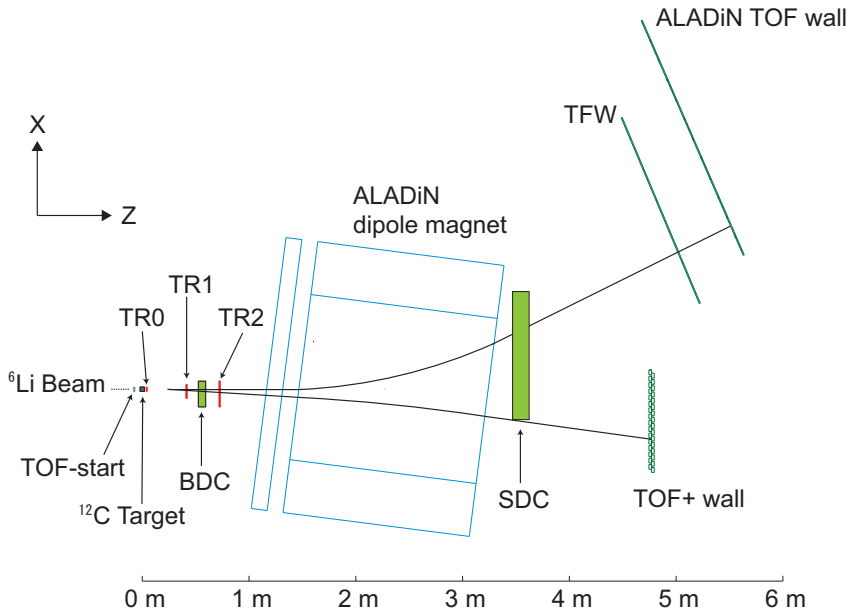

Figure 2.2: HypHI experimental setup

2.1.1 Start counter

The start counter (Figure 2.3) has been designed to be able to sustain a high counting rate up to 3×10^7 particles per second and to be able to distinguish beam particles from possible contamination of ^{12}C coming from the ion source. The start counter is a scintillating hodoscope consisting of 10 bars of Bicron BC-420 arranged in three layers with a 1 mm overlap between neighboring bars as it is shown in Figure 2.4. Two bars are $15 \times 6 \times 50$ mm^3 and the eight others bars are $4 \times 6 \times 50$ mm^3.

The total active area perpendicular to the beam direction is 53×50 mm^2 which covers the beam profile $\sigma_{xy} = 10$ mm. The simulated beam profile is shown in Figure 2.5, the dashed lines shows the detector size. The read out is done by Hamamatsu R7400U-06 MOD photomultipliers from both ends of each bar. These PMT's has been chosen based on a simulated counting rate per bar (Figure 2.6) with the chosen geometry of the detector (Figure 2.4) and the beam intensity of 10^7 particles per second.

The choice of the PMT has been done based on the results of the test experiment of August 2008 in which two types of the photomultipliers were used: H3164-10 MOD and R7400-06 MOD. Both types of the PMT's were modified by adding a booster to the three last dynodes in order to stabilize the voltage under the high counting rate. Both prototypes delivered a similar result for the time ($\sim$ 200 ps) and energy resolution ($\sim$ 50%). The R7400-06 MOD was chosen because its smaller dimensions simplified the construction of the detector.

The analog signals for the photomultipliers of the Start Counter were amplified and then divided into two different branches for the energy and time measurement.

Figure 2.3: Start Counter seen from the side of the incoming beam

The first branch was sent to QDC (charge sensitive analog-to-digital converter), CAEN VME V792, and the second branch was fed into leading-edge discriminators, CAEN V895, and then recorded by TDC (time-to-digital converter) modules, CAEN V775s.

2.1.2 Fiber detectors

A set of arrays of three scintillating fiber detectors (TR0, TR1 and TR2) was placed in front of the magnet. Each of them consists of two planes, X and Y, of four layers of SCSF-78 (Kuraray) scintillating fibers (Figure 2.7 (a)). The inner diameter (core) and the outer diameter (including cladding) of the fibers are 0.73 mm and 0.83 mm respectively. The attenuation length is over 4 m and the decay constant is 2.8 ns. The rows of four layers of fiber bundles are aligned with a 0.59 mm pitch as shown in Figure 2.7 (b). The read out is done by Hamamatsu Photonic H7260KS MOD multi-anode photomultiplier tubes. The PMTs have three booster cables in the last dynode stages in order to stabilize the voltage under the high counting rate. The distance between the center of the target and TR0 is 36.5 mm, TR1 and TR2 are located at 300 mm and 700 mm after TR0 respectively. The dimensions and the number of the readout channels are summarized in Table 2.1.

Analog signals from the PMTs of the fiber detectors are fed into the double-threshold-discriminators (DTDs) to create a low voltage differential signaling (LVDS) level logic signal. These logic signals are sent to the Field Programmable Gate Array (FPGA) based logic module (VUPROM2) [29]. The timing information of leading

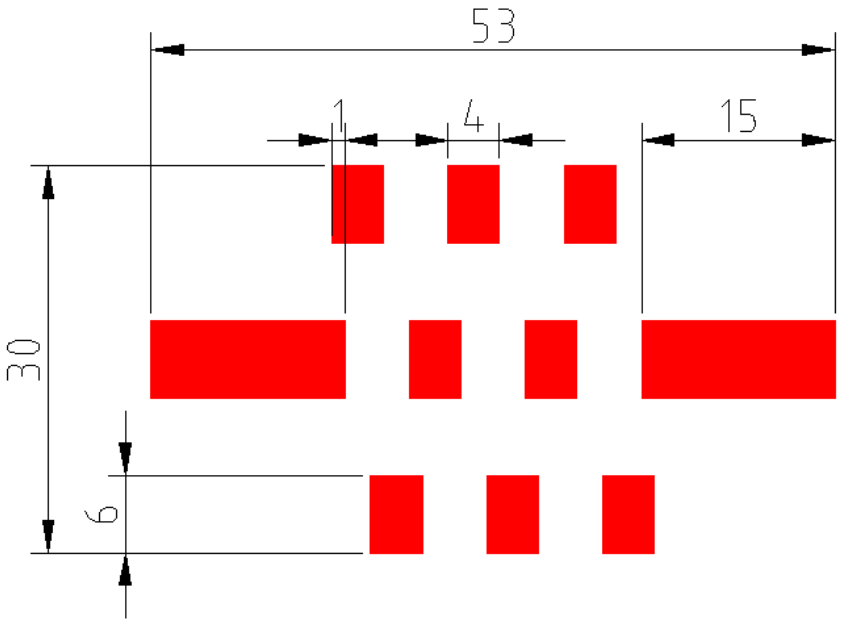

Figure 2.4: Cross sectional view (from the top) of the arrangement of the scintillator bars (red) of the Start Counter. The dimensions are in mm. The beam comes perpendicularly from the bottom of the figure.

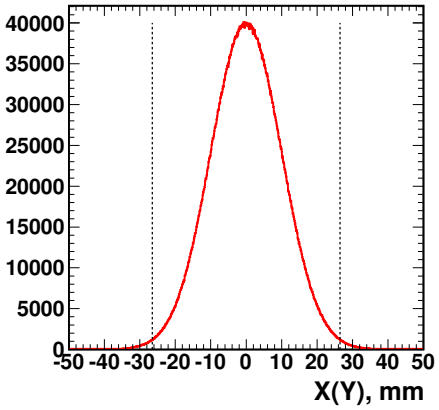

Figure 2.5: Simulated beam profile in X(Y) axis with beam intensity of 10^7 particle per second

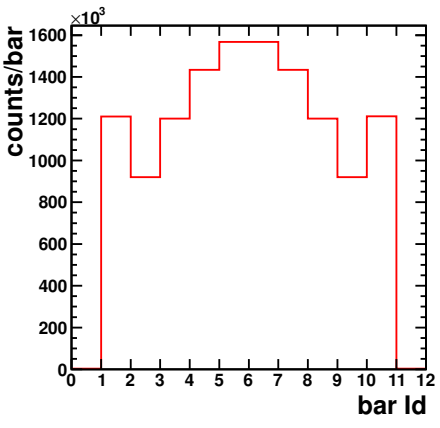

Figure 2.6: Simulated number of counts per bar per second with a beam intensity of 10^7 particle per second

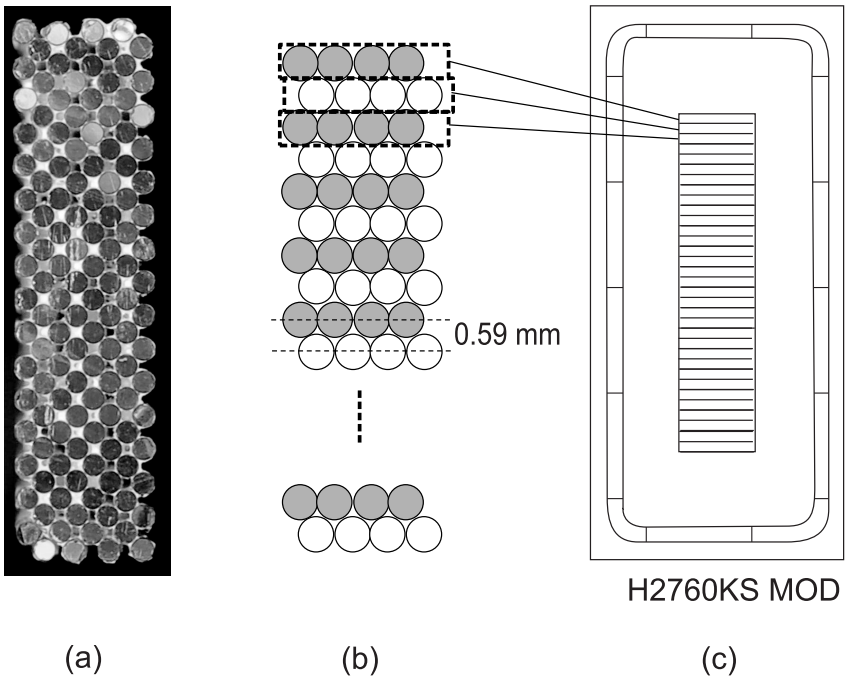

Figure 2.7: Photograph (a) and schematic drawing (b) of cross section of a 32-channels fiber bundle. The panel (c) shows a scheme of a surface of the PMT.

Table 2.1: Dimensions of arrays of fiber detectors, TR0X, TR0Y, TR1X, TR1Y, TR2X and TR2Y, and the number of readout channels and photomultipliers of each layer

Name	Size (mm)	Channels	PMT
TR0X	39	64	3
TR0Y	39	64	3
TR1X	139	224	7
TR1Y	76	128	4
TR2X	245	416	13
TR2Y	113	192	6

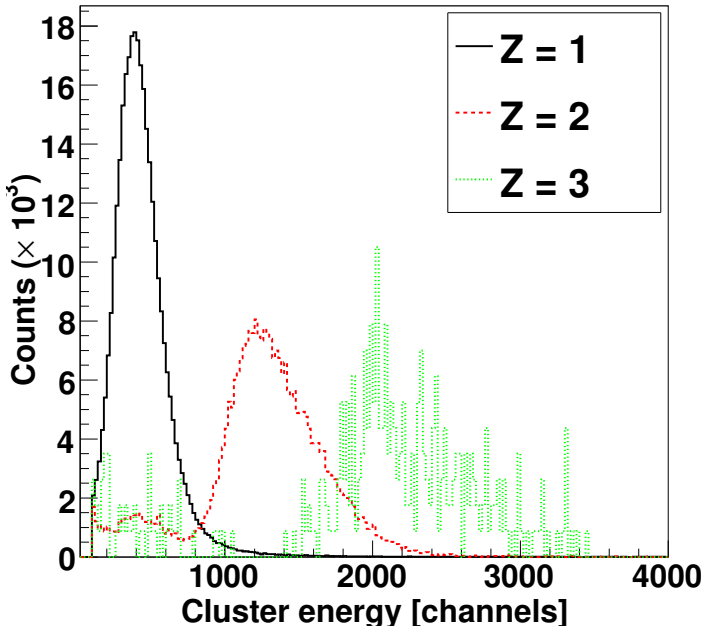

Figure 2.8: Distribution of the energy deposition in TR0 detector for the particles with $Z = 1,\ 2$ and 3

and trailing edges of the signal were registered by the programmed TDC function of VUPROM2 modules with a granularity of 2.5 ns. The existence of the secondary vertex between TR0 and TR1, secondary vertex trigger, was as well examined by VUPROM2 modules. In addition for the TR0 planes, analog readout was performed by QDCs CAEN VME V792.

The performance of the scintillating fiber detectors was studied during several test experiments in August 2008 and April 2009 as well as in the Phase 0 experiment. The final performance was deduced during the Phase 0 experiment. The achieved position resolution is 0.21 mm in RMS for the $Z = 3$ particles (beam) and 0.46 mm in RMS for the $Z = 1$ particles [30]. The energy deposition information form the TR0 was used to distinguish particles with different charges, $Z = 1$, $Z = 2$, $Z = 3$. It is use to discriminate the signals recorded from hydrogen hypernuclei and the others signals (background), dominated by the He isotopes produced in the target. The obtained energy resolution is about 81% for $Z = 1$, 27% for $Z = 2$ and 11% for $Z = 3$ as shown in Figure 2.8.

2.1.3 Drift chambers

Two drift chambers are used for the track reconstruction of charged particles in Phase 0 experiment.

The drift chamber, BDC (Beam Drift Chamber), which was mounted between

TR1 and TR2 was originally developed for the secondary meson beam lines at KEK [31]. A photograph of BDC is shown in Figure 2.9. It consists of three pairs of wire planes XX', UU' and VV'. The UU' and VV' pair-plans have a stereo angle of ± 15 degrees, respectively to the vertical wires of XX' pair plan in order to determine the horizontal and vertical hit positions. The size of the chamber is 24×14 cm^2. The distance between sense wires in one single plane is 5 mm, and pair-planes are shifted by half of cell size (2.5 mm) in order to resolve the right/left ambiguity around the sense wires. Between the sense wires in each single plane there are potential wires. For the Phase 0 experiment BDC was operated with a gas mixture of Ar (70%) and CO_2 (30%). Since the beam particles were passing through the BDC, a part of the sense wires were wrapped with Teflon tape for all 6 layers with a size of 1.5×1.5 cm^2 (Figure 2.10) in order to suppress the gas amplification in this area. Raw signals from a sense wire were first amplified by the pre-amplifier REPIC RPV-040, mounted on the chamber. Amplified raw signals were fed into a discriminator card REPIC RPV-020 equipped with a main-amplifier to produce Emitter-coupled logic (ECL) level signal. The timing of the signals was recorded by the VUPROM2 modules with programmed TDC function with 2.5 ns granularity and two multi hits capability.

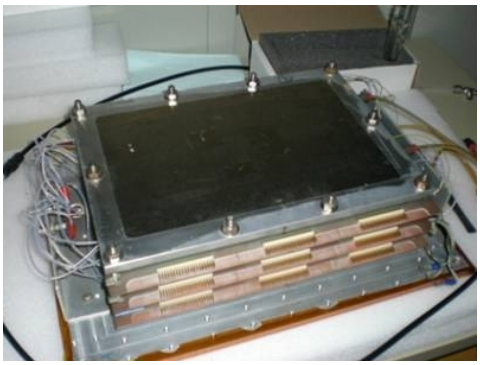

Figure 2.9: Photograph of BDC (Beam Drift Chamber)

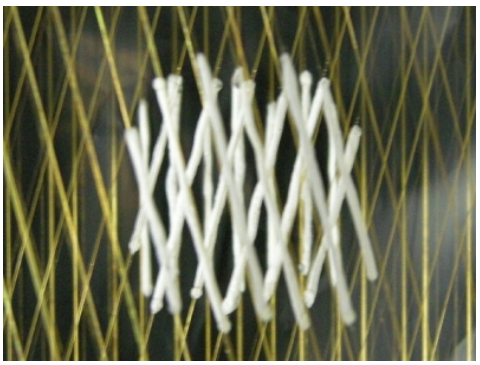

Figure 2.10: Photograph of the masking of the BDC

The design value of the position resolution of BDC is around 0.3 mm, however in the Phase 0 experiment, the readout signals after preamplifier and amplifier/discriminator were fed into VUPROM2 module with a 2.5 ns time readout granularity, and so the achieved position resolution becomes 2.5 mm.

Another drift chamber, SDC (Scattered Drift Chamber), also shipped from KEK [32], was used for the tracking of all charged particles behind the dipole magnet (Figure 2.11). The size of the chamber is 120×90 cm^2. It consists of 5 layers of sense wires XX', YY' and U. The U plain has an angle of 45 degrees in order to resolve the stereo ambiguity of the hits. During the Phase 0 experiment, SDC was operated with the same gas mixture as BDC: Ar (70%) and CO_2 (30%). Since the beam particles are passing through the SDC the area around the beam region

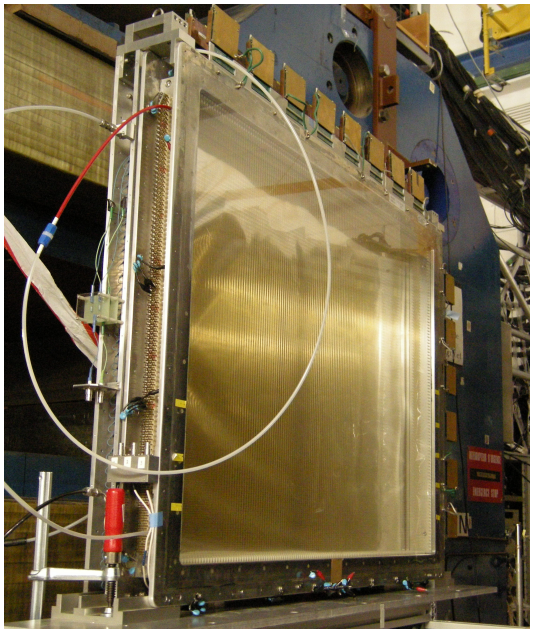

Figure 2.11: Picture of Scattered Drift Chamber

was deactivated to avoid the high counting rate. The cell size for the XX' and YY' layer is 4.5 mm, for the U layer is 9 mm. Scince a similar to a BDC readout system was used for SBD, the achieved position resolution is around 4.5 mm.

2.1.4 Time-Of-Flight walls

Three Time-Of-Flight (TOF) walls were used during the Phase 0 experiment. One of them called **TOF+ wall** (Figure 2.12) has been specially designed and built for the HypHI project for the detection of positively charged particles. The TOF+ wall consists of 32 plastic scintillator bars of Bicron BC-408 with read out from both sides by Hamamatsu H7415 photomultiplier tubes. Each bar has a size of $4.5 \times 2.5 \times 100$ cm^3. The bars are placed in two layers with an overlap of 1.5 cm as shown in Figure 2.13. The active area of the detector is around 1 m^2. To reduce a counting rate and prevent plastic scintillators from the damage by the beam particles a hole of 7.5×6.5 cm^2 has been implemented in TOF+. Each of three bars with the hole was constructed by two smaller bars with a gap to create the hole in their center. Those two smaller bars are wrapped together in a reflective mylar to keep the optical propagation of the produced light in those two scintillator bars. The front-end readout electronics of the detector consists of two different branches for the energy and time measurement. CAEN VME QDC and TDC modules were used for recording the information.

ALADiN TOF wall and TFW LAND were used as stop counters for the detection of negatively charged particles.

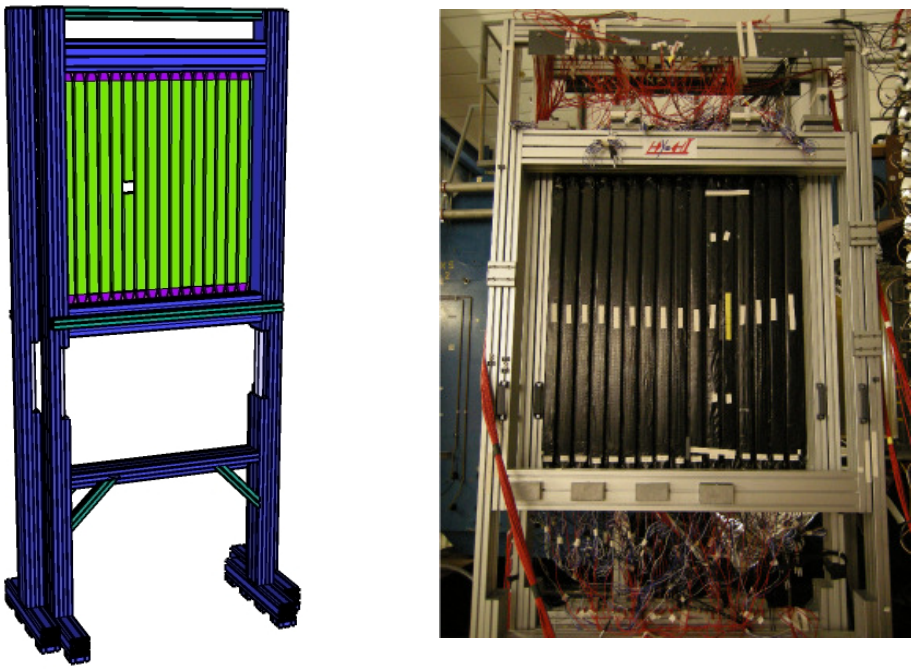

Figure 2.12: Scheme and pictures of the TOF+ wall

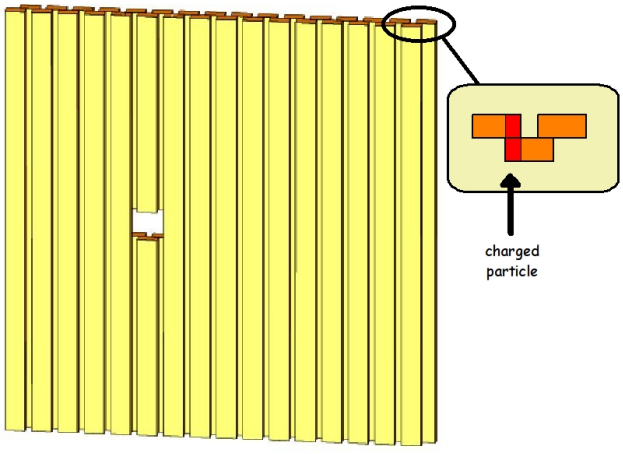

Figure 2.13: Arrangement of the scintillator bars of the TOF+ wall with a partial overlap of adjacent bars as indicated on the top right corner

The **ALADiN** wall has been used for the multi-fragmentation experiments [33]. It consists of two layers of plastic scintillator strips, each with a width of 2.5 cm and thickness of 1 cm. The active area of the detector is 2.4×1.1 m^2. The two layers are shifted with respect to each other by half width of a single strip leading to the effective granularity of the X position measurements of 1.25 cm. The readout is done by Hamamatsu photomultiplier's R3478 from both sides of plastic strips. In the Phase 0 experiment only the first layer of ALADiN TOF wall has been used. Energy and time information were digitized by FASTBUS ADC and TDC. Since the ALADiN TOF wall was designed for the detection of the heavy fragments and not the π^--mesons like in the HypHI experiment, the efficiency of ALADiN TOF was lower than the efficiency of TFW LAND. It is not used for invariant mass reconstruction, but it was used for the calibration and the alignment.

TFW LAND (Figure 2.14) was also used as a stop counter for the detection of negatively charged particles, π^- mesons. It consists of two layers, horizontal and vertical, of the plastic scintillators (SCSN-81). The width of each plastic bar is 10 cm and the thickness is 5 mm. The vertical layer consists of 18 bars, while the horizontal layer has 14 bars. The total detection area is 1.89×1.47 m^2. The readout is done from both ends of the plastic bars with the PMTs (XP2262). The front end readout consists of two branches: for the energy measurements, the information is digitized by FASTBUS ADC and for the time measurement with CAEN VME TDC modules.

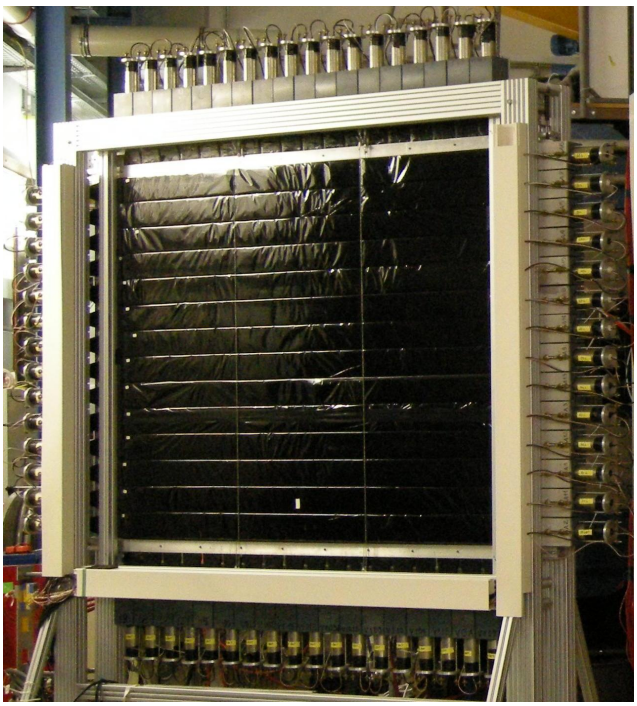

Figure 2.14: Picture of TFW

TOF walls with association to the drift chamber (SDC) give sufficient position resolution for the invariant mass reconstruction of hypernuclei.

2.2 Data acquisition system

The GSI Multi Branch System (MBS) [34] was used as a framework for the Data Acquisition System (DAQ). It has been running on RIO3 VME processor with Lynx OS. Two types of crates were used for the front end electronics: VME and FASTBUS. Each crate was equiped with the RIO3 VME Processor board and the GSI trigger module board. The GSI trigger modules are connected to each other via a trigger bus cable in order to synchronize the data acquisition and to accept trigger signals generated by the master trigger system. The data are then transported via a dedicated network to the memory of the server machine used as "Event builder" to format the event data stream. The delayed data transfer was implemented in such a way that all the data in the "Event builder" are written down to the hard disk device during off-spill via RFIO protocol. The online monitoring was implemented via ethernet socket connected to stream server to check the on-going data stream.

2.3 Trigger system

The Phase 0 experiment has been performed with high intensity ^{6}Li beam on a thick carbon target, and the total reaction rate in the target was expected to be around 2 MHz for the beam intensity of 3×10^6 particle per second. Therefore, the technical challenge was to produce a trigger for the data acquisition system with a reasonable reduction of the background events. The trigger system consists of three simultaneous stages: the secondary vertex trigger produced by the fiber detectors, the π^- trigger by the TFW LAND and the $Z = 2$ trigger produced by the TOF+ wall.

The secondary vertex trigger is based on the fact that hypernuclei and free Λ-hyperons decay well behind the target due to the Lorentz boost. Most of the π^- tracks from the decay of hypernuclei do not match the hit in TR0 due to a large momentum kick, while the nuclear fragments from the decay have a similar momentum vector as the hypernculei produced in the target hypernuclei. In the Figure 2.15 the typical decay of the $^{4}_{\Lambda}$H decay is shown, the fragment track (^{4}He) has a similar direction as the mother particle. The secondary vertex trigger checks if it is possible to associate a hit in TR0 with a combination of the hits between TR1 and TR2 considering all tracks as straight lines. All possible primary tracks are then removed and the remaining hits checked, by the template matching method, if there is an associated hit in TR0. The template has been produced with the Monte Carlo Simulation. This trigger decision procedure is implemented by several stages of VUPROM2 modules.

The π^- trigger requires the simple detection of a hit in TFW LAND above a certain energy threshold.

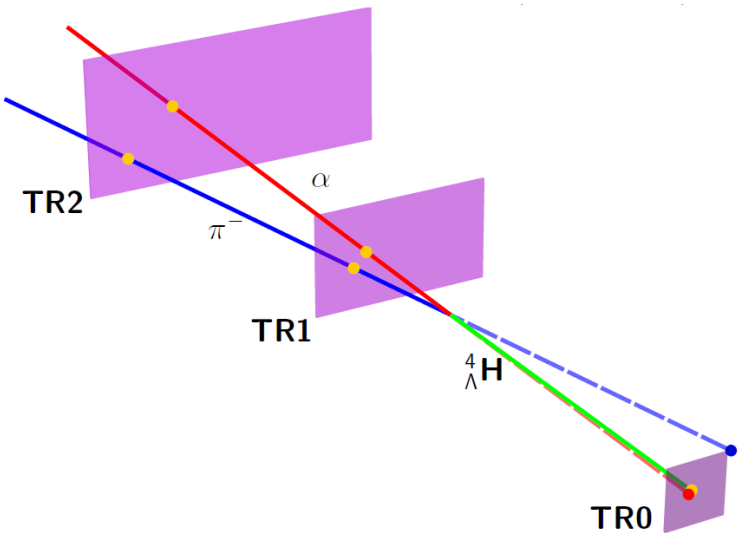

Figure 2.15: Typical ${}^{4}_{\Lambda}\mathrm{H}\rightarrow{}^{4}\mathrm{He}+\pi^{-}$ event whose decay vertex is behind the TR0. Tracks in green, red and blue represent ${}^{4}_{\Lambda}\mathrm{H}$, ${}^{4}\mathrm{He}$ and π^{-}, respectively. The yellow points are the hits of the particles in the TR0, TR1 and TR2.

The $Z = 2$ particle trigger is obtained by the TOF+ wall based on the time-over-threshold method. The signals from the PMTs are fed to the discriminators where the width of the pulse over a certain threshold is measured and the decision is made. Two signals from the scintillating bar are fed into the leading edge discriminator with a pulse width dependence. Once a signal amplitude exceeds the fixed threshold value the LED generates a corresponding logic signal which ends when the analog input signal amplitude crosses again the threshold after reaching the minimum. Figure 2.16 shows the three different signals from the different particles recorded with a digital oscilloscope during the test experiment. If, for example, the threshold of the discriminator is set to -0.1 mV, the resulting measured width of a logic pulse for the different amplitudes is shown in Figure 2.17. With the specific discriminators, it is possible to keep in a certain order the correlation between the charge via signals from energy deposit and the logic pulse after discriminator. This correlation is fair enough to distinguish the particles with $Z = 1$ from the particles with $Z \geqslant 2$.

The trigger efficiency has been investigated with the Monte Carlo simulation with ${}^{4}_{\Lambda}\mathrm{H}$ and associated particle events, and full background events produced by the UrQMD calculations. The estimated trigger rate for the ${}^{4}_{\Lambda}\mathrm{H}$ decay channel is around 340 Hz with the combination of those three trigger stages. Considering the expected cross-section from the other hypernuclei, such as ${}^{3}_{\Lambda}\mathrm{H}$ and ${}^{5}_{\Lambda}\mathrm{He}$, the trigger rate is up to 2.3kHz which fulfills the data acquisition rate.

The experiment has been performed with a beam intencity of 3×10^{6}, four types of physics trigger were implemented as a combination of described earlier triggers and a Minimum bias trigger: Reaction, Vertex and Hypernuclei. The trigger timing

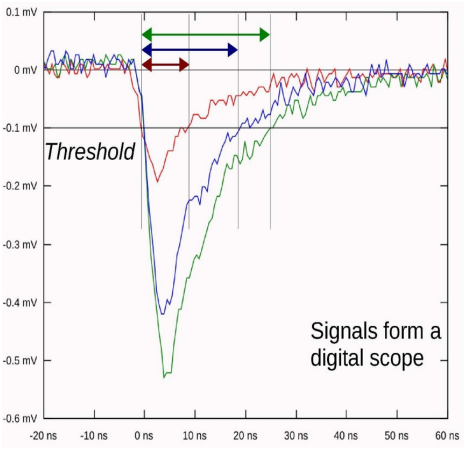

Figure 2.16: Time-over-threshold measurements. Each curve corresponds to a signal from the different particles passing through a scintillating bar.

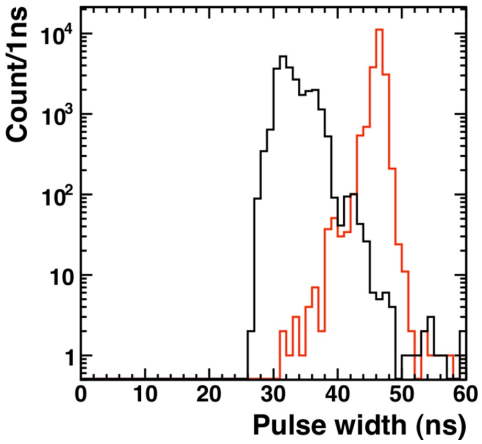

Figure 2.17: Pulse width measured by leading edge discriminator with a pulse width dependency for the particles with $Z = 1$ (black) and $Z = 2$ (red)

Table 2.2: Summary of the trigger patterns for the physics triggers.

Trigger	Secondary Vertex (770 kHz)	$Z = 2$ (846 kHz)	π^- (48 kHz)	Rate	Scale
Reaction	OFF	ON	ON	13 kHz	$1/2^{16}$
Vertex	ON	OFF	OFF	750 kHz	$1/2^{11}$
Hypernuclei	ON	ON	ON	2.3 MHz	1

was defined by the leading edge of the delayed signal of the start detector. Hence, a hit above the certain threshold from the Start Counter is required to produce a Minimum bias trigger. Minimum bias trigger was used to take data without any biases from the other triggers. The typical rate of Minimum bias trigger was 3.0 MHz. This trigger was scaled down by a factor 2^{16} compare to the Hypernuclei trigger. The Reaction and Vertex trigger were implemented in order to check the performance of the Secondary Vertex trigger, $Z = 2$ trigger and π^- trigger. In addition, the hit multiplicity less then three in Start Counter was required for the Hypernuclei trigger. The trigger pattern for the physics triggers, the typical trigger rate and scaling factors are summarised in the Table 2.2.

Chapter 3

Track Reconstruction

Contents

3.1 Introduction

Track reconstruction is an essential step in the data analysis chain of a nuclear physics experiment. The quality of physics analysis depends mainly on the performance of the reconstruction algorithm.

The task of track reconstruction is to determine the location, the direction and the momentum of charged tracks. Traditionally the task of track reconstruction is divided into three steps: track finding (or pattern recognition), track fitting (or estimation), and track quality check (testing).

- **Pattern recognition: track finding**. The assignment of the detector hits to the tracks is unknown a-priori and has to be determined by a pattern recognition algorithm. The latter is usually highly dependent on the detector and the shape of the magnetic field. The track finding or pattern recognition is dividing the measurements coming from tracking detectors into the sets of the

hits originated by the same particle. This sets are called track candidates. The performance of the pattern recognition is strongly influenced by the amount of background, for instance these sets can contain measurements which are not coming from any interesting tracks but from electronic noise or from low energy particles spiraling inside the detector. The pattern recognition algorithm should be conservative and keep all the track candidate in case there is any doubt because it is impossible to recover track candidates in the late stage.

- **Estimation: track fitting**. The track fitting procedure takes a set of measurements of the track candidate as a starting point. The goal of the fitting is to estimate as precise as possible a set of parameters which describe the state of the particle. This requires

  - The track model, i.e, the solution of the equation of motion of the charged particle in the magnetic field. The solutions can be analytical or numerical.
  - The amount of material crossed by the particle in order to account for physics effects such a multiple scattering or energy loss by ionization. These effects can be computed to a good approximation from the theory [35].
  - The covariance matrix of the observation errors.

  The most wide used method for the fitting of the tracks is based on the least-squares methods. The track fitting algorithm should be as fast as possible, should be robust against mistakes made during the track finding and it should be numerically stable.

- **Testing**. After the track fit, the quality of the track candidate is checked, i.e, if the track candidate hypothesis is valid. Such a test can be based on the value of χ^2 statistic, i.e. the sum of the squared standardized deference between the measured positions in the track candidate and the estimated position of the track at the point of intersection of the detectors. If the value of such a statistic is too high, the set of the measurements is not statistically compatible with the hypothesis of having created by the single particle. The reason of this incompatibility could be a single or a few measurements of the track candidate misclassified by the track finding, or the track candidate being completely wrong in the sense that the random collection of the measurements originated from several other particles so called ghost track. The track fit should be able at this stage to remove wrong or outlying measurements in the track candidate list and reduce the amount of ghost tracks.

Once the track reconstruction is performed, one can then determine the location of an interaction point and the momenta of the participating tracks. The tasks following the track reconstruction is called vertex reconstruction algorithm and will be discussed in details in the next chapter.

3.2 The HypHI tracking setup

Modern particles physics experiments generally consist of several kind of detectors which provides the simultaneous measurements of different properties of the particles such as mass, energy loss, momentum. By combining the information coming from each detector it is possible to recognize which particle has been detected. The goal of the tracking system of any setup is to provide the information about the path of the particles starting from the single point measured by each detector plane. The main part of the HypHI experimental setup is made of dedicated tracking detectors up and downstream the ALADiN magnet:

- upstream : TR0, TR1, and TR2 fibers detectors
- downstream: Drift chamber SDC, TFW and TOF+ walls.

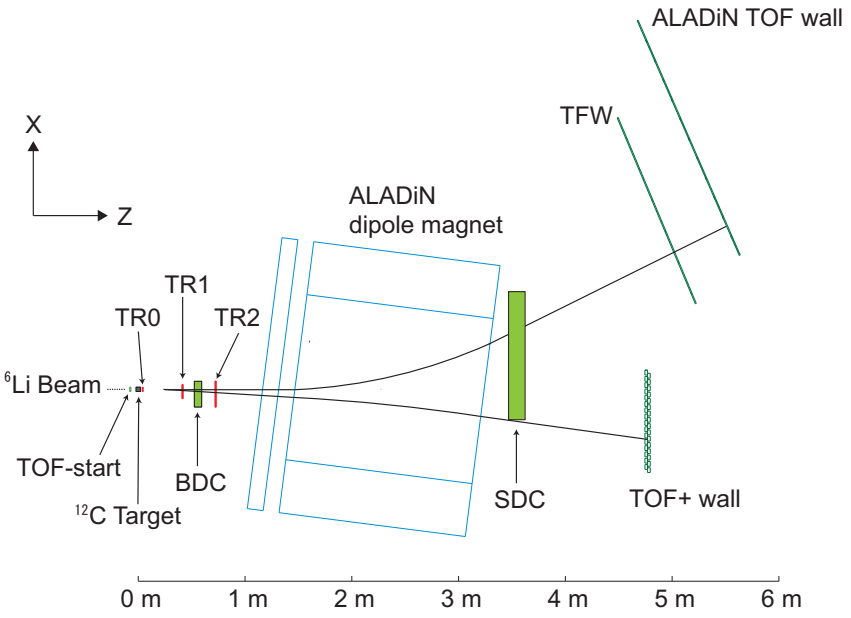

Figure 3.1: Setup of the HypHI tracking system used for the Phase 0 experiment in Cave C

As shown in Figure 3.1, the tracking will be based on the hit information coming from TR1 and TR2 fiber detectors behind the target and the drift chamber together with the two TOF hodoscopes behind the dipole magnet.

3.3 The ALADiN magnetic field

The magnetic field of the dipole magnet ALADiN is typical for any real dipole magnet. It starts to rise at some distance out side the gap of the magnet and reaches its full value B_y^{max} at short distance inside the magnet. This region outside

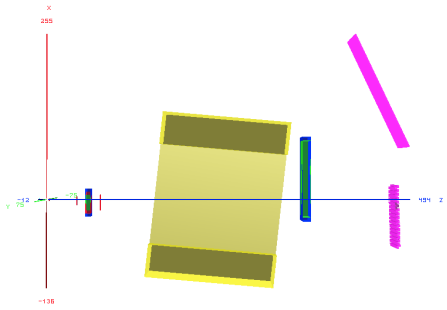

Figure 3.2: Implementation of the HypHI experimental setup in the Monte Carlo simulation. The ALADiN Magnet is rotated by an 5.6 degree angle compare to the Z axis. Tracking in front of the magnet is done using essentially the fibers detectors. In the forward region, the drift chamber and both TOF wall are used.

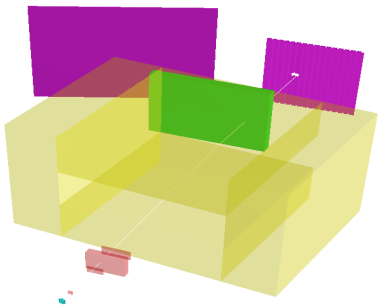

Figure 3.3: Event Display: a 2 AGeV ^{6}Li beam particle through the HypHI tracking system. The ALADiN magnetic field deflects the beam in a way that it will go through the hole of the TOF plus detector. An intensity input of 900 A which corresponds to $B_y^{max} = 0.75$ Tesla is used to obtain such a bending power.

the gap influenced by a residual magnetic field is so-called the *fringing-field* region and is of extreme importance for the exact computation of the particle trajectory. To avoid complications, in the track finding procedure where track reconstruction accuracy has to be balanced with a relatively fast computational time, an effective field length L is introduced. The effective fieldlength of the ALADiN magnet has been measured in [36]. A distance from the center of the magnet to the point where the field drops by a factor of $1/e$ of its maximal value has been taken as a base of the effective fieldlength definition. This distance has been measured at both ends of the magnet giving a total effective fieldlength of $L = 1.36\ m$. This value is in good agreement with the empirical formula given in [28]:

$$L = 2\frac{kG}{cos(\alpha)} + L_0 \tag{3.1}$$

where:
L_0 is the physical length.
G is the height of the magnet gap.
k is the characteristic factor for dipole magnet found to be of order 0.6 ± 0.1 for most magnets.
α is the magnet tilt angle.
For the ALADiN dipole magnet, $G = 50\ cm$, $\alpha = 5.6^o$, $L_0 = 80cm$ which gives an effective fieldlength $L \sim 140cm$ in agreement with the measurement.
On the basis of geometrical considerations [28] the relation between the bending

angle ψ and the radius of curvature ρ can be found:

$$\rho = \frac{L}{2sin(\frac{\psi}{2})cos(\alpha - \frac{\psi}{2})} \tag{3.2}$$

This relation is especially important since the momentum of the particle can be deduced from the curvature of the track. In case of homogeneous magnetic field the motion of the particle is affected by the Lorentz force

$$\overrightarrow{F} = \frac{q}{c}\left(\overrightarrow{v} \times \overrightarrow{B}\right) \tag{3.3}$$

where q is an electric charge, c is a velocity of light, $\overrightarrow{v}$ is the particle velocity and $\overrightarrow{B}$ is a magnetic field. The final trajectory of the particle is a helix whose axis is parallel to the magnetic field direction. This motion consists of two parts

- a circumference in the plane perpendicular to the magnetic field direction
- a straight line in the plane parallel to the magnetic field

In case of a constant field along the y axis, the equation 3.3 simplifies to the momentum-curvature relation

$$p \;=\; 0.3\; B_y\; \rho\; (GeV/c) \tag{3.4}$$

also valid for relativistic particle. The equation 3.2 and the momentum-curvature relation will be used by the track finding to get an approximate value for the momentum of track candidates.

Typical sizes of the magnetic field components B_x, B_y and B_z as a function of z are displayed in fig. 3.4. The main bending component (B_y) has a bell-shaped dependence on z, and there is clearly no significant subset of the magnet tracking system in which the field can be regarded as inhomogeneous. Furthermore Figure 3.4 shows asymmetrical x and z field components which are negligible making it possible to restrict the track reconstruction to projections during the track finding procedure. In Figure 3.5 the profile of the magnetic field $B_y(x, y, z)$ is shown in the (xz), (zy) and (xy) -planes of the laboratory frame. The Figure 3.6 represents the profile of the normalized deviation $\delta B_y/b_y$ as a function of x and y: it can be noticed that the variation of the magnetic field in the x or y direction are less than a few percent.

However in the reality, the trajectory of the particle is not a perfect helix, due to the presence of the materials along the path of the particles (energy loss, multiple scattering) and non-uniformity of the magnetic field. The goal of the track reconstruction is to find the algorithm which will be able to take into account those effects: precision when propagating the track parameter through the magnetic field is required. For this reason measured a precise three dimensional ALADiN field map is used.

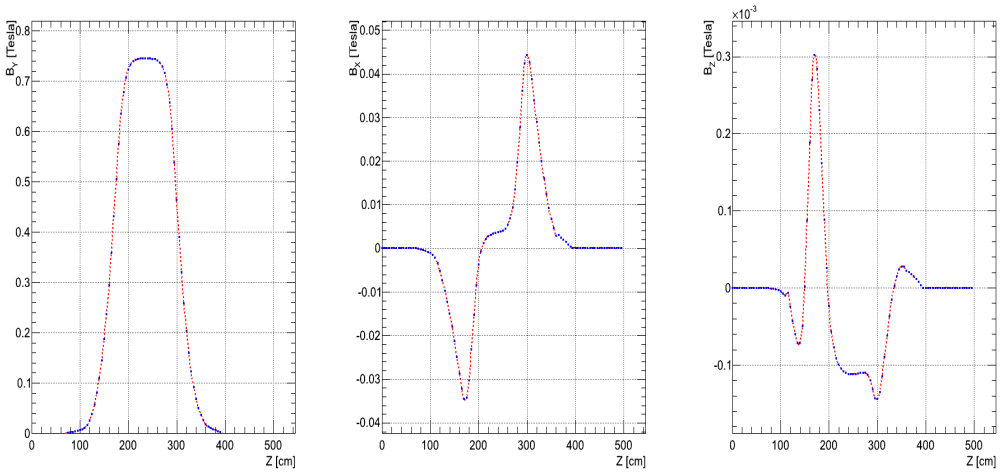

Figure 3.4: Magnetic field components of the ALADiN magnet as function of the z coordinate in the magnet center. The z coordinate corresponds to the exact Cave C position of the ALADiN magnet.

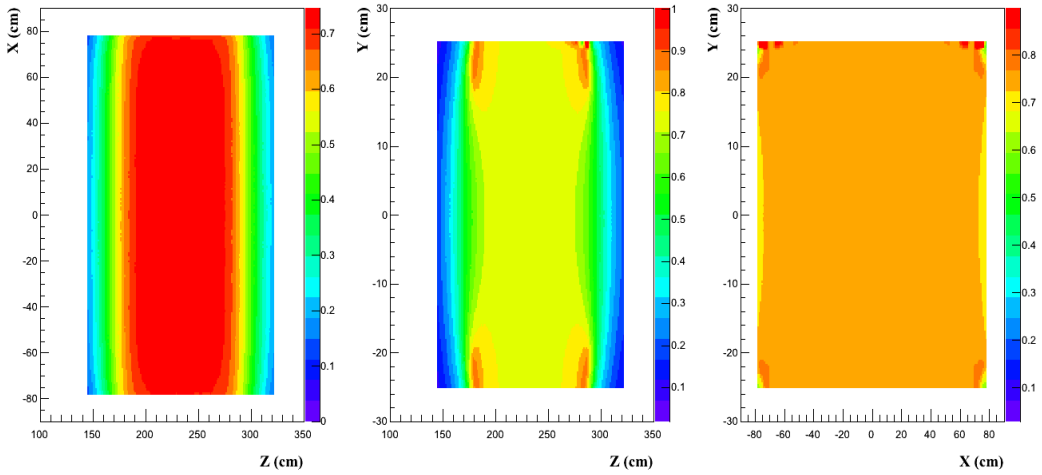

Figure 3.5: Profile of the ALADiN field map in the (xz), (zy) and (xy) -planes of the laboratory frame.

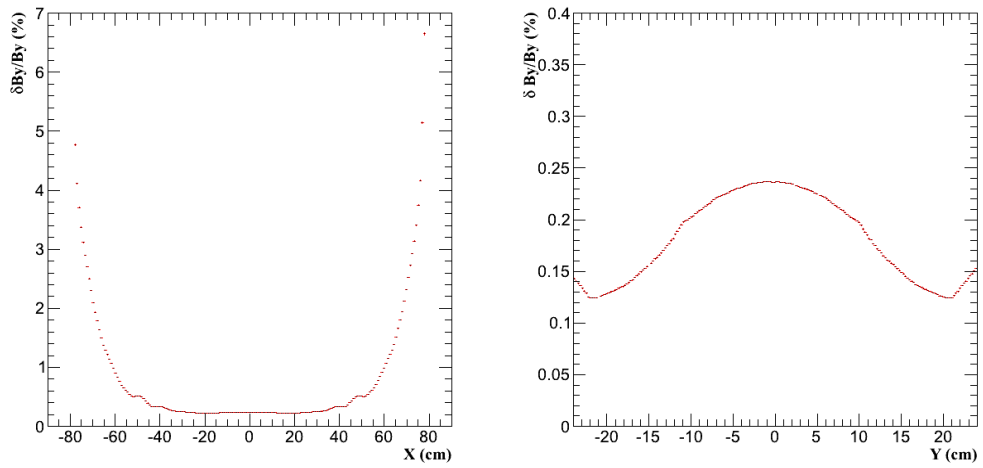

Figure 3.6: Profile of the magnetic field deviation $\delta B_y/B_y$ as a function of x and y coordinates.

3.4 Track finding

As previously mentioned, the track recognition procedure restrict the track reconstruction to projections in the non-bending plane (yz) and the bending plane (xz).

All combinations of hits in the non-bending (yz) plane on TR1, TR2 and one of TOF+ and TFW are checked using a straight line χ^2 fit. Combinations of hits with reduced χ^2_y less than 20 are requested to be considered as track candidates (Figure 3.7). For those track candidates, the momentum is calculated in the bending plane (xz) assuming a uniform field in the ALADiN magnet. Figure 3.8 illustrates the momentum estimation method. An initial track vector is calculated using hits in TR1 and TR2. The distance d_1 is defined as the distance between the entrance of the magnet and an arbitrary point along the line denoted as intersection with the line defined by the initial vector, while d_2 is the distance between the intersection and the exit of the magnet in the line defined by the intersection point to a measured point in the TOF wall. The intersection is found to be a point where d_1 and d_2 are equals. The circle which has the two line as tangent is calculated. The radius of circle is then used to deduce the track candidate momentum using equation 3.4.

Performance studies

The momentum residuals and momentum resolution as a function of the momentum have been studied for all relevant particle species using a dedicated Monte Carlo simulation. Figure 3.9 shows in two columns the momentum residuals and the momentum resolution as a function of the momentum for the particles species which are relevant in the analysis, i.e (π^-, p, d, t, ^{3}He,^{4}He). It can be noticed that the momentum resolution is degraded for low momentum ($p < 0.6$ GeV) and for high momentum ($p > 5$ GeV/c) pattern recognition tracks. High momentum par-

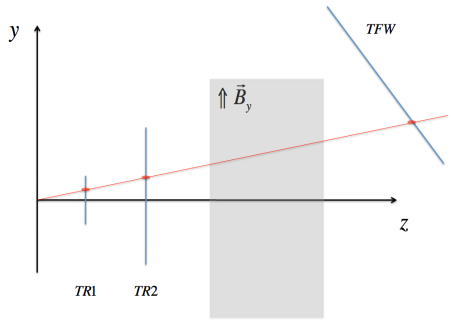

Figure 3.7: Track search in the (yz) non-bending plane .

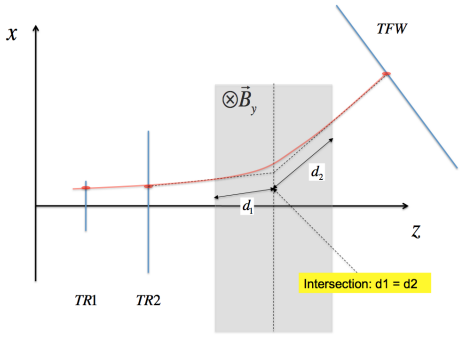

Figure 3.8: Track search in the xz bending plane taking into account the local track curvature.

ticles are not bent enough in the ALADiN magnetic field for a proper momentum reconstruction and resolution can reach for triton ($p > 8$ GeV) $\delta p/p \sim 20\%$. For low momentum particle, the geometrical calculation of the intersection simply fails and resolution can reach for proton ($p < 0.8$ GeV) $\delta p/p \sim 60\%$.

For the analysis, a correction of such an estimated momentum is then mandatory. The hit positions in the detectors including the closest hits in the drift chamber detectors will be fitted by a Kalman Filter method which uses the estimated momentum only as an initial approximation. An improvement of the momentum resolution is expected for the low momentum particle. For the high momentum particle instead, the small track curvature will not allow for much improvement.

3.5 Track fitting

3.5.1 The Kalman filter

The method chosen for the track reconstruction in the HypHI experiment is based on the Kalman filter method [37]. The Kalman filter is a method for pattern recognition and track fitting which is very commonly used in modern high-energy physics experiments. Originally, however the method was developed for radar tracking of spacecraft. It was introduced the first time into high-energy physics by P. Billoir [38] and was called the *progressive* method of track fitting [39]. However, at that time the equivalence between the *progressive* method and the Kalman filter was not known. This was realized a few years later by R. Fruehwirth [39]. It then became clear that the filter could be supplemented by a *smoothing* procedure which enabled the optimal estimation of the track parameters *anywhere* along the track, not only at some reference surface.

The Kalman filter is a linear, recursive method of track fitting which is equivalent to a global, linear least-squares method and is therefore the optimal, linear estimator of the track parameters. If the track model is truly linear and the errors involved

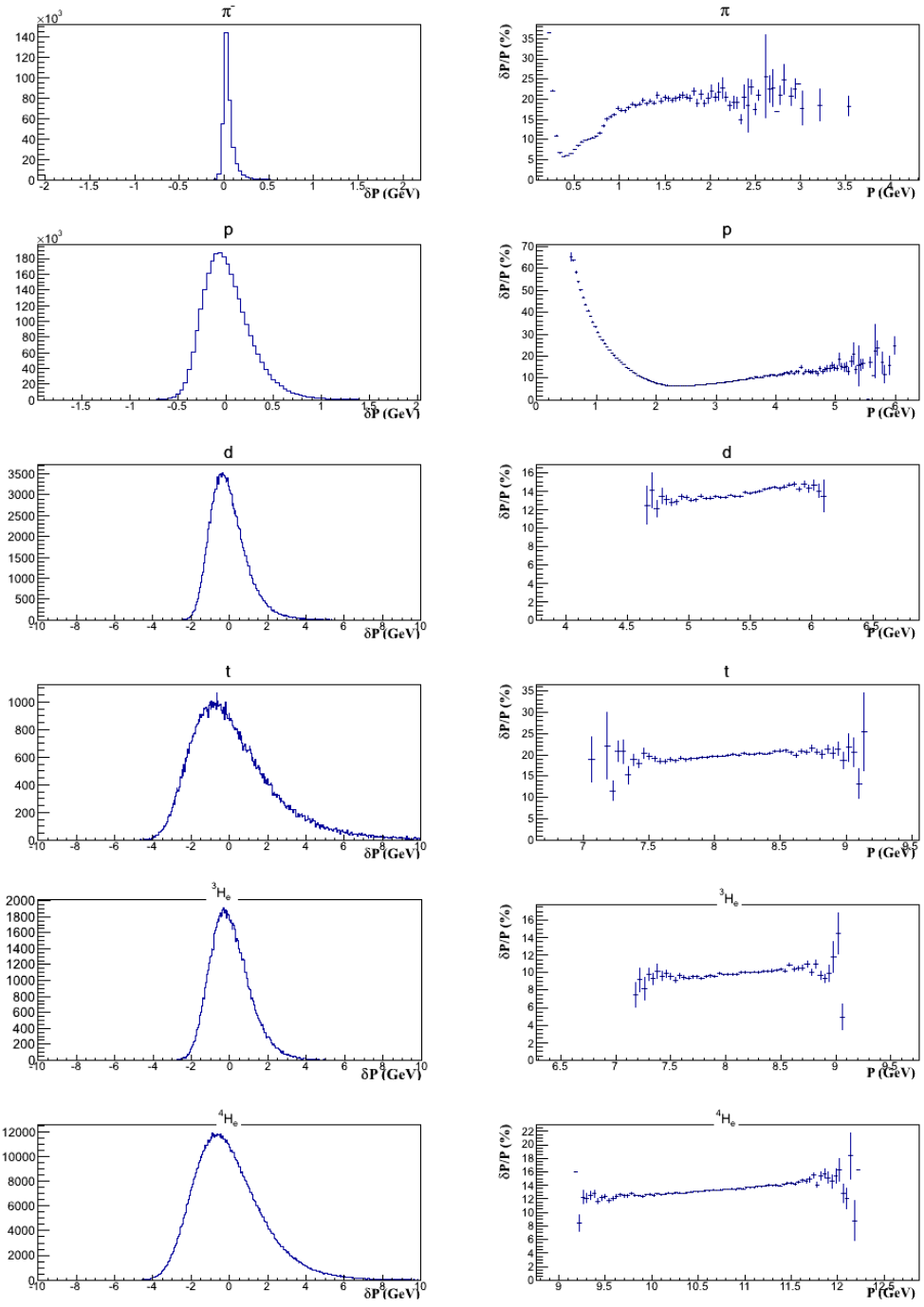

Figure 3.9: Momentum residuals and resolution as a function of the momentum obtain with the track finding procedure for all particulars species.

are Gaussian, it is also *efficient*, i.e no non-linear estimator can perform better. The Kalman filter has some well-known, attractive features which makes it preferable in the case of the HypHI experiment over the least-squares method:

- The recursive nature of the method makes it well-suited for combined track finding and track fitting
- The Kalman filter with its associated smoothing procedure deliver optimal estimates anywhere along the track. This makes it easy to obtain optimal predictions also in detectors lying close to the primary interaction vertex such as TR0 and TR1.
- The ability to obtain smoothed predictions at any detector layer also enables the Kalman filter to efficiently remove *outliers*, i.e. measurements that do not belong to the track.
- Most important advantage in the case of HypHI experiment: in the presence of multiple scattering and many measurements,a large covariance matrix has to be inverted when applying the least-squares method. This is not the case for the Kalman filter.

Generally, The track fitting procedure aims to estimate a set of parameters representing the kinematic state of a charge particle from the information contained in the various position measurements in the track candidate. Since these measurements are stochastic quantities with uncertainties attached to them, the estimation amount of some kind of statistical procedure. In addition to estimated values of the track parameters, the track fit also provides a measure of the uncertainty of these values in the terms of the covariance matrix of the track parameter vector. Most estimation methods can be decomposed into the several stages that will be described in the following.

3.5.2 Track parametrization

Five parameters are sufficient to uniquely describe the state of a charged particle. The choice of the track parameters depends on the geometry of the tracking detectors. In case of cylindrical detector layers the reference surface is often cylindrical and makes the radius times the azimuthal angel the natural choice of one of the position parameters. In the planar detector layers configuration Cartesian position coordinates are more suitable to be used.

The choice of the track parameters is essential for the efficient track fit. The transport operation and the projection into the measurement space should avoid correlations between parameters at any rate, and be as linear is possible. For fixed target experiments such like HypHI, the detector planes are mainly perpendicular to the beam axis, i.e the z-axis. Thus it is natural to parametrize the track parameters as a function of $z : \mathbf{q} = \mathbf{q}(z)$(the xy plane is approximately parallel to the detector

plane). Thereby, the state vector is chosen as follow:

$$\mathbf{q} = \begin{pmatrix} x \\ y \\ t_x \\ t_y \\ k \end{pmatrix}, \tag{3.5}$$

where x and y are local transverse coordinate, $t_x = \tan\theta_x = p_x/p_z$ and $t_y = \tan\theta_y = p_y/p_z$ the track direction tangents at the z reference value, k is inverse radius of curvature, momentum related parameter. For the particle with charge Q, k is related to the momentum component in the bending plane as

$$k = \frac{Q}{p_\perp}. \tag{3.6}$$

In case then the magnetic field is parallel to the y axis momentum transverse to the field is

$$p_\perp = \sqrt{p_x^2 + p_z^2} = p\sqrt{\frac{1+t_x^2}{1+t_x^2+t_y^2}} \tag{3.7}$$

The parameter k is preferred to the inverse total momentum since it is almost decouple transport in the horizontal and vertical planes. But for the realistic detector setup, the field is not homogeneous, but still y component dominant. In this case k strongly depends on the local field strength, so $Q/p_\perp$ will be a more suitable parameter. The local track parameters are associated with the corresponding (5×5) covariance matrix : $\mathbf{C} = \mathbf{cov}(\mathbf{q})$ with entry (ij):

$$C_{ij} = \langle (q_i - < q_j >)(q_j - < q_i >) \rangle.$$

where $< q_i >$ are the expectation values of these parameters. The track propagation algorithm predicts the trajectory of the charged particle in terms of mean values of the track parameters and the corresponding errors assuming a track model. During the propagation, three processes are taken into account:

- Energy loss, which influences both mean values and errors.
- Multiple Coulomb scattering, which affect error calculation only.
- The magnetic field, which influences the average trajectory only.

3.5.3 Track model

In the framework of the Kalman filter, the change of the parameters of a track along its path is regarded as the dynamical evolution of a stochastic *state vector* $\mathbf{q}$. It will be assumed in the following that the detector is a collection of n surfaces, and that both the measurements and the state vectors are defined at these surfaces only. The subscript k will denote quantities at layer number k.

The track model describes how the state vector at given surface k depends on a state vector on a different surface i:

$$\mathbf{q}_k = \mathbf{f}_{k|i}(\mathbf{q}_i) \tag{3.8}$$

where $\mathbf{f}_{k|i}$ is the track propagator from surface i to surface k and $\mathbf{q}$ is a state vector.

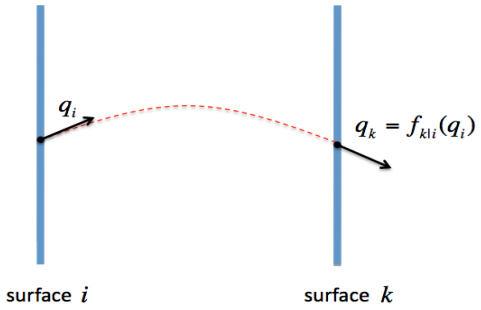

Figure 3.10: Illustration of the track model and propagation concepts. The function $\mathbf{f}_{k|i}$ is the track propagator from surface i to surface k. The exact mathematical form depends on the track model, i.e, the solution of the equation of motion in the ALADiN magnetic field.

The track model is analytical in case of absence of magnetic field (straight line) or in homogeneous field (helix). If the magnetic field is inhomogeneous, one has to use the numerical schemes for the solving of the equation of motion.

3.5.4 Measurement model

The measurement model $\mathbf{h}_k$ describes the functional dependence of the measured quantities in layer k, $\mathbf{m}_k$, on the state vector at the same layer,

$$\mathbf{m}_k = \mathbf{h}_k(\mathbf{q}_k). \tag{3.9}$$

The vector of measurements $\mathbf{m}_k$ usually consist of the measured position but can also contain the other quantities, e.g. measurements of direction or even momentum. During the estimation procedure the Jacobian $\mathbf{H}_k$ of this transformation is often needed,

$$\mathbf{H}_k = \frac{\partial \mathbf{h}_k}{\partial \mathbf{q}_k}. \tag{3.10}$$

In many cases the Jacobian contain only the rotations and the projections and can be calculated analytically.

The majority of experiments use some kind of linear least-squares approach for the track fitting.

The linear, global least-squares method is optimal if track model is linear, i.e. if the propagator $\mathbf{f}_{k|i}$ is a linear function of the state vector, and if all probability densities encountered during the estimation procedure are Gaussian. The starting point for deriving the global least-squares method is the functional relation between the initial state vector $\mathbf{q}_0$ of the particle at the reference surface and the vector of measurements $\mathbf{m}_k$ at detector layer k,

$$\mathbf{m}_k = \mathbf{d}_k(\mathbf{q}_0) + \gamma_k, \tag{3.11}$$

where $\mathbf{d}_k$ is a composition of the measurement model function $\mathbf{m}_k = \mathbf{h}_k(\mathbf{q}_k)$ and the track propagator functions:

$$\mathbf{d}_k = \mathbf{h}_k \circ \mathbf{f}_{k|k-1} \circ ... \circ \mathbf{f}_{2|1} \circ \mathbf{f}_{1|0}. \tag{3.12}$$

γ_k is a stochastic therm and contains all Coulomb multiple scattering up to layer k as well as the measurement error of $\mathbf{m}_k$. A linear estimation requires a linearized track model, and for the Jacobian $\mathbf{D}_k$ of $\mathbf{d}_k$ is needed:

$$\mathbf{D}_k = \mathbf{H}_k\mathbf{F}_{k|k-1}...\mathbf{F}_{2|1}\mathbf{F}_{1|0}, \tag{3.13}$$

where $\mathbf{H}$ is the Jacobian of $\mathbf{h}$ and $\mathbf{F}$ is the Jacobian of $\mathbf{f}$.

The observations $\mathbf{m}_k$, the functions $\mathbf{d}_k$, the Jacobians $\mathbf{D}_k$, and the noise γ_k can be presented as a single vector or matrix,

$$m = \begin{pmatrix} m_1 \\ \vdots \\ m_b \end{pmatrix}, d = \begin{pmatrix} d_1 \\ \vdots \\ d_b \end{pmatrix}, D = \begin{pmatrix} D_1 \\ \vdots \\ D_b \end{pmatrix}, \gamma = \begin{pmatrix} \gamma_1 \\ \vdots \\ \gamma_b \end{pmatrix}, \tag{3.14}$$

where the total number of measurement layers is n. The model now becomes

$$\mathbf{m} = \mathbf{d}(\mathbf{q}_0) + \gamma, \tag{3.15}$$

and the linearized version is

$$\mathbf{m} = \mathbf{D}\mathbf{q}_0 + \mathbf{c} + \gamma, \tag{3.16}$$

where c is a constant vector. The global least-squares estimate of $\mathbf{q}_0$ is given by

$$\tilde{\mathbf{q}}_0 = (\mathbf{D}^T\mathbf{G}\mathbf{D})^{-1}\mathbf{D}^T\mathbf{G}(\mathbf{m} - \mathbf{c}), \tag{3.17}$$

where $\mathbf{V} = \mathbf{G}^{-1}$ is the non-diagonal covariance matrix of γ.

Large number of measurements lead to a high computational cost of the methods due to the need of the inversion of large matrices. A recursive formulation of the least-squares method is a Kalman filter, which requires inversion of only small matrices and the material effects can be taken into account locally.

Compare to the global least-squares fit the Kalman Filter proceeds progressively from on measurement to the next, improving the particle trajectory with each new measurement (see Figure 3.11). Properties of the Kalman Filter approach make it

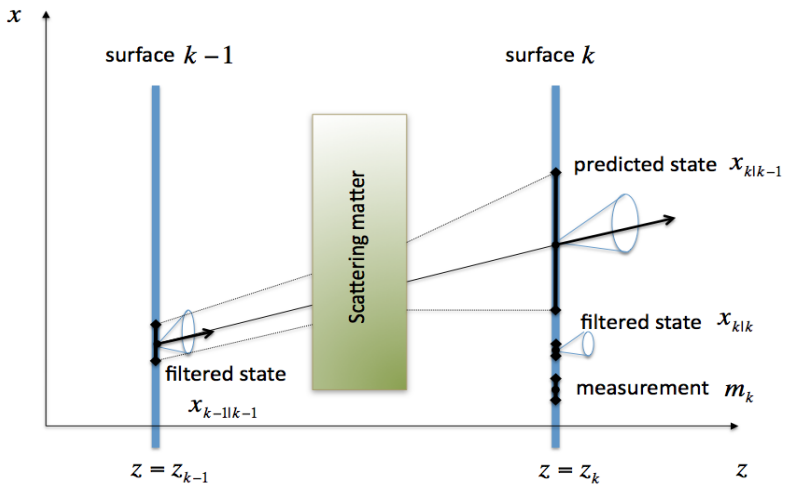

Figure 3.11: Prediction and Filter step of the Kalman filter. The propagation proceeds in the z direction, while the x coordinate is measured. The prediction step propagates the estimated track parameter $\mathbf{q}_{k-1|k-1}$ vector from detector layer $k-1$ to the next layer k containing a measurement. Adapted from [40].

more suitable instrument for the HypHI track reconstruction. The *prediction* step, when the estimation of the state vector from the current knowledge for the next measurement is made, is useful to distinguish a noise signals and the real hits from the other tracks from the fit. The *filter* step, which is updating the state vector, does not require the inversion of the matrix with the state vector as in global approach, but only with a dimension of the measurement. As well as the problem of random perturbation on the trajectory, like Coulomb multiple scattering and energy loss, can be taken into account in a very efficient way.

As already mentioned above, the Kalman filter technique was developed to determine the trajectory of the state vector of the dynamical system from a set of measurements taken at a different times. In the following a brief introduction to the mathematics of the Kalman filter will be given.

The state vector $\mathbf{q}_{k-1|k-1}$ contains the parameters of the fitted track given at the position of the $(k-1)^{th}$ hit, its covariance matrix denoted by $\mathbf{C}_{k-1|k-1}$. In the assumption of linear track model, the prediction step propagates the estimated track parameters $\mathbf{q}_{k-1|k-1}$ from detector layer $k-1$ to the next layer containing a measurement:

$$\mathbf{q}_{k-1|k-1} \equiv \mathbf{f}_{k|k-1}(\mathbf{q}_{k-1|k-1}) = \mathbf{F}_{k|k-1}(\mathbf{q}_{k-1|k-1}) \tag{3.18}$$

where the matrix $\mathbf{F}_{k|k-1}$ is a propagator of the track parameters from $(k-1)^{th}$ to k^{th} hit. A parameter m_k is the coordinate measured by the k^{th} hit, i.e. is a vector with its dimension corresponding to that of the measurement. Matrix V_k describes the measurement error. The relation between track parameters $\mathbf{q}_{k|k-1}$ and the expected

measurement m_k is given by the projection matrix H_k. Then the state vector and its covariance matrix are propagated to the next measurement the prediction equation becomes

$$\mathbf{q}_{k|k-1} = \mathbf{F}_{k|k-1}\mathbf{q}_{k-1k-1} \qquad \mathbf{C}_{k|k-1} = \mathbf{F}_{k|k-1}\mathbf{C}_{k|k-1}\mathbf{F}^T_{k|k-1} + \mathbf{Q}_k \tag{3.19}$$

and the estimated residual becomes

$$\mathbf{r}_{k|k-1} = \mathbf{m}_{k-1} - \mathbf{H}_k\mathbf{q}_{k|k-1} \qquad \mathbf{R}_{k|k-1} = \mathbf{V}_k + \mathbf{H}_k\mathbf{C}_{k|k-1}\mathbf{H}^T_k \tag{3.20}$$

Here $\mathbf{Q}_k$ is an additional error introduced by the process noise, i.e. random perturbations of the particle's trajectory. The updating of the state vector with the k^{th} measurement is performed with the filter equation:

$$\begin{aligned} \mathbf{K}_k &= \mathbf{C}_{k|k-1}\mathbf{H}^T_k(\mathbf{V}_k + \mathbf{H}_k\mathbf{C}_{k|k-1}\mathbf{H}^T_k)^{-1} \\ \mathbf{q}_{k|k} &= \mathbf{q}_{k|k-1} + \mathbf{K}_k(\mathbf{m}_k - \mathbf{H}_k\mathbf{q}_{k|k-1}) \\ \mathbf{C}_{k|k} &= (\mathbf{I} - \mathbf{K}_k\mathbf{H}_k)\mathbf{C}_{k|k-1} \end{aligned} \tag{3.21}$$

with the filtered residual

$$\mathbf{r}_{k|k} = (1 - \mathbf{H}_k\mathbf{K}_k)\mathbf{r}_{k|k-1} \qquad \mathbf{R}_{k|k} = (\mathbf{I} - \mathbf{H}_k\mathbf{K}_k)\mathbf{V}_{k|k} \tag{3.22}$$

where $\mathbf{K}_k$ is a gain matrix. The χ^2 contribution of the filtered point is given by

$$\chi^2_{k,F} = \mathbf{r}^T_k\mathbf{R}^{-1}_{k|k}\mathbf{r}_k \tag{3.23}$$

The state vector at the last point contains always the full information from all points. If it is needed to have a vector at every point of the trajectory, then the new information has to be obtained by passing with the smoother equations:

$$\begin{aligned} \mathbf{A}_k &= \mathbf{C}_{k|k}\mathbf{F}^T_{k+1|k}(\mathbf{C}_{k|k-1})^{-1} \\ \mathbf{q}_{k|n} &= \mathbf{q}_{k|k} + \mathbf{A}_k(\mathbf{q}_{k+1|n} - \mathbf{q}_{k+1|k}) \\ \mathbf{C}_{k|n} &= \mathbf{C}_{k|k} + \mathbf{A}_k(\mathbf{C}_{k+1|k} - C_{k+1|n})\mathbf{A}^T_k \\ \mathbf{r}_{n|k} &= \mathbf{m}_k - \mathbf{H}_k\mathbf{q}_{n|k} \\ \mathbf{R}_{n|k} &= \mathbf{R}_k - \mathbf{H}_k\mathbf{A}_k(\mathbf{C}_{n|k+1} - \mathbf{C}_{k|k-1})\mathbf{A}^T_k\mathbf{H}^T_k \end{aligned} \tag{3.24}$$

Smoothing is also a recursive operation which proceeds step by step in the opposite to the filtering direction. In case then process noise such as multiple scattering is taken into account the smoothed trajectory may in general contains small kinks and thus reproduce more close of the particle real path.

In the equations above, $\mathbf{F}$ and $\mathbf{H}$ are just ordinary matrices if both transport and projection in measurement space are linear. In case of non-linear systems, one has to replace them by the corresponding functions and their derivatives:

$$\mathbf{F}_k\mathbf{q}_{k|k} \to \mathbf{f}_k(\mathbf{q}_{k|k}) \qquad \mathbf{H}_k\mathbf{q}_{k|k} \to \mathbf{h}_k(\mathbf{q}_{k|k}) \tag{3.25}$$

and covariance matrix transformations

$$\mathbf{F}_k \to \frac{\partial \mathbf{f}_k}{\partial \mathbf{q}_{k|k}} \qquad \mathbf{H}_k \to \frac{\partial \mathbf{h}_k}{\partial \mathbf{q}_{k|k}} \tag{3.26}$$

The dependence of $\mathbf{f}_k$ and $\mathbf{h}_k$ on the state vector estimate will in general require iteration until the trajectory converges such that all derivatives are calculated at their proper positions. In this case the $\partial \mathbf{f}_k / \partial \mathbf{q}_{k|k}$ and $\partial \mathbf{h}_k / \partial \mathbf{q}_{k|k}$ are called transport and projection matrix respectively.

3.5.5 Average trajectory and transport matrices

In a fixed target spectrometer like HypHI, the role of the time in the system evolution in the Kalman filter can be associated with the z coordinate of the detector, while the measurements coordinates transverse to the beam.

When dividing the track into n sequential steps, the transport matrix is calculated as repeated multiplications of the transport matrices for each steps:

$$\mathbf{F} = \prod_{k=1}^{n} \mathbf{F}_k \tag{3.27}$$

Field free region

In case of the absence of magnetic field the particle trajectory is resumed to a straight line: only the Y and Y components of the state vector will be changed

$$x_{k|k-1} = x_{k-1} + t_x \Delta z \tag{3.28}$$

$$y_{k|k-1} = y_{k-1} + t_y \Delta z \tag{3.29}$$

with $\Delta z = z_k - z_{k-1}$ The transport matrix $\mathbf{F}_k$ in this case reads:

$$\mathbf{F}_k = \begin{pmatrix} 1 & 0 & \Delta z & 0 & 0 \\ 0 & 1 & 0 & \Delta z & 0 \\ 0 & 0 & 1 & 0 & 0 \\ 0 & 0 & 0 & 1 & 0 \\ 0 & 0 & 0 & 1 & 0 \end{pmatrix} \tag{3.30}$$

Equation of motion in magnetic field

The trajectory of a particle in a static magnetic field $\mathbf{B}$ has to satisfy the equations of motion given by the Lorentz force 3.3.

$$\frac{d}{dt}(m\gamma \frac{d\mathbf{x}}{dt}) = \frac{q}{c} \frac{d\mathbf{x}}{dt} \times \mathbf{B} \tag{3.31}$$

where q is the charge, $\mathbf{v} = \dfrac{d\mathbf{x}}{dt}$ the velocity, and $\mathbf{B}$ the magnetic field vector. The equation 3.31 can be rewritten in terms of the track length parameter s the curvilinear distance along the trajectory

$$\frac{d^2\mathbf{x}}{ds^2} = \frac{q}{cp} \cdot \frac{d\mathbf{x}}{ds} \times \mathbf{B}(\mathbf{x}, s) \tag{3.32}$$

The motion of the charged particle along the z axis can be expressed from 3.32 as:

$$x'' = \kappa \cdot (q/p)(ds/dz)\left[x'y'B_x - (1 + x'^2)B_y + y'B_z)\right], \tag{3.33}$$

$$y'' = \kappa \cdot (q/p)(ds/dz)\left[(1 + y'^2)B_x - x'y'B_y - x'B_z)\right] \tag{3.34}$$

where $ds/dz = \sqrt{1 + x'^2 + y'^2}$, $\kappa = 2.99792458 \cdot 10^{-4}[(\mathrm{GeV/c})\mathrm{T}^{-1}\mathrm{mm}^{-1}]$, and the prime denotes the derivatives with respect to z.
Thereby, the equation of motion can be written as follows using the state vector of track parameters:

$$\frac{d\mathbf{q}}{dz} = \frac{d}{dz}\begin{pmatrix} x \\ y \\ t_x \\ t_y \\ Q/p \end{pmatrix} = \begin{pmatrix} t_x \\ t_y \\ (\kappa Q/p)A_x \\ (\kappa Q/p)A_y \\ 0 \end{pmatrix} \tag{3.35}$$

where A_x and A_y are defined as

$$A_x = \sqrt{1 + t_x^2 + t_y^2}\left(t_x t_y B_x - (1 + t_x^2)B_x + t_y B_z\right) \tag{3.36}$$

$$A_y = \sqrt{1 + t_x^2 + t_y^2}\left((1 + t_y^2)B_x - t_x t_y B_y - t_y B_z\right) \tag{3.37}$$

Then one has to solve the Cauchy problem with the initial value $\mathbf{q}_0$. In our implementation, the problem is solved using the 4^{th} order Runge-Kutta method [41].

3.5.6 Material effects

The most important effect on the path of the charged particle caused by the material presented in the detector volume are ionization energy loss and Coulomb multiple scattering. For the light particles such as electrons, radiation energy loss by bremsstrahlung also plays an important role. The fluctuation of the ionization energy loss are usually quite small, therefore normally treated during track fitting as a deterministic correction to the state vector. Bremsstrahlung energy loss suffers from the large fluctuation and affects both the state vector and the covariance matrix. Coulomb multiple scattering is an elastic process, which in a thin materials affect only the direction of the passing charged particle; in a sufficiently thick material disturbs also the position in the plane transversal to the incident direction. Since the mean value of scattering angle and the eventual offset is zero, only the covariance matrix is updates in order to take into account the effects of multiple scattering into the fitting procedure.

Energy Loss

The energy loss decreases the particle energy and eventually a particle can even be stopped if during such a process it looses all its energy. In the presence of a magnetic field, the energy loss influences the path of charged particles by reducing their momentum. Energy loss of particles traversing material occurs due to

- Electromagnetic effects or ionization in an order proportional to α^2, α denotes the fine structure constant $\alpha = 1/137$.
- Bremsstrahlung in an order proportional to α^3
- Direct pair production in an order proportional to α^4
- Photonuclear interactions [35]

Nevertheless for heavy particles with masses above 100 MeV ionization loss dominates the overall energy loss. In the energy loss correction algorithm only energy loss by ionization is taken into account.

The mean energy loss from ionization for heavy particles is given by the Bethe-Bloch equation [42]:

$$\left(\frac{dE}{dx}\right)_{ionization} = -Kz^2\frac{Z}{A}\frac{1}{\beta^2}\left[\frac{1}{2}ln\frac{2m_ec^2\beta^2\gamma^2T_{max}}{I^2} - \beta^2 - \frac{\delta(\beta\lambda)}{2}\right] \tag{3.38}$$

where $K = 4\pi N_A r_e^2 m_e c^2 = 0.307075\ MeVg^{-1}cm^2$ is a constant, Z is the charge of the particle, Z and A are the atomic number and mass of the absorber, m_ec^2 is the electron mass, I is the mean excitation energy, T_{max} is the maximum kinetic energy which can be transferred to a free electron in a single collision, and $\delta(\beta\lambda)$ is the density effect correction.

For a particle with mass M and momentum $M\beta\gamma c$, T_{max} reads [42]

$$T_{max} = \frac{2m_ec^2\beta^2\gamma^2}{1 + 2\gamma m_e/M + (m_e/M)^2} \tag{3.39}$$

At high energy the density effect is approximate using [42]

$$\delta/2 \to ln\left(\frac{28.816\sqrt{\rho\,\langle Z/A\rangle}}{I}\right) + ln\beta\gamma - 1/2 \tag{3.40}$$

In general the density effect correction δ depends in the properties of the material, for a more accurate estimation the Sternheimer's parametrization are used [42].

The mean excitation energy I depends highly influenced on the internal structure of the atoms in the traversed material as shown by the Figure 3.12.

It is difficult to find a proper approximation which could be valid for all atoms.

In the energy loss correction algorithm, the simple approximation is used:

$$I = 10\ eV \cdot Z,\ Z > 16 \tag{3.41}$$

$$I = 16\ eV \cdot Z^{0.9},\ Z < 16 \tag{3.42}$$

The difference in energy before and after crossing a certain material is given by:

$$\Delta E = \Delta\rho l \tag{3.43}$$

where l is the traversed length in the material and ρ is the material density. Then the Q/p correction is given by

$$\frac{Q}{p} = \frac{Q}{\sqrt{(E_{corr}^2 - M^2)}} \tag{3.44}$$

where $E_{corr} = E_0 + \Delta E$ is the corrected energy of the particles after crossing the material.

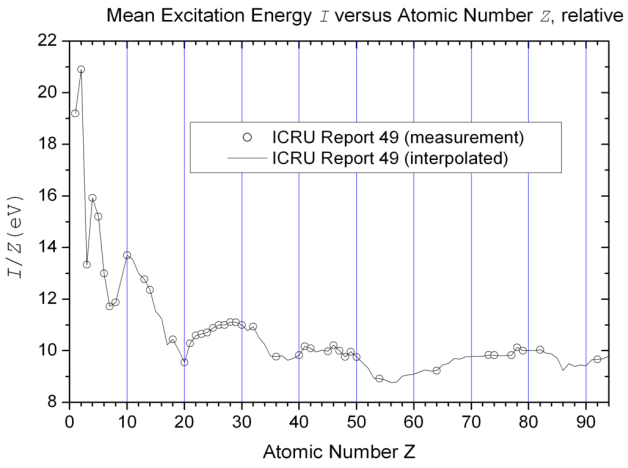

Figure 3.12: Mean excitation energies, I divided by Z in eV units as a function of the Z of the material [42].

Multiple scattering

Multiple scattering occurs through elastic scattering of charged particles in the Coulomb field of the nuclei in the detector material. Since the nuclei are usually much heavier then the traversing particles, the absolute momentum of the latter remains unaffected while their direction is changed. Consequently only track parameters related to particle direction are affected directly, these are the track slopes t_x and t_y in the track parametrization chosen above.

The Coulomb scattering is well represented by the theory of Moliere. It is roughly gaussian for small deflection angles, but at larger angles it behaves like Rutherford scattering, with larger tails than for a gaussian distribution. The multiple scattering correction algorithm uses the well-known Highland formula which is a gaussian approximation for the central 98% of the projected angular distribution, with a width given by [35]:

$$\Theta_0 = \frac{13.6\ MeV}{\beta pc} z \sqrt{\frac{l}{X_0}} \left[1 + 0.038 ln(\frac{l}{X_0})\right] \tag{3.45}$$

Multiple scattering is a random process, therefore, its corrections affects only the process noise matrix $\mathbf{Q}_k$. Corrections to the covariance matrix for an absorber with

thickness Δz are given by the symmetric matrix [43, 42]

$$\mathbf{Q}(\Delta z) = \begin{pmatrix} cov(t_x,t_x)\frac{\Delta z^2}{3} & cov(t_x,t_y)\frac{\Delta z^2}{3} & cov(t_x,t_x)\frac{\alpha\Delta z}{2} & cov(t_x,t_y)\frac{\alpha\Delta z}{2} & 0 \\ \cdots & cov(t_y,t_y)\frac{\Delta z^2}{3} & cov(t_x,t_y)\frac{\alpha\Delta z}{2} & cov(t_y,t_y)\frac{\alpha\Delta z}{2} & 0 \\ \cdots & \cdots & cov(t_x,t_x) & cov(t_x,t_y) & 0 \\ \cdots & \cdots & \cdots & cov(t_y,t_y) & 0 \\ \cdots & \cdots & \cdots & \cdots & 0 \end{pmatrix} \tag{3.46}$$

where symmetric counterparts are symbolized with dots and the slopes covariances reads:

$$\begin{aligned} cov(t_x,t_x) &= (1+t_x^2)(1+t_x^2+t_y^2)\Theta_0^2 \\ cov(t_y,t_y) &= (1+t_y^2)(1+t_x^2+t_y^2)\Theta_0^2 \\ cov(t_x,t_y) &= t_x t_y(1+t_x^2+t_y^2)\Theta_0^2 \end{aligned} \tag{3.47}$$

Δz is the traversed length of the material and $\alpha = \pm 1$ indicating whether the motion will increase (+1) or decrease (-1) the z coordinate.

Geometry Navigation

In order to compute accurately the material effects during track propagation the precise traversed length in the material and the material properties have to be determined. The dynamical estimation of the traversed length and the traversed material properties is done using the ROOT geometry package [44] which takes into account the exact geometry of the HypHI experiments as it is implemented for the simulation.

The navigation through the detector geometry is illustrated in Figure 3.13. The track propagation interval $[z_0, z_f]$ is divided into several steps. The number of steps is obtained using a predefined maximum step size h_{max} which depends on the density of the traversed material: $n_{steps} = |z_f - z_0| / h_{max}$. For each step the navigation algorithm searches for intersections with the material along a straight line marked with white dots in Figure 3.13. In the next stage, a precise extrapolation is done between the intersection points inside each steps and material effects are added at each intersection points as it is done during the internal tracking of the simulation.

3.5.7 Error propagation

During the track parameter estimation procedure, propagation of the track parameter covariance matrix along the track parameters themselves is requested. The standard procedure is called the linear error propagation and it's similar to the transformation between layers i and k

$$\mathbf{C}_k = \mathbf{F}_{k|i}\mathbf{C}_i\mathbf{F}_{k|i}^T, \tag{3.48}$$

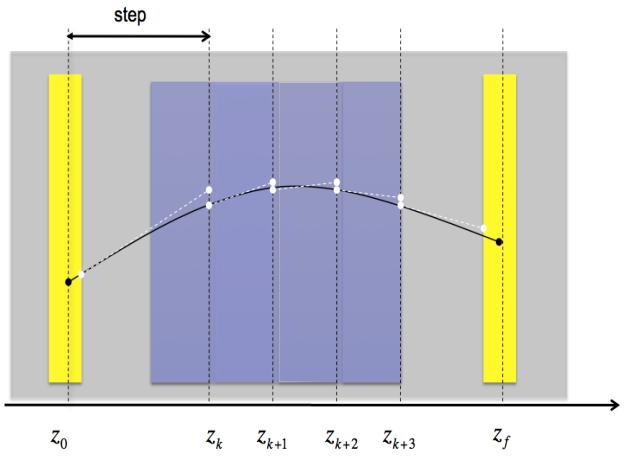

Figure 3.13: Illustration of the calculation of the traversed length using the navigation algorithm of the Geometry Modeller in ROOT [44].

where C is covariance matrix and $\mathbf{F}_{k|i}$ is the Jacobian matrix of the propagation from layer i to k

$$\mathbf{F}_{k|i} = \frac{\partial \mathbf{q}_k}{\partial \mathbf{q}_i}. \tag{3.49}$$

For the analytical track models the Jacobian is also analytical, but in case of inhomogeneous magnetic field, the derivatives are calculated numerically. The most

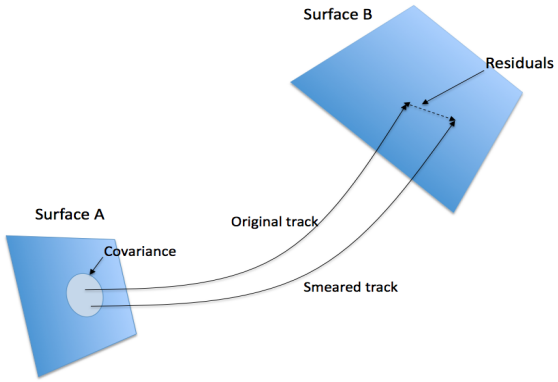

Figure 3.14: Illustration of the error propagation algorithm. The initial track parameters are smeared according the the covariance matrix estimated at surface A. The residuals obtained are then used to compute numerically all the derivatives, components of the Jacobian matrix.

straightforward way is by using the definition of the numerical derivative:

$$f'(q_i) \sim \frac{f(q_i + h_i) - f(q_i)}{h_i} \tag{3.50}$$

where $f(q_i)$ propagates the local track parameters denoted by i, from the initial surface to the target surface, while h_i is kept sufficiently small, ideally zero. By using the above definition of the derivative, the initial local track are varied by a small amount h_i, one at a time. Only such a procedure gives an estimate of how these small variations in initial values translate to the final local track parameters. Registering the changes to the final parameters gives the 25 derivatives of the Jacobian.

Even though the procedure appears to be simple, the method is quite inaccurate. One can increase the algorithm accuracy by using instead of Equation 3.50 the following symmetric derivative [41]

$$g'(h_i) \sim \frac{f(q_i + h_i) - f(q_i - h_i)}{2h_i} \tag{3.51}$$

which has a fractional error two orders of magnitude better than the original definition of derivatives given in equation 3.50. For further improvements in accuracy, the Ridders algorithm has been used [42]. The idea of this algorithm is to parametrize the symmetric derivative as a function of h_i alone by calculating it for decreasing values of h_i (see fig. 3.15). This parametrization of $g(h_i)$ is then used to estimate the derivative at the limit $h_i \to 0$.

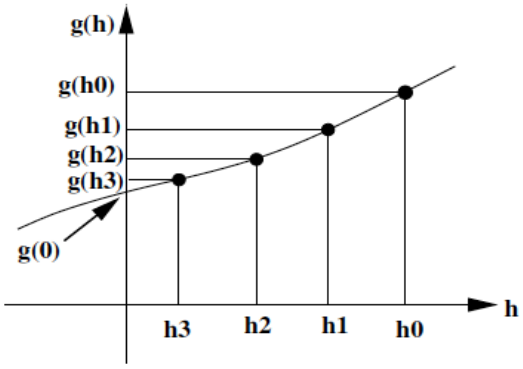

Figure 3.15: Illustration of the Ridder algorithm. The graph shows the parametrization of the symmetric derivative $g(h_i)$.

3.6 Tracking performance

The performance of the tracking algorithm has been evaluated by generating different tracks with the UrQMD heavy ions collisions generators. The generated tracks

were then processed through the HypHI spectrometer using the Virtual Monte Carlo software environment [45]. All material effects, energy loss and multiple scattering, were taken into account in the simulation.

The quality of the tracking algorithm is tested using two different estimators:

- The track parameter residual: the difference between the fitted parameter to the Monte Carlo truth. The distribution of residuals is expected to be centered at zero and normally distributed. The standard deviation obtained by applying a gaussian fit to the distribution measure the *visible track parameter resolution*.

- The track parameter pull or *normalized residual*: is defined by

$$\mathbf{P}(q_i) = \frac{q_i^{rec} - q_i^{MC}}{\sqrt{C_{ii}}} \tag{3.52}$$

  where q_i^{rec} is the reconstructed track parameter and q_i^{MC} the corresponding Monte Carlo value, while C_{ii} is the estimate for the corresponding covariance diagonal element.

Material effects correction

In order to quantify the effectiveness of the multiple scattering correction, two type of particles were fitted[1] using the Kalman filter:

- Slow pion in the momentum range $p_\pi \in [0.2, 2.]$ (GeV/c) with a polar angle $\theta \in [0, 4^o]$ degree

- Slow proton in the momentum range $p_p \in [0.8, 4.5]$ (GeV/c) with a polar angle $\theta \in [0, 4^o]$ degree

The figures 3.16 and 3.17 show the pulls distribution obtains for respectively the pion and the proton tracks without and with material effect corrections. The resulting pull distributions fitted with a gaussian function are superimposed.

The pion tracks fitted without material effects correction show extremely distorted distribution of the parameter estimates (see fig.3.16). For the protons track sample the distortion of the parameter estimates without correction is less pronounced. When the material effects are applied in the Kalman fit, the gaussian core of the pulls agree in all cases (pion an proton tracks) with unity, indicating a reliable estimate of the covariance matrix. Inspection of pull for lower momenta shows that even for very low momenta pion (100 MeV), the estimate of parameters ans covariance matrix is[2] reliable.

[1] the Kalman fit procedure was restricted to two passes

[2] The magnetic field had to be reduced for the low momenta study. It should be noted that these low momenta are considered only for testing purpose because the acceptance of the tracking system - in connection with the strength of the magnetic field-cuts off pions with momenta below 0.4 GeV

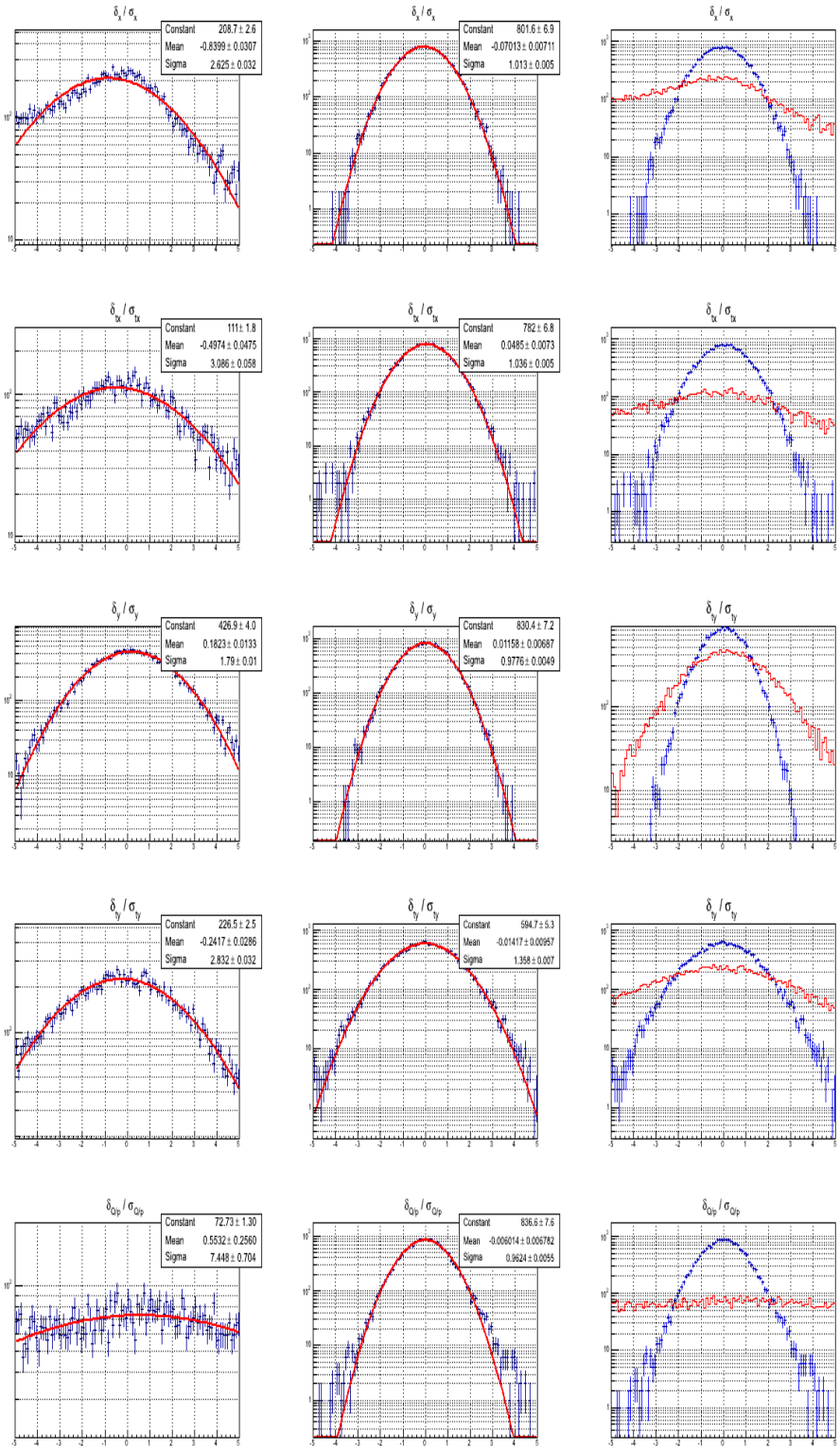

Figure 3.16: Effect of material correction for π fitted tracks in the momentum range $p_\pi \in [0.2, 2.]$. The figure shows 3 columns. The first column shows uncorrected pull distribution, the second the corrected distribution and in the third column the uncorrected and corrected pull distribution are superimposed.

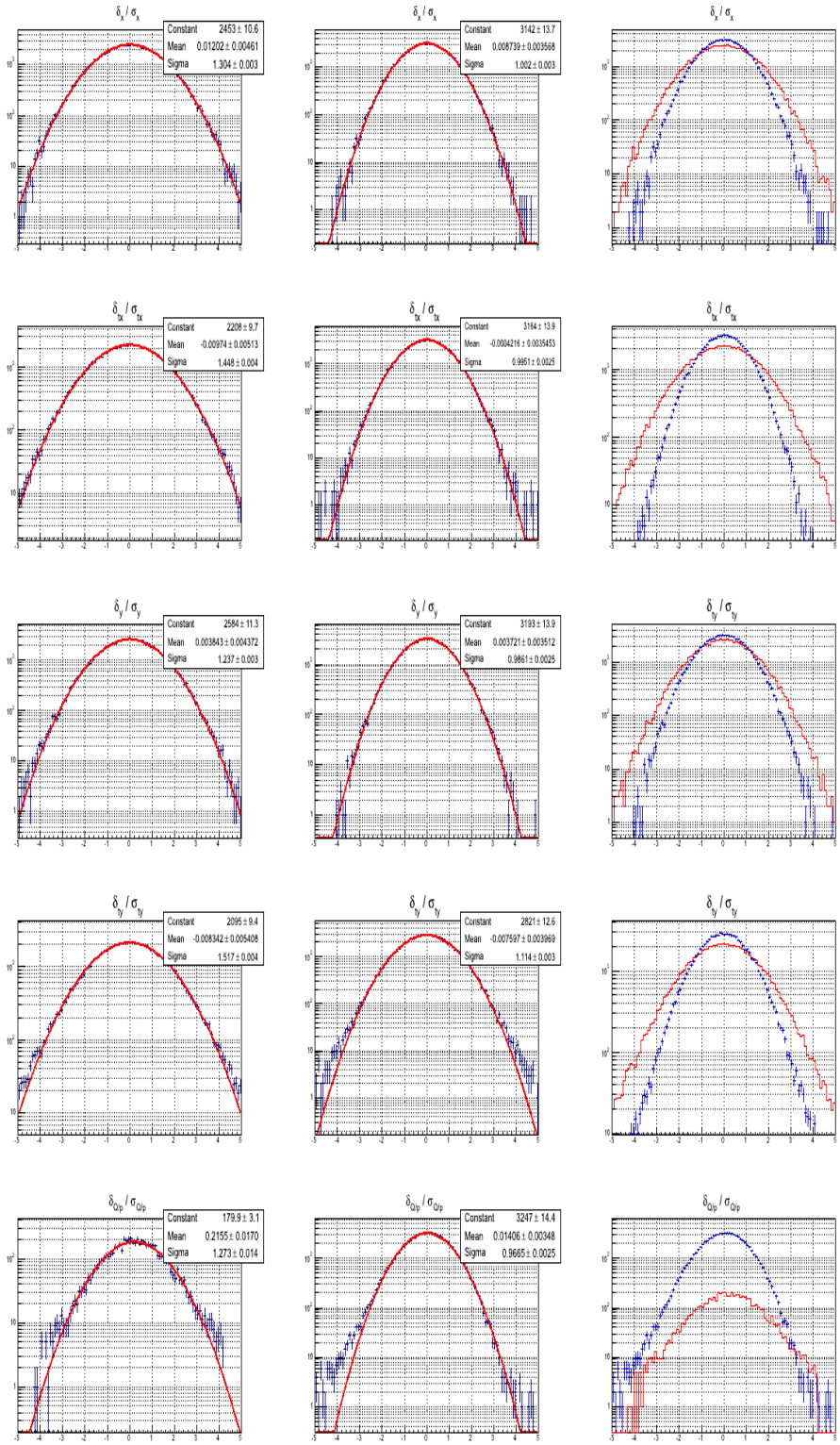

Figure 3.17: Effect of material correction for P fitted tracks in the momentum range $p_P \in [0.8, 4.5]$ GeV. The figure shows 3 columns. The first column shows uncorrected pull distribution, the second the corrected distribution and in the third column the uncorrected and corrected pull distribution are superimposed.

Tracking performance for different types of particles

Different type of particles, i.e π, p, ^{3}He and ^{4}He particles, coming out of a ^{6}Li ion beam at 2 A GeV impinging on a carbon target were generated using the UrQMD heavy ions collisions generators. The momentum range of generated particles should correspond to the visible momentum range in the experiment.

The Figures 3.18, 3.19 , 3.20 and 3.21 show the pull distribution obtained when the Kalman fit was applied to all main tracker hits, i.e. hits measured on TR1, TR2 SDC and TOF plus detector plane for positively charge particle and hits measured on TR1, TR2, SDC and TFW detector plane for negatively charge particle.

For all different types of particles, the gaussian cores pulls agree with unity, indicating a reliable estimate of the covariance matrix. Furthermore all pulls distributions are centered at zero indicating that no bias exists in the estimation of the track parameters.

Tracking quality

Since the Kalman filter is mathematically equivalent to a least-squares estimator, the sum of the filtered χ^2 contributions $\chi^2 = \sum_i \delta\chi^2_F$ will follow a χ^2 distribution assuming that the errors entering into the fit are normally distributed. In this case the χ^2 probability

$$P_{\chi^2} = \int_{-infty}^{\chi^2} f(\chi^2) d\chi^2 \tag{3.53}$$

where $f(\chi^2)$ is the standard χ^2 distribution for the appropriate number of degree of freedom and should be evenly distributed between 0 and 1. However in reality $f(\chi^2)$ is not exactly evenly distributed and deviations are to be expected if multiple scattering[3] is a dominating effect. In the HypHI tracking system, these effects have a much larger influence than in traditional tracking system because of the large amount of plastic scintillator material coming from fiber detectors and TOF walls.

The figure 3.22 shows the normalized χ^2 and χ^2 probability distributions for all type of particle. For the negatively charged particle, the probability of χ^2 deviates slightly from a flat distribution due to the multiple scattering effect that dominates at low momenta. This deviation does not indicate a bad behavior of the fit, but shows the inadequacy of the χ^2 test when errors are not normally distributed.

For the positively charged particles, the probability of χ^2 is nearly uniformly distributed between 0 and 1. All normalized χ^2 shows a mean peaked at one.

3.6.1 Tracking resolution

The relative momentum resolution dp/p and the relative length resolution dl/l as a function of the momentum is shown in figure 3.23. For the negatively low momentum charged particle, the resolution is almost completely dominated by the multiple

[3] Angular deviations due to multiple scattering in the Moliere theory do not results in gaussian distributed position errors.

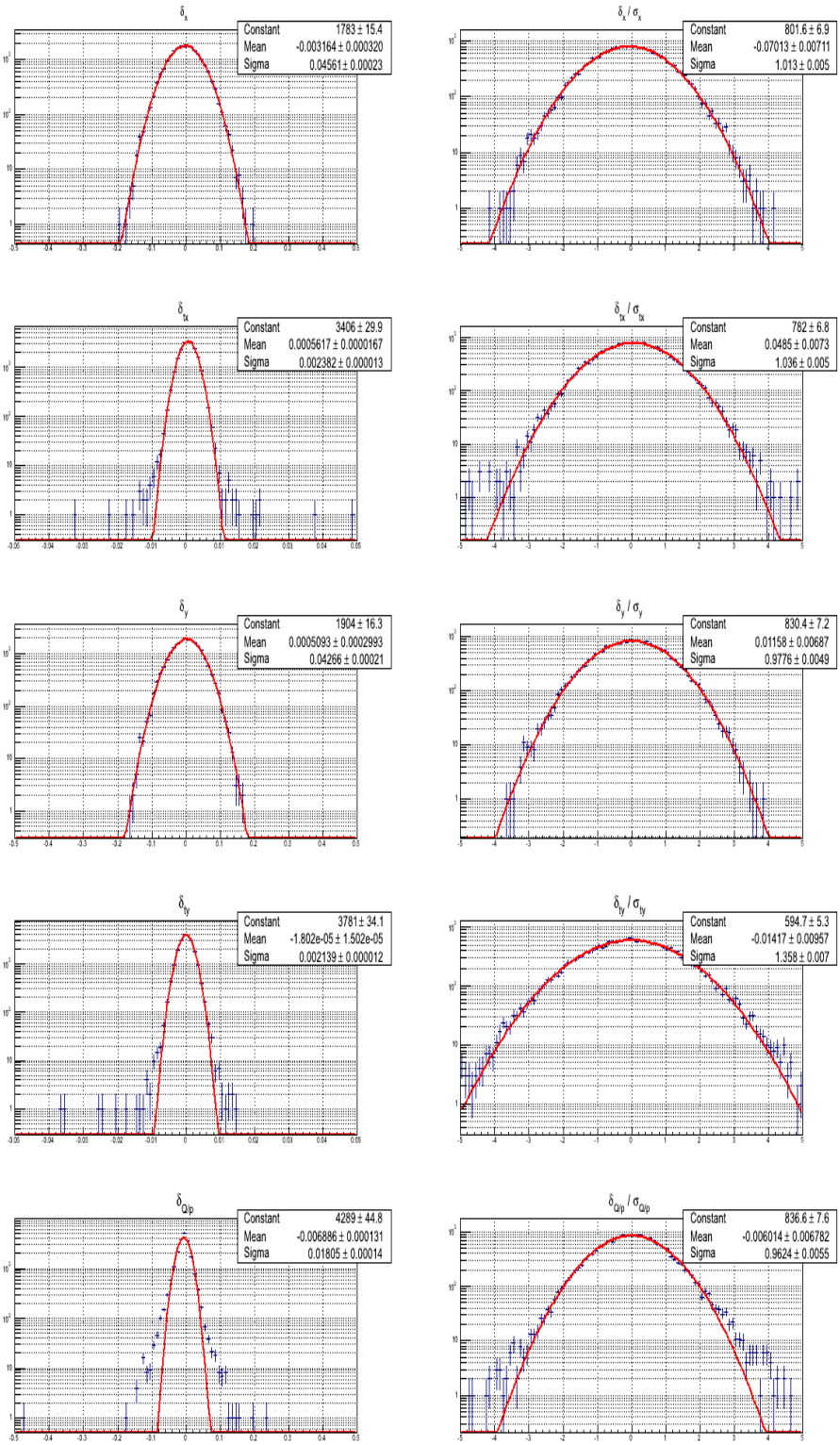

Figure 3.18: State vector pulls (right column) and residuals (left column) distributions for π tracks in the momentum range $p_P \in [0.4, 2.5]$ GeV

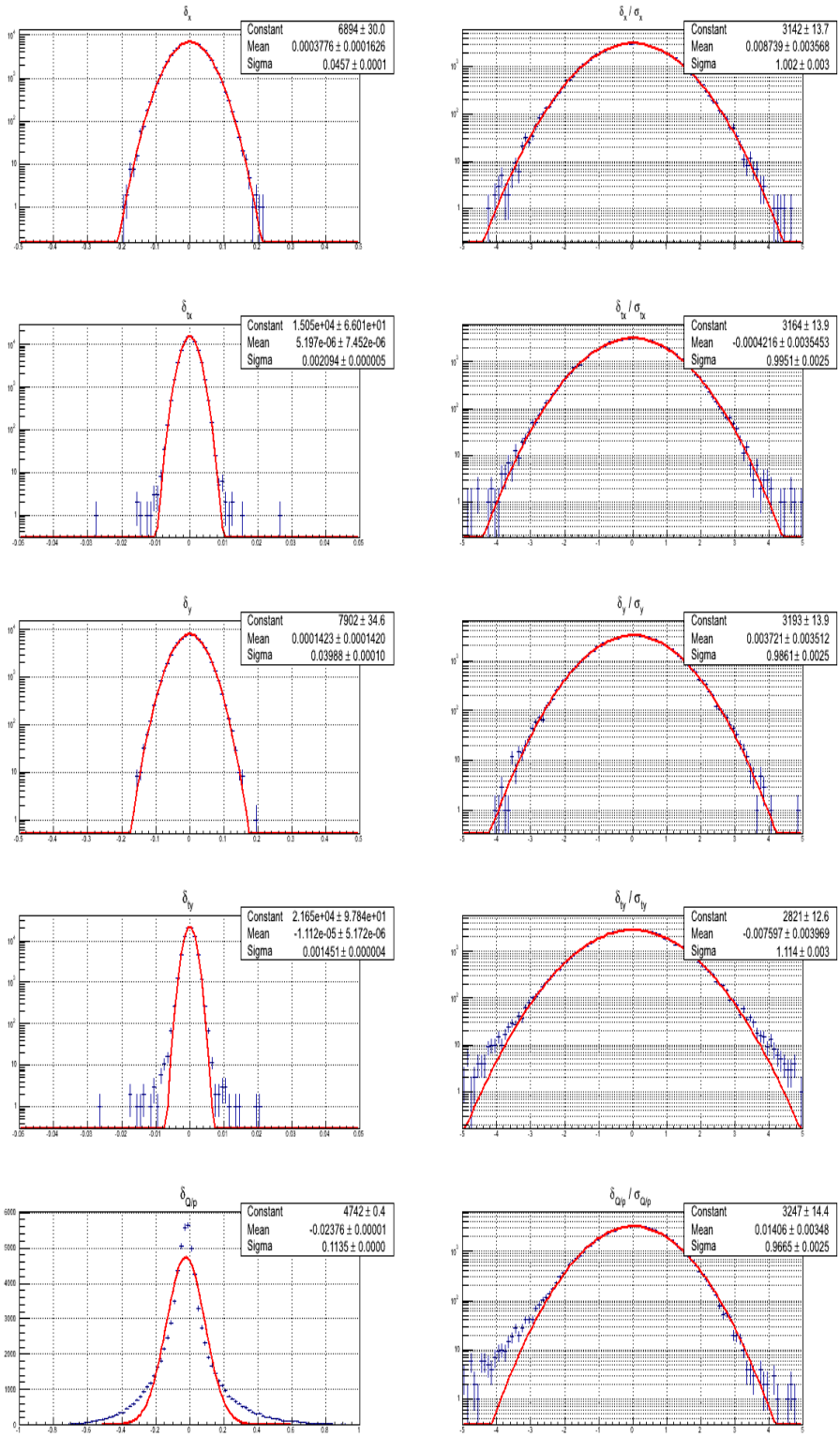

Figure 3.19: State vector pulls (right column) and residuals (left column) distributions for proton tracks in the momentum range $p_P \in [0.8, 4.5]$ GeV

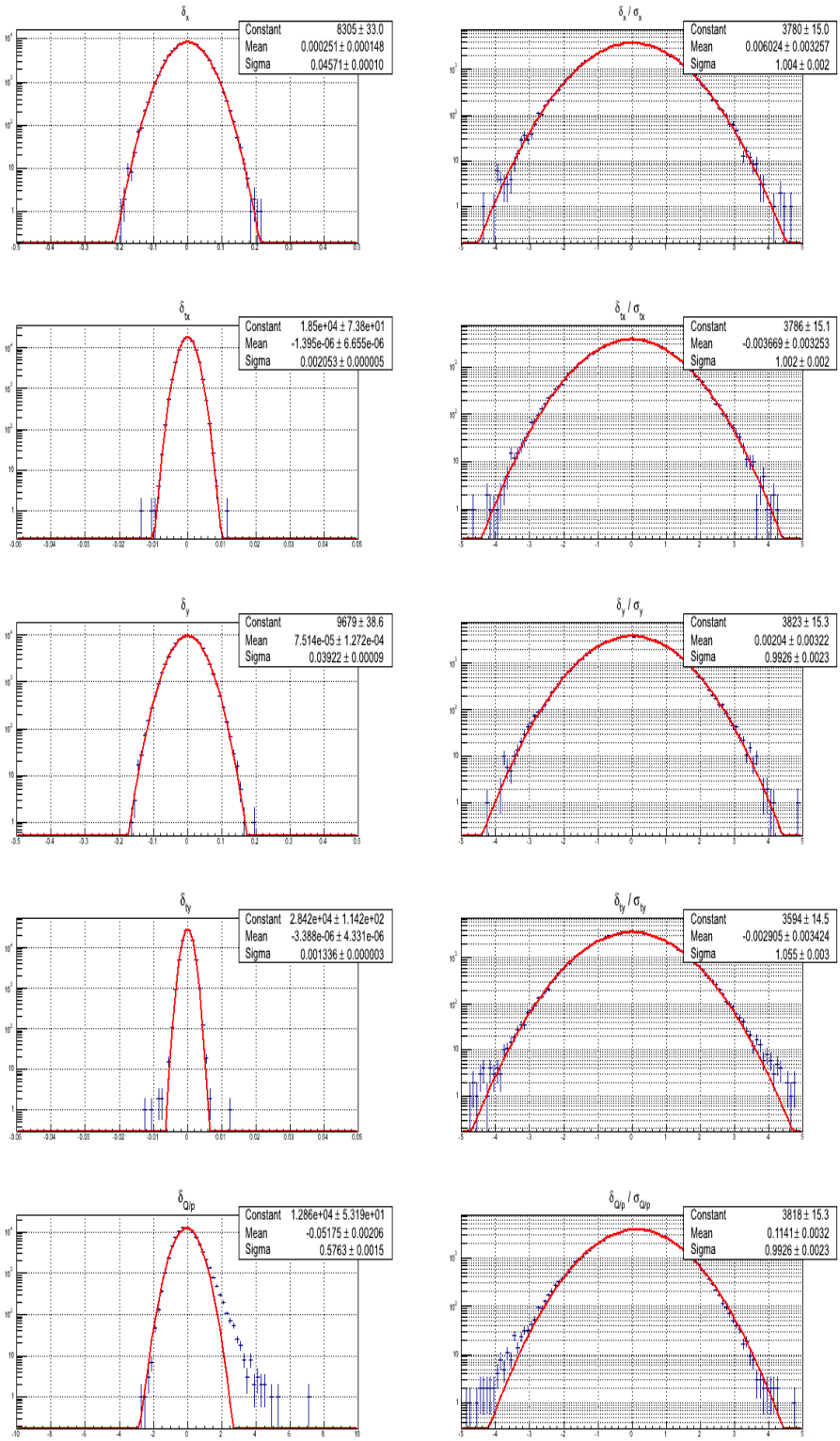

Figure 3.20: State vector pulls (right column) and residuals (left column) distributions for ^{3}He tracks in the momentum range $p_{^3He} \in [3.5, 7.]$ GeV

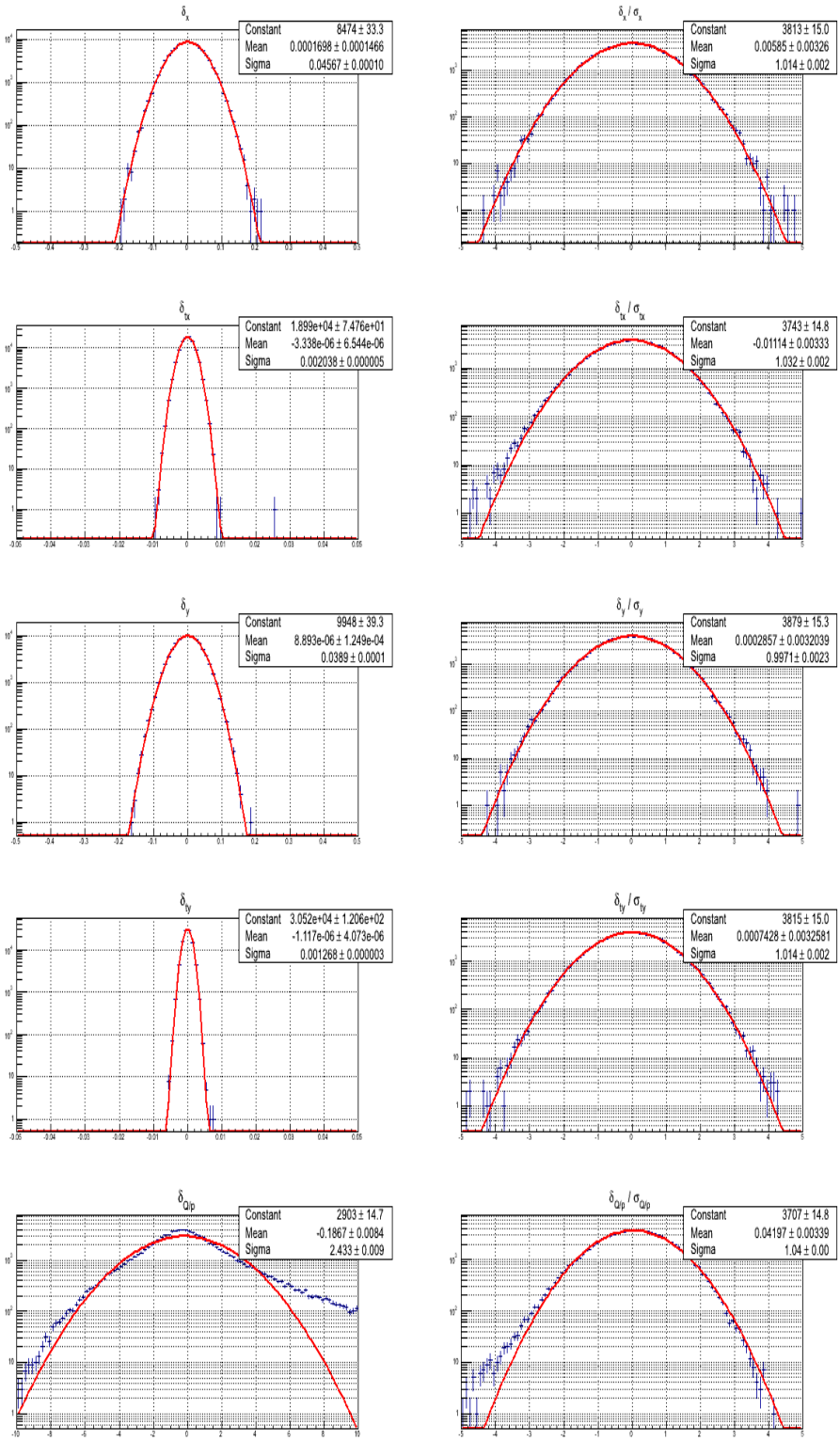

Figure 3.21: State vector pulls (right column) and residuals (left column) distributions for ^{4}He tracks in the momentum range $p_{^4He} \in [7., 25.]$ GeV

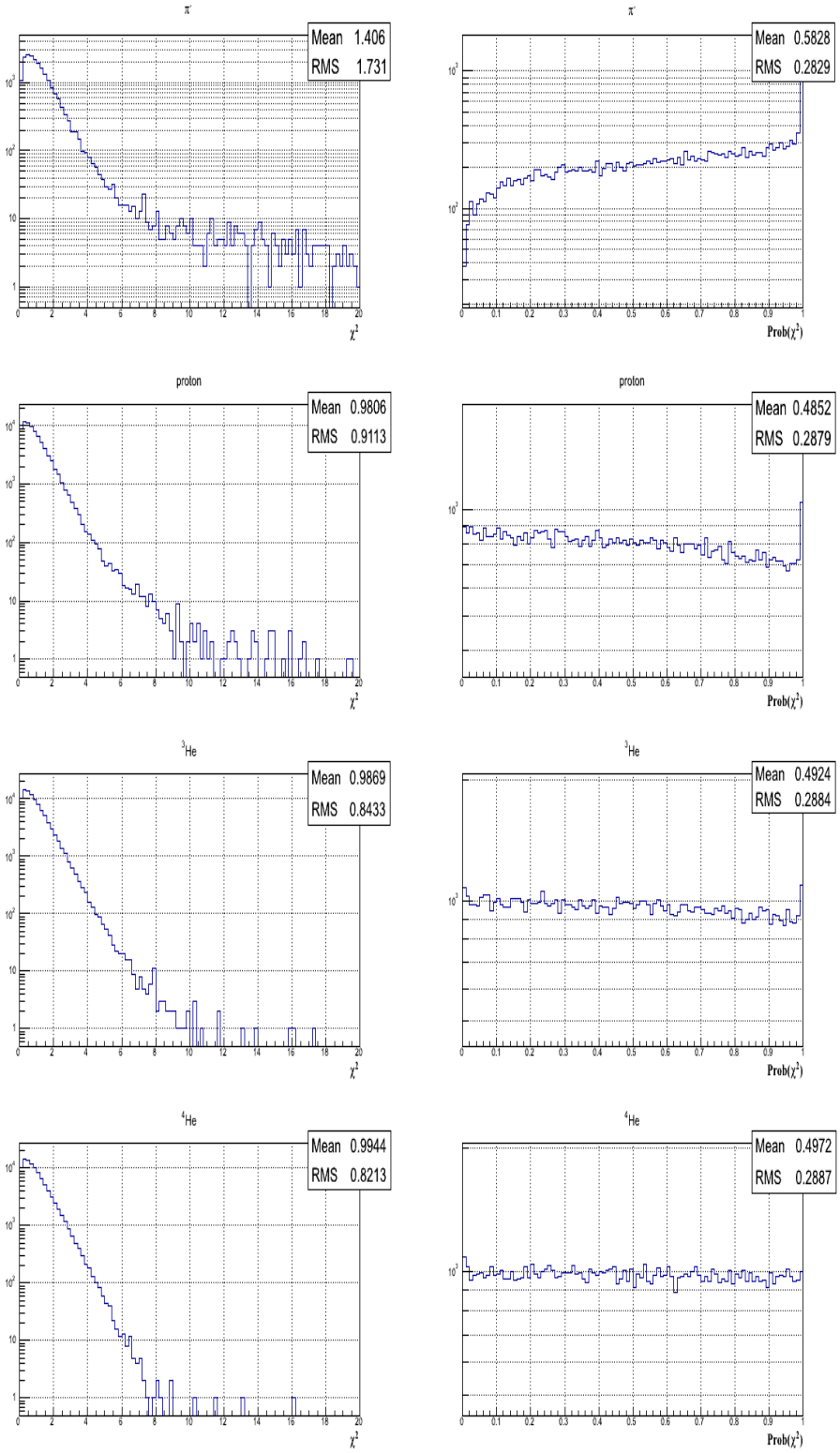

Figure 3.22: Normalized χ^2 and χ^2 probability distributions for all type of particle. For the negatively charged particle, the probability of χ^2 deviates slightly from a flat distribution due to the multiple scattering effect that dominates at low momenta. For the positively charged particles , the probability of χ^2 is nearly uniformly distributed between 0 and 1. All normalized χ^2 shows a mean peaked at one.

scattering as expected. For the positively charged particle the resolution is almost completely dominated by hit position measurement errors. For fast particles such like ^{4}He, the relative momentum resolution $dp/p \sim 10\%$ is nearly two times worse than for slower particle like protons $dp/p \sim 4\%$.

The achieved relative length resolution is better for positively charged particle $dl/l \sim 0.4\%$ than for the low-momenta pions having a more pronounced curvature $dl/l \sim 0.8\%$. For fast particle like ^{3}He and ^{4}He the relative length resolution is nearly constant as a function of the momentum.

3.6.2 Tracking bias studies

No systematic biases were found to be introduced by the Kalman filter algorithm. This search was by plotting the residuals of the state vector as a function of the χ^2 of the fit and the reconstructed momentum for all type of particles.

The results are shown in figures 3.24, 3.25, 3.26, 3.27. From the figures, one can conclude that there is no obvious correlation between the residuals of the local track parameters and the increase in χ^2 or the increase of the reconstructed momentum.

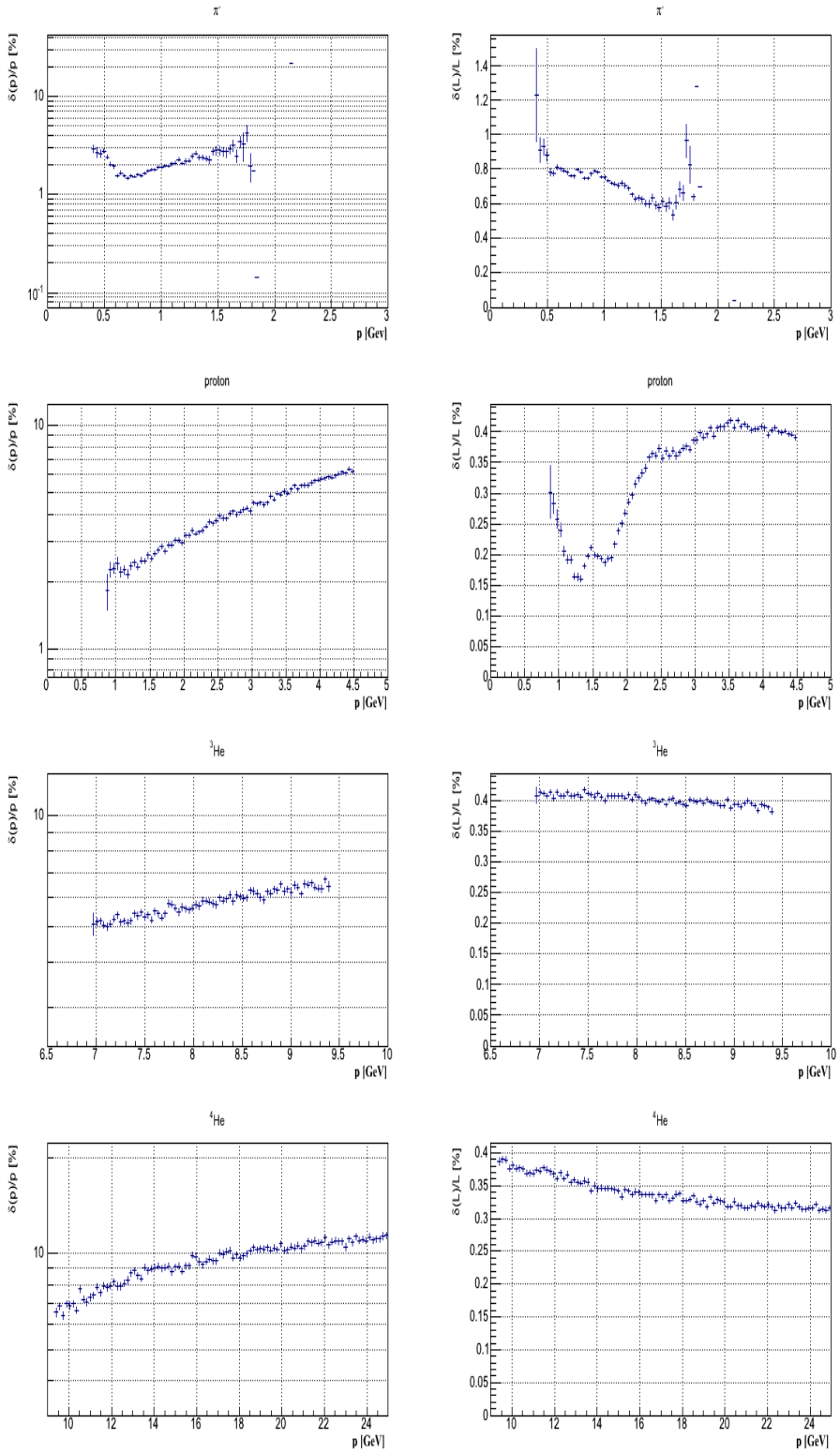

Figure 3.23: Reconstructed momentum and length as a function of the momentum for all type of particles.

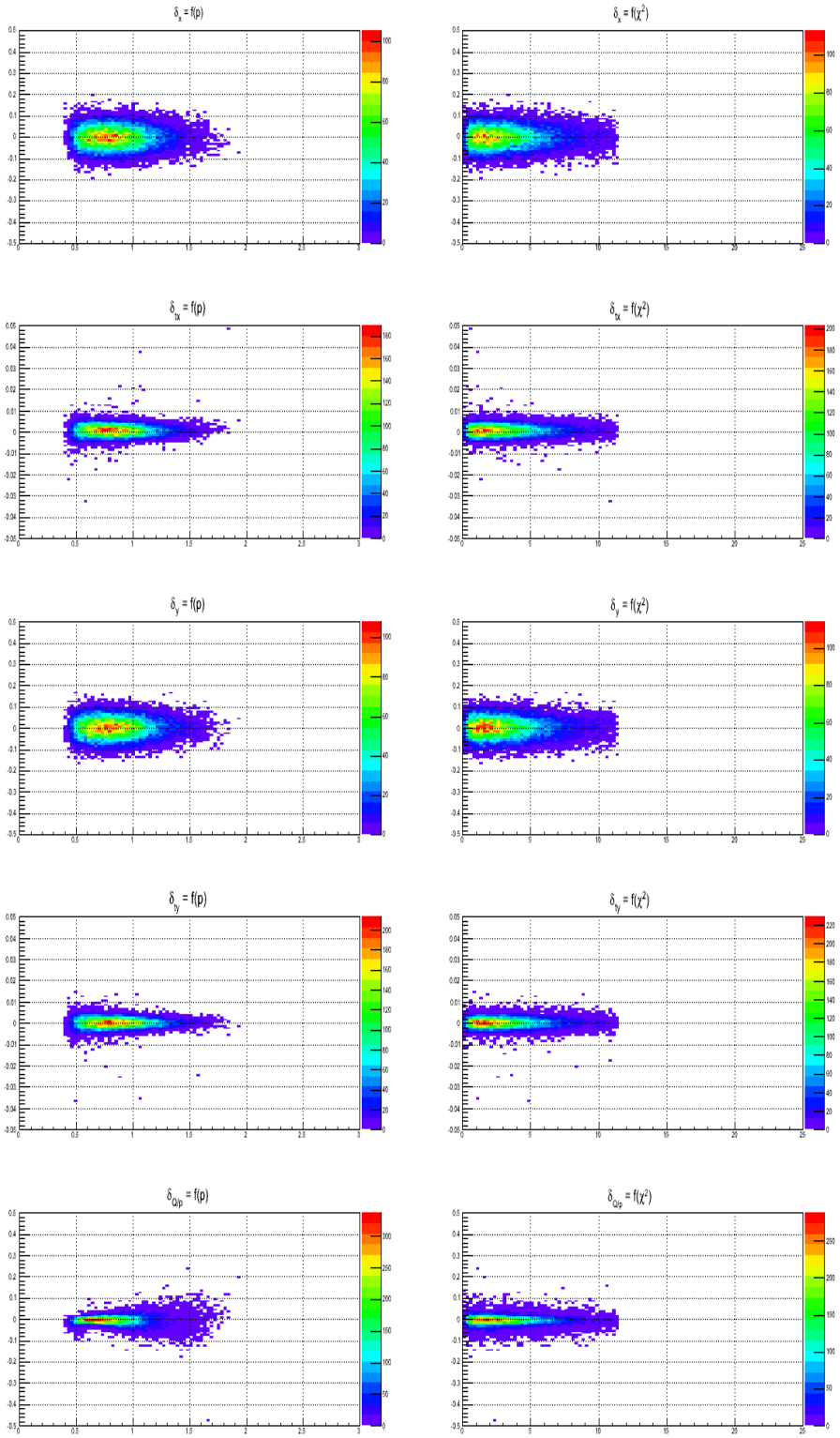

Figure 3.24: Residuals of the local track parameter as a function of χ^2 and reconstructed momentum for π particle.

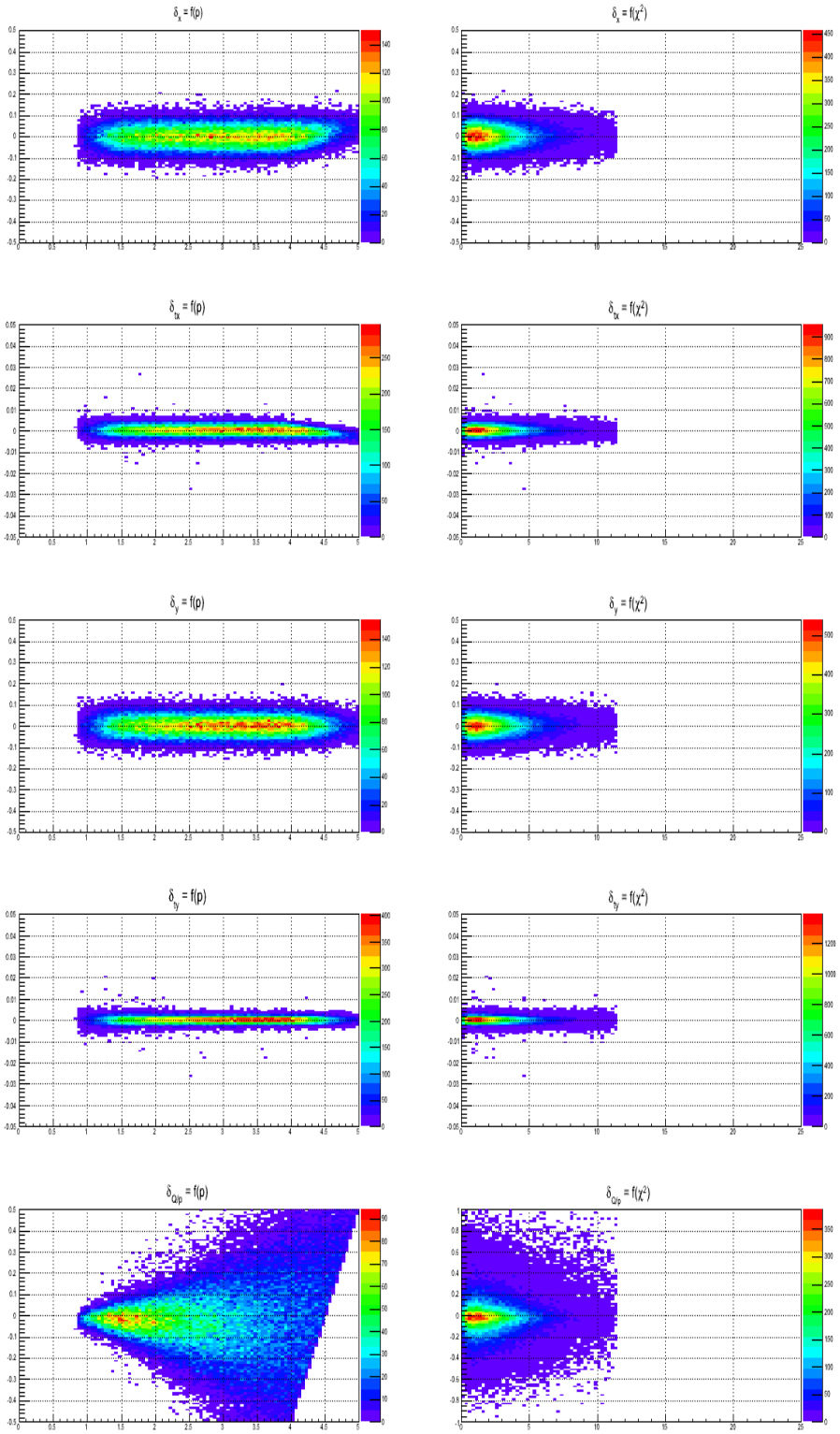

Figure 3.25: Residuals of the local track parameter as a function of χ^2 and reconstructed momentum for protons .

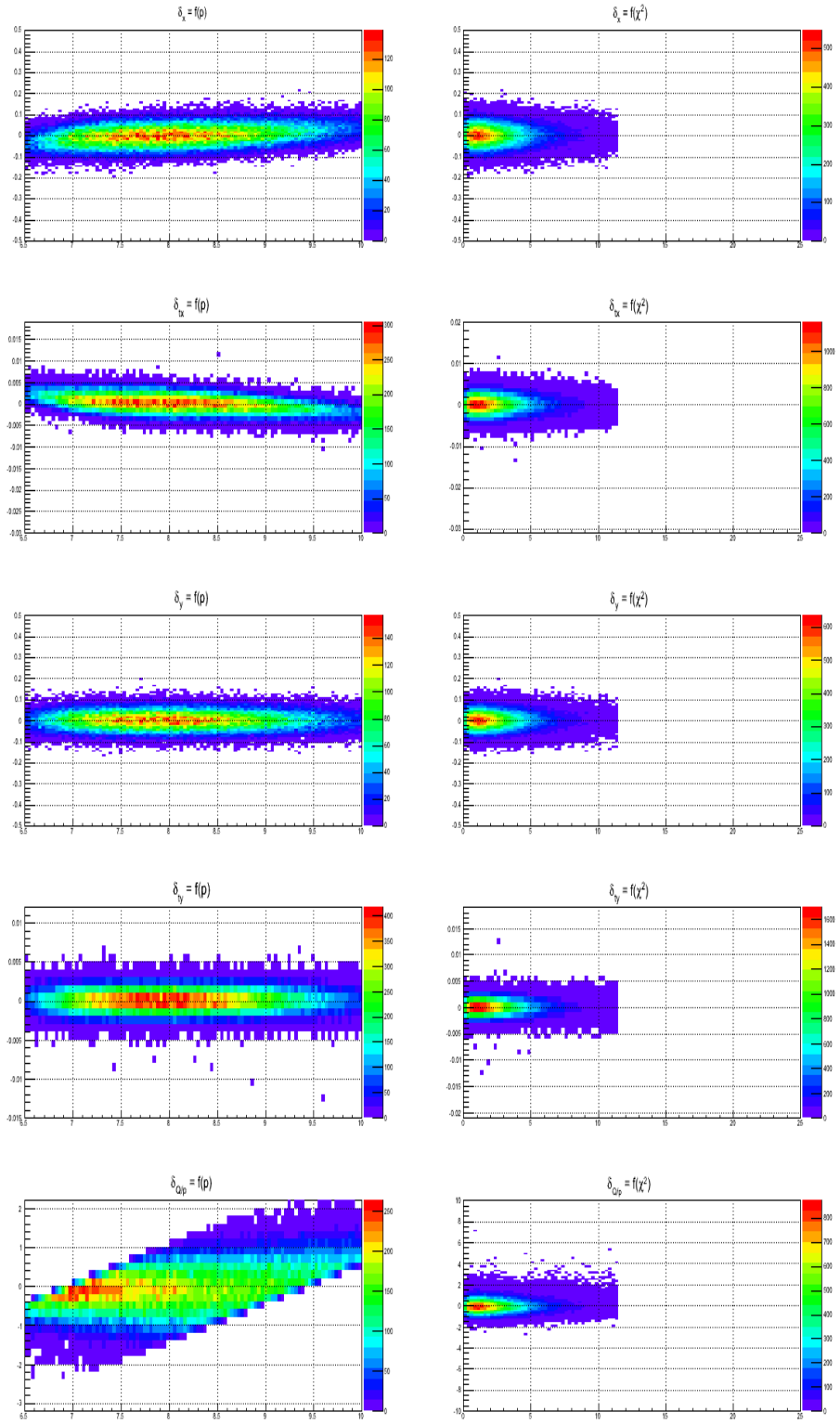

Figure 3.26: Residuals of the local track parameter as a function of χ^2 and reconstructed momentum for ^{3}He particle.

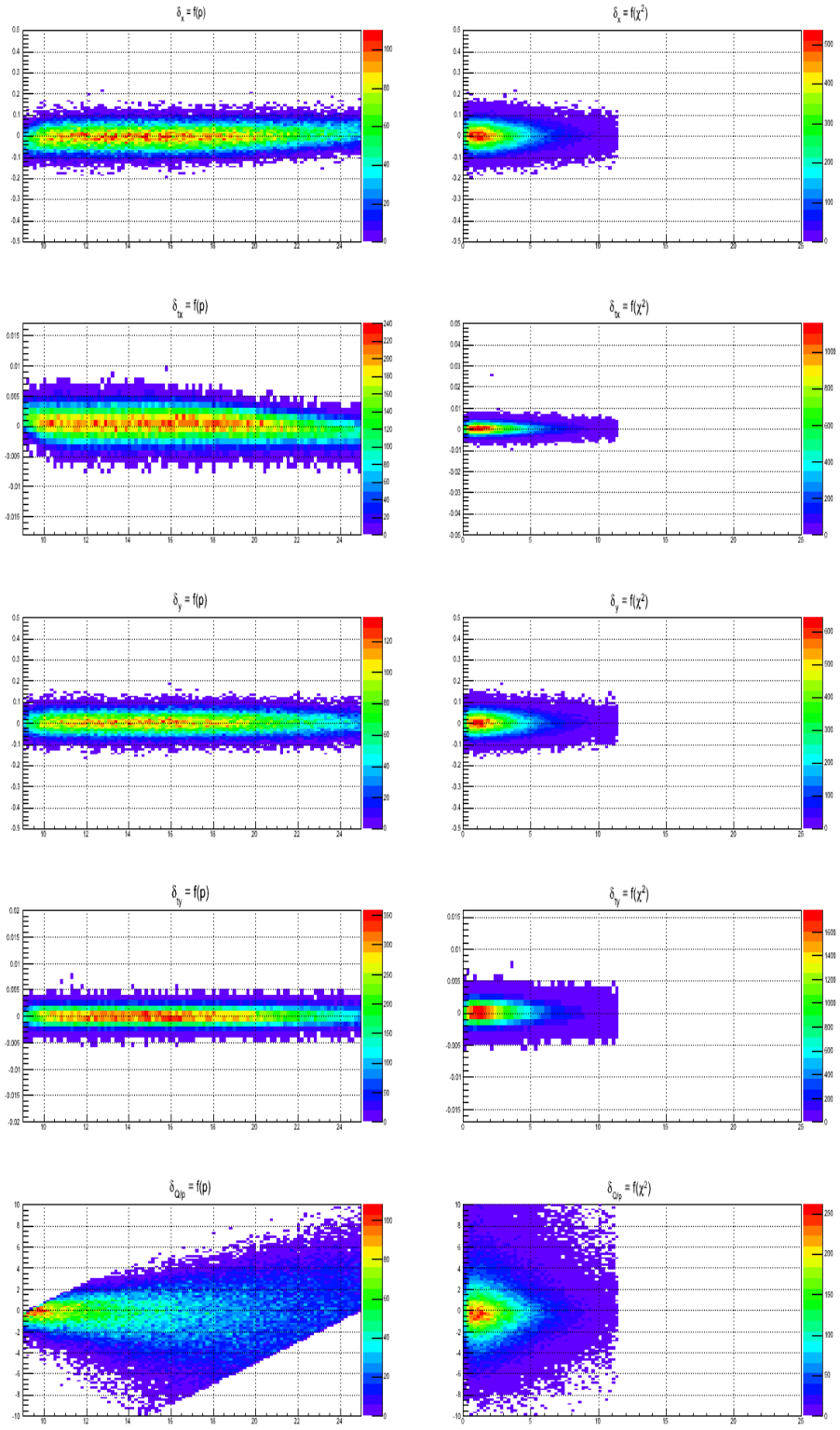

Figure 3.27: Residuals of the local track parameter as a function of χ^2 and reconstructed momentum for ^{4}He particle.

Chapter 4

Vertex Reconstruction

Contents

4.1 Introduction

Vertex reconstruction is one of the important phase in the event reconstruction. Association of tracks to vertices relies on the fitted position of the vertex which is therefore important for physical interpretation of the events. Several articles discussing sophisticated solutions to the vertex reconstruction can be found in the literature [39, 46, 47].

The HypHI Phase 0 experiment focuses on producing and identifying mainly: ${}^{3}_{\Lambda}\mathrm{H}$, ${}^{4}_{\Lambda}\mathrm{H}$, and ${}^{5}_{\Lambda}\mathrm{He}$ by their mesonic weak two or three body decay channels ${}^{3}_{\Lambda}\mathrm{H} \rightarrow \pi^{-}+{}^{3}\mathrm{He}$, ${}^{4}_{\Lambda}\mathrm{H} \rightarrow \pi^{-}+{}^{4}\mathrm{He}$, ${}^{5}_{\Lambda}\mathrm{He} \rightarrow \pi^{-}+{}^{4}\mathrm{He}+p$.

Identification of hypernuclear event is achieved by vertex reconstruction and the invariant mass method from the track reconstruction of particles. The mean decay

length of produced hypernuclei is approximately 15 cm due to a Lorentz factor $\gamma \sim 3$, since the velocity of the produced particle is close to the one of the projectile.

Therefore one can assume for the vertex reconstruction that the decay vertex of the produced hypernuclei takes place between the target and the first position measurement plane (TR1)

$$-2 < z_{decay} < 41.5\ cm\ (z_{TR1})$$

and the vertex reconstruction will then be limited to this region. The distribution of $\Lambda \rightarrow \pi^- + p$ decay along the z axis in Figure 4.1 follows this assumption.

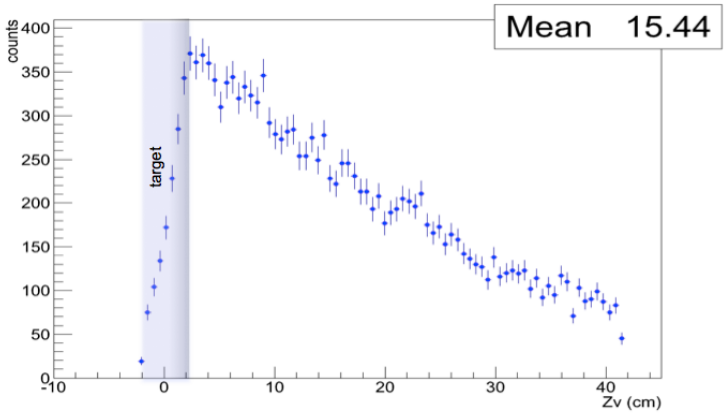

Figure 4.1: Reconstructed secondary vertex Z coordinate of $\Lambda \rightarrow \pi^- + p$.

In fixed target experiments, the tracks are mainly focused around the beamline coinciding with the z axis in the HypHI coordinates system. The vertex position uncertainty in the beamline direction is then expected to be larger than in the transverse direction leading to ambiguities in the separation of primary to secondary tracks and consequently to biases in the estimation of tracks parameters and the final invariant mass measurement. Furthermore large multiplicities in the first fiber detector TR0 make measurements close to the target region difficult thus removing the possibility to reconstruct the primary interaction vertex.

The vertex reconstruction algorithms will have to deal with such inherent ambiguities and may lead to the large uncertainties. Additionally, since vertices are high level reconstructed objects made of reconstructed tracks, it is generally difficult to disentangle effects coming from tracks and vertex reconstruction. It is therefore important to be able to cross check the physical results using different algorithms. In this chapter two different approaches to the vertex reconstruction problem are derived: a global reconstruction based on the least square fitting technique and an iterative reconstruction based on the Kalman filter algorithm.

In both approaches, the algorithm is decomposed into two main steps:

- **the vertex finding** : this step consists in finding clusters of compatible tracks among a set of candidate tracks given on input. The search is guided by the

a-priori knowledge of the decay channel.

- **the vertex fitting** : this step consists in finding the vertex position most compatible with the set of tracks given on input, and applying constraints on the momentum vector using the knowledge of the vertex position.

To illustrate the data reduction after applying the vertex finding and fitting algorithm, one can for example display the selected tracks after each procedure on Monte Carlo simulated data using the UrQMD generator to generate a typical ^{6}Li+^{12}C collision at 2 A GeV which in shown in the Figure 4.2. In Figure 4.3 the high multiplicity of tracks is reduced by applying the vertex finding algorithm and 2 decay candidates are found: $\Lambda \rightarrow \pi^- + p$ and $^{3}_{\Lambda}$He $\rightarrow^{3}$He+π^-.

A more complex statistical algorithm (vertex fitting) can then be applied to solve the ambiguity: the decay $\Lambda \rightarrow \pi^- + p$ is selected based on a χ^2 statistical analysis in Figure 4.4.

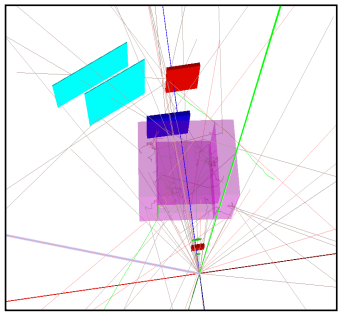

Figure 4.2: UrQMD collision event (^{6}Li+^{12}C)

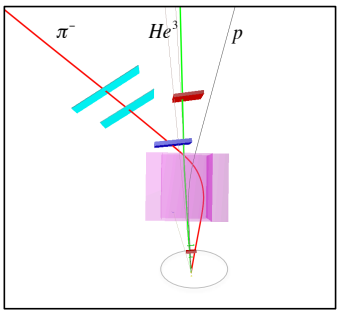

Figure 4.3: Vertex finding: 2 decay candidates

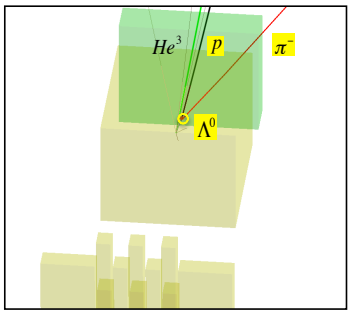

Figure 4.4: Vertex fitting: selection based on χ^2

4.2 The vertex finding

The *vertex finding* algorithm aims at identifying a set of track i which should have been produced at the same vertex of origin. The vertex finding algorithm is supposed to provide the first approximation to the vertex and transport the trajectory parameters and their covariance matrix to the point of closest approach to the estimated vertex. Knowing an approximate vertex position will then simplify the *vertex fitting* algorithm since in the vicinity of the vertex point to be fitted a linearization of the χ^2 function can be applied.

The vertex finding problem can be seen as a clustering problem, in which each vertex is a cluster of tracks. The clustering algorithm should take into account that 2 tracks produced by a real decay will usually not intersect in three dimensional space since the tracks parameters are only known within the accuracy of the track fitting algorithm.

The basic idea for clustering will be to verify if several tracks come close to each other in a small volume. The selection of such close tracks is based on the geometrical distance of closest approach between 2 tracks extrapolated as straight lines in the magnetic field free region between the target and the second fiber detector plane (TR1). A cluster is identified when the distance of closest approach of the track pair $\delta_{i,j}$ is less then a maximal value $\delta_{i,j} < \delta_{max}$ obtained from the Monte Carlo simulated data. The track parameters used for the calculation of distance of closest approach are those obtained a $z = z_{TR1}$ after the track fitting procedure.

4.2.1 Method

In the HypHI experiment, a heavy ion beam, for example (^{6}Li), collides with an elemental target. The information provided for a particle track resulting from this collision includes

- a given position on the track adequately close to, if not, the first possible measured point : the fitted track parameters at the second fiber detector (TR1) at $z_{TR1} = 41.5cm$ from the target will be used.
- the momentum vector at that point
- the magnetic field acting on the particle and the particle charge: in the HypHI experiment, the decay of hypernuclei or lambda particle can only be reconstructed in the geometrical region defined between the target plane and the second fiber detector plane TR1. The magnetic field can be neglected in this region and the tracks will be assumed to have no curvature.

Using this information, the distance and points of closest approach between two of these tracks as shown in the Figure 4.5, one positively charged and the other negatively charged, may be considered to determine if these tracks form a vertex V_0.

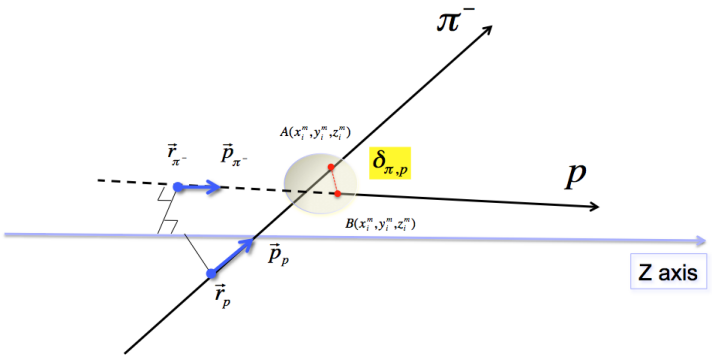

Figure 4.5: Distance and points of closest approach for tracks pairs coming from a $\Lambda \to \pi^- + p$ decay. $\delta_{(\pi^-,p)} = \parallel \vec{AB} \parallel$.

The method for the vertex finding is based on purely geometrical consideration. The equation defining the straight tracks are

$$\vec{r_p} = \vec{r_{0,p}} + \vec{u_p} \cdot t_p \tag{4.1}$$

$$\vec{r_\pi} = \vec{r_{0,\pi}} + \vec{u_\pi} \cdot t_\pi \tag{4.2}$$

with $\vec{r_p}$ representing the position on the positively charged track (proton) and $\vec{r_\pi}$ the negatively charged one. $\vec{r_{0,(p,\pi)}}$ are the position vectors of the given position, $\vec{u_{p,\pi}}$ are the unit vector in the direction of the track momentum i.e

$$\vec{u_{p,\pi}} = \frac{\vec{p_{p,\pi}}}{\| \vec{p_{p,\pi}} \|} \tag{4.3}$$

and $t_{p,\pi}$ are parameters describing position on the tracks.
The distance vector between the two tracks is

$$\vec{\delta_{p,\pi}} = \vec{r_p} - \vec{r_\pi} = \vec{r_{0,p}} - \vec{r_{0,\pi}} + \vec{u_p} \cdot t_p - \vec{u_\pi} \cdot t_\pi \tag{4.4}$$

In the Appendix A, a detailed calculation shows that the distance of closest approach $\delta_{(\pi^-,p)}$ is obtained using the nearest points:

$$\vec{r_p^m} = \vec{r_{0,p}} + \vec{u_p} \cdot \frac{[\vec{r} \cdot \vec{u_p} + (\vec{r} \cdot \vec{u_\pi}) \cdot (\vec{u_\pi} \cdot \vec{u_p})]}{[1 - (\vec{u_\pi} \cdot \vec{u_p})]^2} \tag{4.5}$$

$$\vec{r_\pi^m} = \vec{r_{0,\pi}} + \vec{u_\pi} \cdot \frac{[\vec{r} \cdot \vec{u_\pi} + (\vec{r} \cdot \vec{u_p}) \cdot (\vec{u_\pi} \cdot \vec{u_p})]}{[1 - (\vec{u_\pi} \cdot \vec{u_p})]^2} \tag{4.6}$$

with $\vec{r} = \vec{r_{0,p}} - \vec{r_{0,\pi}}$.

4.2.2 Algorithm

The main steps of vertex finding algorithm can be described as follow:

- the method receives N tracks as input
- each track is approximated by a straight line in the region defined between the target and the fiber detector TR1
- an estimation of the secondary vertex from each pair of tracks is obtained evaluating the point of nearest approach using Equations (4.5) and (4.6)
- the track is selected only if the distance of minimal approach is within a predefined limit $\delta_{i,j} < \delta_{max}$. This selection mechanism in case of $N > 2$ tracks is illustrated with the Figure 4.6: once a first estimate of the vertex position is obtained, the distance from the i-th track to the average vertex point (the estimation of the secondary vertex is computed:

$$r_i = \sqrt{(x_i - x_v)^2 + (y_i - y_v)^2 + (z_i - z_v)^2}$$

the average distance of the cluster of N tracks to the average point and its associated dispersion are then calculated:

$$\bar{r} = \frac{1}{N} \cdot \sum_{i=1}^{N} r_i \ , \ \Delta\bar{r} = \frac{1}{N} \cdot \sqrt{\sum_{i=1}^{N} \Delta^2 r_i}$$

after these calculations some constraints are applied to the distance from the i-th track to the average cluster point:

$$r_i - \Delta r_i > \bar{r} + \Delta\bar{r}$$

if this disparity apply, then the i-th track is rejected from the cluster.

- the coordinates of the secondary vertex are determined averaging among all the track pairs

$$\begin{cases} x_v &= \dfrac{1}{N_{tracks}} \cdot \sum_{i=1}^{N} \omega_i^x \cdot x_i^m \\ y_v &= \dfrac{1}{N_{tracks}} \cdot \sum_{i=1}^{N} \omega_i^y \cdot y_i^m \\ z_v &= \dfrac{1}{N_{tracks}} \cdot \sum_{i=1}^{N} \omega_i^z \cdot z_i^m \end{cases}$$

with the weight

$$w_i = \frac{1}{\sigma_i^2 \cdot \sum_{i}^{N} \dfrac{1}{\sigma_i^2}}$$

which take into account the precision of the track parameters, σ_i^2 being the diagonal element of the covariance matrix of the i-th track estimate V_i.

- a first estimation of the error on the average secondary vertex position

$$\begin{cases} \sigma_{x_v} &= \dfrac{1}{N_{tracks}} \cdot \sqrt{\sum_{i=1}^{N} \omega_i^{x2} \cdot \sigma_{x_i^m}^2} \\ \sigma_{y_v} &= \dfrac{1}{N_{tracks}} \cdot \sqrt{\sum_{i=1}^{N} \omega_i^{y2} \cdot \sigma_{y_i^m}^2} \\ \sigma_{z_v} &= \dfrac{1}{N_{tracks}} \cdot \sqrt{\sum_{i=1}^{N} \omega_i^{z2} \cdot \sigma_{z_i^m}^2} \end{cases}$$

- the last step stores $x_v, y_v, z_v, \sigma_{x_v}, \sigma_{y_v}, \sigma_{z_v}$, position and errors of the secondary vertex respectively

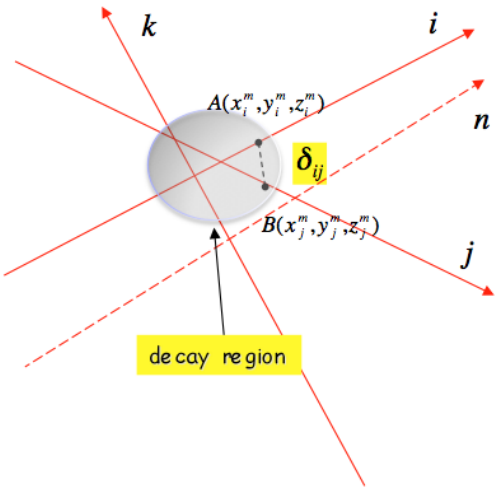

Figure 4.6: The clustering algorithm: track i , j and k are crossing a potential decay region defined by the minimal distance of closest cut approach $\delta_{i,j} < \delta_{max}$. A first estimation of the vertex position can then be extracted by a weighted mean of the points of nearest approach.

4.2.3 Vertex finding performance

In order to validate the algorithms described in this chapter, a full simulation of the Phase 0 HypHI experimental setup has been performed within the VMC (Virtual Monte Carlo) framework [44] [45].

The schematic layout of the experimental setup used in the simulation study is presented in Figure 4.7.

The complete implementation of the experimental setup within the Virtual Monte Carlo framework is presented in Figure 4.8 and an event display of a typical collision ^{6}Li+^{12}C transport through the detectors is presented in Figure 4.9.

As input to the simulation, the event generator based on the UrQMD model [**?**] presented in Chapter 1 is used. Events from the UrQMD event generator are processed in the experimental setup mentioned above by the mean of Monte Carlo simulations within the GEANT3 [48] framework. The measured resolutions of the fibers detectors (TR0, TR1 and TR2), the drift chambers (BDC and SDC), the TFW and the TOF+ walls used for the track reconstruction algorithm described in Chapter 3 have been reused in the Monte Carlo simulations to process events through the experimental setup.

The Monte Carlo simulation performs as follow:

- kinematics and Particle Data Code of UrQMD generated particles are forwarded as primary particles to the Monte Carlo GEANT3 transport engine

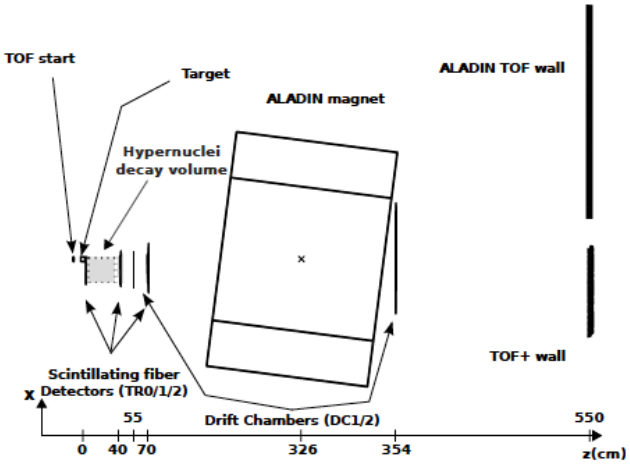

Figure 4.7: The schematic layout of the Phase 0 HypHI experimental setup used in the simulation study with the distance of each detector system from the target.

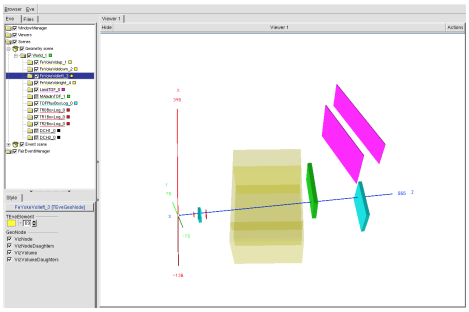

Figure 4.8: Implementation of the HypHI experimental setup in VMC

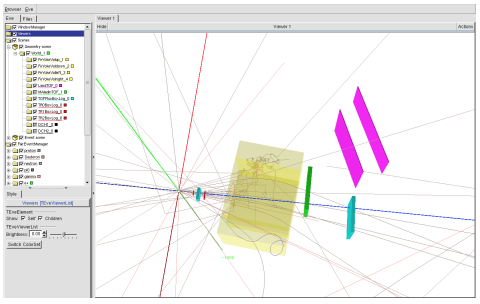

Figure 4.9: Event Display: UrQMD collision event (^{6}Li+^{12}C)

- primary particles are transported through the detector and hits position in the sensitive volume of the detectors are smeared according to the corresponding resolution
- smeared hits are used as input for track finding and Kalman track fitting algorithms.
- fitted track parameters for primary and secondary tracks at the TR1 detector plane are stored

The fitted track parameters obtained at the TR1 detector plane are then used as an input to the vertex reconstruction algorithm. To study the performance of the vertex finding algorithm, the $\Lambda \rightarrow \pi^- + p$ decay is used.

4.2.3.1 Distance of closest approach

The Figure 4.10 shows the distribution of distance of closest approach of track pairs $\delta_{i,j}$ in the case of true Λ decay: $\delta_{i,j} < 1\ cm$. Using this results, a maximal distance of closest approach

$$\delta_{\mathbf{ij}}^{\mathbf{max}} \ = \ \mathbf{2\ cm}$$

will be applied in the vertex fitting algorithm to perform a first selection of decay candidate.

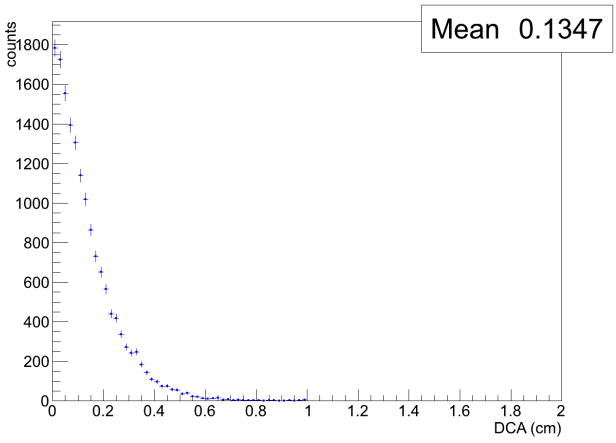

Figure 4.10: Distribution of distance of closest approach in the case of true Λ decay.

4.2.3.2 Resolution

The Figure 4.11 shows the deviations from the true vertex position, or the residuals, distributions for the X, Y and Z coordinates. It is clear from the picture that the dominant error comes from the Z coordinates. Furthermore compared to the transverse plane resolution, the residuals or the deviations from the in Z are not normally

distributed which mainly comes from the uncertainties in the track parameters that are propagated in the vertex finding algorithm. The vertex finding resolution are summarized in Table 5.2

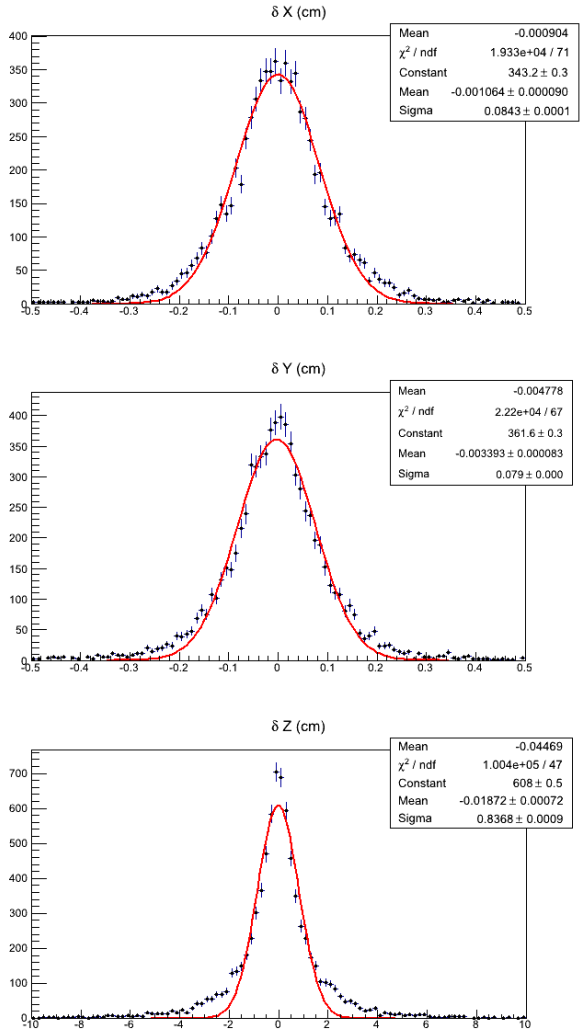

Figure 4.11: Residuals distributions for the X, Y and Z coordinates (blue) fitted by the Gaussian function (red).

The Figures 4.12 and 4.13 shows respectively the transverse and longitudinal resolution as a function of the Z coordinates. In both transverse and longitudinal direction the resolution is improved as the distance of the decaying particle to the target increase. The transverse resolution is linear in Z , the longitudinal resolution follow an exponential decrease in Z coordinate.

The Figure 4.16 shows respectively the transverse and longitudinal resolution as a function of the transverse momentum of the Λ particle. The longitudinal resolution

Table 4.1: Vertex finding Resolutions in X, Y and Z coordinates

δX (cm)	δY (cm)	δZ (cm)
0.084	0.079	**0.83**

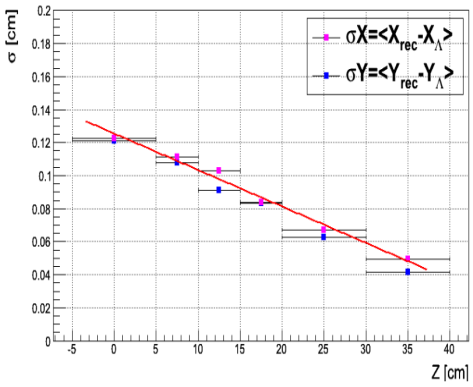

Figure 4.12: Transverse resolution as function of Z.

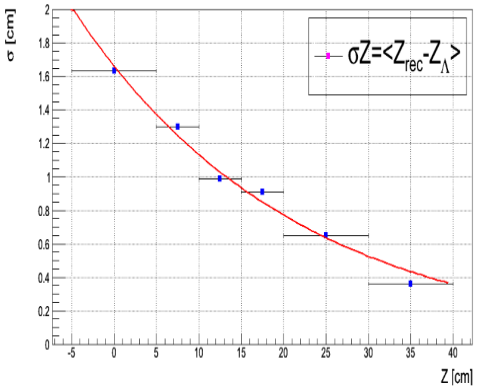

Figure 4.13: Longitudinal Resolution as function of Z.

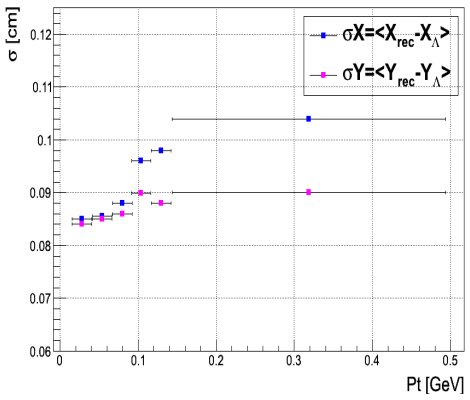

Figure 4.14: Transverse resolution as function of p_Λ^t.

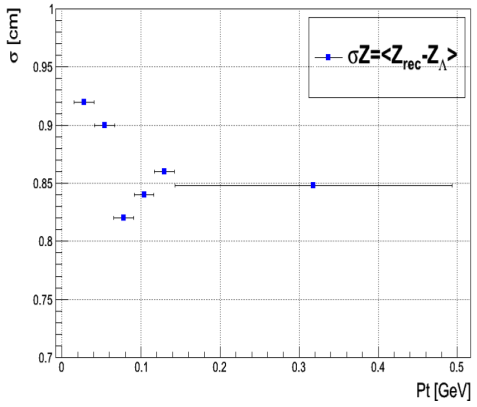

Figure 4.15: Longitudinal Resolution as function of p_Λ^t.

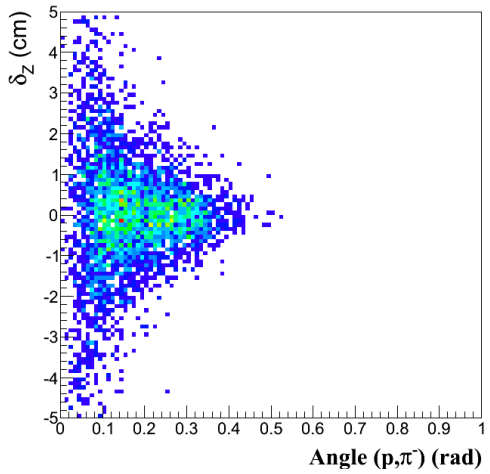

Figure 4.16: The longitudinal discrepancy δ_Z versus the opening angle between the two outgoing tracks (p, π^-) from the Λ decay. The opening angle is calculated with the track parameters extrapolated to the approximate vertex position.

is improve for high value of the transverse momentum p^t_Λ. This can be explained by a pure geometrical consideration: for high p^t_Λ the decay products π^- and p have a larger opening angle and the intersection of the corresponding straight tracks is estimated with a better accuracy. The Figure 4.16 show the small values of the opening angles between the two outgoing tracks (p, π^-) from the Λ decay imply a wider distribution in the longitudinal discrepancy δ_Z.

4.2.3.3 Efficiency

As for the tracking efficiency, the vertex finding efficiency can be defined by the ratio between the number of found Λ particle and the the number of Λ vertices *accepted* in the geometrical acceptance of the experimental setup. A decaying particle (Λ) is considered to be in the geometrical acceptance of the detector if:

- its decay products pass through enough layer of tracking station i.e TR1 TR2 and BDC. These requirements are needed for the proper track reconstruction.

- a hit has been recorded in TOF+ wall for the positively charged particle and in the TFW for the negatively charged particle. These requirements are needed for a proper particle identification.

- the decay position z_{vertex} of the particle candidate must be within the *detectable* z interval $-2 < z_{decay} < 41.5\ cm$ (z_{TR1}) .

In Figures 4.17 and 4.18, the vertex finding efficiency

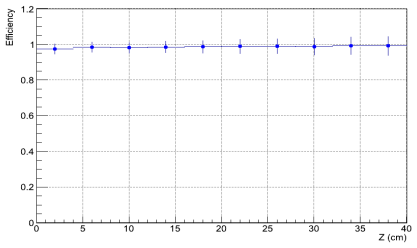

Figure 4.17: Vertex finding efficiency as a function of Z_v coordinate of the decaying particle.

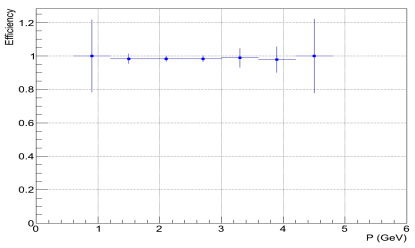

Figure 4.18: Vertex finding efficiency as a function of the momentum p_Λ. of the decaying particle.

$$\varepsilon(z_v) = \frac{N_\Lambda^{found}(z_v)}{N_\Lambda^{accepted}(z_v)} \quad \varepsilon(p_\Lambda) = \frac{N_\Lambda^{found}(p_\Lambda)}{N_\Lambda^{accepted}(p_\Lambda)} \tag{4.7}$$

as a function of of Z_v coordinate of the decaying particle and the momentum p_Λ. of the decaying particle are shown. The efficiency as a function of the variables Z_v and p_Λ is rather constant and reach nearly $98-99$ %.The efficiency decreases a little for decay particle created close to the vertex. It is important that the vertex finding efficiency reaches this maximum for the whole geometrical and kinematical range in order not to introduce any bias for the further data analysis tasks: the vertex fitting.

4.3 The vertex fitting

4.3.1 Motivations

A vertex reconstruction algorithm usually proceed in three stages. At the *first stage* all possible combinations of tracks are considered and a first estimate of the vertex *seeds* $\vec{r_v} = (x_v, y_v, z_v)^T$ is defined. Tracks parameters are swum from the reference plane $z = z_{TR1}$ to the plane $z = z_v$. This first stage, the vertex finding , has been described in detail in the preceding section.

At the *second stage* a mathematical procedure, the *vertex fitting* is applied for each vertex *seeds*. For the exclusive analysis of elementary particle reactions, the complete kinematic of the reaction should be accessible: the 4-momentum $p^\mu = (E, \vec{p})^T$ of all produced particles have to be determined. In the HypHI experimental setup a combination of scintillating fibers and drift chamber detectors are used for the measurement of the particle momenta $\vec{p}$ while the time of flight delivered by the TOF detectors allows to identify the particle and also used as a last tracking plane. After identifying the different particles, the masses are set to the nominal values, enabling, together with the momentum, the calculation of the energy E. Intermediate particles, such as hypernuclei particles, that have a short

lifetime and decay before being detected, can then be reconstructed via the invariant mass technique. The particle tracks are completely defined by their momentum $\vec{p}$, the energy E (or the mass m) and the space point $\vec{r_v}$, at which the momentum is evaluated, the so called vertex point. However, these observables can only be determined within the track parameters uncertainties coming from a finite resolution of the position measurement and of the track reconstruction algorithm. Consequently the mass of intermediate particle is also measured within a certain uncertainty.

The scope of the vertex fitting is to improve the mass resolution of reconstructed particle and to reduce the amount of background reactions contaminating the signal. It uses eventually the physical laws governing a particle interaction or decay to improve the measurements describing the process. For example, the fact that the three particles coming from the hypernuclear ${}^{5}_{\Lambda}\mathrm{He} \rightarrow \pi^- + {}^{4}\mathrm{He} + p$ decay must come from a common space point can be used to improve the momentum vectors of the daughter particles, thus improving the mass resolution of the reconstructed hypernuclei ${}^{5}_{\Lambda}\mathrm{He}$. As a result, the vertex fitting procedure defines an optimal vertex position (3 parameters), momentum vectors at the vertex for all N products particles ($3 \cdot N$ parameters), the covariance matrix and the χ^2 value. This chapter describes two different approaches for the vertex fitting: a global approach based on the least squares method and a progressive method based on the Kalman filter algorithm.

In the *third stage*, which will be described in the next pages, the best seeds (minimal χ^2, corresponding geometrical cuts etc.) is selected and considered as reconstructed particle.

4.3.2 Track parametrization

For the track fitting procedure in a fixed target experiment, each point along the trajectory describes a track by a 5-component Cartesian coordinates state vector

$$\vec{q_i} = (x, t_x, y, t_y, Q/p_{xz})^T \quad \forall i = (1, ..., N) \tag{4.8}$$

and its associated V_q (5×5) covariance matrix.

For vertex fitting it is important to choose a track representation which uses physically meaningfull quantities ans is complete. Unfortunately, the above track parametrization lacks of completeness :

- it does not specify the location in space (3 coordinates) of a particle production or decay
- it does not specify the energy E: in vertex fitting the energy varies independently of the momentum because the mass is in general not constraint, which is always the case for hypernuclei.

For these reasons, in this chapter the above minimal $dim(\vec{q_i}) = 5$ representation is embedded into more dimensions. In particular, we choose the $dim(\alpha q_i) = 7$ representation:

$$\vec{\alpha_i} = (x, y, z, p_x, p_y, p_z, E)^T \quad \forall i = (1, ..., N) \tag{4.9}$$

and its associated V_{alpha} (7×7) covariance matrix which can be deduced from V_q using the Jacabian transformation $J_{q\to\alpha}$:

$$(V_q)_{i,j} = \langle \delta q_i, \delta q_j \rangle \,,\ dim(V_q) = (5 \times 5) \quad (V_\alpha)_{i,j} = \langle \delta \alpha_i, \delta \alpha_j \rangle \,,\ dim(V_\alpha) = (7 \times 7)$$
$$V_\alpha = J_{q\to\alpha} \cdot V_q \cdot (J_{q\to\alpha})^{-1} \tag{4.10}$$

Appendix B describes a procedure for converting the covariance matrix to the new track representation format.

4.3.3 The Least Squares vertex fit

The Least Squares vertex fit is a well established tool to test the hypothesis that a set of measurements represent a given physics reaction [49]. The fit is a least squares error minimization of the tracks measurements that must satisfy some specified constraint equations, namely that the tracks have a common vertex and observe four-momentum conservation. In other words, if the system is overdetermined, the track parameters may be fit such that they abide these constraints while minimizing the deviation from their measured values relative to their uncertainties. If the tracks parameters measurements are normally distributed about their true values, the fit errors from a large data sample follow a χ^2 distribution corresponding to the number of freedom in the fit. The χ^2 distribution can be translated into a confidence level of the fit, which can then be cut on to extract the signal from the background.

The Figure 4.19 shows a scheme of vertex fitting procedure: the input are N fitted tracks parameters at $z = z_{TR1}$. Following the notation in [50] we denote the reconstructed parameters of track i by $\vec{\alpha_i}$ and the corresponding covariance matrix by V_i. Given a set of N outgoing tracks each labeled with an index i, the χ^2 of the vertex can be generally written as

$$\chi^2 = \sum_{i=1}^{N} [\vec{\alpha_i} - h_i(\vec{x}, \vec{p_i})]^T \, V_i^{-1} \, [\vec{\alpha_i} - h_i(\vec{x}, \vec{p_i})] \tag{4.11}$$

where $\vec{x}$ is 3D vector representing the fitted vertex position, $\vec{p_i}$ is the fitted 4-momentum vector of the outgoing track and h_i is a function the expresses the measured track parameters in terms of $\vec{x}$ and $\vec{p_i}$.

The solution to the vertex fit is the set of parameters $\vec{\alpha} \equiv (\vec{x}, \vec{p_1}, \cdots \vec{p_N})$ that minimizes the χ^2. In case the function h_i is linear in the parameters $\vec{\alpha}$, the solution can be expressed generally as

$$\hat{\vec{\alpha}} = \vec{\alpha_0} - \left(\frac{d^2\chi^2}{d\vec{\alpha}^2} \right)^{-1} \frac{d\chi^2}{d\vec{\alpha}} \tag{4.12}$$

where $\vec{\alpha_0}$ is a arbitrary starting point for $\vec{\alpha}$. The inverse of the second derivative matrix on the right hand side is also half the covariance matrix for $\hat{\vec{\alpha}}$. If the derivative of h_i is denoted by H_i, this leads to the well-know expression for the linear least squares estimator,

$$\hat{\vec{\alpha}} = \vec{\alpha_0} - C \cdot \sum_{i=1}^{N} H_i^T V_i^{-1} \, [\vec{\alpha_i} - h_i(\vec{x}, \vec{p_i})] \tag{4.13}$$

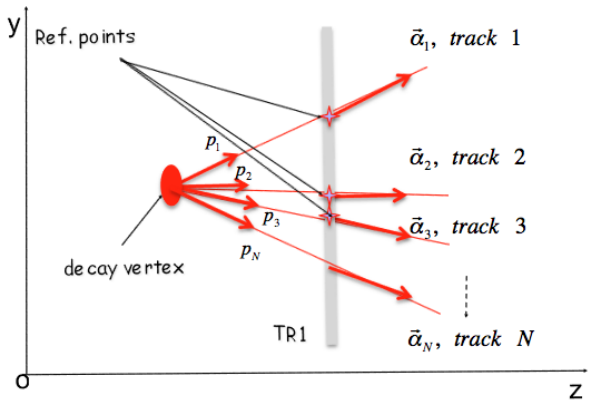

Figure 4.19: Vertex fitting scheme with N tracks parameters as input.

with the covariance matrix

$$C = \left(\sum_{i=1}^{N} H_i^T V_i H_i \right)^{-1} \tag{4.14}$$

In general, the function h_i is not linear and hence its derivative H_i not constant. It is therefore important to begin the iterative vertex fitting procedure with a good estimation of vertex position (vertex finding). Only in that case, the minimum can be obtained by starting from a suitable expansion point ξ_0 and iteratively applying Equation 4.12 until a certain convergence criterion is met, usually a minimum change in χ^2.

As explained in the introduction the minimum χ^2 of the vertex fit will be used in selections further in the data analysis. Assuming that the uncertainties on the track parameters are correctly estimated, that is to say that they are representative of the RMS of the error distribution, the expectation value of the χ^2 of a N-track vertex is $2N - 3$[1].

If the resolution of the tracking detector is good enough to separate decay vertices of different particles, background events consisting of tracks from different vertices have a higher χ^2. The number $2N - 3$ is also called *number of degree of freedom* of the χ^2. In the data analysis selection, the cumulative χ^2 distribution $Prob(\chi^2)$, function will be used as selection variable.

[1] For a N-prong vertex fit the expression for the number of degrees of freedom can be understood as follows. One can show that the expectation value for the minimum χ^2 of a fit with M parameters (or unknowns) to N one-dimensional constraints (or measurements) of the position of a point in 3D to estimate a common, unknown point of origin. Each point contributes 3 independent constraints, for the x,y and z coordinates respectively. The origin point has 3 unknowns. Consequently, the number of degree of freedom of the minimum χ^2 is $3N-3$. If one consider tracks rather than points, the coordinate along the trajectory is not constrained and by the track parameters. Consequently, a track provides only 2 constraints to a vertex. Therefore the χ^2 to a vertex fit to N tracks has $2N - 3$ degrees of freedom.

4.3.3.1 Lagrange Multipliers Formalism

The vertex fitting formalism can be extended with additional constraints, such as an a-priori knowledge of the vertex position or the known mass of the decaying particle. Such constraints always take the form of a constraints equation:

$$\vec{H}(\vec{\alpha}) \;=\; 0. \tag{4.15}$$

A distinction can be made between exact constraints and constraints that have a associated uncertainty. The latter are sometimes called χ^2 constraints. Mass constraints are usually implemented as exact constraints, while vertex constraints are an example of χ^2 constraint. These constraints can be implemented with the *Lagrange Multipliers Method*. Their χ^2 contribution takes the form

$$\Delta\chi^2 \;=\; \vec{\lambda}^T \vec{H}(\vec{\alpha}) \tag{4.16}$$

where the Lagrange multiplier vector $\vec{\lambda}$ is treated as an additional parameter in the fit. The Lagrange Multipliers method for vertex fitting originated from a work by Brandt [51] and by Williams [52]. The application of the method to vertex fitting is discussed in details in the write-ups of Paul Avery [50] where it is shown that the χ^2 minimization of Equation 4.11 is equivalent to minimize the following Lagrange equation with respect to $\vec{\alpha}$ and $\vec{\lambda}$

$$L(\vec{\alpha}, \vec{\lambda}) = (\vec{\alpha} - \vec{\alpha_0})^T \, \mathbf{V}_{\vec{\alpha_0}}^{-1} \, (\vec{\alpha} - \vec{\alpha_0}) + 2\vec{\lambda}^T \vec{H}(\vec{\alpha}) \tag{4.17}$$

$\mathbf{V}_{\vec{\alpha_0}}^{-1}$ is the inverse of the track parameters covariance matrix[2], $\vec{\alpha}$ describes the $7N$ fitted and $\vec{\alpha_0}$ the $7N$ unconstrained parameters for the N tracks.

$$\mathbf{V}_{\vec{\alpha_0}}^{-1} = \begin{pmatrix} \frac{1}{\sigma^2_{\vec{\alpha}_1}} & 0 & \cdots & 0 \\ 0 & \frac{1}{\sigma^2_{\vec{\alpha}_2}} & \cdots & 0 \\ \vdots & \vdots & \ddots & \vdots \\ 0 & 0 & \cdots & \frac{1}{\sigma^2_{\vec{\alpha}_{7N}}} \end{pmatrix} \quad \vec{\alpha} = \begin{pmatrix} \vec{\alpha_1} \\ \vec{\alpha_2} \\ \vdots \\ \vec{\alpha_{7N}} \end{pmatrix} \quad \vec{\alpha_i} = \begin{pmatrix} x_i \\ y_i \\ z_i \\ E_i \\ p_{x,i} \\ p_{y,i} \\ p_{z,i} \end{pmatrix}$$

$\vec{H}(\alpha)$ describes the M holonomic constraints conditions of Equation 4.15 and $\vec{\lambda}$ is the M-dimensional vector of Lagrange multipliers. The factor 2 is added in order to simplifies further calculations.

The first term of Equation 4.17 forces the fitted track parameters $\vec{\alpha}$ fullfilling the constraints to stay as close as possible to the unconstrined parameters $\vec{\alpha_0}$. During

[2] The covariance matrix $\mathbf{V}_{\vec{\alpha_0}}$ is a $(7N \times 7N)$-matrix containing the uncertainties of the measured unconstrained track parameters $\vec{\alpha_0}$. The diagonal elements correspond to the squares of the standard deviations of the parameters, the non-diagonal elements contain the correlated errors. For a complete description, the non-diagonal elements, mainly originating from the multiple scattering, need to be taken into account.

the iterative fit, the parameters will be moved only within an interval defined the measurements uncertainties $\sigma^2_{\alpha_i}$, diagonal elements of the covariance matrix $\mathbf{V}_{\vec{\alpha_0}}$.

Assuming that the parameters uncertainties have a zero expectation value, the Gauss-Markov theorem assures that the fitted parameters are unbiased and have a minimal variance $\sigma^2_{\alpha_i}$, in other words, the fit delivers the best possible set of parameters[3] [42].

The second term of Equation 4.17 describes the M constraints equations. Instead of substituting the M conditions into the Lagrange function L inEquation 4.17 a set of M new variables λ_i (Lagrange multipliers) is included in the expression of L as coefficients of a linear combination of the constraints.

In Figures 4.20 and 4.21 the $7N$-dimensional parameter space to 2 dimension $\vec{\alpha} = (\vec{\alpha_1}, \vec{\alpha_2})^T$ and 1 constraint condition. One can translate the two conditions for the fit as follow: find the minimum of the function $\chi^2(\vec{\alpha_1}, \vec{\alpha_2}) = (\vec{\alpha} - \vec{\alpha_0})^T \mathbf{V}^{-1}_{\vec{\alpha_0}} (\vec{\alpha} - \vec{\alpha_0})$ where the condition $H(\vec{\alpha_1}, \vec{\alpha_2}) = 0$ apply.

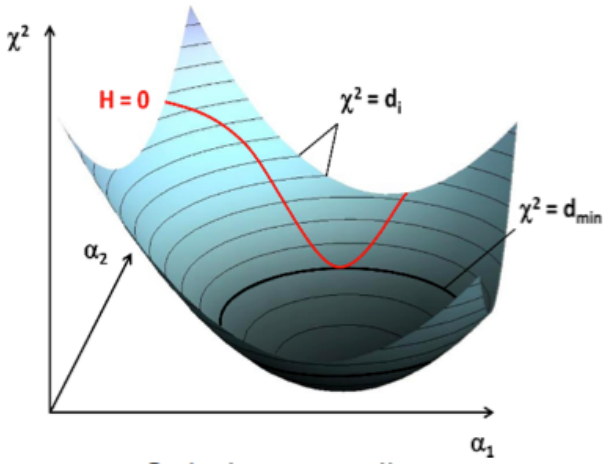

Figure 4.20: Lagrange multiplier method: black lines represents the contours of $\chi^2(\alpha_1, \alpha_2)$, the red line represents the constraints conditions $H(\alpha_1, \alpha_2) = 0$. The minimum id found where both contours touch tangentially.

The solution of the constrained minimization is obtained by minimizing L with respect to $\vec{\alpha}$ and λ.

$$\frac{\partial L(\alpha_1, \alpha_2, \lambda)}{\partial \vec{\alpha}} = \vec{0} \tag{4.18}$$

$$\frac{\partial L(\vec{\alpha_1}, \vec{\alpha_2}, \lambda)}{\partial \vec{\lambda}} = 0 \tag{4.19}$$

From Equations 4.18 and 4.19, one derives respectively

[3] track parameters will converge to proper values if the experiment is repeated enough times [50]

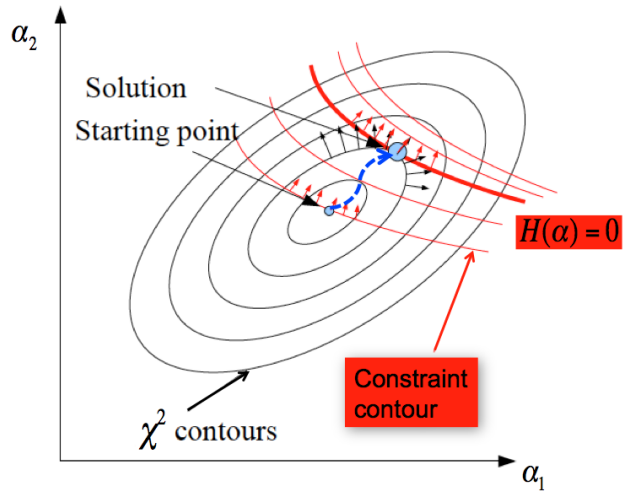

Figure 4.21: Contour map 2D projection. The contours $\chi^2 = min$ and $H = 0$ touch tangentially where the gradients of H (red-arrows) and χ^2 (black arrows) are parallel. The magnitude of the gradients is in general not the same.

- $\frac{\partial L}{\partial \vec{\lambda}} = 2 \cdot H(\vec{\alpha}) = 0$ i.e the solution must lie on a **zero contour** of the constraint (Figure 4.20)
- $\vec{\nabla}_{\alpha_1,\alpha_2}\chi^2 = -2\lambda\vec{\nabla}_{\alpha_1,\alpha_2}H$ i.e the gradients of χ^2 and constraint must be **parallel** at solution. The Figure 4.21 shows that at solution the constraint line is parallel to the χ^2 contour.

4.3.3.2 Linearization

In general, the minimization of Equation 4.17 needs to estimate the derivatives of the constraint equation $\vec{H}(\vec{\alpha})$, which can be non-linear functions of the parameters $\vec{\alpha}$ and consequently, not solvable analytically. Nevertheless, the constraints functions $\vec{H}(\vec{\alpha})$ can be expanded around the approximate solution $\vec{\alpha_A}$ obtained during vertex finding.

$$\vec{H}(\vec{\alpha}) \approx \vec{H}(\vec{\alpha_A}) + \frac{\partial \vec{H}(\vec{\alpha_A})}{\partial \vec{\alpha}}(\vec{\alpha} - \vec{\alpha_A}) \equiv \mathbf{D}\delta\vec{\alpha} + \vec{d} \tag{4.20}$$

where $\delta\vec{\alpha} = \vec{\alpha} - \vec{\alpha_A}$ and

$$\mathbf{D} = \begin{pmatrix} \frac{\partial H_1(\vec{\alpha})}{\partial \alpha_1} & \frac{\partial H_1(\vec{\alpha})}{\partial \alpha_2} & \cdots & \frac{\partial H_1(\vec{\alpha})}{\partial \alpha_{7N}} \\ \frac{\partial H_2(\vec{\alpha})}{\partial \alpha_1} & \frac{\partial H_2(\vec{\alpha})}{\partial \alpha_2} & \cdots & \frac{\partial H_2(\vec{\alpha})}{\partial \alpha_{7N}} \\ \vdots & \vdots & \ddots & \vdots \\ \frac{\partial H_M(\vec{\alpha})}{\partial \alpha_2} & \frac{\partial H_M(\vec{\alpha})}{\partial \alpha_2} & \cdots & \frac{\partial H_M(\vec{\alpha})}{\partial \alpha_{7N}} \end{pmatrix} \qquad \vec{d} = \begin{pmatrix} H_1(\vec{\alpha_A}) \\ H_2(\vec{\alpha_A}) \\ \vdots \\ H_M(\vec{\alpha_A}) \end{pmatrix} \tag{4.21}$$

The linearization is only justified is the approximate solution found by the vertex finding procedure is sufficiently close to the true value. The Equation 4.17 can then be written as

$$L(\vec{\alpha},\vec{\lambda}) = (\vec{\alpha}-\vec{\alpha_0})^T\,\mathbf{V}^{-1}_{\vec{\alpha_0}}\,(\vec{\alpha}-\vec{\alpha_0}) + 2\vec{\lambda}^T(\mathbf{D}\delta\vec{\alpha}+\vec{d}) \tag{4.22}$$

After linearization, the Lagrange equation can be minimized analytically with respect to $\vec{\alpha}$ and $\vec{\lambda}$. Solving the equations for the new parameters $\vec{\alpha}$ and its associated covariance matrix $\mathbf{V}_{\vec{\alpha}}$ yields to the equations [50]

$$\vec{\alpha} = \vec{\alpha_0} - \mathbf{V}_{\vec{\alpha_0}}\mathbf{D}^T\mathbf{V}_D(\mathbf{D}\delta\vec{\alpha_0}+\vec{d}) \tag{4.23}$$

$$\mathbf{V}_{\vec{\alpha}} = \mathbf{V}_{\vec{\alpha_0}} - \mathbf{V}_{\vec{\alpha_0}}\mathbf{D}^T\mathbf{V}_D\mathbf{D}\mathbf{V}_{\vec{\alpha_0}} \tag{4.24}$$

where the matrix $\mathbf{V}_D$ is defined as

$$\mathbf{V}_D = \left(\mathbf{D}\mathbf{V}_{\vec{\alpha_0}}\mathbf{D}^T\right)^{-1} \tag{4.25}$$

Only the $(M\times M)\mathbf{V}_D$ has to be inverted in order to obtain the new expression of the χ^2

$$\chi^2 = (\mathbf{D}\delta\vec{\alpha_0}+\vec{d})^T\mathbf{V}_D^{-1}(\mathbf{D}\delta\vec{\alpha_0}+\vec{d}) \tag{4.26}$$

Because of the non-linearity in $\vec{\alpha}$, the fit has to be applied iteratively, using the values obtained by the equations 4.23-4.26 as input for the next iteration step: $\vec{\alpha_A} = \vec{\alpha}$. Improved values for $\vec{\alpha}$ and $\mathbf{V}_{\vec{\alpha}}$ are calculated , which better fit to the constraints. This procedure is repeated until minimal change in the χ^2 value as shown in the schematic overview of Figure 4.23. The Figure 4.22 shows a simplified picture of the linearization of the constraints. The function $H(\alpha)$ is plotted versus a free parameter α. The linearization, like it is done in the fit, delivers the blue tangent to the curve an a new value α_1. Going on with this linearization procedure will produces new values $(\alpha_2,\alpha_3\cdots\alpha_n)$ which approach the constraints $H(\alpha)=0$.

4.3.3.3 Vertex Constraints

A vertex constraint can be added to the Equation 4.22 in order to enforce the N tracks to pass through a common space point $\vec{v}$. Assuming that a vertex position $\vec{v_A}$ and the covariance matrix $\mathbf{V}_{\vec{v}}$ can be approximated by the vertex finding procedure, the position and the errors of the vertex are taken into account by adding a second term to the χ^2 in the Lagrange Equation 4.17 which will be expanded around $\vec{v_A}$ [50]:

$$L(\vec{\alpha},\vec{v},\vec{\lambda}) = (\vec{\alpha}-\vec{\alpha_0})^T\,\mathbf{V}^{-1}_{\vec{\alpha_0}}\,(\vec{\alpha}-\vec{\alpha_0}) + (\vec{v}-\vec{v_0})^T\,\mathbf{V}^{-1}_{\vec{v_0}}\,(\vec{v}-\vec{v_0}) + 2\vec{\lambda}^T(\mathbf{D}\delta\vec{\alpha}+\mathbf{E}\delta\vec{v}+\vec{d}) \tag{4.27}$$

with $\vec{v_0}$ being the approximated initial vertex position, $\delta\vec{v} = \vec{v}-\vec{v_A}$ and the $(M\times 3)$ matrix

$$\mathbf{E} = \begin{pmatrix} \frac{\partial H_1(\vec{\alpha},\vec{v})}{\partial v_x} & \frac{\partial H_1(\vec{\alpha},\vec{v})}{\partial v_y} & \frac{\partial H_1(\vec{\alpha},\vec{v})}{\partial v_z} \\ \frac{\partial H_2(\vec{\alpha})}{\partial v_x} & \frac{\partial H_2(\vec{\alpha})}{\partial v_y} & \frac{\partial H_2(\vec{\alpha})}{\partial v_z} \\ \vdots & \vdots & \vdots \\ \frac{\partial H_M(\vec{\alpha},\vec{v})}{\partial v_x} & \frac{\partial H_M(\vec{\alpha},\vec{v})}{\partial v_y} & \frac{\partial H_M(\vec{\alpha},\vec{v})}{\partial v_z} \end{pmatrix}$$

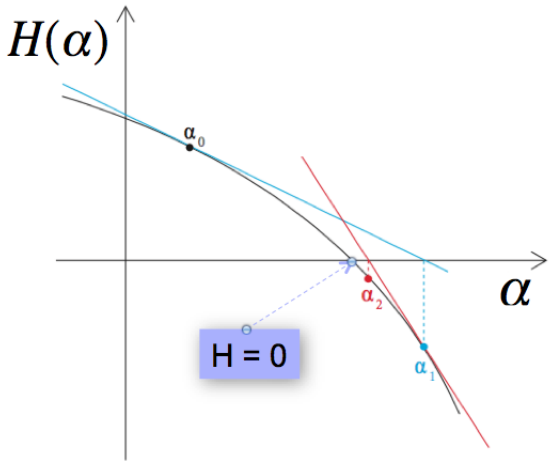

Figure 4.22: Schematic view of the linearization of the constraints in the iterative fit

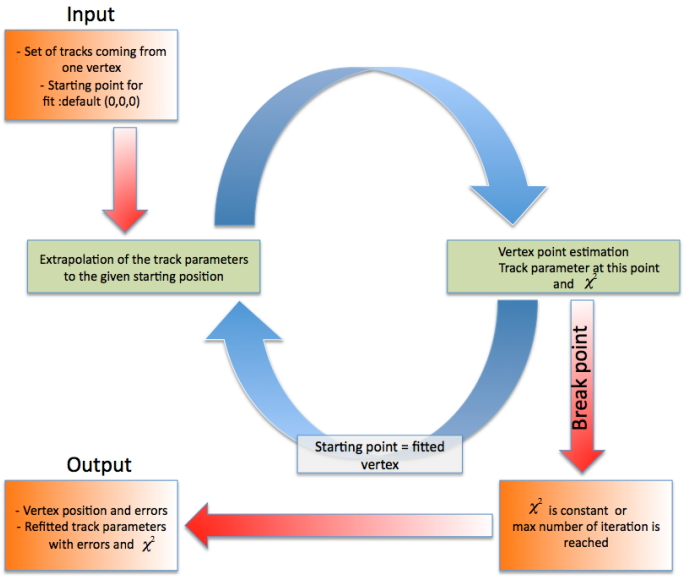

Figure 4.23: Schematic view of the fitting procedure

The minimization of the new Lagrange function of Equation 4.27 with respect to $\vec{\alpha}$, $\vec{v}$ and λ yields the equations

$$\delta\vec{\alpha} = -\mathbf{V}_{\vec{\alpha_0}}\mathbf{D}^T(\mathbf{V}_D - \mathbf{V}_D\mathbf{E}\mathbf{V}_{\vec{v}}\mathbf{E}^T\mathbf{V}_D)(\mathbf{D}\delta\vec{\alpha_0} + \mathbf{E}\delta\vec{v_0} \ + \vec{d}) \tag{4.28}$$

$$\delta\vec{v} = -\mathbf{V}_{\vec{v_0}}\mathbf{E}^T(\mathbf{V}_D - \mathbf{V}_D\mathbf{E}\mathbf{V}_{\vec{v}}\mathbf{E}^T\mathbf{V}_D)(\mathbf{D}\delta\vec{\alpha_0} + \mathbf{E}\delta\vec{v_0} \ + \vec{d}) \tag{4.29}$$

with $\delta\vec{\alpha} = \vec{\alpha} - \vec{\alpha_0}$, $\delta\vec{v} = \vec{v} - \vec{v_0}$ and the auxiliray matrix $\mathbf{V}_D$ being defined in Equation 4.25. The covariance matrices are calculated as:

$$\mathbf{V}_{\vec{\alpha}} = \mathbf{V}_{\vec{\alpha_0}} - \mathbf{V}_{\vec{\alpha_0}}\mathbf{D}^T\mathbf{V}_D\mathbf{D}\mathbf{V}_{\vec{\alpha_0}} + \mathbf{V}_{\vec{\alpha_0}}\mathbf{D}^T\mathbf{V}_D\mathbf{E}\mathbf{V}_{\vec{v}}\mathbf{E}^T\mathbf{V}_D\mathbf{D}\mathbf{V}_{\vec{\alpha_0}} \tag{4.30}$$

$$\mathbf{V}_{\vec{v}} = \left(\mathbf{V}_{\vec{v_0}}^{-1} + \mathbf{E}^T\mathbf{V}_D\mathbf{E}\right)^{-1} \tag{4.31}$$

When applying vertex constraints, the covariance matrix of the track parameters $\mathbf{V}_{\vec{\alpha}}$ is increased by the last term of Equation 4.30 which comes from the vertex fit itself. In particular, this last term contains a track to track correlations information through the matrix $\mathbf{V}_{\vec{v}}$ as reflected by the $(7N \times 3)$ covariance matrix of the vertex and the tracks:

$$Cov(\vec{\alpha}, \vec{v}) = -\mathbf{V}_{\vec{\alpha_0}}\mathbf{D}^T\mathbf{V}_D\mathbf{E}\mathbf{V}_{\vec{v}} \tag{4.32}$$

Other matrices involved in Equation 4.30, $\mathbf{D}$, $\mathbf{V}_D$ and $\mathbf{V}_{\vec{v_0}}$ are block-diagonal so that each track is fitted independently. In Equation 4.30 the new vertex covariance matrix $\mathbf{V}_{\vec{v}}$ can be seen as the weighted mean of the initial vertex error matrix $\mathbf{V}_{\vec{v_0}}$ and the track parameters errors defined in $\mathbf{V}_D$. Additionnaly, both vertex covariance matrices $\mathbf{V}_{\vec{v}}$ and $\mathbf{V}_{\vec{v_0}}$ needs inversion which will increase the fit computing time by a factor $\sim 2 \times O(3^3)$.

The modified expression for the χ^2 is given by

$$\chi^2 = (\mathbf{D}\delta\vec{\alpha} + \mathbf{E}\delta\vec{v} + \vec{d})^T(\mathbf{V}_D - \mathbf{V}_D\mathbf{E}\mathbf{V}_{\vec{v}}\mathbf{E}^T\mathbf{V}_D)^T(\mathbf{D}\delta\vec{\alpha} + \mathbf{E}\delta\vec{v} \ + \vec{d}) \tag{4.33}$$

4.3.3.4 Quality of the fit

The validity of the vertex fit depends in a crucial manner on the correct input of the track parameter covariance matrix $\mathbf{V}_{\vec{\alpha_0}}$. In the preceding Chapter 3, it has been demonstrated that the Kalman track fitting procedure delivers a proper mean estimate of the track parameters uncertainties (Figures 3.18, 3.19, 3.20, 3.21). But even if, on a event by event basis, the track parameter errors are not correct, the vertex fit will force the parameters $\vec{\alpha}$ to satisfy the constraints. As a result, some of the fitted parameters in $\vec{\alpha}$ are not shifted inside the correct error interval and they can be too far away or unnecessary close to $\vec{\alpha_0}$. Therefore, it is important to provide some quality criteria which measure the quality of the fit and that indicate the presence of background events and whether the error input in $\mathbf{V}_{\vec{\alpha_0}}$ is correct.

The vertex fitting is based on the minimization of the χ^2 value defined by the first term of 4.17. The χ^2-value is therefore a good measure of the global performance of the fit.

Furthermore, if the input track parameters errors in $\mathbf{V}_{\vec{\alpha_0}}$ are correctly estimated and normally distributed, the probability density function of the χ^2 is given by the equation [42]

$$f_\nu(\chi^2) = \frac{1}{2^{\nu/2}\Gamma(\nu/2)}(\chi^2)^{\nu/2}e^{-\chi^2/2} \tag{4.34}$$

with a mean value $\left\langle f_\nu(\chi^2)\right\rangle = \nu$, ν being the degree of freedom of the fit and Γ the gamma function. The number of degrees of freedom ν is exactly the number of constraints which are used in the fit[4]. Figure 4.24 shows the χ^2 distribution for different values of ν.

For the data analysis, one can use a selection direclty based on the χ^2 value or, a more convenient way , on the on so-called *p-value*. The *p-value* is a quantity which gives the probability that the same fit, if repeated, will result in a χ^2_{n+1} value as large as or larger than the value of the preceding fit χ^2_n. If the track parameters input errors are correct an normally distributed, the *p-value* is evenly distributed between 0 and 1. The *p-value* is defined as

$$p - value = \int_{\chi^2_{ref}}^{\infty} f_\nu(\chi^2)d\chi^2 \tag{4.35}$$

where χ^2_{ref} is the calculated χ^2-value after the application of the new fit. A high χ^2_{ref} means that the parameters $\vec{\alpha}$ were shifted too far away from $\vec{\alpha}_0$ and this results in a low *p-value*: this property of the *p-value* will be used in the data analysis to reduce background events.

4.3.4 The Kalman vertex fit

In the standard least squares fit formalism for vertex reconstruction, described in the preceding section, all candidate tracks of a decay event are fitted to a single vertex in one single step (4.11). In this sense, it is a *global* method. The expression for the standard fit in Equation 4.11 show that the dimensions of matrices and vectors in this formalism are proportional to the number N of measured tracks of the decay event. Because the required processing time for the inversion of a $(N \times N)$ matrix is $\sim O(N^3)$, the method is unsatifactory in high charged particle muliplicity environment. Furthermore, due to its global structure, this formalism is not flexible in handling different vertex hypothesis within a single decay event, such as dynamically removing spurious tracks or taking a subset of tracks of the decay event to search for secondary vertices.

In this section the method of *Kalman Filter* [54, 55], which has been already used for track fitting in the preceding chapter, is adapted for vertex fitting. The basic idea of the *Kalman Filter* is to use the information of different particle trajectories about the vertex consecutively one after the other. In this sense it is considered as a *local* method.

[4] The dependence between χ^2 and the degree of freedom ν is intuitive: in a fit with 2 constraints, the parameters α have to be shifted further away from α_0 as by applying a fit with only one constraint. Therefore the χ^2 value is larger.

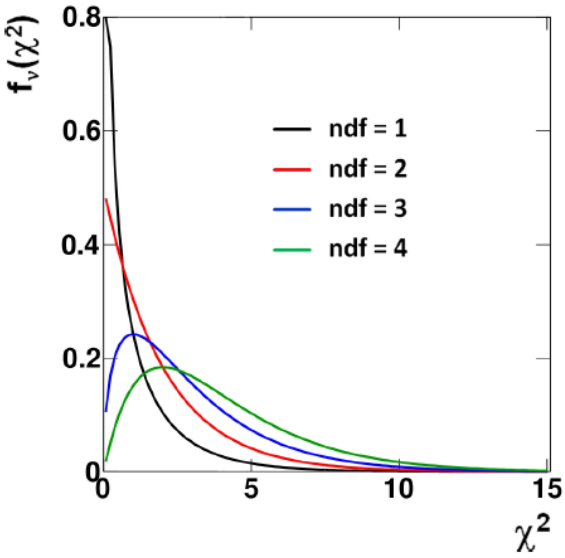

Figure 4.24: Normalized χ^2 distribution for different values of the degree of freedom (ndf). In the limit $\nu \to \infty$, the χ^2 is close to a normal distribution (central limit theorem) apadted from [53].

4.3.4.1 Formalism

In order to describe the formalism, the following notation, close to [55], is used:

$\vec{\mathbf{x}}_\mathbf{k} =$ estimate of the vertex position after using the information of k tracks.

$\vec{\mathbf{x}}^\mathbf{t} =$ the true vertex position.

$\mathbf{C_k} = cov(\vec{\mathbf{x}}_\mathbf{k}) \equiv cov(\vec{\mathbf{x}}_\mathbf{k} - \vec{\mathbf{x}}^\mathbf{t})$

$\vec{\mathbf{q}}_\mathbf{k} =$ estimate of the momentum of track k at $\vec{\mathbf{x}}_\mathbf{k}$

$\vec{\mathbf{q}}^\mathbf{t}_\mathbf{k} =$ the true momentum of track k at $\vec{\mathbf{x}}_\mathbf{k}$

$\mathbf{D_k} = cov(\vec{\mathbf{q}}_\mathbf{k}) \equiv cov(\vec{\mathbf{q}}_\mathbf{k} - \vec{\mathbf{q}}^\mathbf{t})$

$\mathbf{E_k} = cov(\vec{\mathbf{x}}_\mathbf{k}, \vec{\mathbf{q}}_\mathbf{k}) \equiv cov((\vec{\mathbf{x}}_\mathbf{k} - \vec{\mathbf{x}}^\mathbf{t}), (\vec{\mathbf{q}}_\mathbf{k} - \vec{\mathbf{q}}^\mathbf{t}))$

$\vec{\mathbf{m}}_\mathbf{k} = (x, t_x, y, t_y, Q/p_{xz})^T$ the 5 measured parameters of track k estimated from the track fitting at a reference plane $z = z_{ref}$

$\vec{\nu}_\mathbf{k} =$ measurement noise, i.e if there is multiple scattering between the position of the vertex and of the track parameters, its effect has to be included in $vec\nu_\mathbf{k}$.

$\mathbf{V_k} = cov(\vec{\nu}_\mathbf{k}) =$ associated covariance matrix of $\vec{\nu}_\mathbf{k}$.

$\mathbf{G_k} = \mathbf{V_k}^{-1} =$ weightmatrix of track k

The measurement equation describes a projecting function $\mathbf{h}$ of the true vertex position $\vec{\mathbf{x}}^{\mathbf{t}}$ and the true momentum $\vec{\mathbf{q}}^{\mathbf{t}}$ of track k at this position to the measured parameters $\vec{\mathbf{m}}_{\mathbf{k}}$ of this track distorted by the measurement noise $\vec{\nu}_{\mathbf{k}}$:

$$\vec{\mathbf{m}}_{\mathbf{k}} = \mathbf{h}_{\mathbf{k}}(\vec{\mathbf{x}}^{\mathbf{t}}, \vec{\mathbf{q}}^{\mathbf{t}}_{\mathbf{k}}) + \vec{\nu}_{\mathbf{k}} \tag{4.36}$$

All $\vec{\nu}_{\mathbf{k}}$ are assumed to be stochastically independent, unbiased and of finite variance. In the case the meaurement $\vec{\mathbf{m}}_{\mathbf{k}}$ depend non linearly on the vector $(\vec{\mathbf{x}}^{\mathbf{t}}, \vec{\mathbf{q}}^{\mathbf{t}}_{\mathbf{k}})$, it is neccessary to linearize the model of measurement. As reasonable point of linearization, $(\vec{\mathbf{x}}^{(\mathbf{0})}_{\mathbf{k}}, \vec{\mathbf{q}}^{(\mathbf{0})}_{\mathbf{k}})$ is for $\vec{\mathbf{x}}^{(\mathbf{0})}_{\mathbf{k}}$ the estimate after $k-1$ tracks $\vec{\mathbf{x}}_{\mathbf{k-1}}$, and for $\vec{\mathbf{q}}^{(\mathbf{0})}_{\mathbf{k}}$ the momentum at the point of the track k closest to $\vec{\mathbf{x}}^{(\mathbf{0})}_{\mathbf{k}}$.

$$\begin{aligned} \vec{\mathbf{h}_{\mathbf{k}}}(\vec{\mathbf{x}}^{\mathbf{t}}, \vec{\mathbf{q}}^{\mathbf{t}}_{\mathbf{k}}) &\approx \mathbf{h}_{\mathbf{k}}(\vec{\mathbf{x}}^{(\mathbf{0})}, \vec{\mathbf{q}}^{(\mathbf{0})}_{\mathbf{k}}) + \mathbf{A}_{\mathbf{k}}(\vec{\mathbf{x}}^{\mathbf{t}} - \vec{\mathbf{x}}^{(\mathbf{0})}_{\mathbf{k}}) + \mathbf{B}_{\mathbf{k}}(\vec{\mathbf{q}}^{\mathbf{t}}_{\mathbf{k}} - \vec{\mathbf{q}}^{(\mathbf{0})}_{\mathbf{k}}) \\ &= \vec{\mathbf{c}}^{(\mathbf{0})}_{\mathbf{k}} + \mathbf{A}_{\mathbf{k}}\vec{\mathbf{x}}^{\mathbf{t}} + \mathbf{B}_{\mathbf{k}}\vec{\mathbf{q}}^{\mathbf{t}}_{\mathbf{k}} \end{aligned} \tag{4.37}$$

with

$$\mathbf{A}_{\mathbf{k}} = \left.\frac{\partial \mathbf{h}_{\mathbf{k}}}{\partial \vec{\mathbf{x}}^{\mathbf{t}}}\right|_{\vec{\mathbf{x}}^{(\mathbf{0})}_{\mathbf{k}}, \vec{\mathbf{q}}^{(\mathbf{0})}_{\mathbf{k}}} \quad , \quad \mathbf{B}_{\mathbf{k}} = \left.\frac{\partial \mathbf{h}_{\mathbf{k}}}{\partial \vec{\mathbf{q}}^{\mathbf{t}}_{\mathbf{k}}}\right|_{\vec{\mathbf{x}}^{(\mathbf{0})}_{\mathbf{k}}, \vec{\mathbf{q}}^{(\mathbf{0})}_{\mathbf{k}}}$$

$$\vec{\mathbf{c}}^{(\mathbf{0})}_{\mathbf{k}} = \mathbf{h}_{\mathbf{k}}(\vec{\mathbf{x}}^{(\mathbf{0})}, \vec{\mathbf{q}}^{(\mathbf{0})}_{\mathbf{k}}) - \mathbf{A}_{\mathbf{k}}\vec{\mathbf{x}}^{(\mathbf{0}}_{\mathbf{k}} - \mathbf{B}_{\mathbf{k}}\vec{\mathbf{q}}^{(\mathbf{0})}_{\mathbf{k}} \tag{4.38}$$

The Kalman vertex fitting algorithm then proceeds according to the following steps:

1. A start value for the vertex position $\vec{\mathbf{x}}^{(\mathbf{0})}$ and its associated covariance matrix $\mathbf{C_0}$ is taken from the *a priori* estimate of the track finding procedure.

2. This start value $\vec{\mathbf{x}}^{(\mathbf{0})}$ is compared with the information about the vertex position obtained from the measured parameters $\vec{\mathbf{m}}_{\mathbf{1}}$ of one candidate track of the decay event. This is achieved through the weighted addition of the vertex position obtained from one track $\vec{\mathbf{m}}_{\mathbf{1}}$ to the χ^2 of the previous guess $\vec{\mathbf{x}}^{(\mathbf{0})}$:

$$\begin{aligned} \chi^2_1 = (\vec{\mathbf{x}}, \vec{\mathbf{q}}) &= (\vec{\mathbf{x}} - \vec{\mathbf{x_0}})^T {\mathbf{C_0}}^{-1} (\vec{\mathbf{x}} - \vec{\mathbf{x_0}}) \\ &+ (\vec{\mathbf{m_1}} - \vec{\mathbf{c}}^{(\mathbf{0})}_{\mathbf{1}} - \mathbf{A_1}\vec{\mathbf{x}} - \mathbf{B_1}\vec{\mathbf{q}})^T \mathbf{G_1} (\vec{\mathbf{m_1}} - \vec{\mathbf{c}}^{(\mathbf{0})}_{\mathbf{1}} - \mathbf{A_1}\vec{\mathbf{x}} - \mathbf{B_1}\vec{\mathbf{q}}) \end{aligned} \tag{4.39}$$

   The position $\vec{\mathbf{x}}$ and the momentum $\vec{\mathbf{q}}$ that minimize χ^2_1 are the first estimate[5] for $\vec{\mathbf{x_1}}$ and $\vec{\mathbf{q_1}}$. A proper error propagation ([56]) delivers the covariance matrix $\mathbf{C_1}$ of $\vec{\mathbf{x_1}}$.

3. The preceding step is repeated for every single candidate track and after adding the measurement $\vec{\mathbf{m}}_{\mathbf{k}}$ from the k-th track, the minimization of

$$\begin{aligned} \chi^2_k(\vec{\mathbf{x}}, \vec{\mathbf{q}}) &= (\vec{\mathbf{x}} - \vec{\mathbf{x}_{\mathbf{k-1}}})^T {\mathbf{C_{k-1}}}^{-1} (\vec{\mathbf{x}} - \vec{\mathbf{x}_{\mathbf{k-1}}}) \\ &+ (\vec{\mathbf{m}}_{\mathbf{k}} - \vec{\mathbf{c}}^{(\mathbf{0})}_{\mathbf{k}} - \mathbf{A_{k-1}}\vec{\mathbf{x}} - \mathbf{B_{k-1}}\vec{\mathbf{q}})^T \mathbf{G_{k-1}} (\vec{\mathbf{m}}_{\mathbf{k}} - \vec{\mathbf{c}}^{(\mathbf{0})}_{\mathbf{k}} - \mathbf{A_{k-1}}\vec{\mathbf{x}} - \mathbf{B_{k-1}}\vec{\mathbf{q}}) \end{aligned} \tag{4.40}$$

[5] χ^2_1 depends only on the measured parameters of one track, whereas in the standard least square fit the χ^2 contains the parameters of **all candidate tracks.**

This procedure, so-called *filtering*, results in the final estimate of the vertex position $\mathbf{\vec{x}_N}$ and its associated covariance matrix $\mathbf{C_N}$, where N is the total number of candidate tracks.

4. Then the *smoothing* step recalculates the momenta of all tracks at this final vertex position $\mathbf{\vec{x}_N}$

Since especially for a small number of candidate tracks the final vertex position $\mathbf{\vec{x}_N}$ can still depend on the starting value $\mathbf{\vec{x}^{(0)}}$, the entire vertex fitting procedure can be restarted with $\mathbf{\vec{x}_N}$ choosen to be the new start position. These iterations continue until the fit converges according to some predefined criteria, which can be a minimal change in the value of the total chisquare of the fit χ^2_N .

The arguments on the quality of the fit discussed for the least squares based vertex fit holds also for the kalman based vertex fit. In the optimal case[6], the variable χ^2_N behaves like a χ^2 distribution with a uniform probability distribution between 0 and 1. As for the the least squares vertex fit, the probability of χ^2 will be used in the data analysis to test if the track really belong to one vertex.

A more complete derivation of the Kalman filter equations independent of the particle parametrisation is given in [56].

4.3.4.2 Track Parametrisation

The Kalman filter formalism for the vertex reconstruction contains three different vectors

$\mathbf{\vec{x}_k}$ = estimate of the vertex position by using the information of k track

$\mathbf{\vec{q}_k}$ = estimate for the momentum of particle k

$\mathbf{\vec{m}_k}$ = the measured parameters of the tracks k

In the choice of parametrisation for these vectors the following requirements should be met

1. the errors of all these vectors should be unbiased, independent and normally distributed.

2. the measurement projection, which is a mapping between $\mathbf{\vec{x}_k}$ and $\mathbf{\vec{q}_k}$ to the measured track parameters $\mathbf{\vec{m}_k}$ should be linear.

In general, these requirements are difficult to satisfy. When multiple scattering effect are not neglectable, errors on $\mathbf{\vec{x}_k}$ and $\mathbf{\vec{q}_k}$ are correlated as well as errors of measurements.

The choice of the parametrisation used in the Kalman based vertex fit algorithm is the same as for the least squares based vertex fit, i.e

$$\vec{h} \equiv \vec{p} = (\vec{x}, \vec{q})^T = (x, y, z, p_x, p_y, p_z, E)^T \quad dim(\vec{p}) = 7 \tag{4.41}$$

[6] refers to the case when the input track parameters errors are correclty estimated and normally distributed

Using the same representation will ease later the comparison between the two vertex fit method.

For the sake of clarity, the derived mathematics can be found in [56].

4.4 Vertex fitting validation

In this section, the vertex position resolution obtained using the two different vertex fitting algorithms will be presented. Once the vertex position and the kinematics of the outgoing particles at this position are known, two important physical observables, the invariant mass and the lifetime of the decaying particle, can be deduced. The resolution obtained for both invariant mass and lifetime after applying the vertex fitting algorithm will be also be presented.

4.4.1 Monte carlo simulation

As for the performance study of the vertex finding algorithm, collisions of a 2 A GeV ^{6}Li heavy ion beam impinging on a 4 cm thick carbon target are generated using the UrQMD event generator mentionned in Chapter 1 and processed in the HypHI experimental setup. Within one collision event, $\Lambda \rightarrow p\pi^-$ decays wich are in the geometrical acceptance of the detectors are selected. The Λ decay is of special interest for testing the performance of both vertex fitting algorithms since with only two tracks the vertex fitting is susceptible of bad position measurement.

In the Monte Carlo simulation, the extension of the carbon target $\delta_{x,y,z} \sim 2\ cm$ is taken into account by smearing with a uniform distribution the position of the Λ production vertex in the spherical coordinate system. The longitudinal and transversal distributions of the Λ production vertex after the smearing procedure are shown in Figure 4.25.

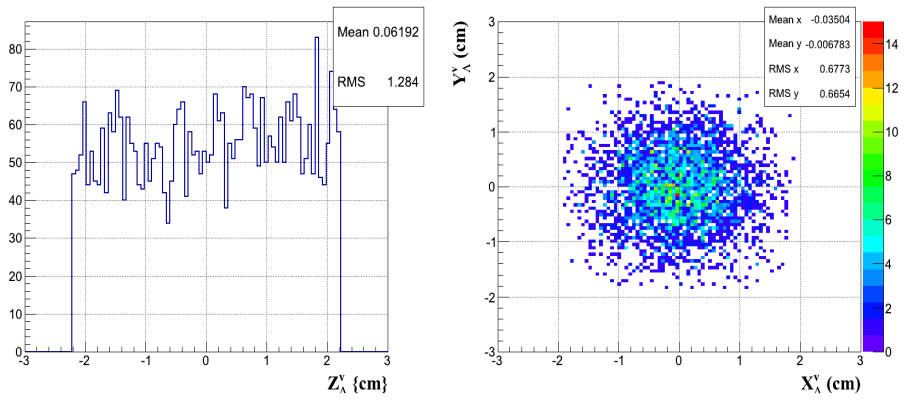

Figure 4.25: Longitudinal and transversal distributions for the Λ production vertex.

The momemtum distribution for the Λ as generated by the UrQMD event generator is shown in Figure 4.26. The momemtum distribution of the Λ decay products

are computed by the transport engine using a direct particle decays in flight routine which simulates the two-body decay with isotropic angular distribution in the center of mass system.

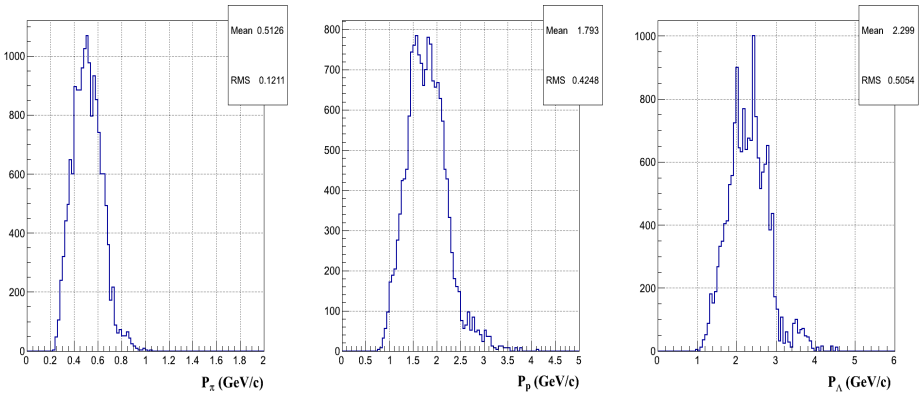

Figure 4.26: Momentum distributions of the Λ particle and the outgoing particles pion and proton.

The track fitting procedure described in Chapter 3, which utilizes position measurements from

- the fibers detector (TR1 and TR2),
- the drift chamber (BDC) placed after the ALADiN magnet
- both the TFW wall for negatively charged particle and the TOF+ wall for the positively charged particle

is used to compute the fitted track parameters for both positively and negatively charged tracks at the TR1 detector plane which will be used as input to the vertex finding to extract a first guess of the decay vertex position.

The identification of the tracks produced by the Λ decay is achieved by comparing, track by track, the measured points found by the track fitter with those generated by the actual particles. This algorithm required all the measured points used to be correclty assigned. Furthermore the correct mass assignements is also known from the Monte Carlo engine itself. Therefore there is no background in the selected Λ decay trials.

The approximate vertex position given by the vertex finding procedure and the extrapolated track parameters this vertex position are then used as input to both the least squared based and the Kalman based vertex fit.

4.4.2 Vertex fit quality

Residuals and Pull distributions

To control the quality of the vertex fitting algorithms, one usually define quantities sensitive to the single track parameters such as [57]

- the **residual** of the value x defined as

$$\delta \mathbf{x} = x_{rec} - x_{sim}.$$

  The mean of this distribution should be zero, the width is defined through its errors

- the **pull** of the value x defined as the residual divided by its error

$$\mathbf{pull(x)} = \frac{x_{rec} - x_{sim}}{\sqrt{cov(x_{rec}, x_{sim})}}.$$

  If the errors are properly taken into account in the error matrix and if there is no systematic shift of the measured parameters, the mean of the pull distribution should be zero and the standard deviation should be 1. In this sense, the effects of wrongly estimated uncertainties or systematic errors can directly be detected out of the shape of the pull distributions.

Figures 4.30 and 4.32 show the residuals and the pulls distributions for the fitted parameters $\vec{\alpha} = (x, y, z, p_x, p_y, p_z, E)^T$ recalculated at the decay vertex position for the least squares based vertex fitting procedure. The Figures 4.31 and 4.33 show the same distributions for the Kalman vertex fitting procedure. Both algorithms show a very similar vertexing and track parameter performance. Furthermore the residuals and the pulls distributions presented show that there are no systematic biases in eitherther vertex position or the kinematic quantities calculated from the track paramters for both vertex fitting algorithm.

For both vertex fitting algorithms, the uncertainties in the decay vertex position is nearly a factor ten smaller in the tranverse plane than in the longitudinal direction. The uncertainty associated with reconstructin the decax vertex position is not, in general, isotropic. It is instead described by an error ellipse when projected into the XY plane, perpendicular to the beam axis. The orientation of the semimajor axis of this ellipse is determined by the opening angles of the fitted decay products and the quality of the fitted track parameters. A track that is well measured in the fibers detector and in the drift chamber, for instance, will tend to produce an error ellipse whose major axis is directed along that particle's flight path at the vertex. The uncertainty associated with the minor axis, which are found to be a factor ten smaller in Figures 4.30 and 4.31 than that of the major axis[7], reflecting the

[7] nearly parallel to Z axis in our case where the Λ particle are boosted very forward ($\gamma \sim 3$). Because of the strong correlations between the decaying particles direction and the error ellipse's orientation, one can assimilate the major and minor axes of the error ellispe as the longitudinal and transverse errors respectively

decreased accuracy in determining the longitudinal coordinate for the intersection of two trackswith relatively small opening angles.

χ^2 and the probability of χ^2

As discussed above, in order to define global criteria evaluating the overall quality of the fit, one uses the χ^2 and/or the **p-value** of the fit.

The Figures 4.27 and 4.28 show the χ^2 and the probability of χ^2 for both algorithms. In both case the mean value of the χ^2 distribution is ~ 1.5 which is greater that the expected value given by degree of freedom for this fit : $ndf = 2 \cdot N_{tracks} - 3 = 1$. This could come from the fact that errors are underestimated. If the uncertainties are underestimated, the parameters are moved outside of their error interval, causing a shift which is larger than the fit would expect due to the covariance matrix. This generally results in larger χ^2 values and consequently leads to lower probablility of χ^2 values $\langle P_{\chi^2} \rangle \sim 0.44$. The probalibilty of $\chi 2$ is evenly spread for both algorithms with an excess at low values. This peak could also originate from the events where only a local minimum of the χ^2 is reached. Furthermore, it has been shown that especially for the kinematical parameters (p_x, p_y, p_z, E) the errors are non-gaussian due to the large fluctuations in the processes of energy loss and the corresponding multiple scattering. These effects also contribute to the low *p-value* peak in the simulation and the broadening ($\sigma > 1.0$) of the pull distributions. Getting optimal values for the covariance matrix $\mathbf{V}_\alpha$ is in practice difficult. The outer-diagonal elements, wich differ from 0, have to be properly estimated and taken into account. Only in this case, the pull-distributions and also the *p-value* will have a correct form.

In an experiment, even if one estimates the covariance matrix $\mathbf{V}_\alpha$ precisely, the quality quantities described above do not exactly behave as expected. There will be always a certain fraction of background, due for example to misidentification of particles, which will satisfy the constraint conditions of the analysis selection. Concerning the simulated $\Lambda \to p\pi$, one can imagine that there will be a certain amount of background below the mass of the Λ. This background will in general not peak at the the Λ nominal mass, but will be more or less flat distributed over a broad mass region. In the analysis, it is unavoidable to fit this background as well as the signal. The fitted background produces an increased amount of large χ^2 values. Thus the *p-value* distribution will inevitably peak at low values, similar to the distributions in Figures 4.27 and 4.28 but with much more counts in the low peak region.

By cutting on *p-values* larger than a minimum value so called significance level α, e.g ($p\text{-}value > \alpha = 0.0005$), one can reduce the background[8]. Therefore it is important to determine the covariance matrix $\mathbf{V}_\alpha$ as precise as possible. If one overestimates the errors, also the background events will in general be shifted to

[8] The significance level α of a test is a value that should be decided upon by the user interpreting the data and is compared against the *p-value*. The significance level α is therefore not determined by the *p-value*. The *p-value* is calculated for each decay event and is equal the the area to the right of χ^2, which differs from fit to fit. If the *p-value* is smaller that the fixed significance α (or the χ^2 is larger than the respective significance level) the decay event is rejected.

larger *p-values*, and the efficiency of the cut is reduced. On the other hand, if one underestimates the errors as it is shown by the pulls distributions of both vertex fit algorithms in Figures 4.30 and 4.32, also the true Λ events will be shifted at too low *p-values*, and the cut can exclude the signal. Is it then important to choose *p-values* cut which is not too low in order to reduce the backgroung but also not too high in order to reduce a minimum of signal. The Figure 4.29 shows how much signal is excluded in % as a function of *p-values* cut[9].

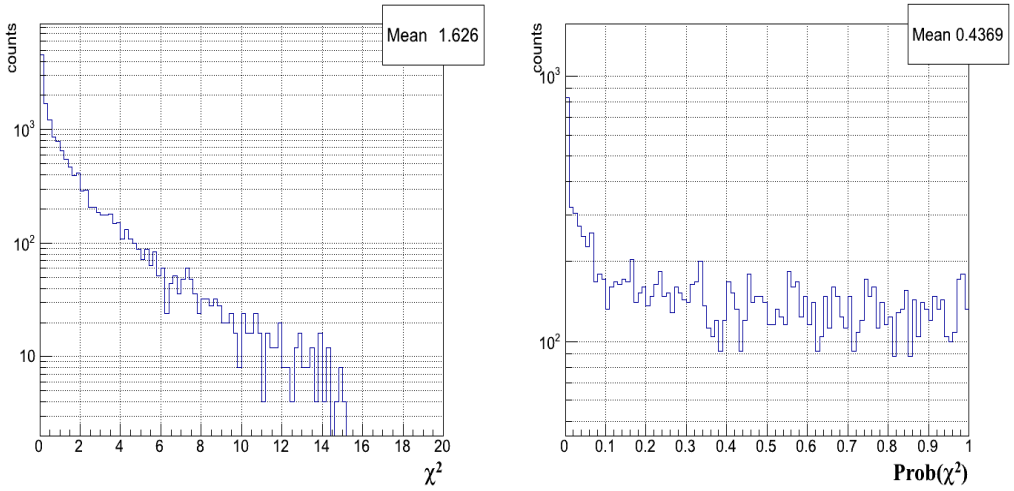

Figure 4.27: χ^2 and probability of χ^2 distributions for the reconstructed Λ particle using the least square vertex fit.

4.4.3 Vertex fitting efficiency

In the Figures 4.34 and 4.35, the vertex fitting efficiency

$$\varepsilon(z_v) = \frac{N_\Lambda^{fitted}(z_v)}{N_\Lambda^{accepted}(z_v)} \ , \ \varepsilon(p_\Lambda) = \frac{N_\Lambda^{fitted}(p_\Lambda)}{N_\Lambda^{accepted}(p_\Lambda)} \tag{4.42}$$

as a function of of Z_v vertex coordinate and the momentum p_Λ. of the reconstructed Λ for both vertex fitting algorithms are shown. The efficiency as a function of the variables Z_v and p_Λ is rather constant and reach nearly $95 - 99$ %.

4.4.4 Invariant Mass reconstruction

If all decay products of a decaying particle reached, are detected an identified using the required detectors for the track reconstruction and identification procedure, one

[9] In precise technical terms, the probability to reject non-background event with *p-values* $< \alpha$ by mistake is called the *error of first kind* or type I error α since it usually equals the significance α.

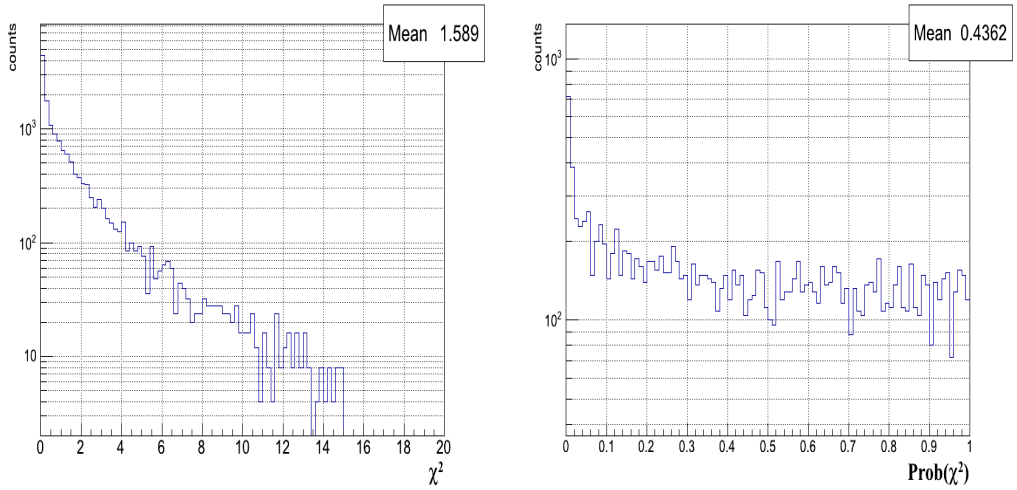

Figure 4.28: χ^2 and Probability of χ^2 distributions for the reconstructed Λ particle using the Kalman vertex fit.

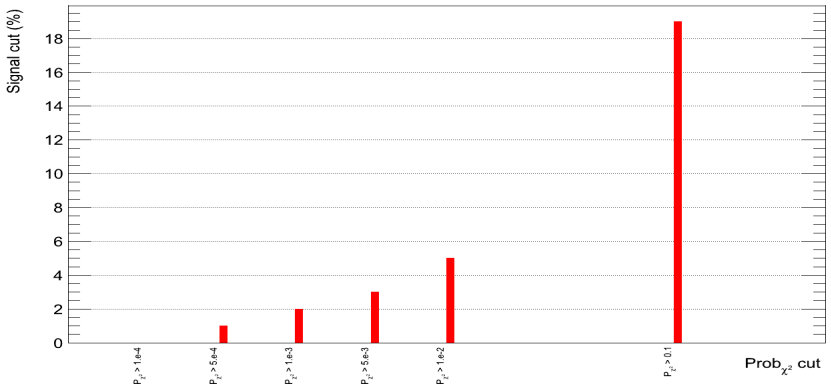

Figure 4.29: Evolution of the cut Λ signal in % as a function of the minimal p-value cut. Too high p-value such as $p - value > 0.1$ cut will exclude a lot of signal and should be avoided. A good compromise will be to use p-value cut in the range $\left[10^{-4}; 10^{-3}\right]$ wich exclude a maximum of 2% of the Λ signal. This range will be used in the hypernuclei event selection.

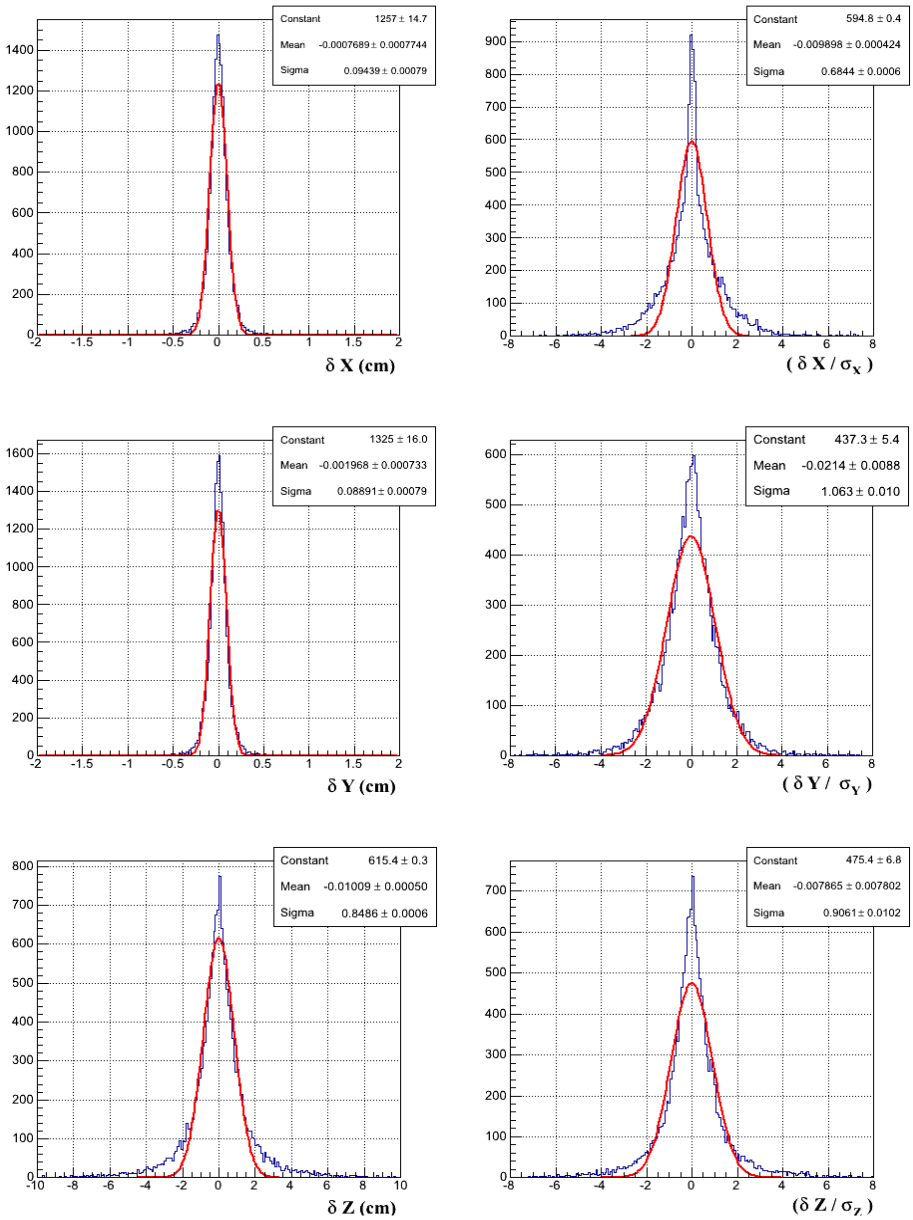

Figure 4.30: Residual and pulls distributions for the fitted vertex position for the least squares based vertex fit (in blue). The pull distribution in the bending X direction shows discrepancy compared to a gaussian distribution (in red). Furthermore the errors in the bending X direction seems to be $\sim 25\%$ overestimated.

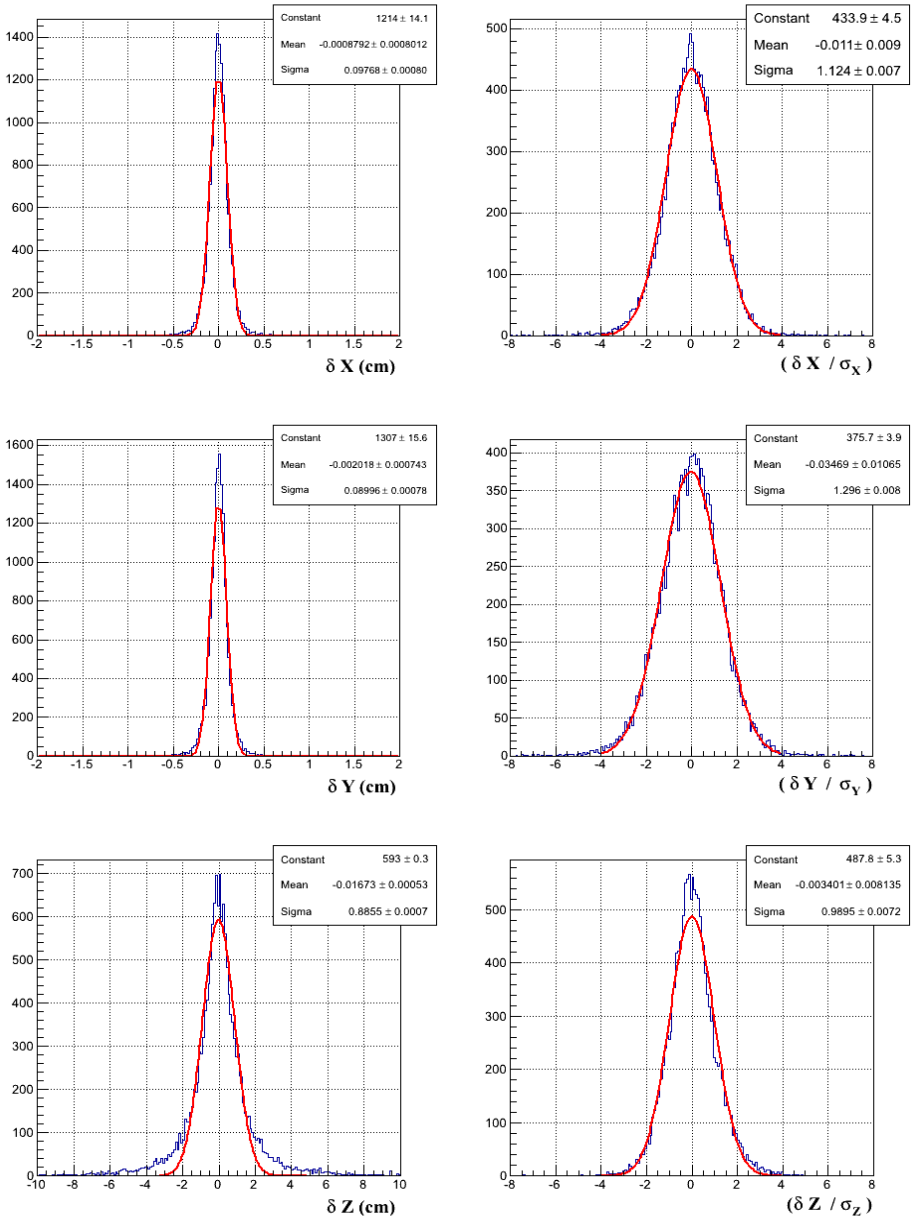

Figure 4.31: Residual and pulls distributions for the fitted vertex position for the Kalman based vertex fit (in blue) compared to a gaussian distribution (in red). The pull distributions show that the Kalman algorithm estimate properly the errors in all directions.

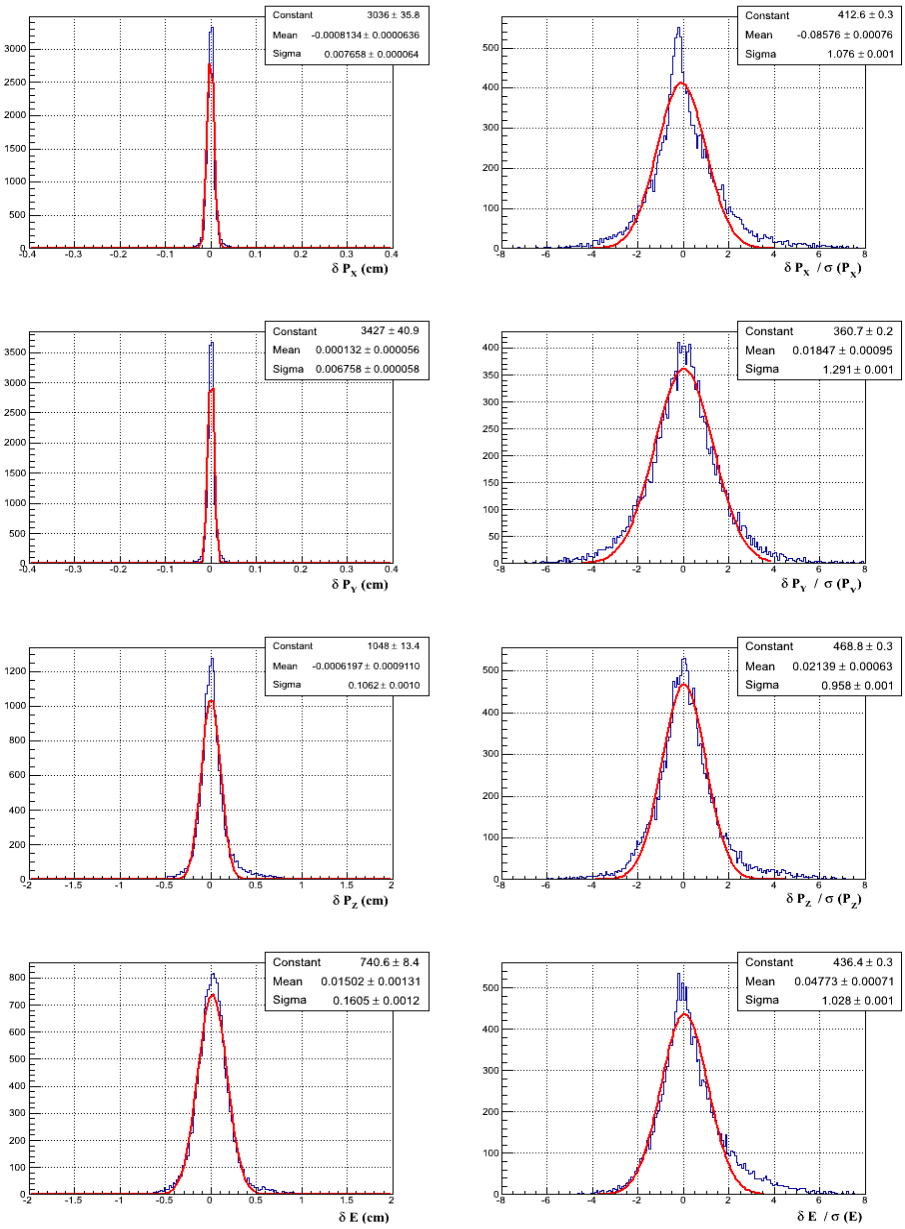

Figure 4.32: Residual and pulls distributions for the fitted kinematic parameter of the reconstructed Λ when applying the least square based vertex fit (in blue) compared to a gaussian distribution (in red). The pull distribution in the bending X direction do not follow an exact gaussian model.

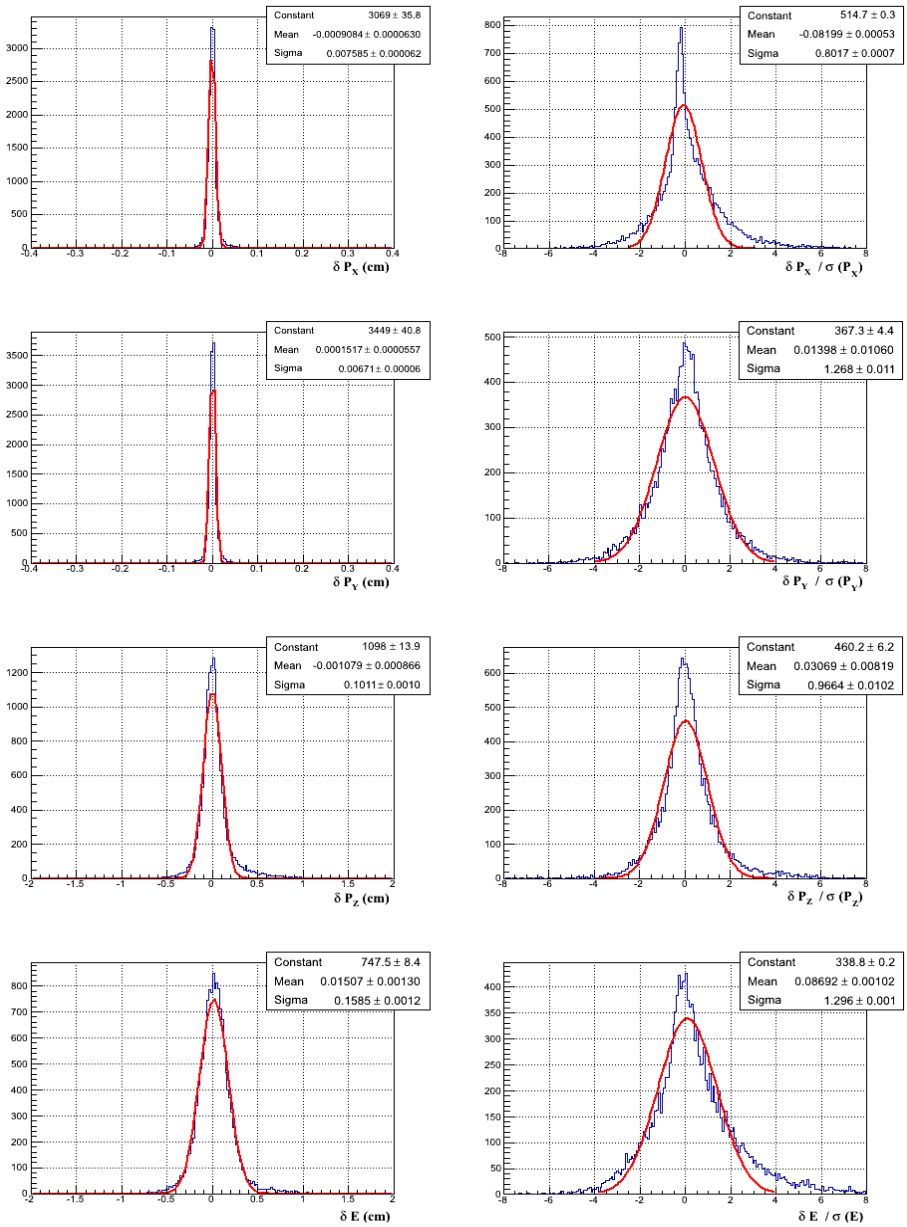

Figure 4.33: Residual and pulls distributions for the fitted kinematic parameter of the reconstructed Λ when applying the Kalman vertex fit (in blue) compared to a gaussian distribution (in red). As for the least squares based vertex fit, the pull distribution in the bending X direction do not follow an exact gaussian model.

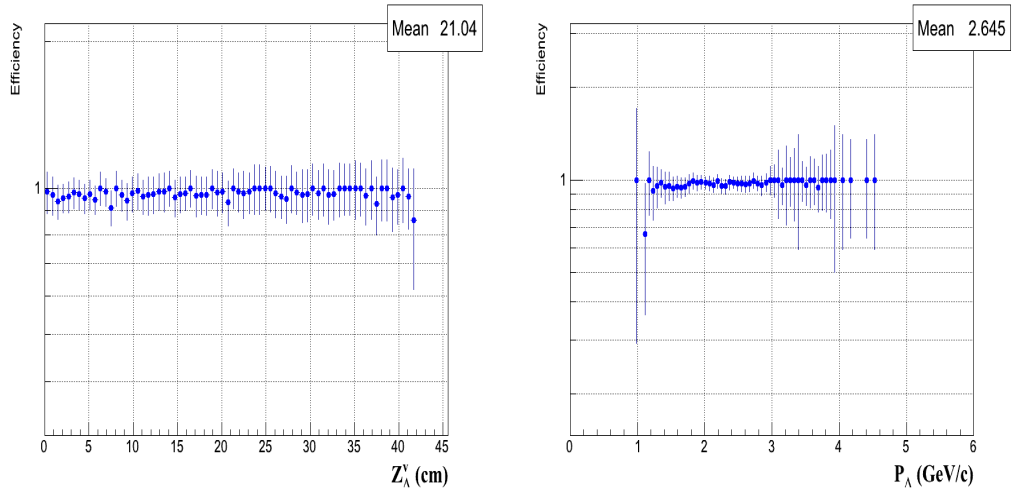

Figure 4.34: Vertex fitting efficiency as a function of the Z vertex position and the momentum p_Λ of the reconstructed Λ particle using the least square vertex fit.

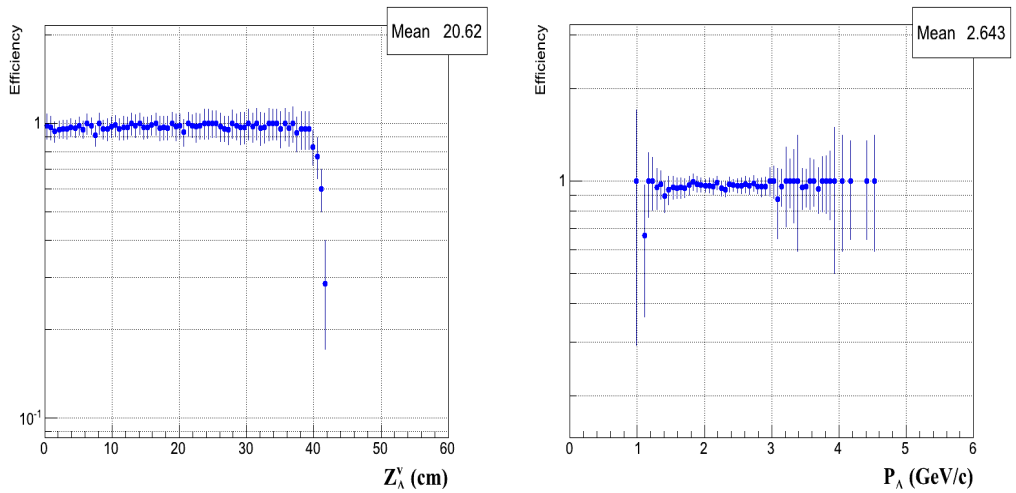

Figure 4.35: Vertex fitting efficiency as a function of the Z vertex position and the momentum p_Λ of the reconstructed Λ particle using the Kalman vertex fit. The efficiency shows a sensible decrease for high Z values but is still flat as a function of $_\Lambda$.

can appy the invariant mass technique.

In the center of mass (CMS) reference frame of the daughter particles, the mother particle is at rest at the time of the decay. Therefore the sum of the 4-momenta $p_i^\mu = (E_i, \vec{p}_i)^T$ of the daughter particles is exclusively determined by the mass of the mother, referred to as the invariant mass. The sum being connected to the square of the mother particle 4 momentum as follow

$$M_{inv} \equiv p^\mu_{mother} \cdot p_{\mu,mother} \tag{4.43}$$

the mass is a Lorentz invariant scalar and its value is the same in every choosen reference frame. If all N decay products of the mother particle are detected, its mass is reconstructed using the equation:

$$M_{inv} = \frac{1}{c^2} \cdot \sqrt{p^\mu_{mother} \cdot p_{\mu,mother}} = \frac{1}{c^2}\sqrt{\left(\sum_{i=1}^{N} E_i\right)^2 - \left(\sum_{i=1}^{N} \vec{p}_i\right)^2 c^2} \tag{4.44}$$

where the decay products track parameters are the one obtained after applying the vertex fitting procedure.

The Figures 4.36 and 4.37 show the reconstructed Λ invariant mass using respectively the least squares and the Kalman vertex fitting procedures. The results in terms of mean mass value and mass resolution are compatible for both vertex fitting approaches and summarized in the Table 4.2.

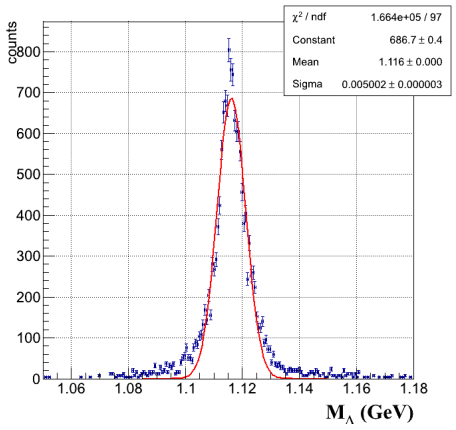

Figure 4.36: Λ invariant mass using the χ^2 vertex fit procedure (blue) compared to a gaussian distribution (red).

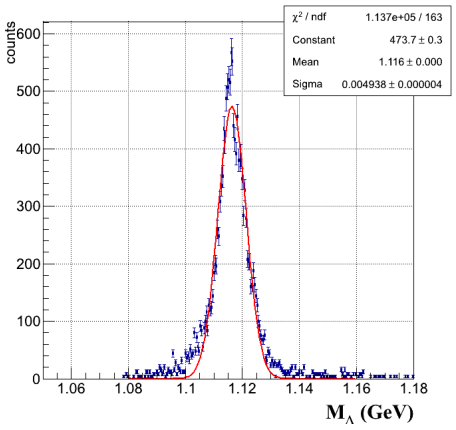

Figure 4.37: Λ invariant mass using the Kalman vertex fit procedure (blue) compared to a gaussian distribution (red).

4.4.5 Lifetime reconstruction

In order to determine the proper decay time, both momentum and *the flight distance* of the decaying particle need to be reconstructed. The lifetime measurement make

Table 4.2: Λ invariant mass results obtained after using the least square based vertex fit the Kalman based vertex fit procedure. The Λ reconstructed mass mean value is slightly overstimated compared to the nominal $M_\Lambda = 1.115684\ (GeV)$ used in the Monte Carlo simulation.

vertex fit	M_Λ (GeV)	σ_M (MeV)
χ^2 based	1.1161	5.002
Kalman based	1.1164	4.933

use of the relativistic relation $L_{decay} = \beta ct = \gamma\beta c\tau = (p/m)c\tau$ which leads to the simple formula

$$c\tau = \frac{L_{decay} \cdot m}{p} \tag{4.45}$$

where $c\tau$ is the proper time measured in units of distance, the mass m in GeV/c^2 and the momentum p in GeV/c^2 .

After the vertex fitting procedure only the momentum and the endpoint (secondary vertex position) are accessible. However an accurate determination of the lifetime requires that both the beginning (primary interaction point) and endpoint of the particle's flight vector be determined precisely as shown in Figure 4.38. Unfortunately with the HypHI experimental setup a precise measurement of the primary interaction point is not possible to obtain with reasonable accuracy. One should then take the assumption that the most probable position for the primary interaction is in the middle of the 4 cm large carbon target which is the origin point $(0, 0, 0)$ of the experiment reference frame. This assumption will immediately smear the flight distance measurement by a systematic error of $\delta_L = \pm 2\ cm$ which correspond to the geometrical extension of the target.

This section describes the proper decay time measured on simulated decay $\Lambda \rightarrow p\pi^-$ using the above assumption for the primary interaction point.

Momentum reconstruction

After the vertex fit procedure, the extrapolated momentum of the Λ daughter particles (p, π^-) are combined to reconstruct the total Λ momentum. Figures 4.39 and 4.40 show the total momentum p_Λ distributions as well as the momentum residual distributions $\delta_p = (p_\Lambda - p_{sim})$ for both χ^2 based and Kalman based vertex fitting algorithms. The *ideal* total momentum resolution achieved in both algorithm are summarized in Table 4.3. The error on the total momentum p_Λ is clearly dominated by the error along the longitudinal direction δp_z, but the residual mean value show that the reconstructed momentum using both the least square and the kalman based vertex fit is unbiased.

Flight distance reconstruction

Two ingredients are used to reconstruct the flight distance of the Λ baryon:

1 the production vertex of the Λ baryon in three dimensional coordinates xyz.

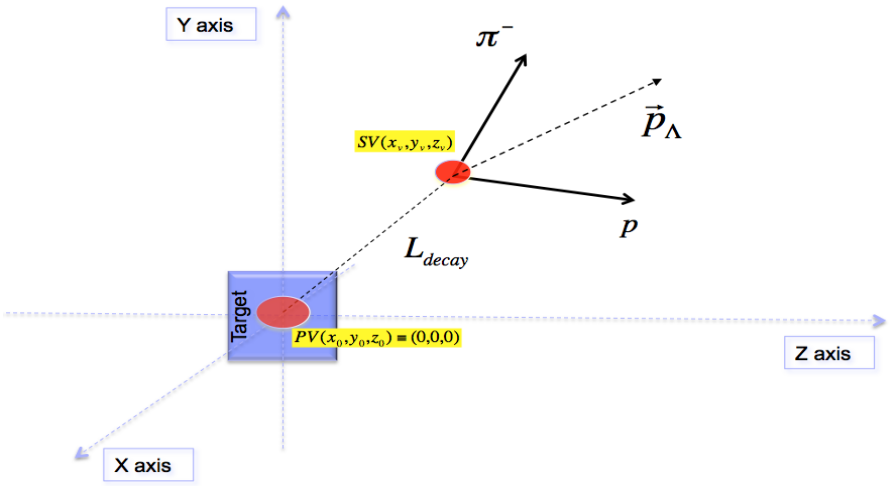

Figure 4.38: The particle Λ is produced at the center of the 4 cm large carbon target taken as the $(0,0,0)$ point of the HypHI experiment reference frame. Then the Λ travels a certain distance L_{decay} so called *the flight distance* before decaying into its $p + \pi^-$ daughters. These daughters are subsequently measured by the tracking system.

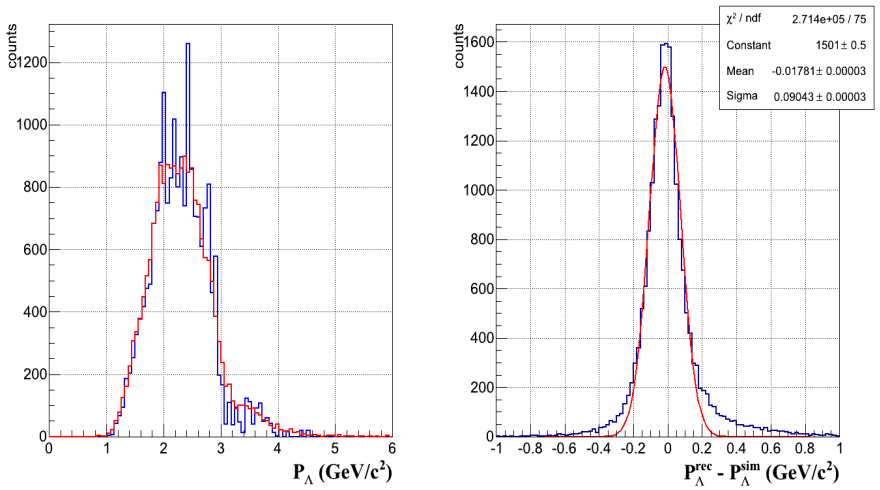

Figure 4.39: Λ momentum distributions and residuals obtained after using the least square based vertex fit. The residual mean value $\langle p^{rec}_\Lambda - p^{rec}_\Lambda \rangle = -0.017$ show that the momentum reconstruction is unbiased.

2 the decay vertex the Λ baryon in three dimensional coordinates xyz.

The decay vertex of the Λ baryon is determined by the vertex fit algorithms.

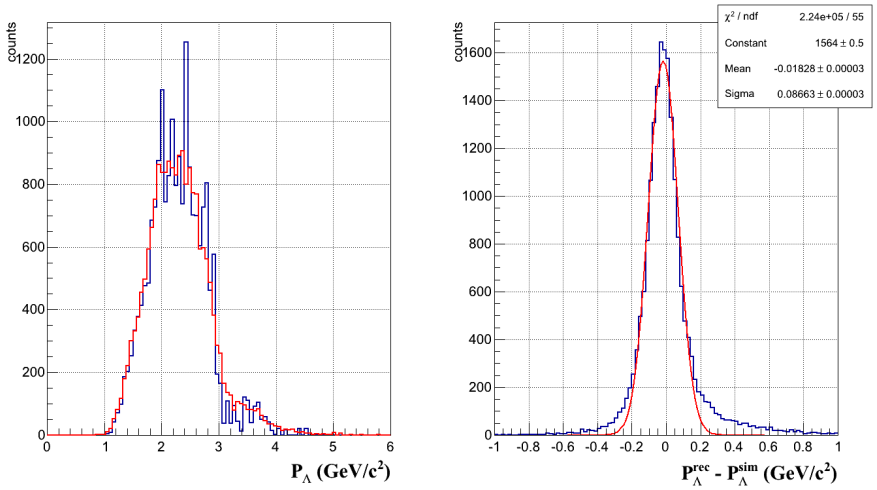

Figure 4.40: Λ momentum distributions and residuals obtained after using the Kalman based vertex fit. The residual mean value $\langle p^{rec}_\Lambda - p^{rec}_\Lambda \rangle = -0.018$ show that the momentum reconstruction is unbiased.

Table 4.3: Reconstructed Λ momentum distributions and residuals obtained after using the least square based vertex fit and the Kalman based vertex fit

Vertex fit	$\langle p^{rec}_\Lambda - p^{rec}_\Lambda \rangle$ (GeV)	$\sigma_{p^{rec}_\Lambda - p^{sim}_\Lambda}$ (MeV)
χ^2 based	-0.017	9.04
Kalman based	-0.018	8.66

The production vertex of the Λ baryon corresponds to the interaction point of the ^{6}Li beam and a ^{12}C nucleus in the 4 cm thick carbon target. Many charged particles are created in the collision process and originate from this interaction point. Unfortunately only few tracks of these particles coming from the primary collisions can be reconstructed using the HypHI experimental setup which prevent an accurate event-by-event reconstruction of the primary interaction point. As mentionned before, on can only assume that the most probable primary interaction point is situated at the middle of the 4 cm target at the origin point $(0, 0, 0)$ of the HypHI reference frame. Consequently, the corresponding errors in the three dimensional coordinates for the primary interaction point are

1. $\delta_Z = \pm 2\ cm$ correponding to the longitudinal extension of the carbon target.
2. $\delta_{X,Y} = \pm 1\ cm$ corresponding to the constraint that in the transverse direction the primary vertex should be within the beamspot area.

Nevertheless in the Monte Carlo simulation, the primary interaction point is exactly known. One can use this information in order to estimate the bias introduced

in the flight distance measurement of the mother particle when using the origin point as the primary interaction point.

The quality of the reconstructed flight distance from the interaction point to the Λ baryon decay vertex for both vertex fitalgorithms is shown in Figures 4.41 and 4.42. The flight distance is calculated by using either the exact primary interaction position from the Monte Carlo simulation or the origin position. Using the asumption, the error on the flight distance measurement is systematically multiplied by a factor 2. The flight distance resolution fo both vertex fit algorithms is summarized in Table 4.4.

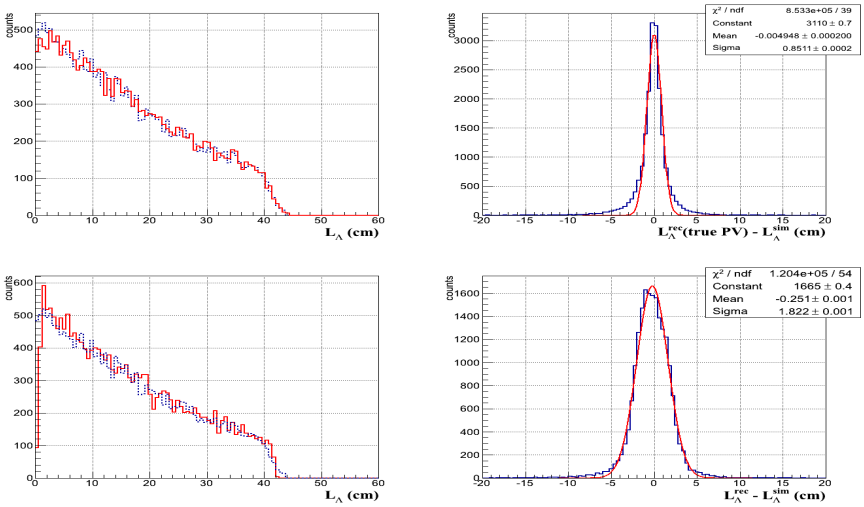

Figure 4.41: Λ Flight distance distribution and residual using the least squares based vertex fit. The upper part show reconstructed flight distance and residual when using the exact primary interaction position from the simulation. The lower part show the same distributions when using the asumption that the primary vertex is at the origin point $(0, 0, 0)$.

Proper time reconstruction

The reconstructed proper decay time τ_Λ in second units is directly derived from Equation 4.45:

$$\tau_\Lambda^{rec} = \frac{m_\Lambda^{rec} \cdot L_\Lambda^{rec}}{c \cdot p_\Lambda^{rec}} \tag{4.46}$$

here, c is the speed of light, m_Λ^{rec} is the reconstructed Λ mass, p_Λ^{rec} is the reconstructed Λ momentum and L_Λ^{rec} is the Λ reconstructed flight distance. Figures 4.43, 4.44 show the quality of the reconstructed Λ proper time τ_Λ in picosecond units (ps) and the corresponding error σ_τ obtained on a event-by-event basis calculation for both vertex fit algorithms.

The event-by-event basis proper time error σ_τ is calculated using the errors on the momentum σ_p and the flight distance σ_L:

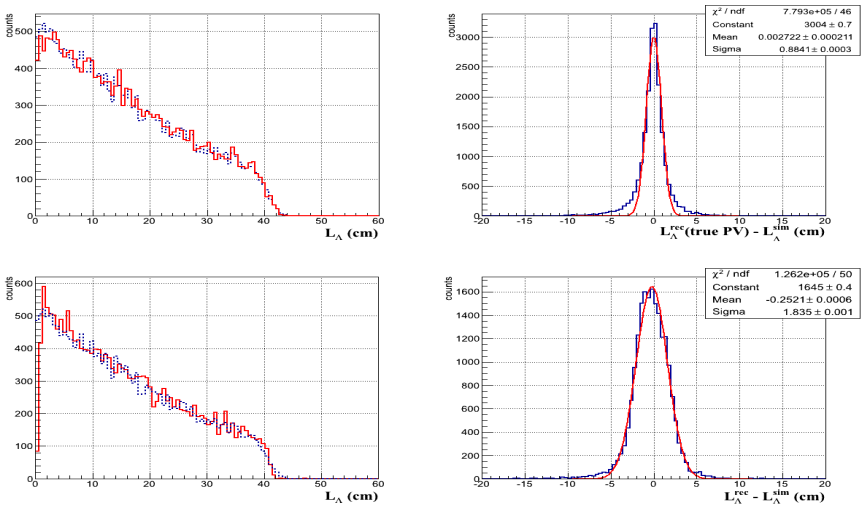

Figure 4.42: Λ Flight distance distribution and residual using the Kalman based vertex fit. The upper part show reconstructed flight distance and residual when using the exact primary interaction position from the simulation. The lower part show the same distributions when using the asumption that the primary vertex is at the origin point $(0, 0, 0)$.

Table 4.4: Reconstructed Λ flight distance distributions and residuals obtained after using the least square based vertex fit and the Kalman based vertex fit. For both vertex algorithms the true primary vertex (PV) position and the origin asumption (PV = (0,0,0)) was used. When using the origin as the primary vertex position, the error on the flight distance reconstruction is multiply by nearly a factor 2.

Vertex fit + (PV= MC true)	$\langle L_\Lambda^{rec} - L_\Lambda^{sim} \rangle$ (cm)	$\sigma_{L_\Lambda^{rec} - L_\Lambda^{sim}}$ (cm)
χ^2 based	-0.004	0.85
Kalman based	+0.003	0.88
Vertex fit + (PV=(0,0,0))		
χ^2 based	-0.251	1.82
Kalman based	-0.252	1.83

$$\sigma_\tau = \tau_{rec} \cdot \sqrt{\left(\frac{\sigma_L}{L_{rec}}\right)^2 + \left(\frac{\sigma_p}{p_{rec}}\right)^2} \tag{4.47}$$

This error has to be used as a weight in the measurement of the average Λ decay time.

As for the flight distance distributions, two proper time calculations are presented: one measurement (the upper histograms in each Figures) uses the exact pri-

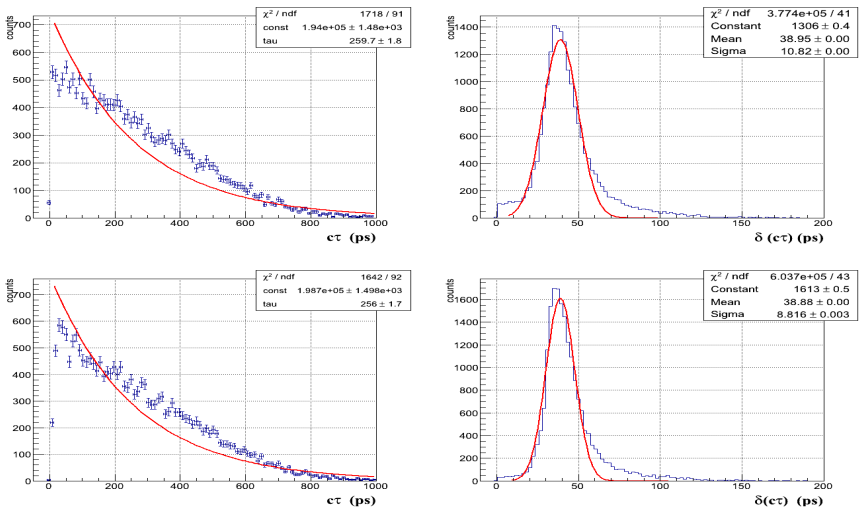

Figure 4.43: Λ proper time distribution and the event-by-event associated error δ_τ in pico-second units (ps) using the least square based vertex fit. The upper part show reconstructed proper time and the event-by-event associated error δ_τ when using the exact primary interaction position from the simulation. The lower part show the same distributions when using the asumption that the primary vertex is at the origin point $(0, 0, 0)$.

mary vertex position taken from the Monte Carlo, the other (the lower histograms in each Figures) uses the assumption that the primary vertex is at the origin point. A exponential decay time function $exp(-t/\tau)$ is used to fit the proper time distribution which shows that the expected exponential shape is distorted by combined detector resolution and different acceptance effects. These effects have to be taken into account in order to properly fit the decay time distribution.

Figures 4.45 and 4.46 show the difference between reconstructed and simulated proper time together with the evolution of the error $\sigma\tau$ as a function of the decay time for both vertex fitting algorithms. It should be noted that the error on the decay time increases with the decay time itself as is shown in Figures 4.45 and 4.45. This effect becomes clear when Equation 4.47 is rewritten as :

$$\sigma_\tau = p_{rec}^{-1} \cdot \sqrt{\frac{m^2}{c^2} \cdot \sigma_L^2 + t_{rec}^2 \cdot \sigma_p^2} \tag{4.48}$$

At small decay times the error on the proper decay time is dominated by the error on the flight distance, while at large decay times the momentum error dominates. Consequently the error on the proper time measurement depends on the number of selected signal events, $\sim 1/\sqrt{(N)}$ and, strongly, on the time interval covered by the event selection in the analysis.

The reconstructed proper time results and associated errors are summarized in Table 4.5.

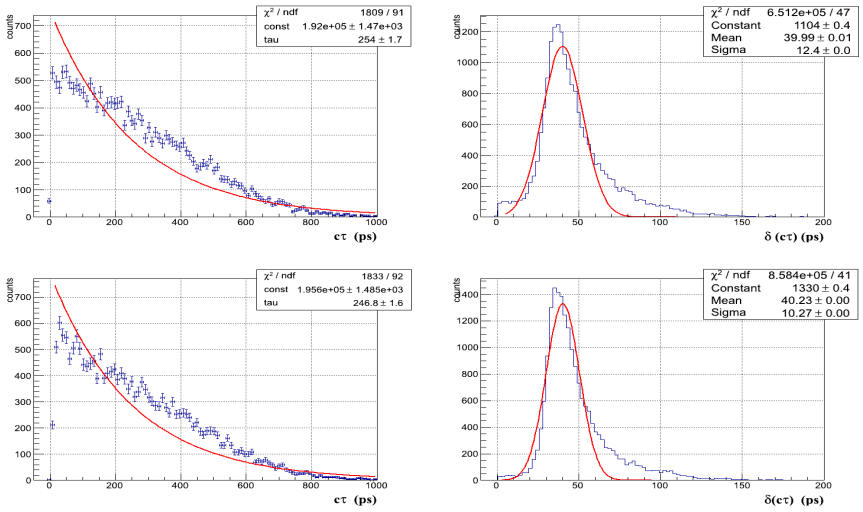

Figure 4.44: Λ proper time distribution and the event-by-event associated error δ_τ in pico-second units (ps) using the Kalman based vertex fit. The upper part show reconstructed proper time and the event-by-event associated error δ_τ when using the exact primary interaction position from the simulation. The lower part show the same distributions when using the asumption that the primary vertex is at the origin point $(0, 0, 0)$.

Table 4.5: Reconstructed Λ proper time distributions and residuals obtained after using the least square based vertex fit and the Kalman based vertex fit. For both vertex algorithms the true primary vertex (PV) position and the origin asumption (PV = (0,0,0)) was used. When using the origin as the primary vertex position, the resolution on the proper time is $\sigma_\tau \sim 35$ (ps) and the measured proper time is sytematically lower compared to the true MC value by $\Delta_\tau \sim 4.9$ (ps). Within the obtained proper time resolution σ_τ the fitted proper times are compatible with the PDG nominal value of the Λ proper lifetime $\tau_\Lambda = 262$ (ps).

Vertex fit + (PV= MC true)	$\langle \tau_\Lambda^{rec} - \tau_\Lambda^{sim} \rangle$ (ps)	$\sigma_{\tau_\Lambda^{rec} - \tau_\Lambda^{sim}}$ (ps)	τ^{fit} (ps)
χ^2 based	-1.126	24.71	259.7
Kalman based	-4.948	35.13	256.0
Vertex fit + (PV=(0,0,0))			
χ^2 based	-1.053	24.63	254.0
Kalman based	-4.889	35.13	246.8

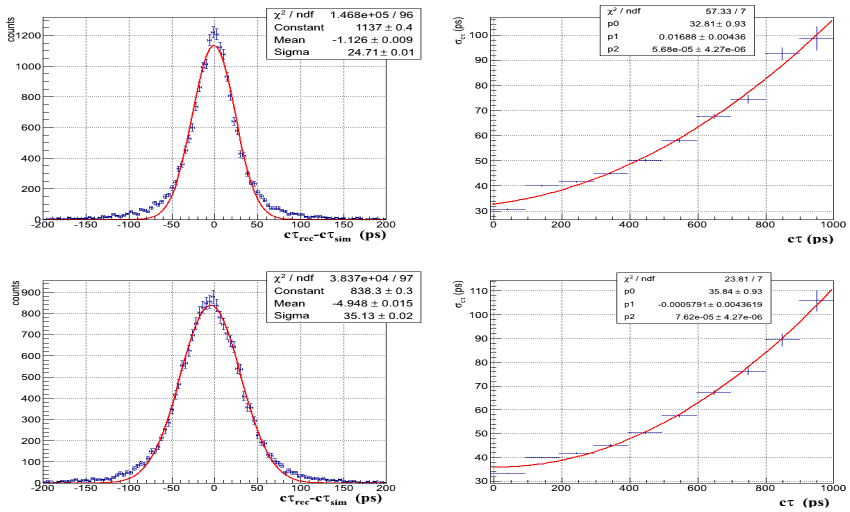

Figure 4.45: Proper time residual distribution and the event-by-event associated error δ_τ as a function of τ in pico-second units (ps) using the least square based vertex fit. The upper part show the distributions when using the exact primary interaction position from the simulation. The lower part show the same distributions when using the asumption that the primary vertex is at the origin point $(0, 0, 0)$.

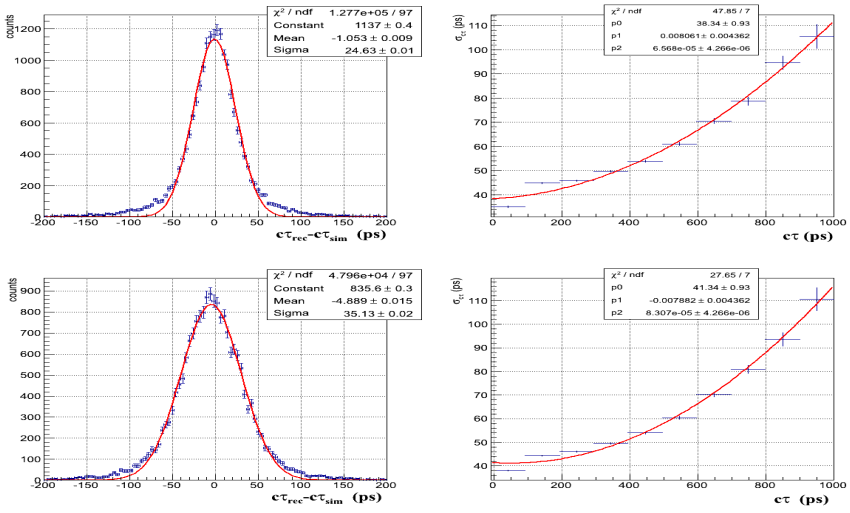

Figure 4.46: Proper time residual distribution and the event-by-event associated error δ_τ as a function of τ in pico-second units (ps) using the Kalman based vertex fit. The upper part show the distributions when using the exact primary interaction position from the simulation. The lower part show the same distributions when using the asumption that the primary vertex is at the origin point $(0, 0, 0)$.

4.4.6 Systematic bias studies

It is important to notice if there are effects which can systematically influence the results of the vertex fitting procedure. Knowing these effects can help in more careful design of the main analysis strategy for hypernuclei selection.

As already mentionned above, all the residual and pull distributions (Figures 4.30, 4.32, 4.31 and 4.33) show a mean value well centered at zero for both least squares based and Kalman based algorithms.

Further search was made by plotting the spatial and the Λ momentum residuals versus various kinematic and geometric quantities associated with the vertex fit. For instance, Figures 4.47 and 4.48 show the longitudinal discrepancy δ_Z and the Λ momentum discrepancy δ_P as a function of the χ^2 value for both vertex fit algorithms: there is no correlation between the longitudinal and the Λ momentum discrepancy and the increase of χ^2 due to the vertex fit. A large change in χ^2 does, however, imply a wider distribution of the δ_Z residuals.

Furthermore, Figures 4.49 and 4.50 show that the mass of the set of tracks, as calculated using the vertex fit's track parmeters for the decay $\Lambda \rightarrow p\pi^-$ is not correlated with the longitudinal discrepancy δ_Z but only with the δ_{P_Λ} momentum residual as expected.

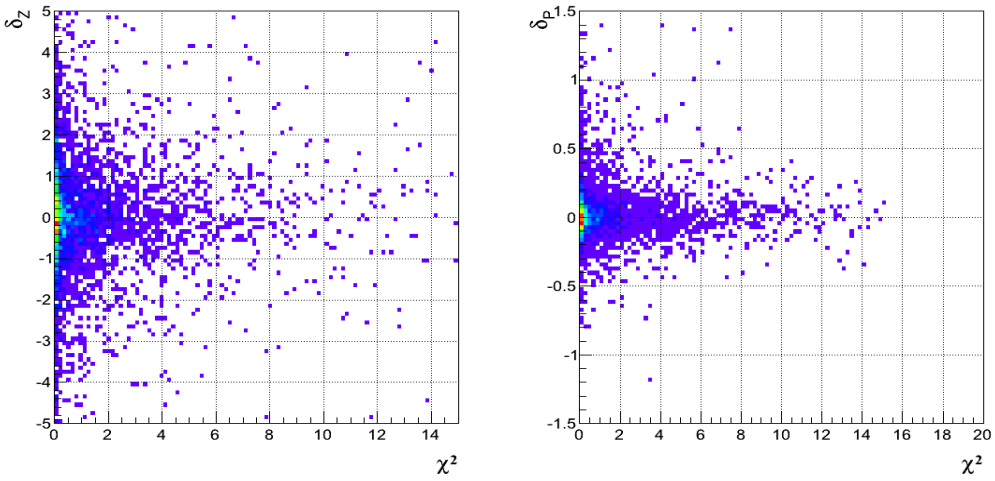

Figure 4.47: The longitudinal δ_Z and δ_{P_Λ} momentum residual versus the χ^2 of the least squares based vertex fit for the decay $\Lambda \to p\pi^-$.

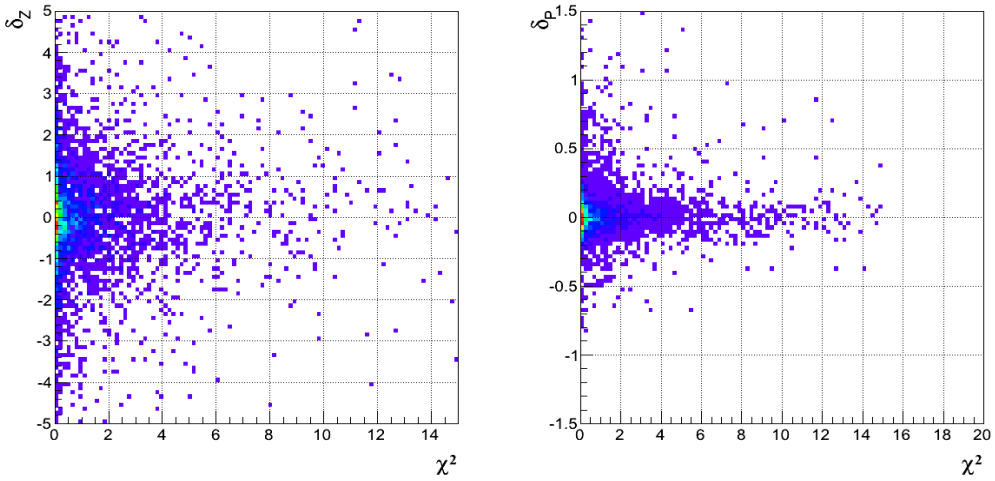

Figure 4.48: The longitudinal δ_Z and δ_{P_Λ} momentum residual versus the χ^2 of the Kalman based vertex fit for the decay $\Lambda \to p\pi^-$.

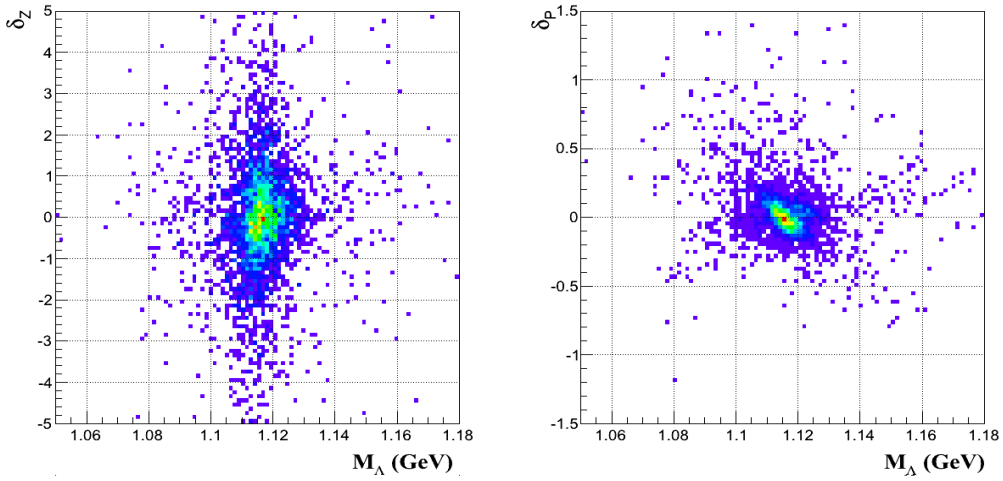

Figure 4.49: The longitudinal δ_Z and δ_{P_Λ} momentum residual versus the mass calculated M_Λ using the least squares based vertex fit.

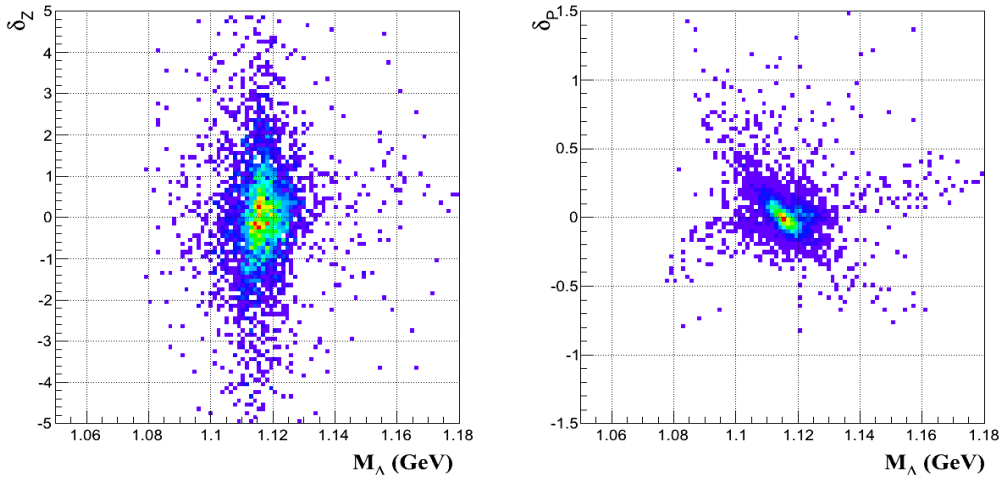

Figure 4.50: The longitudinal δ_Z and δ_{P_Λ} momentum residual versus the mass calculated M_Λ using the Kalman based vertex fit.

Chapter 5

Analysis of ^{6}Li on ^{12}C collision data

Contents

5.1 Introduction

Any experiment attempting to measure the invariant mass of hypernuclei produced in relativistic heavy ions collisions has to deal with major experimental challenges. First, the relatively large number of produced particles leads to a high detectors occupancy resulting in a serious load of the detectors. In a fixed target experimental setup particles are typically produced with a large Lorentz boost which leads to high track density in the forward direction. In case of HypHI, a hit density is high on the tracker detectors situated before the ALADiN magnet. Additionally, deflections of particles caused by multiple scattering, especially within two fiber detector planes, reduces the track resolution and as a consequence the vertex resolution and might results in the reconstruction of fake secondary vertexes. Furthermore only a small fraction of all produced tracks comes from hyperons or hypernuclei decay compared to primary tracks created in the target region. Finally, uncorrelated positively charged and negatively charged particles originating from a large fraction of partially reconstructed pairs form a huge combinatorial background when combined to pairs.

Although the HypHI experiment has been designed to detect hypernuclei under such conditions, a sophisticated data analysis is mandatory in order to extract a statistically significant hypernuclear signal. In this sense, robust track and vertex reconstruction algorithms are the key elements to achieve an efficient mass reconstruction of hypernuclei. In this chapter, the track and vertex algorithms described in Chapters 3 and 4 will be applied to the ^{6}Li+^{12}C collision data at 2 A GeV/c collected during the Phase 0 experiment in October 2009.

5.2 Analysis procedure

The data analysis consists of the following steps:

- calibration of detector raw data
- reconstruction of hits in each detector
- track reconstruction: combination of hits of all detectors to particles tracks and momentum determination
- particle identification using the TOFs system
- determination of relevant selection criteria in order to reject accidentally matched tracks and reduce the combinatorial background
- subtraction of the combinatorial background from the invariant mass distribution using the "event-mixing" technique
- estimation of reconstruction efficiency by means of a realistic Monte Carlo detector simulation.

The data flow of the reconstruction chain up to the secondary vertex reconstruction is shown in the Figure 5.1. The first step of the analysis is to convert recorded digitized data into the data structure suitable for the physics analysis. The main part of the analysis before event reconstruction process is to produce proper data structure for calibration of each detector system.

Unpacking or bytestream conversion is the first stage of the data analysis. The conversion is performed within the GSI Object Oriented Online Offline framework (GO4) [58]. The GO4 framework is a GSI standard tool for the online and offline analysis based on C++ and ROOT framework [44]. The GO4 library has been chosen because it allows the conversion of the list mode data stream, the GSI standard data protocol of the DAQ system MBS [34]. Additionally the GO4 system can connect to various MBS online data servers facilitating the online monitoring of the detectors. The data structure is organized with respect to each electronic module. In this step a pedestal subtraction for the QDC and zero suppression of the null data words are done.

The second step is called Detector Analysis, there the data is splitted into tree independent parts corresponding to the detector type: fiber detectors, time-of-flight

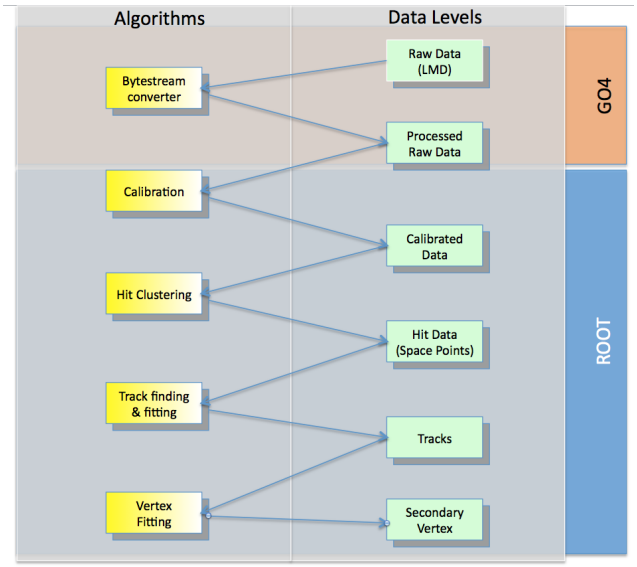

Figure 5.1: Analysis reconstruction chain. The column at the right side represents the different data levels, whilst the column at the left side show the algorithms which work on them. The arrows shows the direction of the data flow. Only bytestream conversion is done using the GO4 framework, the rest of the analysis is performed using the standard ROOT library.

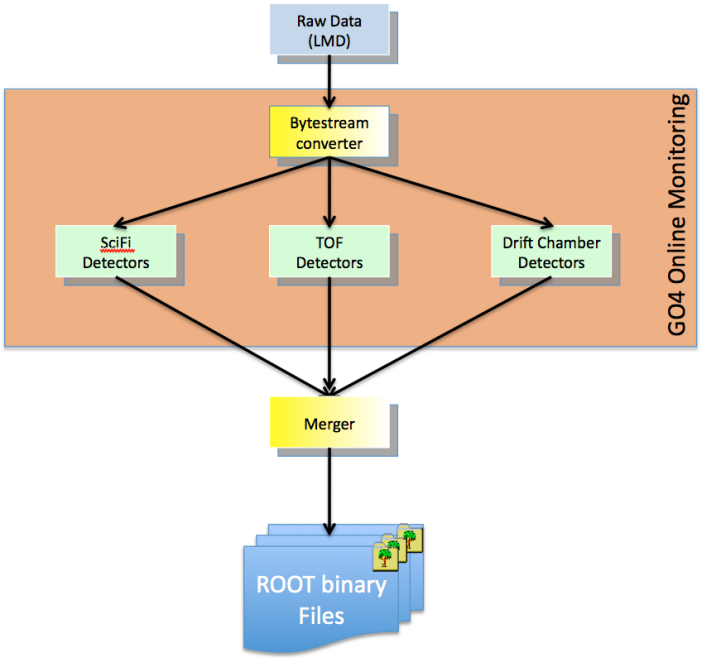

Figure 5.2: Online monitoring scheme based on the GO4 framework.

detectors and drift chambers. This approach allows to run each of them in parallel or reprocess one without affecting the others. The calibration of each detector is also performed at this stage. The calibration step includes several operations on unpacked data such as gain matching of amplitude measurements, time reference adjustment and/or position offset of each sub-detector layer from the target. Since those parts are focused on detectors, the output data is organized detector-wise and written in a ROOT binary format independently.

The first two step of the analysis: Unpacking and Detector Analysis are used for the online data monitoring system based on GO4 during the beam time (Figure 5.2).

In the next step of the data analysis so called "Merger" all calibrated detector information is combined and the final precise detector calibration is performed. The alignment of the detectors in the global coordinate system based on the geometrical pre-tracking described in Chapter 4 is performed.

All track candidates found by the pre-tracking are then fitted by the track fitting procedure based on Kalman filter technique described in the Chapter 3. The last step of the analysis is the recognition and fitting of secondary vertices using the reconstructed tracks. Once all the vertex candidates are produced by combining of 2 or 3 outgoing tracks, a set of dedicated selection criteria will be applied in order to determine the invariant mass of the mother particle in order to reduce to the minimum the amount of background.

5.3 Calibration of Time-Of-Flight detectors

The measurement principle is common for the all TOF detector used in the HypHI setup: Start counter, TOF+ and TFW. All timing is measured relatively to the Start counter.

The typical raw QDC spectra of the Start counter is shown in Figure 5.3, where the presence of beam pile-up. The second peak centered around 500 channels corresponds to the detection of the two ^{6}Li ions in the same bar of the Start counter. These events corresponds to 10% and have been excluded from the further analysis.

An important step in the data analysis is to correct the timing for slewing or walk. The slewing is caused by the dependence of the discriminator response on the pulse height. The walk correction was done for the TOF+ wall and the Start counter with a method described in [59]. The Figure 5.4 shows the time difference between two neighboring bars of the Start counter before and after walk correction. In the test experiment the designed and measured time resolution of the Start counter was about 200 ps [60], however due to high beam intensity during Phase 0 experiment the average for the complete detector achieved time resolution is $\sigma_t \sim 300$ ps.

The time walk correction was also performed for the TOF+ wall. The achieved time and Y position resolution per bar is shown in Figure 5.5.

The amplitude (QDC) calibration of TOF+ wall consists of two parts: first the gain matching of two QDC signals from same bar and second matching of the energy of all bars to the same value. The raw QDC spectrum of one of the channel of TOF+

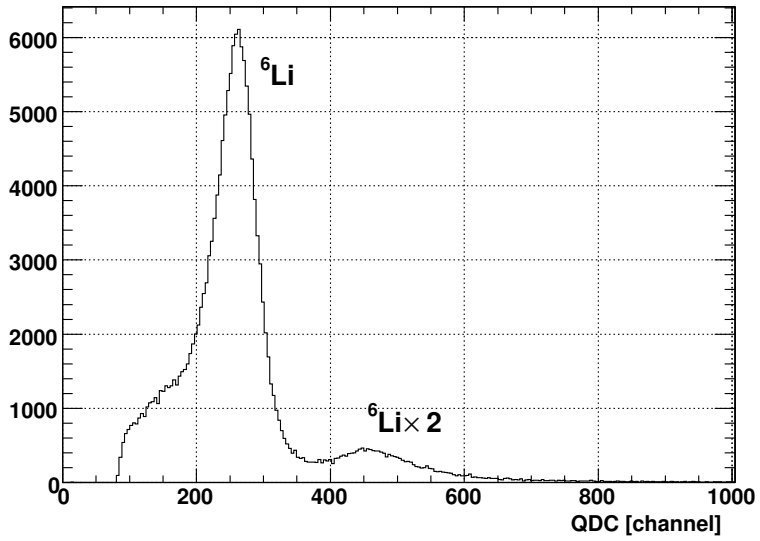

Figure 5.3: Typical raw QDC spectrum of Start counter. The clear signal of ^{6}Li and two ions of ^{6}Li are visible.

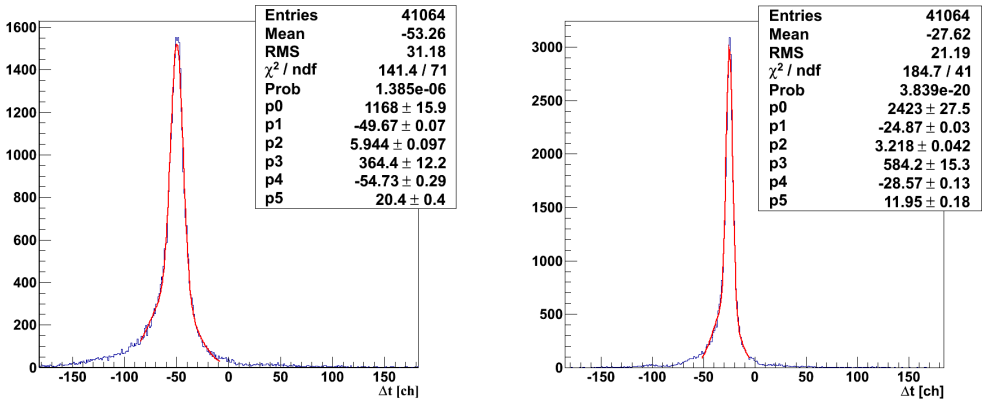

Figure 5.4: The time difference between two neighboring bars of Start counter before (left) and after (right) walk correction.

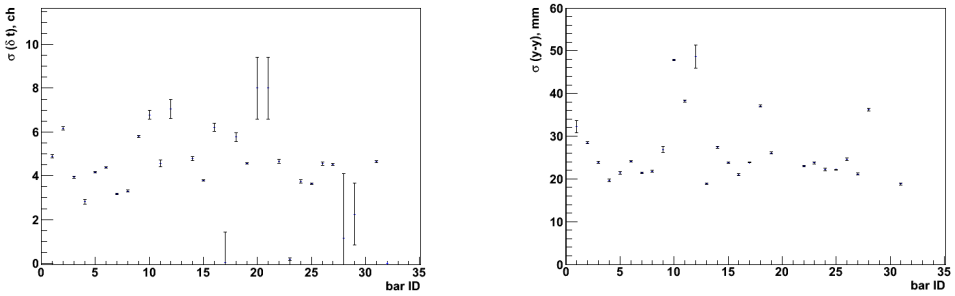

Figure 5.5: *Left panel*: TOF+ time resolution for each bar, the average value $\sigma_t \sim$ 200 ps. *Right panel*: TOF+ Y position resolution for each bar, the average value $\sigma_Y \sim 2.5$ cm

is shown in Figure 5.6. The clear separation between peaks for $Z = 1$, $Z = 2$ and $Z = 3$ is visible. The two signals from different ends of one plastic bar have to be matched to obtain the same position of the peaks. Then the total energy deposit in the bar is calculated as $E = \sqrt{QDC_{top} \times QDC_{bottom}}$ and matched to the same peaks position for all 32 bars of TOF+ wall. The result of the calibration is shown in Figure 5.7.

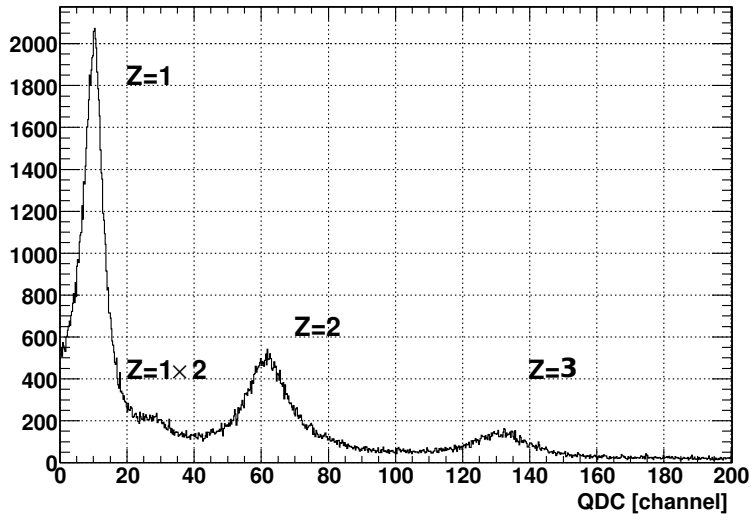

Figure 5.6: Typical raw QDC spectrum of TOF+ wall for different daughter particle in ^{6}Li on ^{12}C collision. $Z = 1 \times 2$ corresponds to the 2 particle with $Z = 1$ detected in the same bar of TOF+.

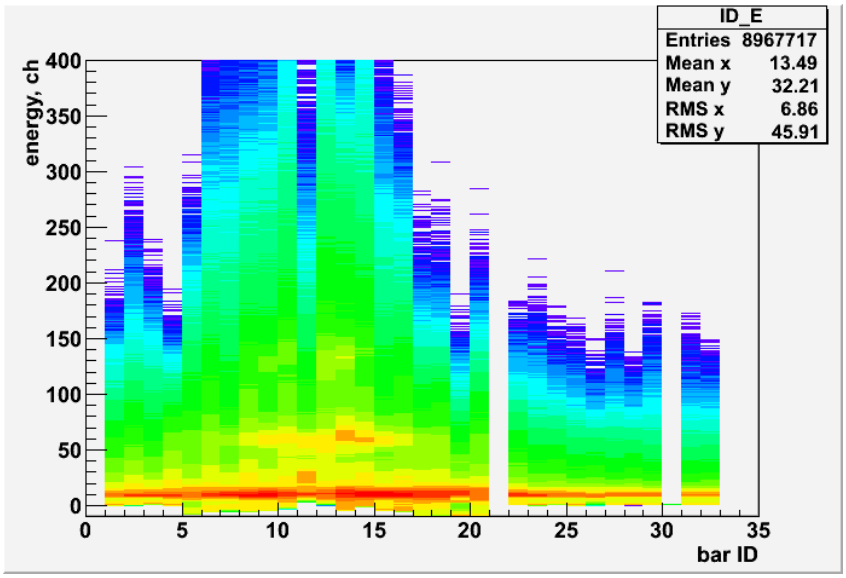

Figure 5.7: Calibrated energy deposit in channels for each bar in TOF+ wall

5.4 Particle identification

The particle identification (PID) of positively charged particles is performed in two steps. In the first step the charge of the particle is defined by using the energy deposition in TOF+ wall. In the second step the type of the particle from the momentum for $Z = 2$ particles and momentum and Time-of-flight for $Z = 1$ particles is defined. The charge identification is based on the calibrated energy deposit (Fig. 5.7):

- for $Z = 1$: $6 < dE < 15$ channels,
- for $Z = 2$: $40 < dE < 90$ channels,
- for $Z = 3$: $110 < dE < 150$ channels.

The momentum distribution of the $Z = 2$ particles is shown in Figure 5.9. The particle with the momentum-over-charge ratio $p/Z \in [3.4; 4.5]$ GeV/c is identified as ^{3}He; $p/Z \in [4.5; 6.0]$ GeV/c corresponds to the ^{4}He.

Figure 5.10 shows the correlation between the velocity factor β and the momentum of the particles. The velocity β is calculated for each particle having a certain momentum p as follow

$$\beta = \frac{p}{\sqrt{m^2 + p^2}} \tag{5.1}$$

From the correlation, protons and deuteron are clearly distinguished among a wide momentum region. The light particles, such as π^+ and K^+, are not clearly separated because of the limited acceptance for their low momentum. Additional conditions in momentum range are applied for the PID:

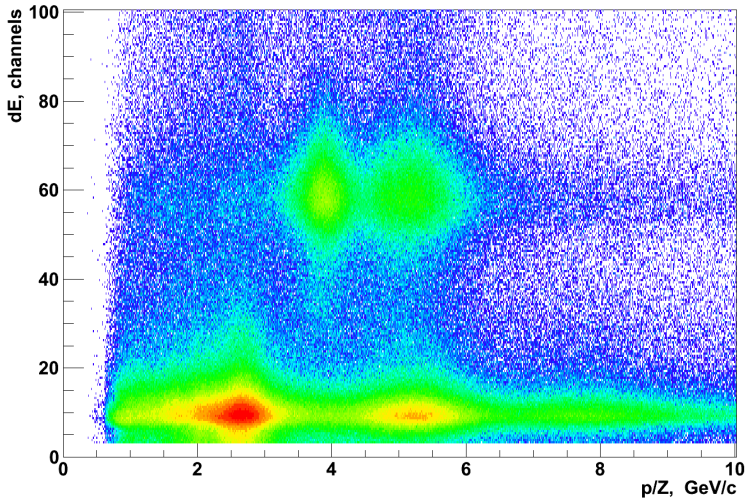

Figure 5.8: Correlation between the energy deposit of charged particles in the TOF+ wall and the momentum-to-charge ration p/Z

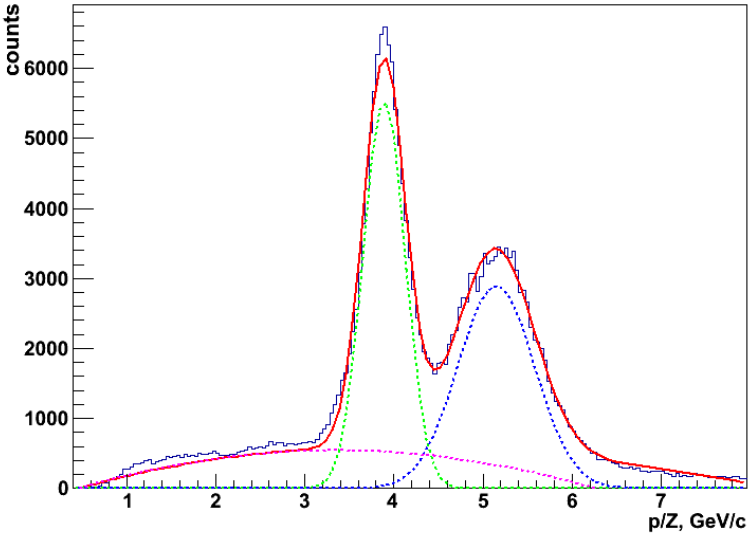

Figure 5.9: $Z = 2$ momentum distribution. The distribution is fitted by the sum of two Gaussians and polynomial of third order.

- $p \in [0.0; 4.5]$ GeV/c for proton,
- $p \in [4.5; 6.5]$ GeV/c for deuteron,
- $p \in [6.5; 9.5]$ GeV/c for triton.

The calculated mass is used only for the identification of the particle. If the particle identified as a proton, the known mass of the proton $m = 0.938$ GeV/c^2 is assumed for further analysis.

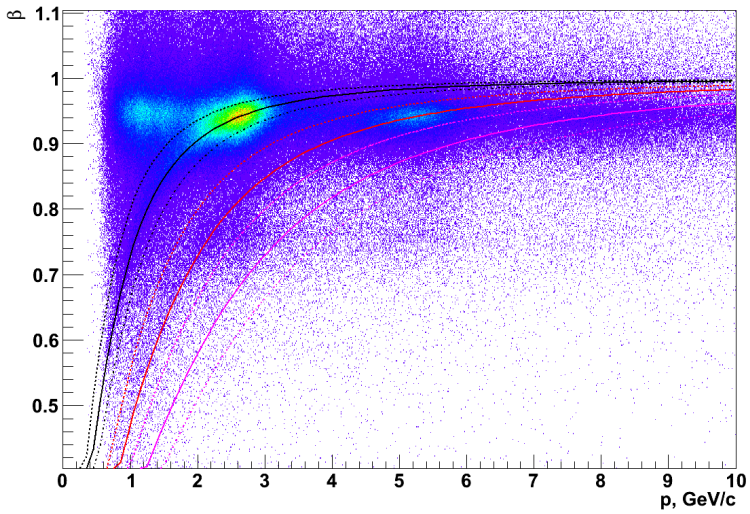

Figure 5.10: Correlation between velocity β and momentum p of the $Z = 1$ particles. Continuous lines show the theoretical expectation, the dashed lines indicate the PID cut ±20% from the known mass of the particle. Black lines corresponds to proton, red to deuteron, purple to triton.

For the identification of π^-, a correlation between the velocity β and the momentum shown in the Figure 5.11 is used. The theoretical line calculated from the Equation. 5.1 and the cut conditions are also shown. The cut conditions used in this analysis is ±50% from the known mass of π^-.

5.5 Simulation studies

A realistic simulation of the HypHI experimental setup is mandatory for defining an optimized set of selection criteria in order to extract meaningful signal events out of the experimental data. Furthermore, the physical interpretation of the results obtained by applying such selection criteria on the experimental data requires a precise estimation of the corresponding reconstruction efficiencies. These efficiencies can only be calculated using a full scale Monte Carlo simulation of the HypHI setup.

The full Monte Carlo simulation consists of two steps:

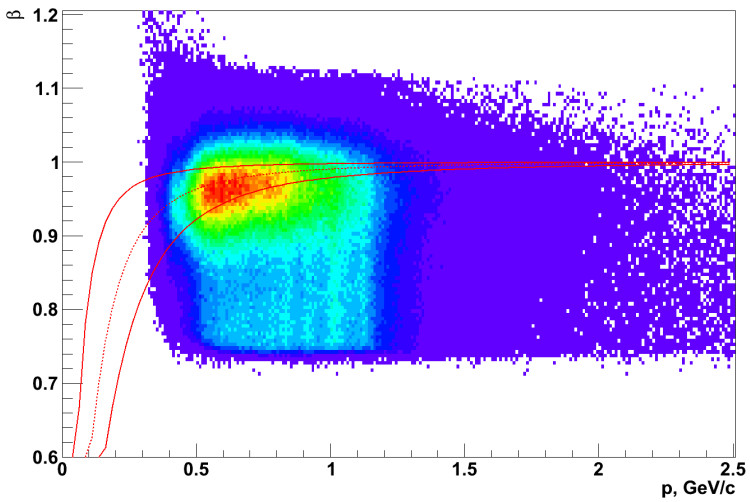

Figure 5.11: Correlation between velocity β and momentum p of the negatively charged particles. Dashed line shows the theoretical expectation, continuous lines indicate the PID cut conditions for π^-.

- **particles generation**: the particles are created with the UrQMD event generator which modelizes the ^{6}Li @ ^{12}C heavy ion collision as straight lines, satisfying energy and momentum conservation.
- **particles transport**: subsequently, the generated particle tracks are further propagated through simulated detector material taking into account the deflection in the ALADiN magnetic field.

Particle Generation with UrQMD

UrQMD, the Ultrarelativistic Quantum Molecular Dynamics model [20], is a non equilibrium hadronic transport approach using Monte Carlo simulation techniques in order to describe consistently heavy ion collisions from the beginning of the reaction (initialization of projectile and target nuclei) until the end of the reaction (final state of the system). The approach simulates multiples interactions of ingoing and newly produced particles and constitutes an effective solution of the relativistic Boltzmann equation and is restricted to binary collision of the propagated hadrons. The underlying degrees of freedom are strings and hadrons that are excited in high energetic binary collisions ($2 \rightarrow n$ processes). Projectiles and target nuclei are initialized according to a Woods-Saxon profile in coordinate space. Fermi momenta for each nucleon are randomly assigned in the rest frame of the projectile and target nucleus, respectively. The initial nucleons and, later on, newly produced hadrons are propagated on straight lines until the collision criterion is fulfilled:

$$d_{trans} \leq d_0 \;=\; \sqrt{\frac{\sigma_{tot}}{\pi}}, \qquad \sigma_{tot} = \sigma(\sqrt{s}, type) \tag{5.2}$$

If the covariant relative distance d_0 between two particles is smaller than a critical distance determined by the corresponding total cross section, a collision of those particle occurs. In UrQMD the elementary cross section are fitted according to available data or parametrized using the quark model.

Particle production is described by excitation and fragmentation of classical color strings with quarks (antiquarks) or diquarks (antidiquarks) at their ends and by excitation and decay of hadronic resonances. Color string excitation and fragmentation are treated using the Lund phenomenological model of hadronization [61]. After particles production, this microscopic transport approach generates the full space-time dynamics of string and hadrons.

Within UrQMD all hadrons and resonances up to 2.2 GeV are considered which led to a successful description of different observables in a broad range of collision systems and energies [62]. Consequently, the UrQMD event generator is assumed to provide a realistic description of the background medium in ^{6}Li $+^{12}$C collisions at 2 A GeV.

The production of hypernuclei assumes the absorption of hyperons in the spectator fragments of non central heavy ion collision. In this approach, a hyper-system is formed considering hyperons which propagates with velocities close to the initial velocities of the nuclei which means in the vicinity of the nuclear spectators [63]. Such hyper-systems will decay into hyperfragments later on [64]. The computed kinematics of such clusterized hyperfragments will then be used as input to the GEANT program which, assuming that the hyperfragments are known to the program, can modelize their decay into 2 or 3 outgoing particles according to Lorentz invariant Fermi phase space [65]. The definition of the particles in GEANT are summarized in Table 5.1.

Table 5.1: Definition of hypernuclei particles used in Monte Carlo simulation and their corresponding decay mode [24]

Hypernucleus	Decays	mass $[GeV]$	$\tau\,[ns]$	$\sigma\,[\mu b]$
${}^{3}_{\Lambda}$H	$\pi^{-}+{}^{3}$He	2.99114	0.246	0.1
${}^{4}_{\Lambda}$H	$\pi^{-}+{}^{4}$He	3.9225	0.1946	0.1
${}^{5}_{\Lambda}$He	$\pi^{-}+p+{}^{4}$He	4.8399	0.256	0.5

Particle Transport through material

The particle transport through the HypHI experimental setup is done with the GEANT program, which additionally simulates the energy loss and the multiple scattering of the particles in the detectors. The detector response to the simulated hit points is modeled using a Gaussian smearing which takes into account realistic resolution of the detectors summarized in Table 5.2. The smeared Monte Carlo hits also called digits are then taken as input to the full reconstruction chain (Figure 5.12). This ensures that the same reconstruction algorithms are used for both simulation and real data which is mandatory for the precise estimation of the

reconstruction efficiencies.

Table 5.2: Detector resolution used in the Monte Carlo simulation.

Detector	Fibers	SDH	TOF+	TFW
σ_x	460. μm	4.5 mm	1.5 cm	10. cm
σ_y	460. μm	4.5 mm	3.5 cm	10. cm

The Figure 5.13 shows the display of a GEANT simulated event which is composed of background particles coming from a UrQMD simulated ^{6}Li + ^{12}C collisions at 2 A GeV and an embedded $^{3}_{\Lambda}$H $\rightarrow \pi^{-}+^{3}$He decay signal. Similar embedding of signal overlayed with a UrQMD simulated background has been produced for all hypernuclei decay studied in this thesis.

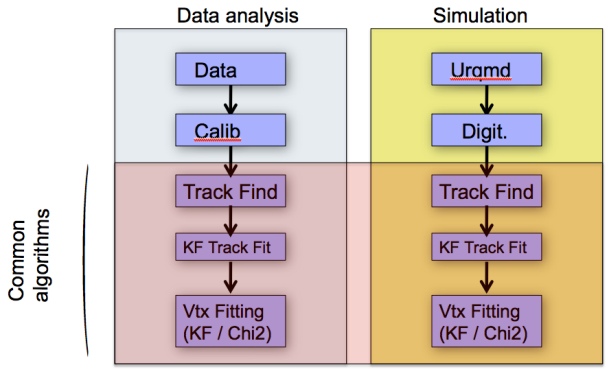

Figure 5.12: The full scale simulation chain compared to the reconstruction chain.

5.5.1 Signal selection

According to the UrQMD generator, a ^{6}Li+^{12}C collision at 2 A GeV produces about 20 primary tracks (Fig. 5.14). According to the GEANT transport code, these primary tracks produce on average additionally 10 secondary tracks during the transport through the detectors material. If one tries to calculate the invariant masses of all two-tracks pairs, one would produce about a thousand candidates per event and the vast majority of them would be fake i.e the invariant mass distribution would be swamped with background. For the invariant mass analysis one must reduce the number of combinations in a consistent way.

Assuming the particle identification procedure described previously, this section focuses on the improvement of the signal quality and the reduction of the background by applying dedicated selection criteria for the following exclusive reactions:

- $\Lambda \rightarrow p + \pi^{-}$

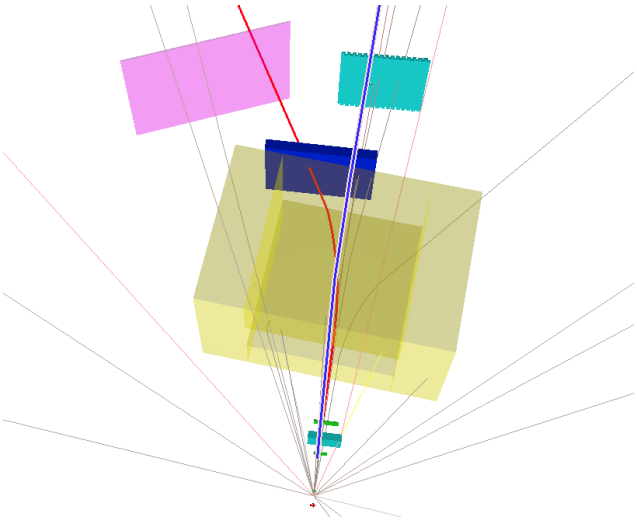

Figure 5.13: GEANT simulated event of ${}^{3}_{\Lambda}$H production and subsequent decay into π^{-}+^{3}He. It consists of background particles coming from a UrQMD simulated ^{6}Li+^{12}C collisions at 2 GeV/A and an embedded ${}^{3}_{\Lambda}$H $\rightarrow$ π^{-}+^{3}He decay signal. The red and the blue trajectories correspond respectively to the pion and the ^{3}He particles emitted by the ${}^{3}_{\Lambda}$H hypernucleus. Since the hypernucleus definition has been implemented, the GEANT Monte Carlo can calculate itself the kinematics of produced particles using a Lorentz invariant Fermi phase space algorithm.

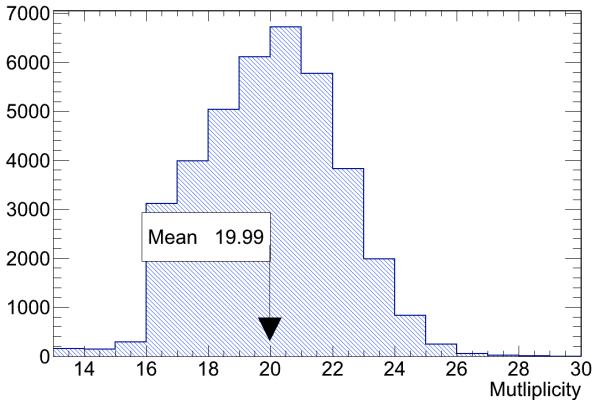

Figure 5.14: Primary tracks multiplicity produced with ^{6}Li+^{12}C collisions at 2 A GeV using the UrQMD generator.

- ${}^{3}_{\Lambda}\mathrm{H} \rightarrow \pi^{-} + {}^{3}\mathrm{He}$
- ${}^{4}_{\Lambda}\mathrm{H} \rightarrow \pi^{-} + {}^{4}\mathrm{He}$
- ${}^{5}_{\Lambda}\mathrm{He} \rightarrow \pi^{-} + p + {}^{4}\mathrm{He}$

Once a set of optimized selection criteria is defined, the full scale simulation is used to obtain the corresponding reconstruction efficiencies.

Geometrical acceptance

The geometrical acceptance is defined as the probability that all outgoing particles of a decay cross the Fibers detectors (TR1 and TR2) the drift chamber situated after the magnetic field and one of the TOF wall[2] leaving at least one hit in each detectors. The geometrical acceptance efficiencies for the Λ, ${}^{3}_{\Lambda}\mathrm{H}$, ${}^{4}_{\Lambda}\mathrm{H}$ and ${}^{5}_{\Lambda}\mathrm{He}$ are summarized in Table 5.3.

Table 5.3: Geometrical acceptance efficiency for Λ and hypernuclei decays.

Decay	$\varepsilon_{acceptance}$ [%]
$\Lambda \rightarrow p + \pi^{-}$	0.17
${}^{3}_{\Lambda}\mathrm{H} \rightarrow \pi^{-} + {}^{3}\mathrm{He}$	10.0
${}^{4}_{\Lambda}\mathrm{H} \rightarrow \pi^{-} + {}^{4}\mathrm{He}$	6.85
${}^{5}_{\Lambda}\mathrm{He} \rightarrow \pi^{-} + p + {}^{4}\mathrm{He}$	6.64

Signal preselection

In order to keep the calculation numerically tractable, one has to reject at early stage of the analysis a maximum of fake vertices. This is done by applying a set of loose selection criteria which perform a first discrimination between signal and background independently of a specific decay. Assuming the single-track particle identification procedure described previously, the set of pre-selection criteria is summarized in Table 5.4.

The Figure 5.15 shows the reconstructed invariant mass obtained after applying the pre-selection criteria for the Λ and hypernuclei decays. On the reconstructed invariant mass spectra, the signal (in red) and the background (in blue) have been overlayed. As expected, the background shape for the reconstructed Λ decay corresponds to a decreasing exponential. For the hypernuclei decay however, the background shape is more complicated and a noticeable part of background events seems to accumulate under the signal mass region.

[2] TOF+ for positively charged particles and TFW for negatively charged particles

Table 5.4: Definition of the pre-selection criteria applied to Λ and hypernuclei decay. The quantities p_i and $P^i_{\chi^2}$ denotes the single track momentum range and probability of χ^2 respectively whilst $P^{vtx}_{\chi^2}$ denotes the reconstructed vertex probability of χ^2 . The quantity DCA corresponds to the *distance of closest approach* in cm described in the Chapter 4.

Cut on	Units	Lower bound	Upper bound
$P^{\pi}_{\chi^2}$	val.	0.001	1.
$P^{+}_{\chi^2}$	val.	0.001	1.
p_{π}	[GeV]	0.5	2.
p_p	[GeV]	0.	4.5
$p_{^3H_e}$	[GeV]	6.	9.
$p_{^4H_e}$	[GeV]	9.	12.
$P^{vtx}_{\chi^2}$	val.	10^{-4}	1.
DCA	[cm]	0.	1.

$\Lambda \to p\pi^-$ decay selection

Before digging into the complicated analysis of hypernuclei reaction, one needs to prove that the whole reconstruction chain is able to measure the invariant mass of a well-known particle without any bias. For this purpose, the exclusive analysis of the $\Lambda \to p\pi^-$ is of particular importance. Since in the experimental data this reaction is not trigger favored, the definition of efficient selection criteria is mandatory in order to extract the Λ signal with the best possible signal over background ratio.

For sake of clarity, only the least square based vertex fit results will be presented in this section. The corresponding results using the Kalman based algorithm for vertex fitting is presented in Appendix C.

A *simple* geometrical selection of the Λ candidates is first applied by considering the reconstructed *distance of closest approach* introduced in the vertex reconstruction Chapter 4. The Figure 5.16 represents the *distance of closest approach* (DCA) distribution for both signal and background events.

Another natural criteria is to apply a selection based on the quality of the vertex fitting. This is done by applying a lower bound to the vertex probability of $\chi 2$. Fig. 5.17 shows the probability of $\chi 2$ for both signal and background events.

Same as Λ hypernuclei, the free Λ hyperon is mostly produced via strong interactions i.e in the reaction processes

$$\pi^+ n \to \Lambda K^+, K^- n \to \pi^- \Lambda,\ K^- p \to \pi^0 \Lambda \tag{5.3}$$

using pion and kaon beams. And also the same way, both Λ hypernuclei and the free Λ hyperon basically decay through the weak interactions. The free Λ hyperon decays nearly 100% of the time via the $\Lambda \to N\pi$ weak mesonic mode:

$$\Lambda \to \begin{cases} p + \pi^-(64.1\%) \\ n + \pi^0(35.7\%) \end{cases} \tag{5.4}$$

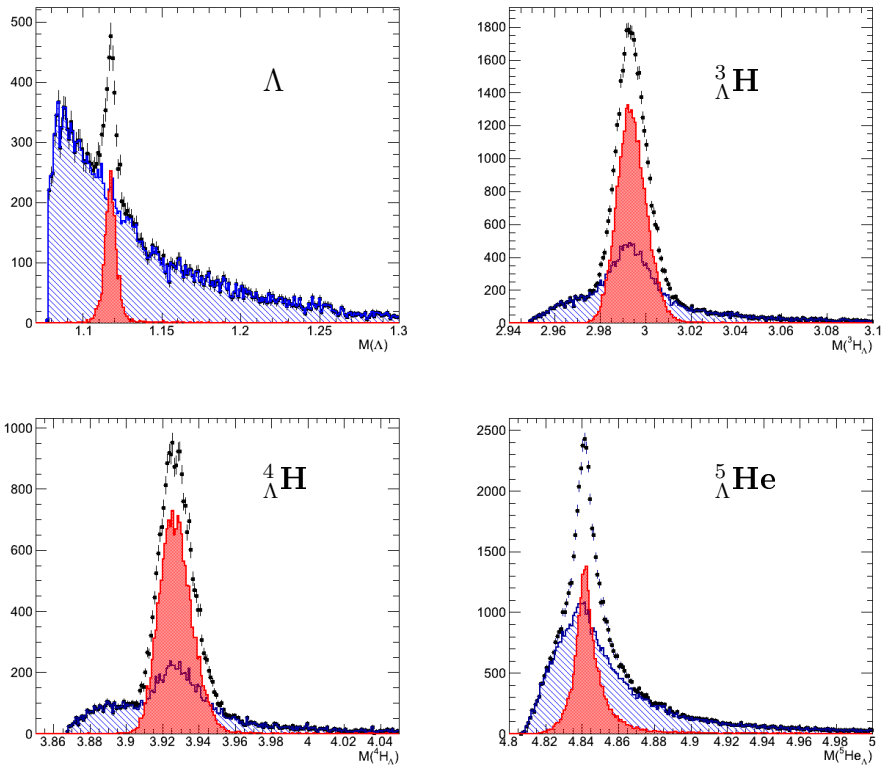

Figure 5.15: Reconstructed invariant mass obtained after applying the pre-selection criteria for the Λ and hypernuclei decays. The blue and the red filled area correspond to the background and the signal respectively. The overall reconstructed invariant mass spectrum is represented using black dots.

with the lifetime $\tau^0 \sim 263\ ps$ [4]. In the full scale simulation both decay modes are activated according to the branching ratios defined previously.

As a consequence of the relatively large lifetime ($c\tau \sim 7.89\ cm$), the Λ decay far outside the target region. This displacement in the Z coordinate of Λ decay vertex relative to the target position is used to efficiently discriminate between fake Λ vertices using primary tracks combination and real vertices. Furthermore, the longitudinal position of the Λ vertex should not be too close from the first fiber tracking detector plane $Z_{TR1} = 41.5$ cm: the closer the Λ vertex is to the TR1 plane the closer the hits will be measured in the detector. From a pure geometrical point of view is is difficult for such close tracks in space to estimate the longitudinal position of the vertex, and the vertex fitting procedure will have difficulty to converge. The Figure 5.18 shows the Λ vertex longitudinal position distribution for both signal and background. It is clear from the picture that reconstructed vertices situated too close to the target and the first plane of fiber detector are mainly fake vertices and should then be excluded in the analysis. The Figure 5.18 shows additionally

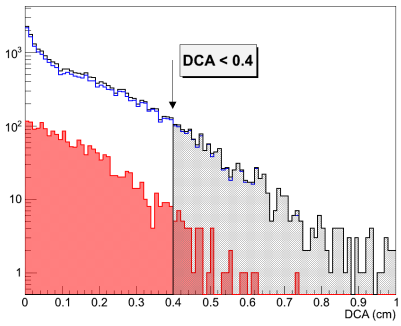

Figure 5.16: The DCA distribution in cm for both signal (red) and background (blue) Λ candidates.

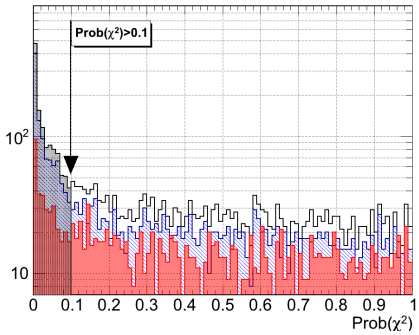

Figure 5.17: Probability of $\chi 2$ for both signal (red) and background (blue) Λ candidates.

the calculated Λ invariant mass as a function of the vertex longitudinal position: the vertices reconstructed near the target populates the low mass region of the invariant mass spectrum while those reconstructed too close to the fiber detector populate both low and high mass region of the invariant mass spectrum.

The Podolanski-Armenteros variables are commonly used as criteria to select $\Lambda \to p + \pi^-$ candidates [66]. The momenta of the daughter particles, p_1 and p_2, can be decomposed to components parallel and perpendicular to the momentum of the mother particle, $\vec{p} = \vec{p_1} + \vec{p_2}$. The longitudinal components can be obtained by

$$p_{1L} = \vec{p} \cdot \vec{p_1} / |\vec{p}|\,, \qquad p_{2L} = \vec{p} \cdot \vec{p_2} / |\vec{p}| \tag{5.5}$$

Then the Armenteros variables i.e the transverse momentum p_T and the longitudinal asymmetry α are defined by :

$$p_t = |\vec{p_1} \times \vec{p_2}| \,/\, |\vec{p}| \tag{5.6}$$

and

$$\alpha = (p_{1L} - p_{2L})/(p_{1L} + p_{2L}) = (\vec{p_1}^{\,2} - \vec{p_2}^{\,2})/\vec{p}^{\,2} \tag{5.7}$$

Using these variables the Λ particles are distinguishable, as shown in Figure 5.19 for simulated collision: the true Λ-hyperons form an typical arc placed the right of the (p_t, α) plane. Additionally a systematic bias in the reconstructed invariant mass distribution of the Λ candidates for low α value ($\alpha < 0.45$) can be noticed in Figure 5.20.

Thus, the Armenteros plots suggests that the background can be suppressed by cutting on the arcs in the Armenteros plane. Unfortunately, cutting on the Armenteros variables generally imply a *filter* on the invariant mass distribution of the Λ candidates. This *filter* leads to the distortion of the background shape in the invariant mass distribution. Such a *filter* makes the description of the background more complicated. Since in the analysis, the background needs to be fitted using a

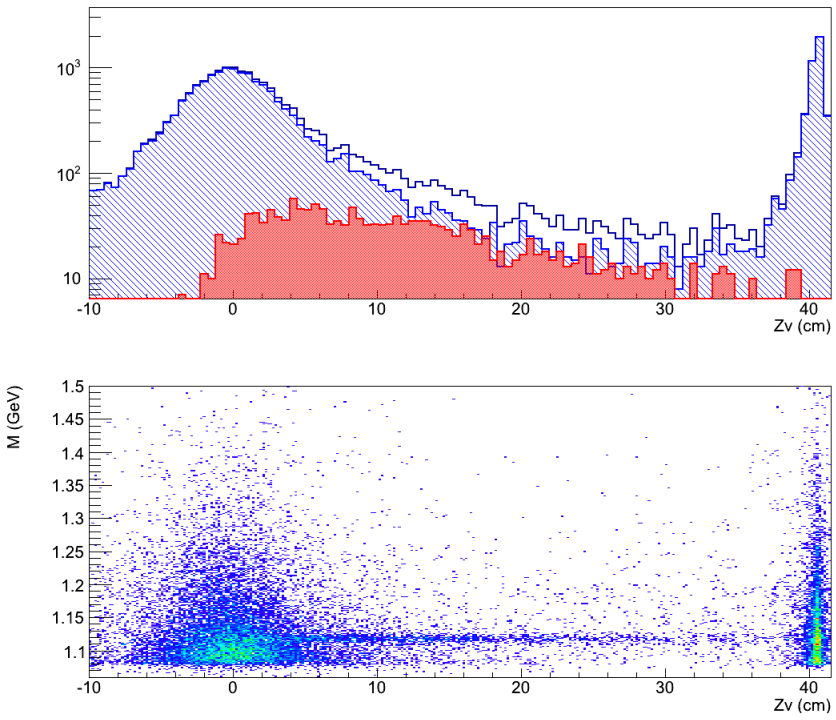

Figure 5.18: The histogram on the top represents the reconstructed Λ vertex longitudinal position. The blue area corresponds to the true Λ signal whilst the blue area correspond to the background. The second histogram represents the calculated Λ invariant mass as a function of the vertex longitudinal position. It is striking that fake reconstructed vertices situated too close to the target mainly populate the low mass tail while those too close to the fiber detector populate both low and high mass region of the invariant mass spectrum.

model function, it is preferable to have featureless, easily fittable background over more complex one, even if it comes at the price of increasing the overall background fraction. Taking this into account, only a loose selection based on the transverse momentum variable $p_t < 0.1$ has been applied for the data and the asymmetry cut $\alpha > 0.45$ has been applied on the simulated Λ candidates.

Two set of selection for the Λ reconstruction which correspond to loose and tight criteria have been studies with the realistic simulation. They are summarized in Table 5.5.

The left part of Figure 5.21 shows the Λ invariant mass distributions for both signal and background events for the pre-selection,loose and tight criteria. The right part of Figure 5.21 shows the fitted Λ invariant mass distribution for the pre-selection, loose and tight criteria respectively. The mass fit uses a unbinned likelihood fit performed using a gaussian model for the signal and Chebychev poly-

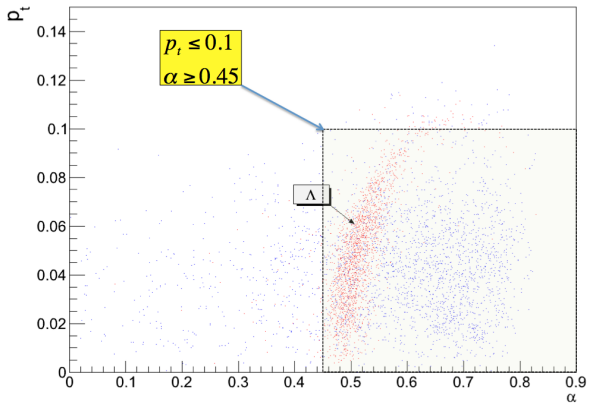

Figure 5.19: Armenteros variables (α, p_t) for the reconstructed Λ candidates. The true Λ decays (in red) populate the typical arc-segment in the Armenteros plane (α, p_t). Instead the fake decays (in blue) are distributed uniformly in the Armenteros plane.

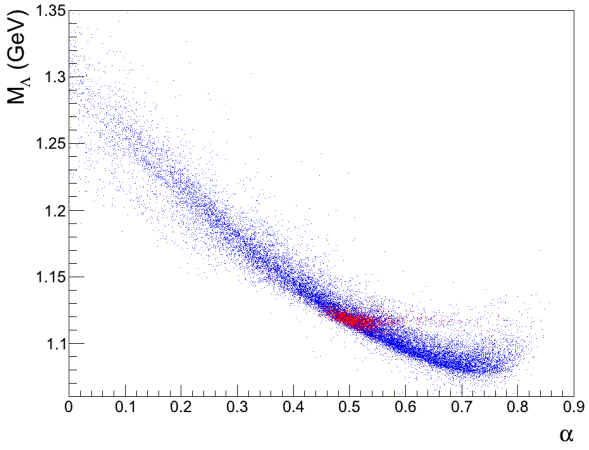

Figure 5.20: Invariant mass of the reconstructed Λ candidates as a function of the longitudinal momentum asymmetry α. Low α value Λ candidates ($\alpha < 0.45$) populate the high mass region of the invariant mass distribution. High α values ($\alpha > 0.6$) populate the low mass region of the invariant mass distribution.

Table 5.5: Definition of the selection criteria (loose and tight) for the Λ candidates. The variables are the same as for Table 5.4. Additionally the Armenteros variables are used.

Cut on	Units	Lower bound	Upper bound	Loose selection	Tight Selection
$P^{\pi}_{\chi^2}$	val.	0.1	1.	on	on
$P^{+}_{\chi^2}$	val.	0.1	1.	on	on
p_{π}	[GeV]	0.5	2.	on	on
p_p	[GeV]	0.	4.5	on	on
$P^{vtx}_{\chi^2}$	val.	0.01	1.	on	on
DCA	[cm]	0.	0.4	on	on
z_v	[cm]	0.	35.	on	on
p_t	[GeV]	0.	0.1	on	on
α	val.	0.45	1.	off	on

nomials of third order for the background.

Hypernuclei decay selection

This section focuses on the reconstruction of light Λ hypernuclei $^{3}_{\Lambda}$H, $^{4}_{\Lambda}$H and $^{5}_{\Lambda}$He.

The Λ hypernuclei are reconstructed via their corresponding mesonic weak decay modes. The branching ration for this decay channels are summarized in the Table 5.6.

Table 5.6: Branching ration of mesonic weak decay modes for the light hypernuclei.

Reaction	Branching ratio [%]
$^{3}_{\Lambda}\mathrm{H} \rightarrow \pi^{-} + {}^{3}\mathrm{He}$	25 [67, 68]
$^{4}_{\Lambda}\mathrm{H} \rightarrow \pi^{-} + {}^{4}\mathrm{He}$	50 [69]
$^{5}_{\Lambda}\mathrm{He} \rightarrow \pi^{-} + p + {}^{4}\mathrm{He}$	43 [70]

The mesonic weak decay modes of hypernuclei of interest systematically lead to a ^{3}He or ^{4}He particle in the final state. Since the tracking resolution for these particles is worse than for protons due to a lower bending in the magnetic field, the final hypernuclei invariant mass resolution is expected to be worse than for the Λ.

The Λ hypernuclei lifetimes of $\sim 2 \cdot 10^{-10}$ sec ($c\tau \sim 6\ cm$) imply, as for the Λ decay, that they decay far outside the target region. Thus, a first selection on the longitudinal position of their reconstructed vertex helps to reduce fake pairs combinations. Same as for the Λ, the hypernuclei should not decay in the vicinity of the first fiber detector plane.

As for the Λ reconstruction, two set of selection for the hypernuclei reconstruc-

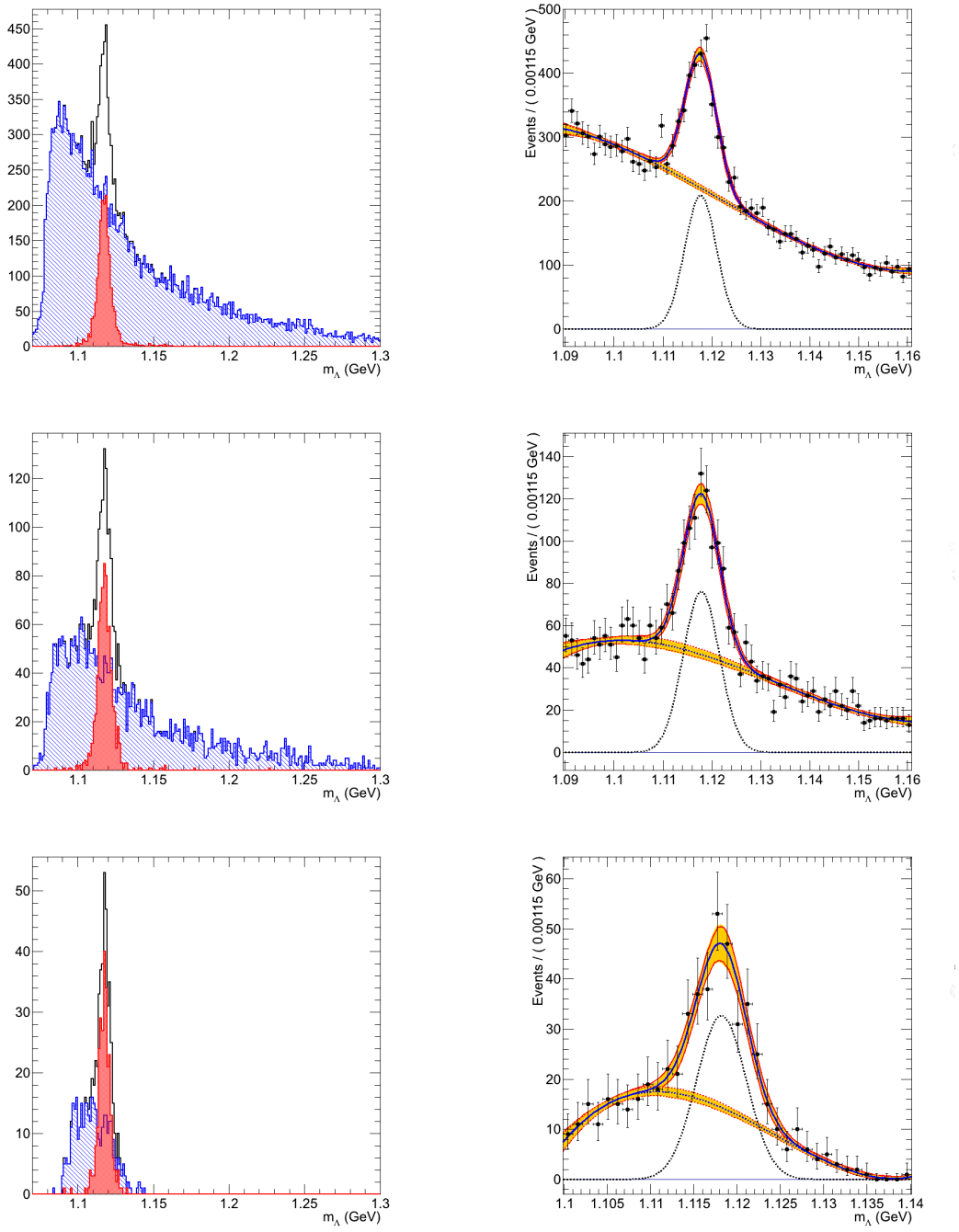

Figure 5.21: Λ invariant mass distribution for both signal (red) and background (blue) events presented in left column. Unbinned likelihood fit performed on Λ invariant mass distribution shown in right column. The blue line represent the most probable solution, the red lines and yellow area show the 1σ uncertainty band, the dotted black line corresponds to a pure signal.The invariant mass distributions are reconstructed using the pre-selection criteria only - first line, the loose criteria - second line, tight criteria - third line.

tion which correspond to loose and tight criteria (Table 5.7) have been studies with the realistic simulation.

Table 5.7: Definition of the selection criteria for the hypernuclei candidates. The variables are the same as for table 5.4.

Cut on	units	Lower bound	Upper bound
$P^{\pi}_{\chi^2}$	val.	0.1	1.
$P^{+}_{\chi^2}$	val.	0.1	1.
p_{π}	[GeV]	0.5	2.
$p_{^3He}$	[GeV]	6.	9.
$p_{^4He}$	[GeV]	9.	12.
$P^{vtx}_{\chi^2}$	val	0.01	1.
DCA	[cm]	0.	0.4
z_v (loose selection)	[cm]	0.	35.
z_v (tight selection)	[cm]	0.	20.

The Figures 5.22, 5.23 and 5.24 are showing the invariant mass distribution for the ${}^{3}_{\Lambda}$H, ${}^{4}_{\Lambda}$H and ${}^{5}_{\Lambda}$He decay respectively. The left column of figures shows the invariant mass distributions for both signal and background events and the right column shows the corresponding fitted invariant mass distribution for the pre-selection (top), loose (middle) and tight criteria (bottom) respectively. The mass fit, as for the Λ case, uses an unbinned likelihood fit performed using a gaussian model for the signal and Chebychev polynomials of third order for the background. Unlike the Λ decay reconstruction, the reconstruction of hypernuclei produce a non negligible amount of background event accumulating under the signal mass region. This amount is even more pronounced in the case of the ${}^{5}_{\Lambda}$He 3-body decay but can be reduced by applying the tight selection criteria.

The Table 5.8 summarize the performance of the Λ and hypernuclei decay reconstruction using the least square based vertex fit method for the different set of selection criteria. The corresponding performance for the Kalman based vertex fit is presented in Appendix C.

Background study

The major problem in reconstructing Λ or hypernuclei signal from their decay products is the combinatorial background produced by uncorrelated (p, π^-), $(^3\text{He}, \pi^-)$ or $(^4\text{He}, \pi^-)$ pairs. In order to subtract away this background, one should be able to reproduce it.

The experiment measures a certain number of positive tracks n_+ and negative track n_-. Considering all combinations of observed positive and negative tracks, on can distinguish two classes of unlike-sign pairs: the actual signal of correlated positive and negative particle S_{+-} and the combinatorial background pairs B_{+-}.

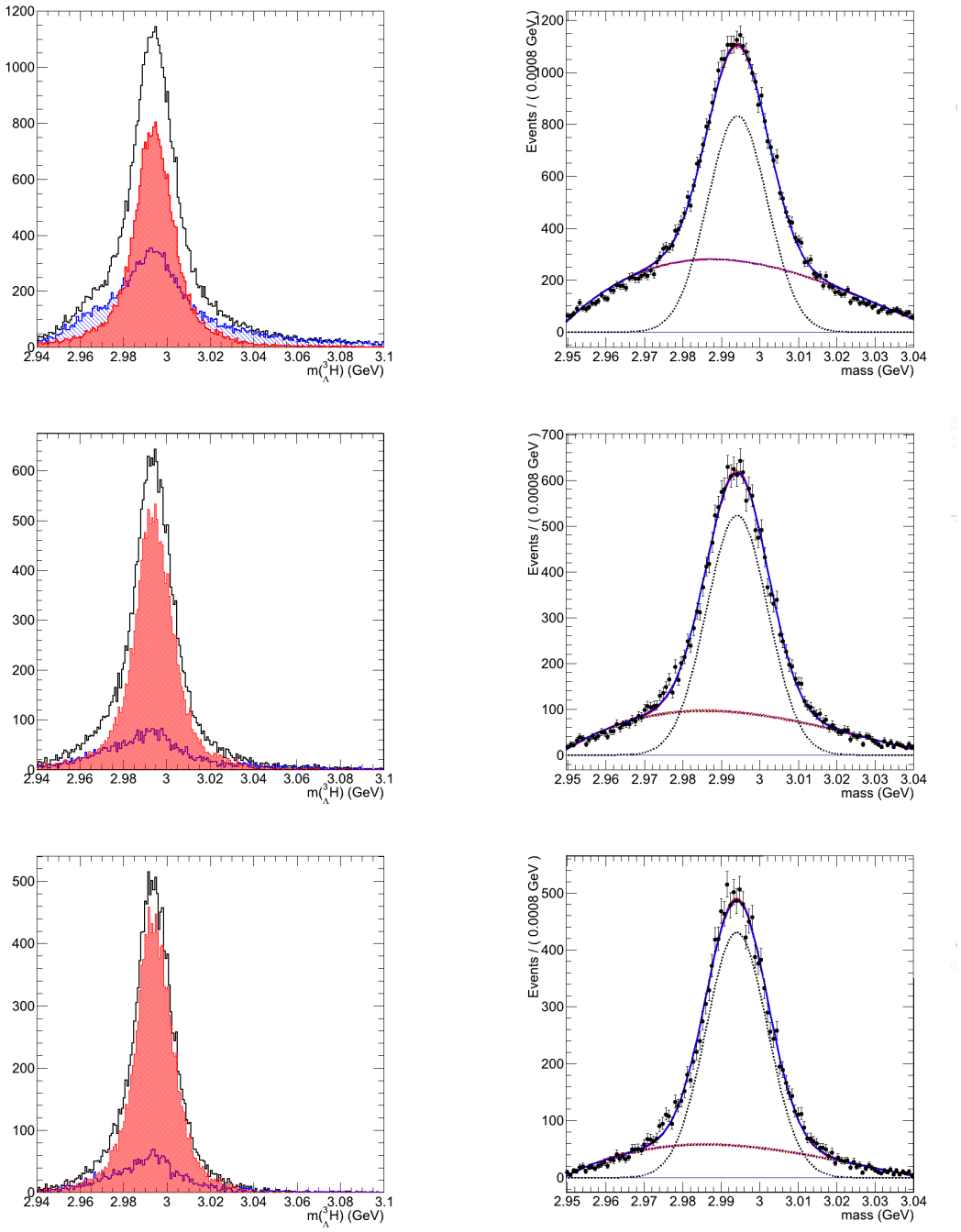

Figure 5.22: $^3_\Lambda$H invariant mass distribution for both signal (red) and background (blue) events presented in left column. Unbinned likelihood fit performed on $^3_\Lambda$H invariant mass distribution shown in right column. The blue line represent the most probable solution, the red lines and yellow area show the 1σ uncertainty band, the dotted black line corresponds to a pure signal.The invariant mass distributions are reconstructed using the pre-selection criteria only - first line, the loose criteria - second line, tight criteria - third line.

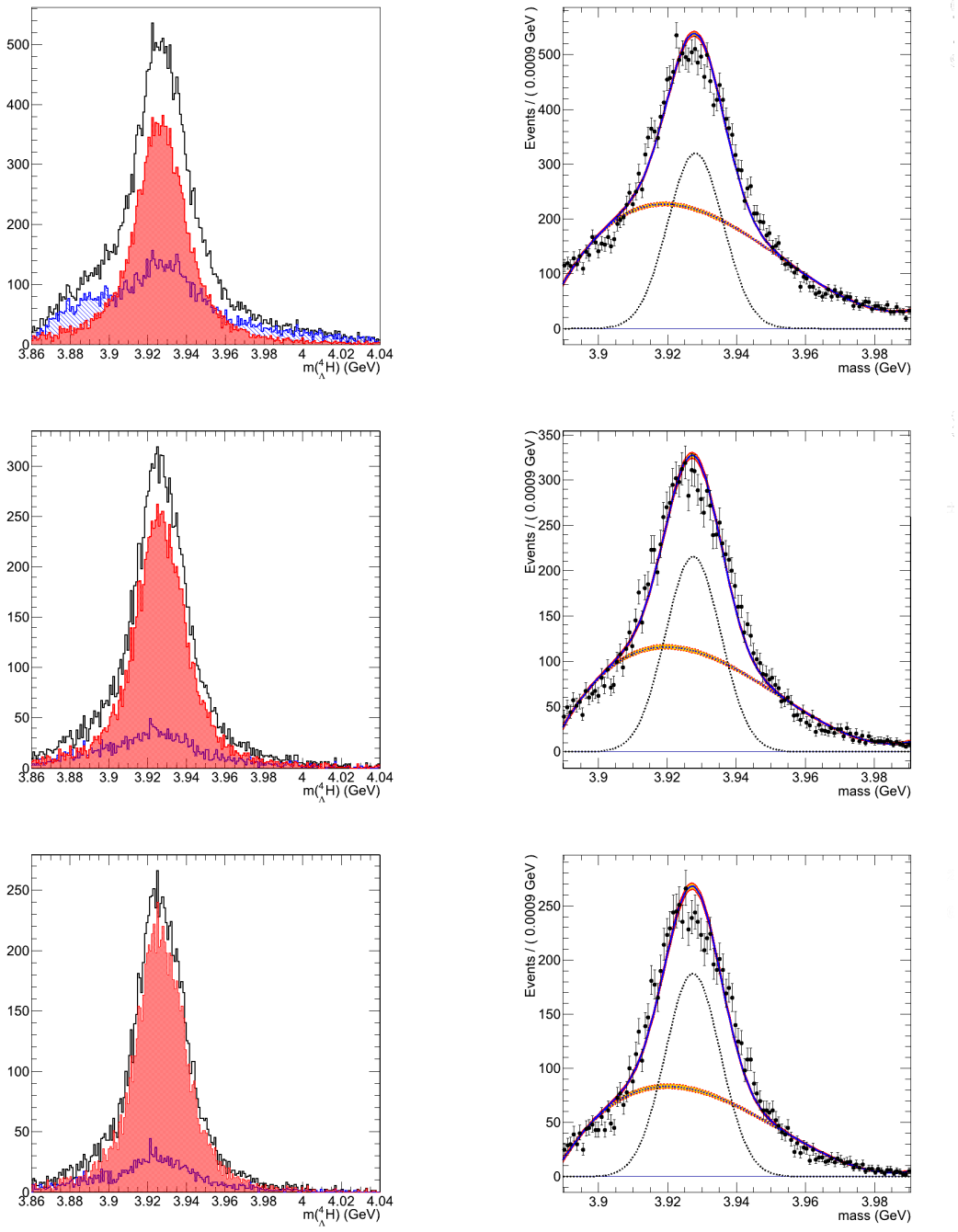

Figure 5.23: $^{4}_{\Lambda}$H invariant mass distribution for both signal (red) and background (blue) events presented in left column. Unbinned likelihood fit performed on $^{4}_{\Lambda}$H invariant mass distribution shown in right column. The blue line represent the most probable solution, the red lines and yellow area show the 1σ uncertainty band, the dotted black line corresponds to a pure signal.The invariant mass distributions are reconstructed using the pre-selection criteria only - first line, the loose criteria - second line, tight criteria - third line.

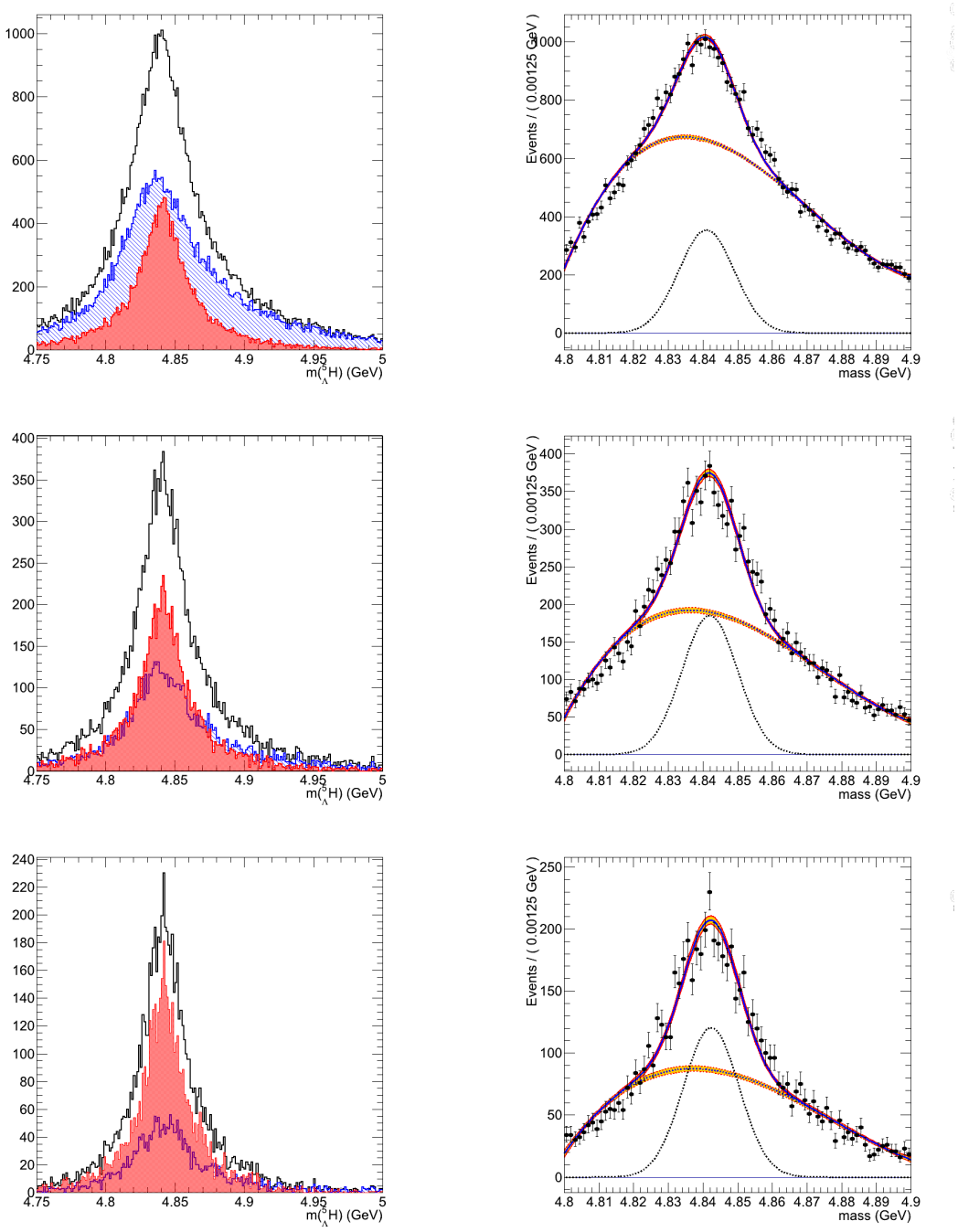

Figure 5.24: $^5_\Lambda$He invariant mass distribution for both signal (red) and background (blue) events presented in left column. Unbinned likelihood fit performed on $^5_\Lambda$He invariant mass distribution shown in right column. The blue line represent the most probable solution, the red lines and yellow area show the 1σ uncertainty band, the dotted black line corresponds to a pure signal.The invariant mass distributions are reconstructed using the pre-selection criteria only - first line, the loose criteria - second line, tight criteria - third line.

Table 5.8: Comparison of the performance obtained on the Λ and hypernuclei decay reconstruction for the different set of selection criteria. The quoted numbers have been obtained by using an unbinned likelihood mass fit.

Λ Selection	Mass [GeV/c^2]	σ [MeV/c^2]	S/B
pre-selection	1.117	3.2	0.62
loose	1.117	2.9	0.98
tight	1.117	2.8	1.42
$^{3}_{\Lambda}$H Selection			
pre-selection	2.994	8.1	1.81
loose	2.994	8.0	3.44
tight	2.994	8.0	4.87
$^{4}_{\Lambda}$H Selection			
pre-selection	3.928	8.0	0.90
loose	3.927	7.9	1.20
tight	3.927	7.9	1.46
$^{5}_{\Lambda}$He Selection			
pre-selection	4.84	8.0	0.32
loose	4.84	8.0	0.60
tight	4.84	8.0	0.86

The total observed unlike-sign pair distribution N_{+-} can be expressed as:

$$N_{+-} = S^{corr}_{+-} + B^{comb.}_{+-} \tag{5.8}$$

The combinatorial background can be estimated by the so called mixed-event technique. The basic idea of this technique is that unlike-sign pairs, obtained by combination of opposite charged tracks of different events, are inherently independent. Thus, the background shape is obtained by constructing the invariant mass spectrum of uncorrelated (p, π^-), $(^3\mathrm{He}, \pi^-)$ or $(^4\mathrm{He}, \pi^-)$ pairs that comes from different events. A special care is given in order to use the sub-sample of events of similar multiplicity and containing at least one pair of the particles of interest. Specifically,we combine the daughter particle of the other type from a number of subsequent similar events.

The Figures 5.25, 5.26, 5.27 and 5.28 represent a comparison between background shape obtained with the mixed-event technique and the simulation for the Λ , $^{3}_{\Lambda}$H, $^{4}_{\Lambda}$H and $^{5}_{\Lambda}$He reconstruction respectively. On the figures, the bottom histograms bin per bin ratio between the number of mixed-event background N^{mix}_{bkg} and the corresponding simulated one N^{sim}_{bkg} is also presented. There is an agreement between simulated background and mixed background for the Λ reconstruction. A linear fit in the bin per bin ratio histogram gives a mean value close to 1: 1.05 ± 0.05. Instead for hypernuclei reconstruction the background shape between simulated background and mixed events differs by a systematic factor 2 under the peak mass region. A

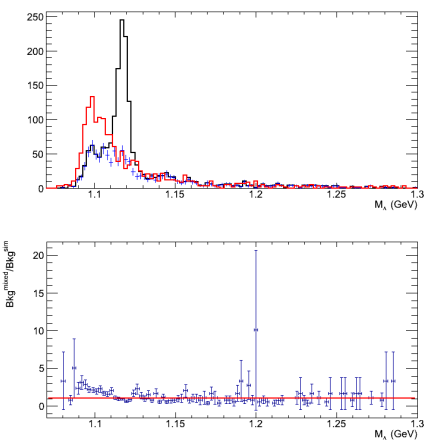

Figure 5.25: Comparison between background shape obtained with the mixed-event technique and the simulation for the Λ reconstruction.

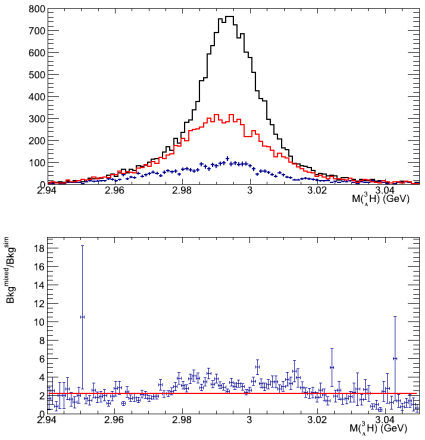

Figure 5.26: Comparison between background shape obtained with the mixed-event technique and the simulation for the ${}^{3}_{\Lambda}$H reconstruction.

linear fit in the bin per bin ratio histogram gives a mean value of 2.19±0.05, 2.7±0.07 and 2.01 ± 0.06 for the ${}^{3}_{\Lambda}$H, ${}^{4}_{\Lambda}$H and ${}^{5}_{\Lambda}$He decay respectively.

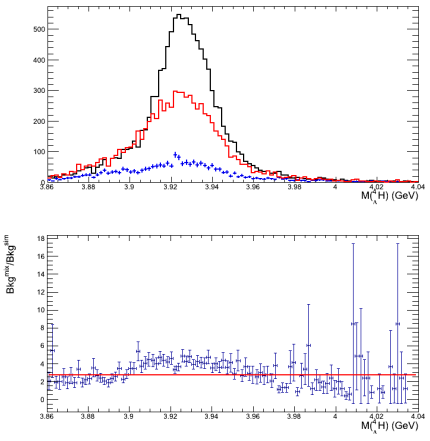

Figure 5.27: Comparison between background shape obtained with the mixed-event technique and the simulation for the ${}^{4}_{\Lambda}$H reconstruction.

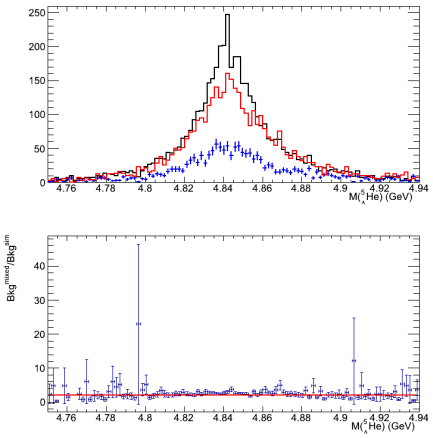

Figure 5.28: Comparison between background shape obtained with the mixed-event technique and the simulation for the ${}^{5}_{\Lambda}$He reconstruction.

5.6 Invariant mass reconstruction

The selection criteria applied for the real data, shown in the Table 5.9, are based on the Monte Carlo simulation previously presented and optimized in order to obtain for each reconstructed decay the best statistical signal significance possible.

Table 5.9: Selection criteria for the Λ and hypernuclei candidates.

Cut on	Units	Lower bound	Upper bound
$P^{\pi}_{\chi^2}$	val.	0.1	1.
$P^{+}_{\chi^2}$	val.	0.1	1.
p_{π}	[GeV]	0.5	1.5
p_{p}	[GeV]	0.	4.5
$p_{^3He}$	[GeV]	6.	9.
$p_{^4He}$	[GeV]	9.	12
$P^{vtx}_{\chi^2}$	val.	0.1	1.
DCA	[cm]	0.	0.4
z_v incl.target	[cm]	-10.	35.
z_v excl.target	[cm]	2.	35.
p_t	val	0.	0.1

The red hatched histograms in Figure 5.29 shows the invariant mass distribution for the p + π^-, ^{3}He + π^- and ^{4}He + π^- respectively. The blue hatched histogram are the distributions obtained from mixed event analysis. The scaling factors for the mixed events distributions are determined by the ratio of the areas defined in the Table 5.10. The right panels of Figure 5.31 shows the fitted invariant mass distributions, the fitting procedure was described previously in the signal selection session, background is describes by the Chebyshev polynomial of second order. The results are summarized in the Table 5.11.

Table 5.10: Mass ranges [GeV/c^2] used for the scaling of the mixed events.

Particle	Lower bound	Upper bound
Λ	1.15	1.3
$^{3}_{\Lambda}$H	3.0	3.1
$^{4}_{\Lambda}$H	3.92	4.0

The Figure 5.30 shows the longitudinal distribution of the reconstructed vertex in the case of unlike sign pairs in the same event and in the case of mixed events. One can notice that in the case of reconstructed vertex from uncorrelated particles coming from different events the longitudinal vertex position is uniformly distributed. It shows that the observed background comes from uncorrelated particles.

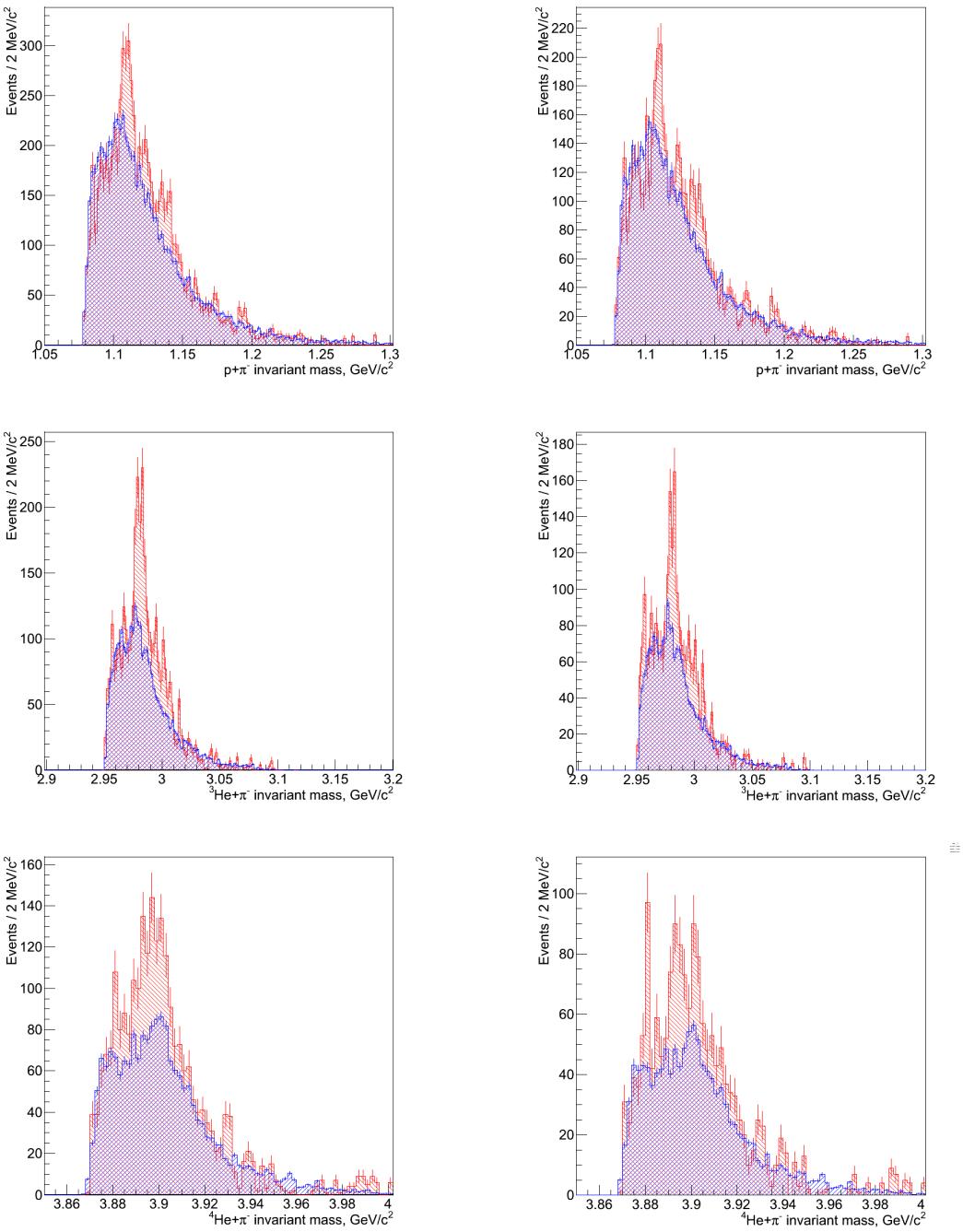

Figure 5.29: Invariant mass spectra of $p + \pi^-$ system - top row, ^{3}He$+\pi^-$ - middle row and ^{4}He$+\pi^-$ - bottom row. The distribution on the left side includes the target region for the reconstructed vertex position, on the one on right side target region is excluded

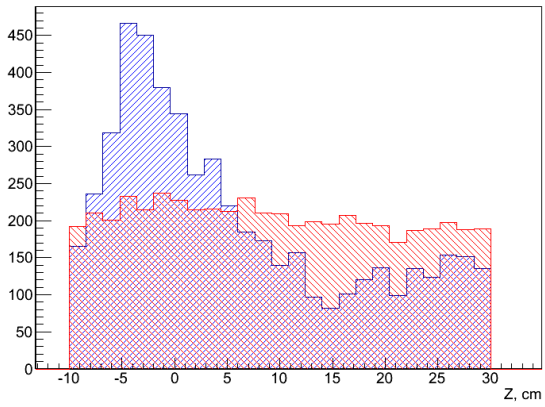

Figure 5.30: Secondary vertex position distribution for the signal (blue) and the mixed events (red). Scaling factor defined from the integral

The right panels of Figure 5.31 shows the rapidity distribution of the observed particles. It is found that rapidity of observed hypernuclei is localized in the region of $1.6 < y < 2.0$ which include the projectile rapidity (~ 1.81), while the Λ has a tail in the low rapidity region because they are produced in fireball and, as previously discussed in Chapter 1, have a wide rapidity distribution. It indicates that the formation of hypernuclei is dominated by the capture of a hyperon produced in the participant zone by the projectile fragments. Many theoretical model calculations predict that the dominant process of the formation of the hypernuclei is described by the coalescence scenario. Therefore, the observed kinematic is in agreement with theoretical models [19, 71, 72, 73].

Table 5.11: Result of the fitting of invariant mass distribution presented in Figure 5.31.

Particle	integral	mean value [MeV/c^2]	σ [MeV/c^2]	significance [σ]
Λ	417 ± 54	1109.6 ± 0.38	3.04 ± 0.41	9.8
${}^{3}_{\Lambda}$H	323 ± 36	2981.0 ± 0.30	3.16 ± 0.25	12.8
${}^{4}_{\Lambda}$H	170 ± 21	3898.1 ± 0.68	4.47 ± 0.66	7.3

5.7 Lifetime measurement

In order to measure the lifetime from the Λ, ${}^{3}_{\Lambda}$H and ${}^{4}_{\Lambda}$H candidates, one has to correct not only for the effects of the applied selection on the proper time distribution but also for background contamination. Yet, the background events passing the selections cuts can only be separated from the signal events in a statistical way. To

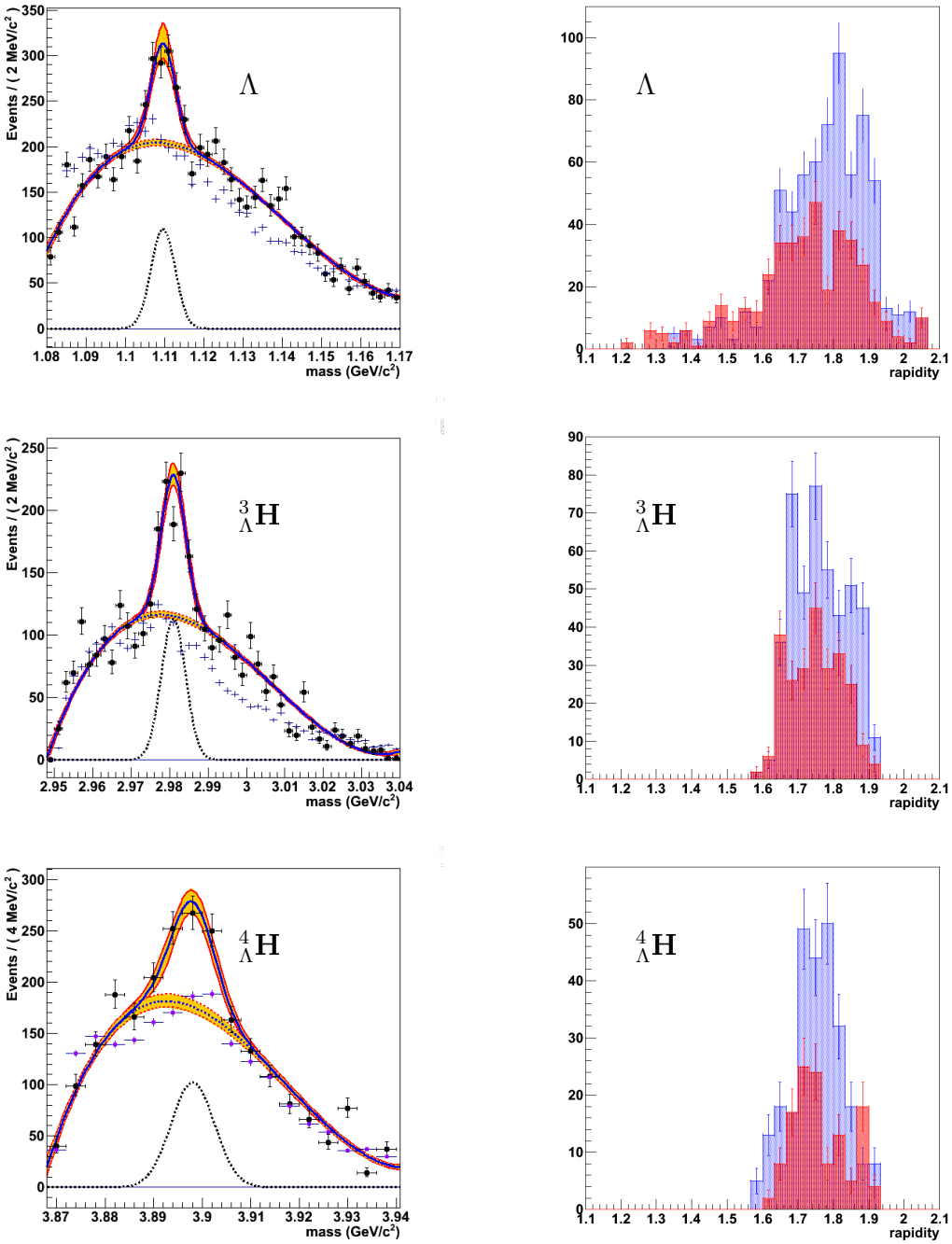

Figure 5.31: *Left panels*: fitted by the *signal+ background* distribution for Λ, ${}^{3}_{\Lambda}$H and ${}^{4}_{\Lambda}$H. The blue lines represent the most probable solution, the red lines and yellow area show the σ uncertainty band, the dotted black line corresponds to a pure signal. The light purple markers corresponds to the scaled mixed event invariant mass distributions. *Right panels*: Rapidity distribution for Λ, ${}^{3}_{\Lambda}$H and ${}^{4}_{\Lambda}$H. The distributions obtained from the signal region are in red, ones from the sideband are shown in blue.

this purpose, it is convenient to fit the data with a likelihood function which separate the signal and background observables in two different parts using probability density distributions:

$$\begin{aligned}\mathcal{L} &= \prod_{i=0}^{N_{obs}} (f_i \cdot \mathcal{M}_{sig}(m_i|\sigma_{m_i}, m) \cdot \mathcal{T}_{sig}(\tau_i|\sigma_{\tau_i}, \tau) \\ &+(1-f_i)\mathcal{M}_{bkg}(m_i|\sigma_{m_i}, m) \cdot \mathcal{T}_{bkg}(\tau_i|\sigma_{\tau_i}, \tau))\end{aligned} \tag{5.9}$$

where f_i is the fraction of signal event in the total number of observed events N_{obs}. $\mathcal{M}_{sig}$ and $\mathcal{M}_{bkg}$ are the probability density function modeling the signal and background mass distributions. The terms $\mathcal{T}_{sig}$ and $\mathcal{T}_{bkg}$ describe the decay time distribution of the signal and the background respectively. The input variables to the likelihood function extracted from the data are the proper decay time τ_i , its uncertainty σ_{τ_i} the mass m_i and its uncertainty σ_{m_i}.

Since both mass and proper decay time are included in the likelihood function, both parameter are fitted simultaneously. Furthermore, the likelihood function is calculated per event and do not assume an arbitrary binning which is an advantage when dealing with low data sample size.

The best choice for the set of parameter (m, τ) is the one which yields the maximum value of the likelihood function in Equation 5.9 or, in a numerically more convenient way, which minimizes the negative logarithm of the likelihood $-log(\mathcal{L})$.

In this section, an unbinned maximum likelihood fit to the reconstructed Λ, ${}^{3}_{\Lambda}$H and ${}^{4}_{\Lambda}$H mass and proper decay time is performed to extract the lifetime of the corresponding particles.

5.7.1 Proper time model

The probability density distribution to describe the proper time in absence of any kind of bias is written out as :

$$\begin{aligned}\mathcal{T}(\tau_i|\sigma_{\tau_i}, \tau_{sig,bkg}) &= E(\tau_i|\tau_{sig,bkg}) \otimes G(\tau_i|\sigma_{\tau_i}) \\ &= \int_0^{\infty} \frac{1}{\tau_i} \mathrm{e}^{-\frac{\tau'}{\tau_{sig,bkg}}} \cdot \frac{1}{\sqrt{2\pi}\sigma_{\tau_i}} \mathrm{e}^{-\frac{(\tau_i-\tau')^2}{2\sigma^2_{\tau_i}}} d\tau'\end{aligned} \tag{5.10}$$

where τ_i is the measured proper time of event i; σ_{τ_i} is the estimated proper decay time uncertainty of event i and τ is the extracting lifetime.

As selection cuts has been used to suppress the abundant background, the reconstructed proper decay time distribution may be distorted and consequently the lifetime fit could be bias. An acceptance correction function is required to describe such distortions. The acceptance function $\varepsilon(\tau)$ defined as the ratio between the measured proper decay time distribution and the true proper decay time distribution has been extracted from the Monte Carlo simulation. Figures 5.32, 5.33 and 5.34 shows the result of a polynomial fit to model the acceptance function for reconstructed Λ, ${}^{3}_{\Lambda}$H and ${}^{4}_{\Lambda}$H particles.

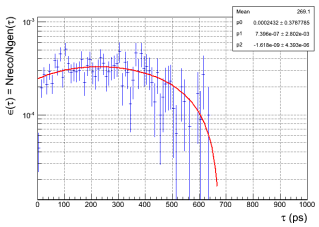

Figure 5.32: Acceptance function $\varepsilon(\tau)$ for the reconstructed Λ.

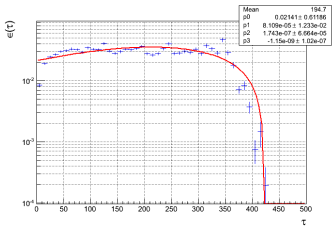

Figure 5.33: Acceptance function $\varepsilon(\tau)$ for the reconstructed ${}^{3}_{\Lambda}\mathrm{H}$.

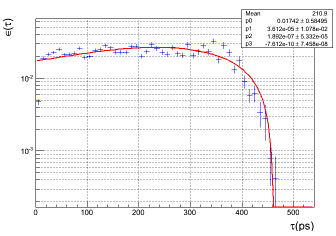

Figure 5.34: Acceptance function $\varepsilon(\tau)$ for the reconstructed ${}^{4}_{\Lambda}\mathrm{H}$.

Taking into account the selection bias the probability density function written by Equation 5.10 describing the signal proper time is finally written out as:

$$\mathcal{T}(\tau_i|\sigma_{\tau_i},\tau_{sig}) = E(\tau_i|\tau_{sig}) \otimes G(\tau_i|\sigma_{\tau_i}) \cdot \varepsilon(\tau_{sig}) \tag{5.11}$$

where the acceptance function $\varepsilon(\tau)$ depends on the reconstructed particle.

5.7.2 Mass model

The probability distribution function adopted for the description of the signal invariant mass distribution is described by a single Gaussian function:

$$f^m_{sig}(m_i|M,\sigma_m) = \frac{1}{\sqrt{2\pi}\sigma_m} \mathrm{e}^{-\frac{(m_i-M)^2}{2\sigma^2_m}} \tag{5.12}$$

where, m_i is the measured mass of the i-th event; M is the signal mass. The σ_m term corresponds to the overall mass resolution which was used for the mass part while the event by event resolution was used for the lifetime part.

A third order Chebyshev polynomial [74] is used to describe the invariant mass distribution of the background:

$$f^m_{bkg}(m|c_0,...,c_n) = \frac{1}{N} \cdot \left(T^0(m) + \sum_{k=0}^{n} c_k T^k(m) \right) \quad (n=2) \tag{5.13}$$

where $T^k(m)$ is the k^{th} order Chebyshev polynomial. Chebyshev polynomials are chosen over regular polynomials because of their superior stability in fits. Chebyshev and regular polynomials can describe the same shapes, but a clever reorganization of power terms in Chebyshev polynomials results in much lower correlations between the coefficients in a fit, and thus to a more stable fit behavior.

5.7.3 Fit results

The combined mass-lifetime unbinned likelihood fit was applied first on the Monte Carlo simulation. The Figure 5.35 shows the invariant mass and proper decay time

Table 5.12: The mass, signal yield and proper decay lifetime returned by the unbinned likelihood fit for the different reconstructed particles in their respective decay channel.

fitted values	M (GeV/c^2)	σ_M (MeV/c^2)	N_{sig}	τ (ps)
Λ	1.10927	1.97	152 ± 26	$269.37\ ^{+93.13}_{-62.57}$
$^{3}_{\Lambda}$H	2.98175	3.25	146 ± 20	$239.07\ ^{+61.19}_{-43.72}$
$^{4}_{\Lambda}$H	3.89248	1.83	46 ± 11	$209.39\ ^{+135.34}_{-64.72}$

distributions for the reconstructed Λ using the Monte Carlo simulation. The left column shows the fitted invariant mass distribution overlayed with the extracted signal (in red) and the background (in blue) together with the profile logarithm likelihood as a function of the fitted mass parameter. The right columns shows the fitted proper decay time distribution overlayed with the extracted signal (in red) and the background (in blue) together with the profile logarithm likelihood as a function of the fitted proper decay time parameter. The result obtained for the Λ proper decay lifetime $\tau_{\Lambda}^{fit} = 264 \pm 18$ ps is compatible with the Λ lifetime definition $\tau_{\Lambda}^{sim} = 263$ ps in GEANT.

Using the same presentation format, the figures 5.36, 5.37 and 5.38 shows the fitted invariant mass and proper decay time distributions for the selected Λ, $^{3}_{\Lambda}H$ and $^{4}_{\Lambda}H$ candidates using the combined mass-lifetime unbinned likelihood fit. In order to have favorable signal over background ratio a systematic cut on the secondary vertex of $z > -2.cm$ for the reconstructed Λ and $^{3}_{\Lambda}H$ and $z > 5.cm$ for the reconstructed $^{4}_{\Lambda}H$ was applied.

The mass and proper decay lifetime returned by the fit for the different reconstructed particles in their respective decay channel is summarized in Table 5.12.

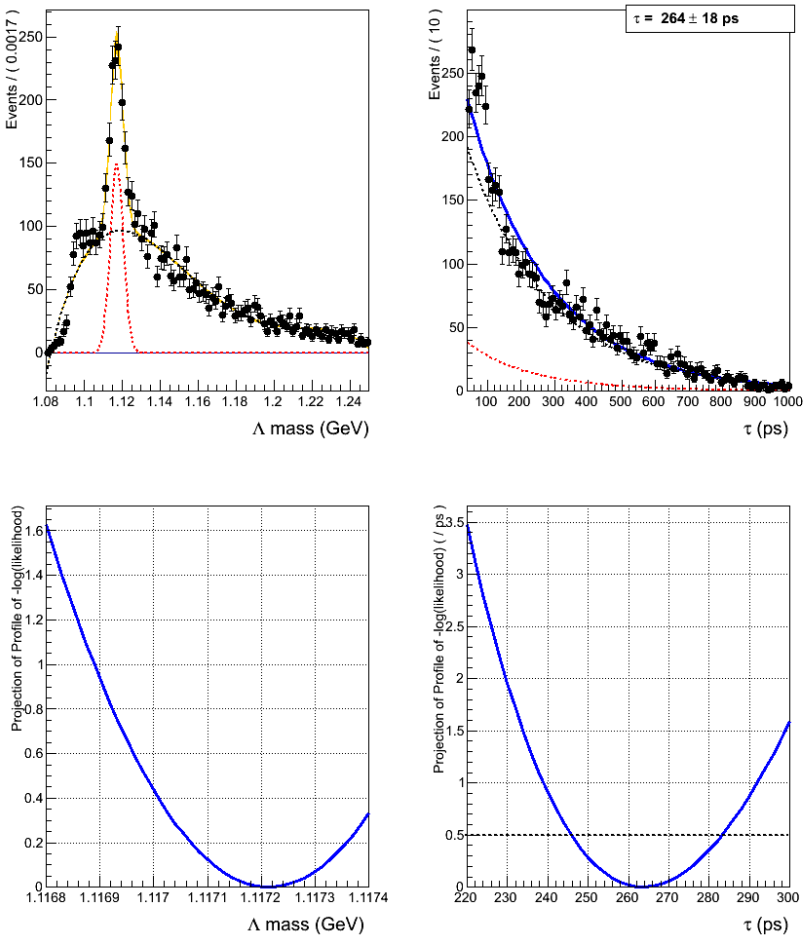

Figure 5.35: Invariant mass and proper decay time distributions for the reconstructed Λ using the Monte Carlo simulation. The left column shows the on top the fitted invariant mass distribution overlayed with the extracted signal (in red) and the background (in blue) and down the profile logarithm likelihood as a function of the fitted mass parameter. The right columns shows the fitted proper decay time distribution overlayed with the extracted signal (in red) and the background (in blue) together with the profile logarithm likelihood as a function of the fitted proper decay time parameter.

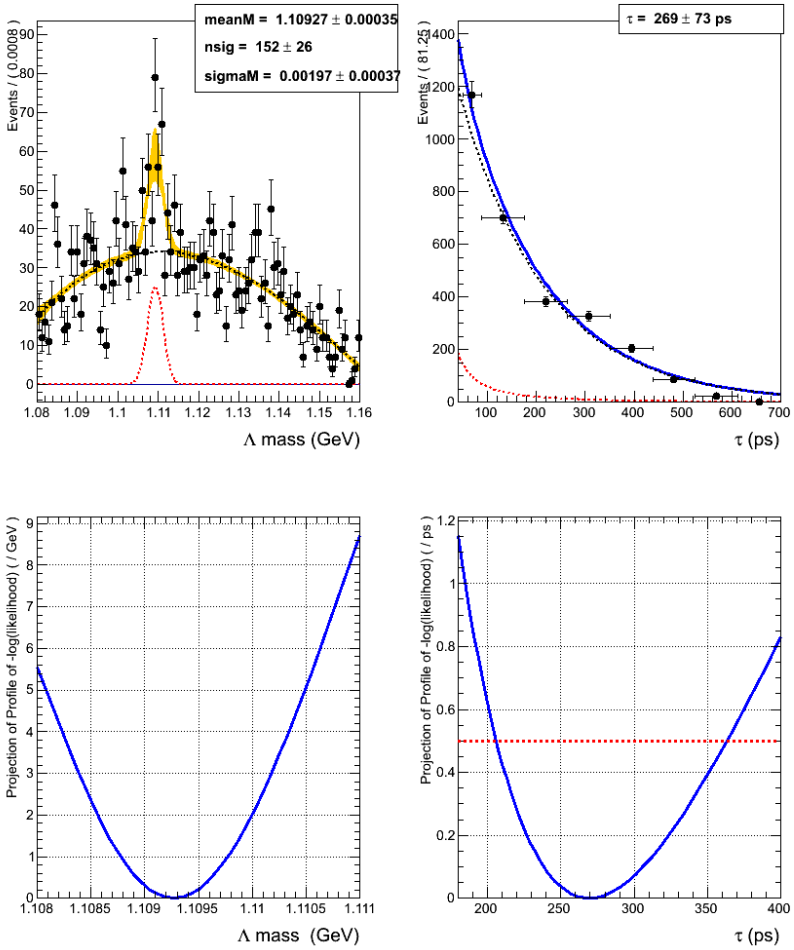

Figure 5.36: Invariant mass and proper decay time distributions for the Λ candidates selected in the real data. The left column shows on the top the fitted invariant mass distribution overlayed with the extracted signal (in red) and the background (in blue) and down the profile logarithm likelihood as a function of the fitted mass parameter. The right columns shows the fitted proper decay time distribution overlayed with the extracted signal (in red) and the background (in blue) together with the profile logarithm likelihood as a function of the fitted proper decay time parameter. The decay time errors are clearly asymmetric.

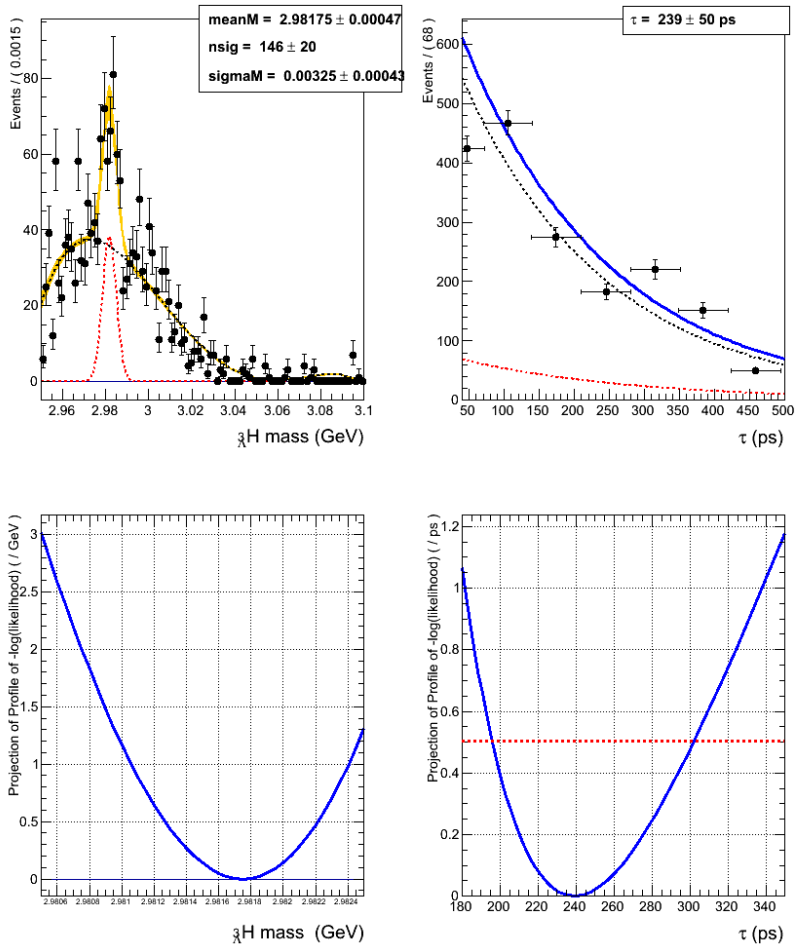

Figure 5.37: Invariant mass and proper decay time distributions for the ${}^{3}_{\Lambda}\mathrm{H}$ candidates selected in the real data. The left column shows on the top the fitted invariant mass distribution overlayed with the extracted signal (in red) and the background (in blue) and down the profile logarithm likelihood as a function of the fitted mass parameter. The right columns shows the fitted proper decay time distribution overlayed with the extracted signal (in red) and the background (in blue) together with the profile logarithm likelihood as a function of the fitted proper decay time parameter. The decay time errors are clearly asymmetric.

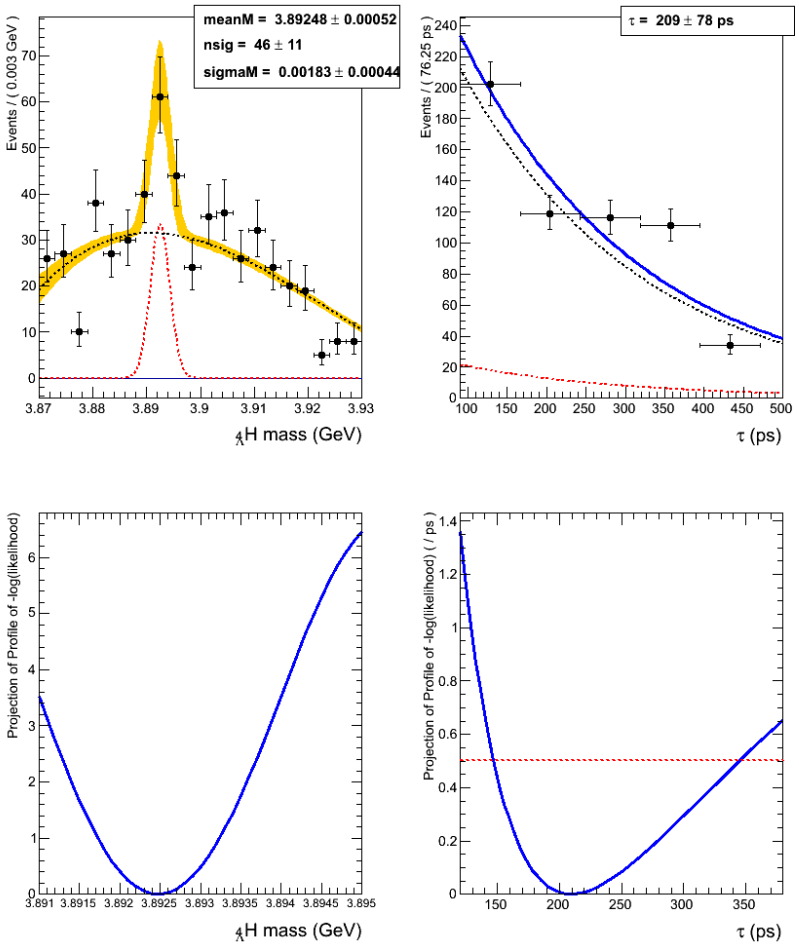

Figure 5.38: Invariant mass and proper decay time distributions for the ${}^{4}_{\Lambda}$H candidates selected in the real data. The left column shows on the top the fitted invariant mass distribution overlayed with the extracted signal (in red) and the background (in blue) and down the profile logarithm likelihood as a function of the fitted mass parameter. The right columns shows the fitted proper decay time distribution overlayed with the extracted signal (in red) and the background (in blue) together with the profile logarithm likelihood as a function of the fitted proper decay time parameter. The decay time errors are clearly asymmetric.

5.7.4 Estimation of the ratio ${}^{3}_{\Lambda}\mathrm{H}$ / ${}^{4}_{\Lambda}\mathrm{H}$

The yield ratio ${}^{3}_{\Lambda}\mathrm{H}$ / ${}^{4}_{\Lambda}\mathrm{H}$ can be deduced from the result obtained from the fitted invariant mass spectra with *signal + background* model. The trigger efficiency is assumed to be similar for both reconstructed decays. One can express the ratio as

$$\frac{N({}^{3}_{\Lambda}\mathrm{H})}{N({}^{4}_{\Lambda}\mathrm{H})} = \frac{N^{obs}_{{}^{3}_{\Lambda}\mathrm{H}} \times \frac{\Gamma_{tot}({}^{3}_{\Lambda}\mathrm{H})}{\Gamma_{\pi^-}({}^{3}_{\Lambda}\mathrm{H})} \times \frac{1}{\varepsilon({}^{3}_{\Lambda}\mathrm{H})}}{N^{obs}_{{}^{4}_{\Lambda}\mathrm{H}} \times \frac{\Gamma_{tot}({}^{4}_{\Lambda}\mathrm{H})}{\Gamma_{\pi^-}({}^{4}_{\Lambda}\mathrm{H})} \times \frac{1}{\varepsilon({}^{4}_{\Lambda}\mathrm{H})}} \tag{5.14}$$

Assuming that the branching ratio for ${}^{3}_{\Lambda}\mathrm{H} \rightarrow \pi^- + {}^{3}\mathrm{He}$ is $\sim 25\%$ and branching ratio for ${}^{4}_{\Lambda}\mathrm{H} \rightarrow \pi^- + {}^{4}\mathrm{He}$ is $\sim 50\%$, and using for the reconstruction efficiency respectively

- $\varepsilon({}^{3}_{\Lambda}\mathrm{H}) = 0.0211416 \pm 0.000198$
- $\varepsilon({}^{4}_{\Lambda}\mathrm{H}) = 0.0163757 \pm 0.000192$

one obtains the following value for the yield ratio $N({}^{3}_{\Lambda}\mathrm{H})/N({}^{4}_{\Lambda}\mathrm{H}) = 2.94 \pm 0.69$. The same ratio can be calculated using the results obtained with the Kalman vertex fit (presented in the Appendix C). In this case the result is $N({}^{3}_{\Lambda}\mathrm{H})/N({}^{4}_{\Lambda}\mathrm{H}) = 3.21 \pm 1.11$ which is compatible with the previous value within the statistical errors. It demonstrates that both methods are in agreement. The weighted mean is 3.02 ± 0.59.

If the theoretical explanation for the hypernuclear production in peripheral heavy ion collisions is described only by the coalescence scenario, the ${}^{3}_{\Lambda}\mathrm{H}$ and ${}^{4}_{\Lambda}\mathrm{H}$ would be respectively formed by the coalescence of $deuteron + \Lambda$ and $triton + \Lambda$. It would mean that the ratio of ${}^{3}_{\Lambda}\mathrm{H}/{}^{4}_{\Lambda}\mathrm{H}$ is comparable to the ratio of the numbers of deuterons to the numbers of tritons produced in the fragmentation reaction together with a Λ-hyperon in the rapidity region of the reconstructed hypernuclei assuming the coalescence phenomenon is independent of the isospin of the involved systems.

Recent theoretical studies show that several additional concurrent production mechanisms could be involved into the hypernuclei formation in the heavy ion collision and especially at the projectile rapidity, such as pion-/kaon- secondary induced reaction [64, 72] and Fermi break-up [75]. Those subsidiary mechanisms could contribute in different ways to the ratios $N({}^{3}_{\Lambda}\mathrm{H})/N({}^{4}_{\Lambda}\mathrm{H})$ and $N(d)/N(t)$.

The number of observed tritons and deuterons detected with the minimum bias trigger flag was deduced from the fit of the momentum distribution of the particle with $Z = 1$ [76]

$$\frac{N(\mathrm{d})}{N(\mathrm{t})} = \frac{N^{obs}_{\mathrm{d}} \times \frac{1}{\varepsilon(\mathrm{d})}}{N^{obs}_{\mathrm{t}} \times \frac{1}{\varepsilon(\mathrm{t})}} = 2.58 \pm 0.29. \tag{5.15}$$

This value can be compared with that deduced from the hybrid theoretical model, the Dubna cascade model (DCM) including Fermi break-up [75]. The obtained theoretical value is $N(d)/N(t) = 2.56$[1]. This model also predicts the hypernuclei

[1] A. Botvina, personal communication

yield ratio $N(^{3}_{\Lambda}\mathrm{H})/N(^{4}_{\Lambda}\mathrm{H}) = 5.0$ which is larger then the extracted ratio mentioned above.

Unfortunately the present version of coalescence model described by [72] does not generate any $^{4}_{\Lambda}$H in the projectile rapidity region [77], which is not realistic and requires the additional work on these calculations.

The observed values for $N(\mathrm{d})/N(\mathrm{t}) = 2.58 \pm 0.29$ and $N(^{3}_{\Lambda}\mathrm{H})/N(^{4}_{\Lambda}\mathrm{H}) = 3.02 \pm 0.59$ are supporting, within errors, the coalescence model as a main mechanism of the hypernuclear production in heavy ion induced reaction at the projectile rapidity [19]. However, this small difference between 2.58 and 3.02, not significant at present, may be taken as an indication that additional processes are involved in the hypernuclear formation. It leaves room for additional studies with a higher experimental accuracy and more detail theoretical calculations.

Chapter 6

Summary and Outlook

The aim of the HypHI Phase 0 experiment is to demonstrate the feasibility of the hypernuclear production in heavy ion induced reactions where the reaction mechanism is well explained by the participant-spectator model. In the peripheral high energy heavy ions collision a hyperon is produced in the participant region at mid-rapidity and may coalesce with a projectile fragments, so that the velocity of hypernuclei is close to that of the projectile. This gives a unique opportunity to study hypernuclei in flight: because of an energy threshold of 1.6 GeV for the Λ production in the elementary process $NN \rightarrow \Lambda KN$, high incident energies have to be chosen. The produced hypernuclei have thus a large velocity and so a large Lorentz factor leading to a longer effective lifetime. It also makes feasible to produce hypernuclei far from the β-stability line and to study several hypernuclei within the same data set, because the variety of produced hypernuclei depends on the variety of isotopes produced in the reaction.

The HypHI Phase 0 experiment was performed in October 2009 at GSI with ^{6}Li beams on a ^{12}C target with an average intensity of 3×10^{6} particles per second. The integrated luminosity is 0.06 pb^{-1}. The experimental setup is a typical forward spectrometer setup with the ALADiN dipole magnet operated at 0.75 T. It consists of arrays of scintillator fiber detectors placed in front of the magnet and a drift chamber associated with time-of-flight walls behind the magnet, which were used for the momentum reconstruction and the particle identification.

A dedicated track fitting algorithm based on the Kalman Filter technique was implemented for the track reconstruction. In order to improve the performance of the method, a precise calculation of the physical effects, mainly the energy loss and multiple scattering effects affecting the track parameters and its errors, have been included at each iteration of the Kalman filter algorithm. In order to optimize the removal of fake tracks, the *canonical* Kalman filter has been modified and supplemented by a smoothing algorithm.

Two independent secondary-vertex fitting algorithms, a global χ^2 fit and an iterative vertex fit based on the Kalman filter approach, were developed in order to perform secondary vertex reconstruction with a statistical selection criterion. The obtained results are shown in the Figure 6.1, and fit results are summarized in Table 6.1. The obtained masses are in excellent agreement, within typically 2 MeV, with the results of [76]. The widths are smaller which is due to the improved methods used. It shows that addition of the vertex fitting improve significantly the final invariant mass resolution. A comparison of the methods applied here shows

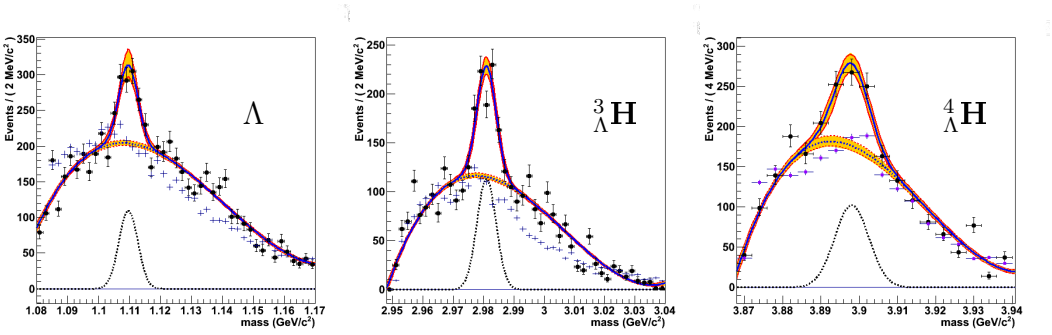

Figure 6.1: Invariant mass distribution (black dots) fitted with the *signal+ background* distribution for Λ (left), $^{3}_{\Lambda}$H (middle) and $^{4}_{\Lambda}$H (right). The blue lines represent the most probable solution returned by the fit, the red lines and yellow area show the 1σ uncertainty band. The light purple markers correspond to the scaled mixed event invariant mass distributions

Table 6.1: Summary of the obtained results with the χ^2 fit (first three rows) and with the Kalman fit (bottom three rows).

	Particle	integral	mean value [MeV/c^2]	σ [MeV/c^2]	significance [σ]
	Λ	417 ± 54	1109.6 ± 0.4	3.04 ± 0.41	9.8
χ^2	$^{3}_{\Lambda}$H	323 ± 36	2981.0 ± 0.3	3.16 ± 0.25	12.8
	$^{4}_{\Lambda}$H	170 ± 21	3898.1 ± 0.7	4.47 ± 0.66	7.3
	Λ	658 ± 73	1110.3 ± 0.5	3.57 ± 0.42	12.0
KF	$^{3}_{\Lambda}$H	417 ± 43	2981.3 ± 0.4	4.61 ± 0.37	10.8
	$^{4}_{\Lambda}$H	201 ± 44	3896.1 ± 1.1	6.39 ± 1.05	6.2

that the widths are method dependent.

An unbinned-likelihood lifetime fit was achieved using the results obtained from the χ^2 vertex fit. The obtained lifetime of the Λ-hyperon is 269.37 $^{+93.13}_{-62.57}$ ps which is in good agreement with the known value of 263 ps [4]. The deduced lifetime of the hypernuclei are 239.07 $^{+61.19}_{-43.72}$ and 209.39 $^{+135.34}_{-64.72}$ ps for $^{3}_{\Lambda}$H and $^{4}_{\Lambda}$H, respectively. The obtained results are compared to the world known data in Figure 6.2 and are seen to be in agreement within the errors, giving additional support for the validity of the obtained results.

The observed rapidity distribution, shown in Chapter 5 in Figure 5.31, shows that the reconstructed particles are observed at the projectile rapidity region which was expected from several theoretical models [19, 71, 72, 73].

The yield ratio $N(^{3}_{\Lambda}\mathrm{H})/N(^{4}_{\Lambda}\mathrm{H})$ was found to be 3.02±0.59 and the ratio $N(d)/N(t)$ with the minimum bias trigger flag was deduced to be 2.58 ± 0.29. The values are very similar, in fact overlapping within their uncertainties, which may be considered as generally supporting coalescence as a dominant mechanism for the hypernuclear

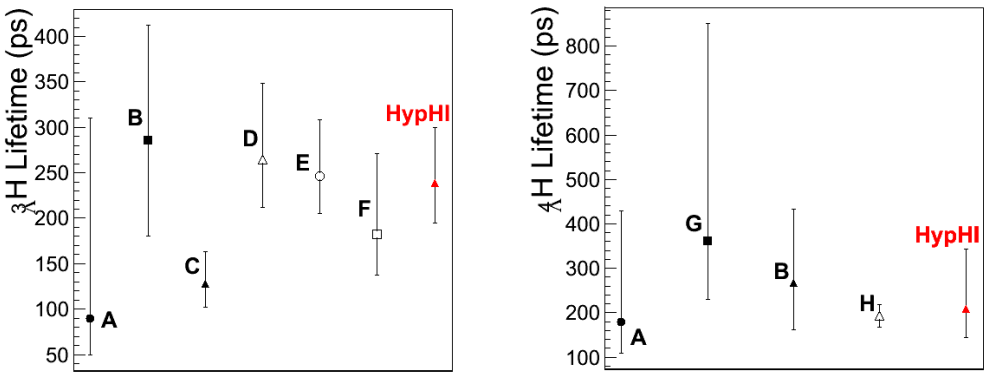

Figure 6.2: The world data on the lifetime of $^{3}_{\Lambda}$H (left panel) and $^{4}_{\Lambda}$H (right panel) from the following references: A [78], B [79], C [80], D [81], E [82], F [23], G [83], H [69]. The red markers represent results obtained in the current work.

production. However, the theoretical approaches to explain this mechanism of the hypernuclear production in heavy ion collisions have uncertainties regarding the concurrent physics processes that are involved.

First of all, theoretical models based on a coalescence phenomenon as a primary source of hypernuclear production use a fixed coalescence radius which may be oversimplified [19, 72].

Furthermore, secondary processes exist and are considered in several theoretical models. At first only pion-/kaon-induced production mechanisms were taken into account [84], which had impacts on the results obtained with different models [72, 84, 64]. Later on, the Fermi break-up of excited hypernuclei has been discussed [75], which has several uncertainties with respect to the excitation-energy distribution which affect the importance of this mechanism for the hypernuclear formation.

The obtained value of 3.02 ± 0.59 for the ratio $N(^{3}_{\Lambda}\mathrm{H})/N(^{4}_{\Lambda}\mathrm{H})$ reflects all these concurring mechanisms and may permit new insight regarding the fundamental processes involved in the formation of hypernuclei in heavy-ion induced reactions.

As a final conclusion the present work proves the feasibility of the study of hypernuclei produced in peripheral heavy ion collisions at projectile rapidity region. This method gives an unique opportunity to study several hypernuclei within the same data taking.

Appendix A

Distance and points of closest approach for track pairs

The method for obtaining the distance of closest approach of two trajectories in three-dimensional space, and the point on each trajectory that is closest to the other (the point of closest approach) is described. The calculations are done for straight lines but can be generalized for curved lines. The distance and points of closest approach are crucial in the first approximation of the vertex position by the vertex finding algorithm.

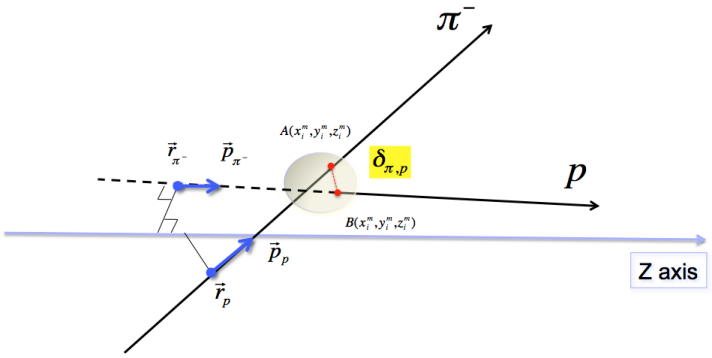

Figure A.1: Distance and points of closest approach for tracks pairs coming from a $\Lambda^0 \to \pi^- + p$ decay. $\delta_{(\pi^-,p)} = \parallel \vec{AB} \parallel$.

The method is based on purely geometrical consideration as shown in figure A.1. The equation defining the straight tracks are

$$\vec{r_p} = \vec{r_{0,p}} + \vec{u_p} \cdot t_p \tag{A.1}$$

$$\vec{r_\pi} = \vec{r_{0,\pi}} + \vec{u_\pi} \cdot t_\pi \tag{A.2}$$

with $\vec{r_p}$ representing the position on the positively charged track (proton) and $\vec{r_\pi}$ the negatively charged one. $r_{0,(\vec{p},\pi)}$ are the position vectors of the given position, $\vec{u_{p,\pi}}$ are the unit vector in the direction of the track momentum i.e

$$\vec{u_{p,\pi}} = \frac{\vec{p_{p,\pi}}}{\parallel \vec{p_{p,\pi}} \parallel} \tag{A.3}$$

and $t_{p,\pi}$ are parameters describing position on the tracks.
The distance vector between the two tracks is

$$\vec{\delta_{p,\pi}} = \vec{r_p} - \vec{r_\pi} = \vec{r_{0,p}} - \vec{r_{0,\pi}} + \vec{u_p} \cdot t_p - \vec{u_\pi} \cdot t_\pi \tag{A.4}$$

and using the notation $\delta\vec{r_0} = \vec{r_{0,p}} - \vec{r_{0,\pi}}$, the distance squared reads:

$$\| \vec{\delta_{p,\pi}} \|^2 = \delta\vec{r_0}^2 + 2\delta\vec{r_0} \cdot \vec{u_p} \cdot t_p - 2\delta\vec{r_0} \cdot \vec{u_\pi} \cdot t_\pi - 2\vec{u_p} \cdot \vec{u_\pi} \cdot t_\pi \cdot t_p + t_p^2 + t_\pi^2$$

The derivatives with respect to the parameters t's are

$$\frac{\partial \| \vec{\delta_{p,\pi}} \|^2}{\partial t_p} = 0 = 2\delta\vec{r_0} \cdot \vec{u_p} - 2\vec{u_p} \cdot \vec{u_\pi} \cdot t_\pi + 2t_p$$

$$\frac{\partial \| \vec{\delta_{p,\pi}} \|^2}{\partial t_\pi} = 0 = 2\delta\vec{r_0} \cdot \vec{u_\pi} - 2\vec{u_p} \cdot \vec{u_\pi} \cdot t_p + 2t_\pi$$

The derivatives rewritten in canonical form are:

$$\frac{\partial \| \vec{\delta_{p,\pi}} \|^2}{\partial t_p} = t_p - (\vec{u_p} \cdot \vec{u_\pi}) \cdot t_\pi = -\delta\vec{r_0} \cdot \vec{u_p}$$

$$\frac{\partial \| \vec{\delta_{p,\pi}} \|^2}{\partial t_\pi} = t_\pi - (\vec{u_p} \cdot \vec{u_\pi}) \cdot t_p = \delta\vec{r_0} \cdot \vec{u_\pi}$$

the solutions of the linear system are

$$t_p = \frac{[-\delta\vec{r_0} \cdot \vec{u_p} + (\delta\vec{r_0} \cdot \vec{u_\pi}) \cdot (\vec{u_\pi} \cdot \vec{u_p})]}{1 - (\vec{u_\pi} \cdot \vec{u_p})^2}$$

$$t_\pi = \frac{[-\delta\vec{r_0} \cdot \vec{u_\pi} + (\delta\vec{r_0} \cdot \vec{u_p}) \cdot (\vec{u_\pi} \cdot \vec{u_p})]}{1 - (\vec{u_\pi} \cdot \vec{u_p})^2}$$

The values of (t_p, t_π) can be substitued into equations A.1 and A.2 respectively in order to obtain the point on each line that is closest to the other.
The method can be generalized to two tracks having curvature. In this case, the equations A.1 and A.2 include a term describing the curve:

$$\vec{r_p} = \vec{r_{0,p}} + \vec{u_p} \cdot t_p + c_p \cdot t_p^2 \tag{A.5}$$

$$\vec{r_\pi} = \vec{r_{0,\pi}} + \vec{u_\pi} \cdot t_\pi + c_\pi \cdot t_\pi^2 \tag{A.6}$$

where

$$c_{p,\pi} = \mathbf{k} \cdot \frac{\vec{u_{p,\pi}} \times \hat{y}}{|\vec{u_{p,\pi}} \times \hat{y}|}$$

the unit vectors $\vec{u_{p,\pi}}$ are perpendicular to both the momentum and the y-axis muliplied by $\mathbf{k}$ a parameter describing the curve.

Appendix B

Covariance matrice conversion

The change of the track representation from canonical state representation used in the Kalman track reconstruction algorithm:

$$\vec{\mathbf{q_A}}^T = (x, y, t_x, t_y, Q/p_{xz})_{z=z_{ref}} \tag{B.1}$$

to the representation adopted in the vertex reconstruction algorithm can be considered as a two step transformation $(\mathbf{A}) \rightarrow (\mathbf{B}) \rightarrow (\mathbf{C})$:

$$\vec{\mathbf{q_A}}^T : (x, y, t_x, t_y, Q/p) \rightarrow \vec{\mathbf{q_B}}^T : (x, y, z, t_x, t_y, Q/p) \rightarrow \vec{\mathbf{q_C}}^T : (x, y, z, p_x, p_y, p_z, E)$$

The (5×5) covariance matrix $\mathbf{V_A}$ for the parameters $\vec{\mathbf{q_A}}$ is well assumed to be well-defined and non-singular: $\mathbf{G_A} = \mathbf{V_A}^{-1}$. Both corresponding covariance matrices for the parameters $\vec{\mathbf{q_B}}$ and $\vec{\mathbf{q_C}}$, $\mathbf{V_A}(6 \times 6)$ and $\mathbf{V_C}(7 \times 7)$ are either singular or not existing. It can be shown that one can define the formal inverse covariance matrix $\mathbf{G_B} = \mathbf{V_B}^{-1}$ but there is not way to define neither the proper matrix $\mathbf{V_C}$ nor the proper matrix $\mathbf{G_C}$.
The re-parametrization $\vec{\mathbf{q_A}} \rightarrow \vec{\mathbf{q_B}}$ with *additionnal* parameter z does not allow to write the sensible covariance matrix for $\vec{\mathbf{q_B}}$. But one can write the *formal* expression for the inverse covariance matrix:

$$\mathbf{G_B} = \mathbf{J^T_{A \rightarrow B}} \cdot \mathbf{G_A} \cdot \mathbf{J_{A \rightarrow B}} \tag{B.2}$$

and the Jacobian of the $(\boldsymbol{A \rightarrow B})$ transformation reads:

$$\mathbf{J_{A \rightarrow B}} = \left[\frac{\partial \vec{\mathbf{q_A}}}{\partial \vec{\mathbf{q_B}}}\right] = \begin{pmatrix} 1 & 0 & -t_x & -z & 0 & 0 \\ 0 & -1 & -t_y & 0 & -z & 0 \\ 0 & 0 & 0 & 1 & 0 & 0 \\ 0 & 0 & 0 & 0 & 1 & 0 \\ 0 & 0 & 0 & 0 & 0 & 1 \end{pmatrix} \tag{B.3}$$

The matrix $\mathbf{J_{A \rightarrow B}}$ could be represented in a more simple way as a block matrix:

$$\mathbf{J_{A \rightarrow B}} = \begin{pmatrix} \mathbf{V} & \mathbf{U} \\ 0 & 1 \end{pmatrix}$$

where the matrices $\mathbf{V}(2 \times 3)$ and $\mathbf{U}(2 \times 3)$ and correspondingly the Jocabian transformation $\mathbf{J_{A \rightarrow B}}$ have the following block structure:

$$\mathbf{V} = \begin{pmatrix} 1 & 0 & -t_x \\ 0 & 1 & -t_y \end{pmatrix} \quad , \qquad \mathbf{U} = \begin{pmatrix} -z & 0 & 0 \\ 0 & -z & 0 \end{pmatrix} \quad \mathbf{J^T_{A \rightarrow B}} = \begin{pmatrix} \mathbf{V^T} & 0 \\ \mathbf{U^T} & 1 \end{pmatrix}$$

The above block structure for $\mathbf{V}(2\times 3)$, $\mathbf{U}(2\times 3)$ and $\mathbf{J_{A\to B}}$ can be used to write:

$$\begin{aligned}
\mathbf{G_B} &= \mathbf{J^T_{A\to B}}\cdot\mathbf{G_A} = \begin{pmatrix}\mathbf{V^T} & 0\\ \mathbf{U^T} & 1\end{pmatrix}\cdot\begin{pmatrix}\mathbf{G_{Ax}} & \mathbf{G_{Axt}}\\ \mathbf{G^T_{Axt}} & \mathbf{G_{At}}\end{pmatrix}\cdot\begin{pmatrix}\mathbf{V} & \mathbf{U}\\ 0 & 1\end{pmatrix} = \begin{pmatrix}\mathbf{G_{Bx}} & \mathbf{G_{Bxt}}\\ \mathbf{G^T_{Bxt}} & \mathbf{G_{Bt}}\end{pmatrix}\\
\mathbf{G_{Bx}} &= \mathbf{V^T}\cdot\mathbf{G_{Ax}}\cdot\mathbf{V}\\
\mathbf{G_{Bxt}} &= \mathbf{V^T}\cdot\mathbf{G_{Ax}}\cdot\mathbf{U^T}+\mathbf{V^T}\cdot\mathbf{G_{Axt}}\\
\mathbf{G_{Bt}} &= \mathbf{U^T}\cdot\mathbf{G_{Ax}}\cdot\mathbf{U}+\mathbf{U^T}\cdot\mathbf{G_{Axt}}+\mathbf{G^T_{Axt}}\cdot\mathbf{U}+\mathbf{G_{At}}
\end{aligned}$$

The block representation of the matrix $\mathbf{G_A}$ has been used:

$$\mathbf{G_A} = \begin{pmatrix}\mathbf{G_{Ax}} & \mathbf{G_{Axt}}\\ \mathbf{G_{Axt}} & \mathbf{G_{At}}\end{pmatrix}$$

The (6×6) matrix $\mathbf{G_B}$ is singular of rank 5. The upper top (3×3) block

$$\mathbf{G_{Bx}} = \mathbf{V^T G_{Ax} V}$$

is a singular rank 2 matrix while the the lower right block $\mathbf{G_{At}}$ is generally not singular and so has the inverse $\mathbf{G_{At}}^{-1}$. The components of the inverse are:

$$\mathbf{V_B} = \mathbf{G_B^{-1}} = \begin{pmatrix}\mathbf{V_{Bx}} & \mathbf{V_{Bxt}}\\ \mathbf{V^T_{Bxt}} & \mathbf{V_{Bt}}\end{pmatrix}$$

The parametrization $\boldsymbol{(A\to B)}$ formally allows to express the covariance matrix $\mathbf{V_C}$ throught the matrix $\mathbf{V_B}$ as:

$$\begin{aligned}
\mathbf{V_C} &= \mathbf{J_{C\to B}V_B J^T_{C\to B}}\\
\mathbf{J_{C\to B}} &= \left[\frac{\partial\vec{\mathbf{q_C}}}{\partial\vec{\mathbf{q_B}}}\right] = \begin{pmatrix}1 & 0\\ 0 & \mathbf{K}\end{pmatrix}
\end{aligned}$$

The matrix $\mathbf{J_{C\to B}}(7\times 6)$ is represented as block matrix where the $\mathbf{K}$ component matrix is defined as:

$$\mathbf{K} = \left[\frac{\partial(p_x,p_y,p_z,E)}{\partial(t_x,t_y,t_z)}\right] = \begin{pmatrix} p_z\dfrac{1+t_y^2}{1+t_x^2+t_y^2} & -p_z\dfrac{t_xt_y}{1+t_x^2+t_y^2} & -p_z\cdot p\cdot Q\\ -p_z\dfrac{t_xt_y}{1+t_x^2+t_y^2} & p_z\dfrac{1+t_x^2}{1+t_x^2+t_y^2} & -p_y\cdot p\cdot Q\\ -p_z\dfrac{}{1+t_x^2+t_y^2} & -p_z\dfrac{}{1+t_x^2+t_y^2} & -p_z\cdot p\cdot Q\\ 0 & 0 & -\dfrac{p^3}{E}\cdot Q\end{pmatrix}$$

The $\mathbf{V_C}$ expression reads:

$$\mathbf{V_C} = \begin{pmatrix}\mathbf{V_{Cx}} & \mathbf{V_{Cxt}}\\ \mathbf{V^T_{Cxt}} & \mathbf{KV_{Ct}}\end{pmatrix} = \begin{pmatrix}\mathbf{V_{Bx}} & \mathbf{V_{Bxt}K^T}\\ \mathbf{KV^T_{Bxt}} & \mathbf{KV_{Bt}K^T}\end{pmatrix}$$

where the lower right (4×4) block of the matrix $\mathbf{V_{Ct}} = \mathbf{K V_{Bt} K^T}$ is singular. Comparing these expressions gives all formal expression needed for the Kalman Filter based vertex fitting procedure:

$$\begin{array}{rcll} \mathbf{G_{Cx}} - \mathbf{G_{Cxp}} \mathbf{G_{Cp}^{-1}} \mathbf{G_{Cxp}^T} & = & \mathbf{V_{Cx}^{-1}} & = & \mathbf{G_{Bx}} - \mathbf{G_{Bxt}} \mathbf{G_{Bt}^{-1}} \mathbf{G_{Bxt}^T} \\ \mathbf{G_{Cp}^{-1}} & = & \mathbf{V_{Cp}} - \mathbf{V_{Cxp}^T} \mathbf{V_{Cx}^{-1}} \mathbf{V_{Cxp}} & = & \mathbf{K G_{Bt}^{-1}} K^T \\ \mathbf{G_{Cp}^{-1}} \mathbf{G_{Cxp}^T} & = & -\mathbf{V_{Cxp}^T} \mathbf{V_{Cx}^{-1}} & = & -\mathbf{K G_{Bt}^{-1}} \mathbf{G_{Bxt}^T} \end{array}$$

Eventhough neither the matrix $\mathbf{V_B}$ nor matrices $\mathbf{V_C}, \mathbf{G_C}$ could be constructed explicitely, all required matrix expressions needed for the Kalman Filter based vertex algorithm are valid matrix expressions.

Appendix C

Result of the data analysis with KF vertex fit

This appendix presents the performance of the Kalman based secondary vertex reconstruction described in Chapter 4 applied for both simulated and real data.

Simulated Data

For the Kalman vertex fit performance check the realistic simulation presented in Chapitre 4 has been used. A set of selection for the particle reconstruction which corresponds to loose criteria has been applied. The choosen selection criteria are summarized in table C.1.

Table C.1: Definition of the loose selection criteria for the reconstructed particles. The variable p_t stands for the Armenteros transverse momentum.

Cut on	Units	Lower bound	Upper bound
$P^{\pi}_{\chi^2}$	val.	0.1	1.
$P^{+}_{\chi^2}$	val.	0.1	1.
p_π	[GeV]	0.5	2.
p_p	[GeV]	0.	4.5
$P^{vtx}_{\chi^2}$	val.	0.01	1.
DCA	[cm]	0.	0.4
z_v	[cm]	0.	35.
p_t	[GeV]	0.	0.1

Real Data

The red hatched histograms in the left panel of Figure C.9 shows the invariant mass distribution for the p + π^-, ^{3}He + π^- and ^{4}He + π^-. The blue hatched histogram are the distributions obtained from mixed event analysis. The scaling factors for the mixed events distributions are determined by the ratio of the areas defined in the Table 5.10.

The right panels of Figure C.9 shows the fitted invariant mass distributions, the fitting procedure was described previously in Chapter 5, background is describes by the Chebyshev polynomial of second order. The results are summarized in the Table C.2.

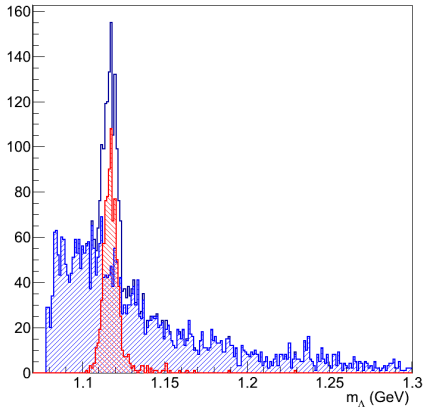

Figure C.1: Λ invariant mass distribution for both signal (red) and background (blue) events using the selection criteria from table C.1.

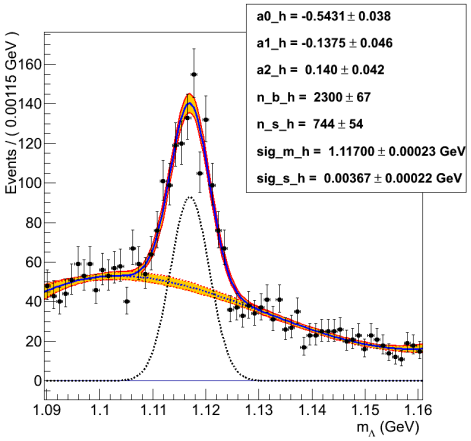

Figure C.2: Unbinned likelihood fit performed on Λ invariant mass distribution reconstructed using the selection criteria from table C.1.

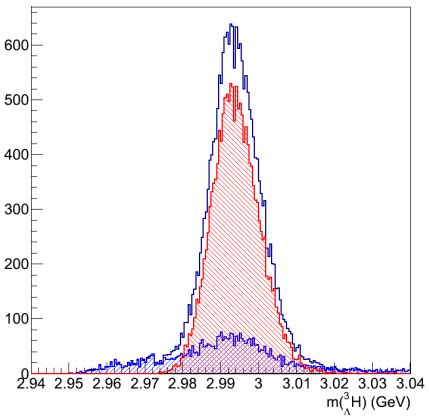

Figure C.3: ${}^{3}_{\Lambda}$H invariant mass distribution for both signal (red) and background (blue) events using the criteria from table C.1.

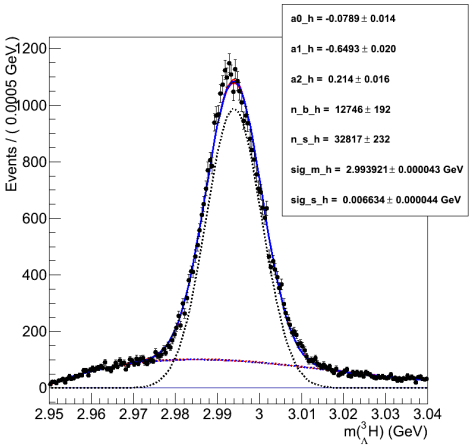

Figure C.4: Unbinned likelihood fit performed on ${}^{3}_{\Lambda}$H Invariant mass distribution reconstructed using the criteria from table C.1.

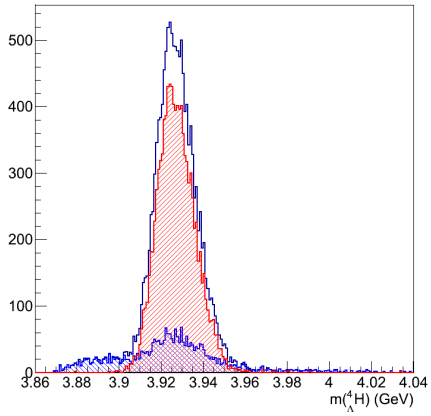

Figure C.5: ${}^{4}_{\Lambda}\mathrm{H}$ invariant mass distribution for both signal (red) and background (blue) events using the criteria from table C.1.

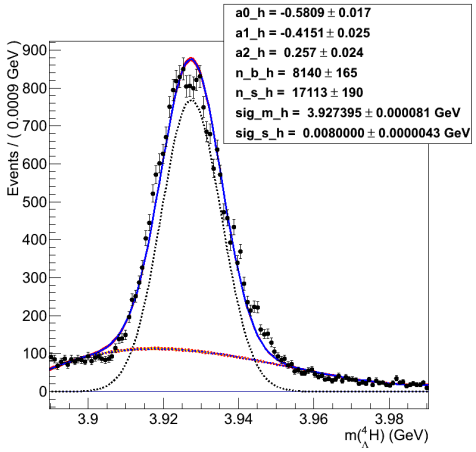

Figure C.6: Unbinned likelihood fit performed on ${}^{4}_{\Lambda}\mathrm{H}$ invariant mass distribution reconstructed using the criteria from table C.1.

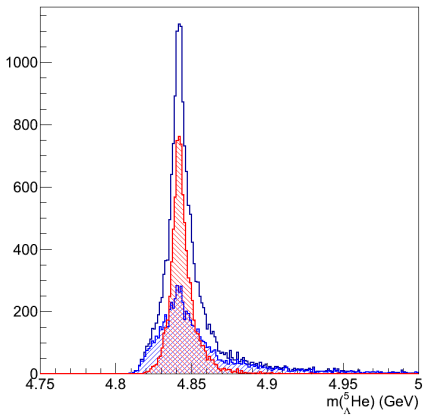

Figure C.7: ${}^{5}_{\Lambda}\mathrm{He}$ invariant mass distribution for both signal (red) and background (blue) events using the criteria from table C.1.

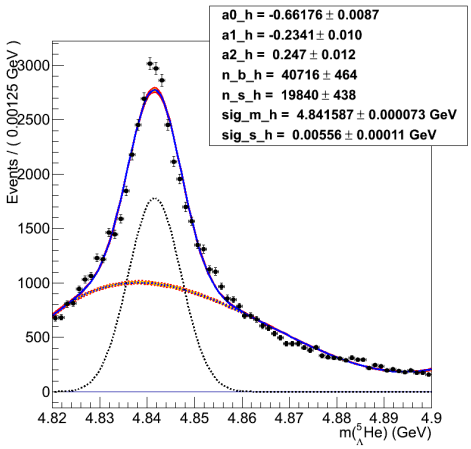

Figure C.8: Unbinned likelihood fit performed on ${}^{5}_{\Lambda}\mathrm{He}$ invariant mass distribution reconstructed using the criteria from table C.1.

Assuming that the branching ratio for ${}^{3}_{\Lambda}\mathrm{H} \rightarrow \pi^{-} + {}^{3}\mathrm{He}$ is $\sim 25\%$ and branching ratio for ${}^{4}_{\Lambda}\mathrm{H} \rightarrow \pi^{-} + {}^{4}\mathrm{He}$ is $\sim 50\%$, and using for the reconstruction efficiency respectively

- $\varepsilon({}^{3}_{\Lambda}\mathrm{H}) = 0.0242265 \pm 0.0002135$
- $\varepsilon({}^{4}_{\Lambda}\mathrm{H}) = 0.0160858 \pm 0.0001900$

one obtains the following value for the yield ratio $N({}^{3}_{\Lambda}\mathrm{H})/N({}^{4}_{\Lambda}\mathrm{H}) = N({}^{3}_{\Lambda}\mathrm{H})/N({}^{4}_{\Lambda}\mathrm{H}) = 3.21 \pm 1.11$ which is compatible with a previous value obtained in Chapter 5 with global χ^2 vertex fit within the statistical errors. It demonstrates that both methods are in agreement.

Table C.2: Summary of the obtained results with the fit KF vertex fit

Particle	integral	mean value [MeV/c^2]	σ [MeV/c^2]	significance [σ]
Λ	658 ± 73	1110.3 ± 0.5	3.57 ± 0.42	12.0
${}^{3}_{\Lambda}\mathrm{H}$	417 ± 43	2981.3 ± 0.4	4.61 ± 0.37	10.8
${}^{4}_{\Lambda}\mathrm{H}$	201 ± 44	3896.1 ± 1.1	6.39 ± 1.05	6.2

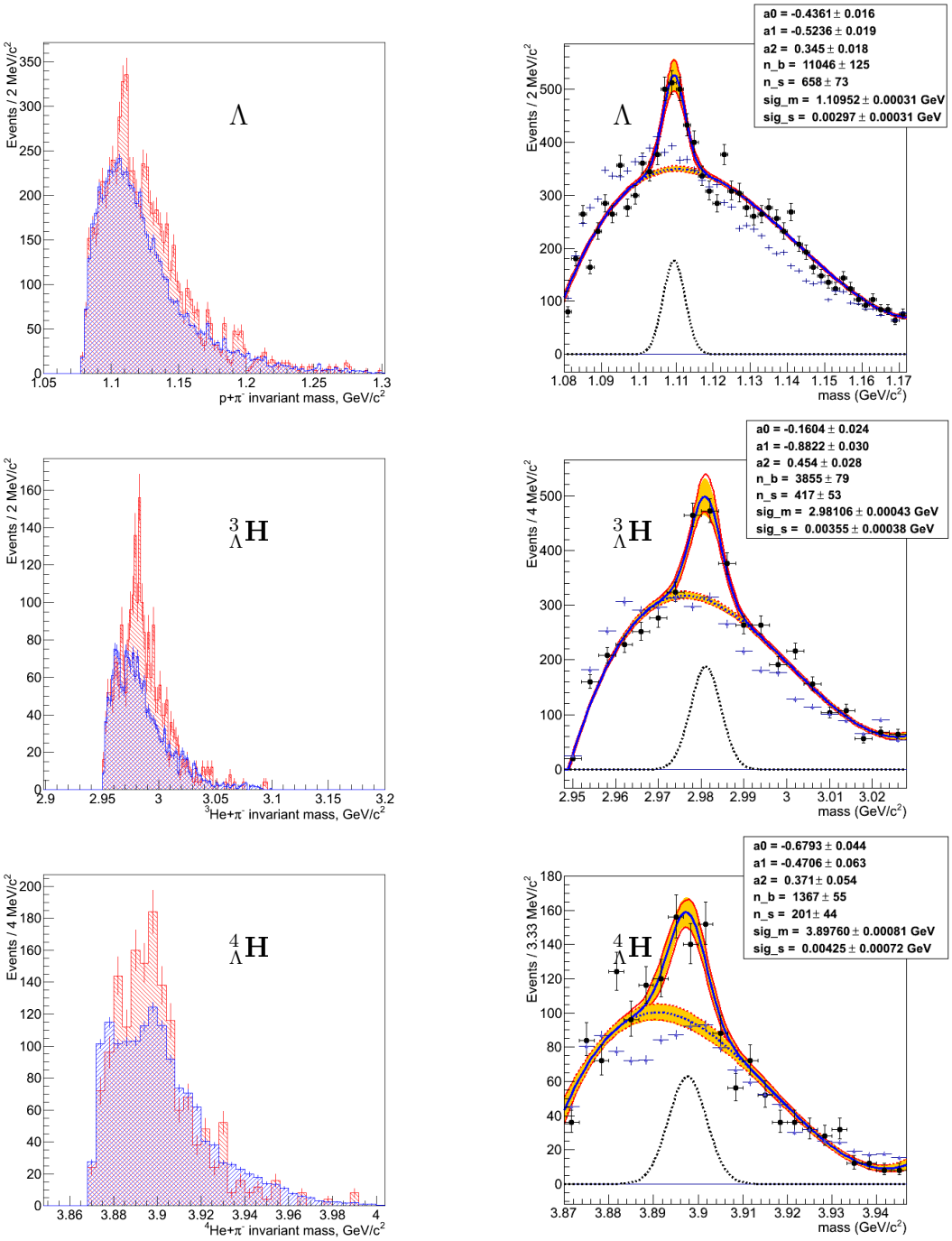

Figure C.9: *Left panels*: Invariant mass spectra of Λ, ${}^{3}_{\Lambda}\mathrm{H}$ and ${}^{4}_{\Lambda}\mathrm{H}$. The distribution includes the target region for the reconstructed vertex position. *Right panels*: Invarian mass distribution (black dots) fitted with the *signal+ background* distributions for Λ, ${}^{3}_{\Lambda}\mathrm{H}$ and ${}^{4}_{\Lambda}\mathrm{H}$. The blue lines represent the most probable solution, the red lines and yellow area show the σ uncertainty band. The light purple markers correspond to the scaled mixed event invariant mass distributions.

Bibliography

[1] F. Weber, R. Negreiros, P. Rosenfield, and M. Stejner. Pulsars as astrophysical laboratories for nuclear and particle physics. *Progress in Particle and Nuclear Physics*, 59(1):94 – 113, 2007. 1

[2] Jürgen Schaffner-Bielich. Hypernuclear physics for neutron stars. *Nuclear Physics A*, 804(1-4):309 – 321, 2008. 1

[3] W.M. Alberico and G. Garbarino. Weak decay of Λ-hypernuclei. *Physics Reports*, 369(1):1 – 109, 2002. 1

[4] Particle data group. 1, 126, 152

[5] M. M. Nagels, T. A. Rijken, and J. J. de Swart. Baryon-baryon scattering in a one-boson-exchange-potential approach. II. Hyperon-nucleon scattering. *Phys. Rev. D*, 15:2547–2564, May 1977. 2

[6] M. M. Nagels, T. A. Rijken, and J. J. de Swart. Baryon-baryon scattering in a one-boson-exchange-potential approach. III. A nucleon-nucleon and hyperon-nucleon analysis including contributions of a nonet of scalar mesons. *Phys. Rev. D*, 20:1633–1645, Oct 1979. 2

[7] P. M. M. Maessen, Th. A. Rijken, and J. J. de Swart. Soft-core baryon-baryon one-boson-exchange models. II. Hyperon-nucleon potential. *Phys. Rev. C*, 40:2226–2245, Nov 1989. 2

[8] Th. A. Rijken, V. G. J. Stoks, and Y. Yamamoto. Soft-core hyperon-nucleon potentials. *Phys. Rev. C*, 59:21–40, Jan 1999. 2

[9] B. Holzenkamp, K. Holinde, and J. Speth. A meson exchange model for the hyperon-nucleon interaction. *Nuclear Physics A*, 500(3):485 – 528, 1989. 2

[10] K. Holinde. The Juelich hyperon-nucleon interaction models. *Nuclear Physics A*, 547(1 - 2):255 – 264, 1992. 2

[11] M. Danysz and J. Pniewski. TDelayed Disintegration of a Heavy Nuclear Fragment. *Philosophical Magazine Series 7*, 44(350):348–350, 1953. 2

[12] O. Hashimoto and H. Tamura. Spectroscopy of hypernuclei. *Progress in Particle and Nuclear Physics*, 57(2):564 – 653, 2006. 2, 3

[13] D.H. Davis. Hypernuclei-the early days. *Nuclear Physics A*, 547(2):369 – 378, 1992. 2

[14] M. May et al. Observation of Levels in ${}^{13}_{\Lambda}$C, ${}^{14}_{\Lambda}$N, and ${}^{18}_{\Lambda}$O Hypernuclei. 3

[15] M. Akel et al. The (π^+, K^+) reaction on ^{12}C and ^{56}Fe. *Nuclear Physics A*, 534(4):478 – 492, 1991. 3

[16] T. Hasegawa et al. Core-Excited States of $^{12}_{\Lambda}$C Hypernuclei Formed in the (π^+, K^+) reaction. 3

[17] H. Tamura and K. Tanida. Observation of a Spin-Flip $M1$ Transition in $^{7}_{\Lambda}$Li. *Phys. Rev. Lett.*, 84:5963–5966, Jun 2000. 3

[18] A. K. Kerman and M. S. Weiss. Superstrange Nuclei. *Phys. Rev. C*, 8:408–410, Jul 1973. 3

[19] M. Wakai, H. Band, and M. Sano. Hypernucleus formation in high-energy nuclear collisions. *Phys. Rev. C*, 38:748–759, Aug 1988. 4, 140, 150, 152, 153

[20] S.A. Bass et al. Microscopic models for ultrarelativistic heavy ion collisions. *Progress in Particle and Nuclear Physics*, 41(0):255–369, 1998. 5, 120

[21] S. Avramenko et al. A study of the production and lifetime of the lightest relativistic hypernuclei. *Nuclear Physics A*, 547(2):95 – 100, 1992. 5

[22] T. A. Armstrong et al. Production of $^{3}_{\Lambda}$H and $^{4}_{\Lambda}$H in central 11.5 GeV/c Au + Pt heavy ion collisions. 5

[23] The STAR Collaboration. Observation of an Antimatter Hypernucleus. *Science*, 328:4, April 2010. 5, 153

[24] T.R. Saito for the HypHI collaboration. Hypernuclei with a Stablle Heavy Ion Beam and RI-beam Induced Reactions at GSI (HypHI), Feb 2005. 5, 121

[25] Jan Steinheimer, Michael Mitrovski, Tim Schuster, Hannah Petersen, Marcus Bleicher, and Horst Stöcker. Strangeness fluctuations and MEMO production at FAIR. *Physics Letters B*, 676(1 - 3):126 – 131, 2009. 5

[26] A. Andronic, P. Braun-Munzinger, J. Stachel, and H. Stöcker. Production of light nuclei, hypernuclei and their antiparticles in relativistic nuclear collisions. *Physics Letters B*, 697(3):203 – 207, 2011. 5

[27] GSI Helmholtzzentrum für Schwerionenforschung GmbH web page. `http://gsi.de`. 9

[28] John J. Livingood. The optics of Dipole Magnets. *Academic Press, New York and London*, 1969. 10, 26

[29] Programmable Trigger Processing Module, VUPROM. *GSI Scientific Report 2007*, page 256, 2007. 12

[30] D. Nakajima et al. Scintillating fiber detectors for the HypHI project at GSI. *Nuclear Instruments and Methods in Physics Research Section A: Accelerators, Spectrometers, Detectors and Associated Equipment*, 608(2):287 – 290, 2009. 15

[31] T. Fukuda et al. The superconducting kaon spectrometer - SKS. *Nuclear Instruments and Methods in Physics Research Section A: Accelerators, Spectrometers, Detectors and Associated Equipment*, 361(3):485 – 496, 1995. 16

[32] K. Miwa et al. Search for the Θ^+ via the $K^+p \to \pi^+X$ reaction with a 1.2 GeV/c K^+ beam. 16

[33] A. Schüttauf et al. Universality of spectator fragmentation at relativistic bombarding energies. *Nuclear Physics A*, 607(4):457 – 486, 1996. 19

[34] H. G. Essel and N. Kurz. The general purpose data acquisition system MBS. *IEEE Transactions on Nuclear Science*, 47:337–339, 2000. 20, 112

[35] C. Amsler. The Review of Particle Physics. *Phys. Lett. B*, page 667, 2008. 24, 40, 41

[36] H. Klinger. Johann Wolfgang Goethe-Universitaet, Frankfurt am Main. *Ph.D. Thesis*, page 667, 1996. 26

[37] A. Gelb. Applied Optimal Estimation. *The MIT press, Cambridge*, 1974. 30

[38] P. Billoir. Track fitting with multiple scattering: a new method. *Nuclear Instruments and Methods in Physics Research*, 225:352–356, 1984. 30

[39] P. Billoir, R. Frühwirth, and M. Regler. Track element merging strategy and vertex fitting in complex modular detectors. *Nuclear Instruments and Methods in Physics Research Section A: Accelerators, Spectrometers, Detectors and Associated Equipment*, 241(1):115 – 131, 1985. 30, 61

[40] M. Regler, R. Frühwirth, and W. Mitaroff. Filter methods in track and vertex reconstruction. *International Journal of Modern Physics C*, 07(04):521–542, 1996. 36

[41] William Press. Numerical recipes 3rd edition: The Art of Scientific Computing. *Cambridge Univ. Press*, A 241, 2007. 39, 44

[42] R. Fruehwirth, M. Regler, R.K. Bock, H. Grote, and D. Notz. Data Analysis Techniques for High Energy Physics. *Cambrige University Press*, 2000. 40, 41, 42, 44, 78, 83

[43] E.J. Wolin and L.L. Ho. Covariance matrices for track fitting with the Kalman filter. *Nucl. Instr. Meth*, A 329:493, 1993. 42

[44] R. Brun and F. Rademakers. ROOT - an object oriented data analysis framework. *Nucl. Instr. and Meth. in Physics Research A*, A389:81–86, 1997. 42, 43, 67, 112

[45] F. Carminati, R. Brun, I. Hrinacova, and A. Morsch. Virtual monte carlo. In *Computing in High Energy and Nuclear Physics*, pages 24–28, 2003. 45, 67

[46] G.N. Patrick and B. Schorr. Vertex fitting of several helices in space . *Nucl. Instr. and Meth.*, A241(132), 1985. 61

[47] P. Billoir and S. Qian. Fast vertex fitting with a local parametrization of tracks. *Nucl. Instr. and Meth.*, A311(139), 1992. 61

[48] Geant3. Detector description and simulation tools. *GEANT3 manual, CERN Program Library Long Writeup W5013*, pages 81–86, 1993. 67

[49] J. List M. Beckmann, B. List. Treatment of Photon Radiation in Kinematic Fits at future e^+ e^- colliders. *Nucl. Instr. and Meth. in Physics Research A*, 624:184–191, 2010. 75

[50] P. Avery. Fitting Theory Writeups and References. *http://www.phy.ufl.edu/ avery/fitting.html*, 1998. 75, 77, 78, 80

[51] S. Brandt. *Statistical and Computational Methods in Data Analysis*. 1970. 77

[52] M. Williams. Kinematic Fitting in CLAS. *CLAS-Note 2003-017*, Nov. 2003. 77

[53] Wikipedia, Chi distribution. `http://en.wikipedia.org/wiki/Chi_distribution`. 84

[54] R.E Kalman. New Method and Results in Linear Prediction an Filtering Theory. *RIAS Techn. Report 61-1*, 1961. 83

[55] R. Fruehwirth. Application of Kalman filtering to track and vertex fitting . *Nucl. Instr. and Meth.*, A262:444, 1987. 83, 84

[56] Wouter D. Hulsbergen. Decay chain fitting with a kalman filter. *Nuclear Instruments and Methods in Physics Research Section A: Accelerators, Spectrometers, Detectors and Associated Equipment*, 552(3):566 – 575, 2005. 85, 86, 87

[57] Volker Blobel and Erich Lohrmann. Statistische und numerische Methoden der Datenanalyse. *Teubner Studienbücher, B.G. Teuchner, Stuttgart*, 1998. 89

[58] J. Adamczewski, M. Al-Turany, D. Bertini, H. G. Essel, M. Hemberger, N. Kurz, and M. Richter. Go4 multitasking class library with ROOT. *IEEE Transactions on Nuclear Science*, 49:521–524, 2002. 112

[59] T. Tanimori et al. A test of 150 cm × 20 cm wide time-of-flight scintillation counters. *Nuclear Instruments and Methods in Physics Research*, 216(1-2):57 – 65, 1983. 114

[60] S. Bianchin, O. Borodina, et al. Progress on the Time-of-Flight detectors for the HypHI project. *GSI Scientific Report 2008*, page 233, 2008. 114

[61] B. Anderson. Parton fragmentation and string dynamics. *Phys. Rev.*, (97):31–145, 1983. 121

[62] E. L. Bratkovskaya. Strangeness dynamics and transverse pressure in relativistic nucleus-nucleus collisions. *Phys. Rev. C*, 054907(69), 2004. 121

[63] H. Lenske T. Gaitanos and U. Mosel. Fragment formation in proton induced reactions within a BUU transport model. *Phys. Lett. B*, (663):197, 2008. 121

[64] J. Steinheimer M. Bleicher A. S. Botvina, K. K. Gudima and I. N. Mishustin. Production of spectator hypermatter in relativistic heavy-ion collisins. *Phys. Rev. C*, 064904(84), 2011. 121, 149, 153

[65] F. James. Monte Carlo Phase Space. *CERN 68-15*, 1968. 121

[66] J. Podolanski and R. Armenteros. III. Analysis of V-events. *Philosophical Magazine Series 7*, 45(360):13–30, 1954. 127

[67] H. Kamada, J. Golak, K. Miyagawa, H. Witała, and W. Glöckle. π-mesonic decay of the hypertriton. *Phys. Rev. C*, 57:1595–1603, Apr 1998. 130

[68] W. Glöckle, K. Miyagawa, H. Kamada, J. Golak, and H. Witala. The hypertriton and its decays. *Nuclear Physics A*, 639(1 - 2):297c – 306c, 1998. Proceedings of the International Conference on Hypernuclear and Strange Particle Physics. 130

[69] H. Outa et al. Mesonic and non-mesonic decay widths of ${}^{4}_{\Lambda}$H and ${}^{4}_{\Lambda}$He. *Nuclear Physics A*, 639(1 - 2):251c – 260c, 1998. Proceedings of the International Conference on Hypernuclear and Strange Particle Physics. 130, 153

[70] J. J. Szymanski et al. Nonleptonic weak decay of ${}^{5}_{\Lambda}$He and ${}^{12}_{\Lambda}$C. *Phys. Rev. C*, 43:849–862, Feb 1991. 130

[71] J. Bondorf, R. Donangelo, I.N. Mishustin, and H. Schulz. Statistical multifragmentation of nuclei: (II). Application of the model to finite nuclei disassembly. *Nuclear Physics A*, 444(3):460 – 476, 1985. 140, 152

[72] T. Gaitanos, H. Lenske, and U. Mosel. Formation of hypernuclei in high energy reactions within a covariant transport model. *Physics Letters B*, 675(3 - 4):297 – 304, 2009. 140, 149, 150, 152, 153

[73] A.S. Botvina, A.S. Iljinov, I.N. Mishustin, J.P. Bondorf, R. Donangelo, and K. Sneppen. Statistical simulation of the break-up of highly excited nuclei. *Nuclear Physics A*, 475(4):663 – 686, 1987. 140, 152

[74] Wolfram. Chebyshev Polynomial of the First Kind. `http://mathworld.wolfram.com/chebyshevpolynomialofthefirstkind.html`. 143

[75] A. S. Botvina, I. N. Mishustin, and J. Pochodzalla. Production of exotic hypernuclei from excited nuclear systems. *Phys. Rev. C*, 86:011601, Jul 2012. 149, 153

[76] Daisuke Nakajima. *Hypernulei productionwith heavy ion reaction of* $^{6}Li + {}^{12}C$ *at* 2 *A GeV*. PhD thesis, The University of Tokyo, Japan, 2011. 149, 151

[77] T. Gaitanos, A.B. Larionov, and U. Mosel. Production of Hypernuclei at FAIR. In *Deutsche Physikalische Gesellschaft Frühjahrstagung*, 2011. 150

[78] R. J. Prem and P. H. Steinberg. Lifetimes of hypernuclei, ${}^{3}_{\Lambda}$H, ${}^{4}_{\Lambda}$H, ${}^{5}_{\Lambda}$H. *Phys. Rev.*, 136:B1803–B1806, Dec 1964. 153

[79] R. E. Phillips and J. Schneps. Lifetimes of light hyperfragments. ii. *Phys. Rev.*, 180:1307–1318, Apr 1969. 153

[80] G. Bohm et al. On the lifetime of the ${}^{3}_{\Lambda}$H ypernucleus. *Nucl. Phys. B*, 16(1):46 – 52, 1970. 153

[81] G. Keyes et al. Properties of ${}^{3}_{\Lambda}$H. *Phys. Rev. D*, 1:66–77, Jan 1970. 153

[82] G. Keyes et al. A measurement of the lifetime of the ${}^{3}_{\Lambda}$H hypernucleus. *Nucl. Phys. B*, 67(2):269 – 283, 1973. 153

[83] Y. W. Kang et al. Lifetimes of light hyperfragments. *Phys. Rev.*, 139:B401–B406, Jul 1965. 153

[84] M. Wakai. Energy dependence of hypernucleus production in high-energy nuclear collision. *Nuclear Physics A*, 547(1 - 2):89 – 93, 1992. 153